

# **Calorimetry at a Future Linear Collider**

Steven Green  
of Emmanuel College

A dissertation submitted to the University of Cambridge  
for the degree of Doctor of Philosophy



# Abstract

This thesis describes the optimisation of the calorimeter design for collider experiments at the future Compact Linear Collider (CLIC) and the International Linear Collider (ILC). The detector design of these experiments is built around high-granularity Particle Flow Calorimetry that, in contrast to traditional calorimetry, uses the energy measurements for charged particles from the tracking detectors. This can only be realised if calorimetric energy deposits from charged particles can be separated from those of neutral particles. This is made possible with fine granularity calorimeters and sophisticated pattern recognition software, which is provided by the PandoraPFA algorithm. This thesis presents results on Particle Flow calorimetry performance for a number of detector configurations. To obtain these results a new calibration procedure was developed and applied to the detector simulation and reconstruction to ensure optimal performance was achieved for each detector configuration considered.

This thesis also describes the development of a software compensation technique that vastly improves the intrinsic energy resolution of a Particle Flow Calorimetry detector. This technique is implemented within the PandoraPFA framework and demonstrates the gains that can be made by fully exploiting the information provided by the fine granularity calorimeters envisaged at a future linear collider.

A study of the sensitivity of the CLIC experiment to anomalous gauge couplings that effect vector boson scattering processes is presented. These anomalous couplings provide insight into possible beyond standard model physics. This study, which utilises the excellent jet energy resolution from Particle Flow Calorimetry, was performed at centre-of-mass energies of 1.4 TeV and 3 TeV with integrated lumi-

nosities of  $1.5\text{ab}^{-1}$  and  $2\text{ab}^{-1}$  respectively. The precision achievable at CLIC is shown to be approximately one to two orders of magnitude better than that currently offered by the LHC.

Finally, a study into various technology options for the CLIC vertex detector is described.

## Declaration

This dissertation is the result of my own work, except where explicit reference is made to the work of others, and has not been submitted for another qualification to this or any other university. This dissertation does not exceed the word limit for the respective Degree Committee.

Andy Buckley



## Acknowledgements

Of the many people who deserve thanks, some are particularly prominent, such as my supervisor...



## **Preface**

This thesis describes my research on various aspects of the LHCb particle physics program, centred around the LHCb detector and LHC accelerator at CERN in Geneva.

For this example, I'll just mention Chapter ?? and Chapter ??.



# Contents

<b>1</b>	<b>Introduction</b>	<b>1</b>
1.1	Future Linear Colliders . . . . .	3
1.1.1	The International Linear Collider . . . . .	3
1.1.2	The Compact Linear Collider . . . . .	4
<b>2</b>	<b>Anomalous Gauge Coupling Theory</b>	<b>9</b>
2.1	The Standard Model . . . . .	9
2.2	Higgs Physics . . . . .	12
2.2.1	Spontaneous Symmetry Breaking . . . . .	13
2.2.2	Electroweak Interactions . . . . .	14
2.3	Effective Field Theory . . . . .	18
2.4	Electroweak Chiral Lagrangian . . . . .	19
<b>3</b>	<b>Particle Flow Calorimetry for Future Linear Colliders</b>	<b>23</b>
3.1	Particle Flow Calorimetry . . . . .	23
3.2	International Large Detector . . . . .	25
3.2.1	Overview . . . . .	26
3.2.2	Vertex Detector . . . . .	27
3.2.3	Time Projection Chamber . . . . .	28
3.2.4	Supplemental Silicon Tracking System . . . . .	29
3.2.5	Electromagnetic Calorimeter . . . . .	31
3.2.6	Hadronic Calorimeter . . . . .	34
3.2.7	Solenoid, Yoke and Muon System . . . . .	35
3.2.8	Forward Calorimetry . . . . .	36
3.3	Simulation . . . . .	38
3.4	CLIC ILD . . . . .	39
3.5	Particle Flow Reconstruction . . . . .	40
3.5.1	PandoraPFA . . . . .	41

3.6	Performance . . . . .	45
3.6.1	Jet Energy Resolution . . . . .	46
3.6.2	Jet Energy Resolution Decompositions . . . . .	48
3.6.3	Single Particle Energy Resolution . . . . .	49
3.7	Summary of ILD Detector Performance . . . . .	50
<b>4</b>	<b>Capacitively Coupled Pixel Detectors for the CLIC Vertex Detector</b>	<b>55</b>
4.1	Introduction . . . . .	55
4.1.1	HV-CMOS . . . . .	56
4.1.2	CLIC ASICs . . . . .	58
4.1.3	Capacitive Coupling . . . . .	60
4.2	Device Fabrication . . . . .	60
4.3	Device Characterisation . . . . .	61
4.3.1	Source Measurements . . . . .	62
4.3.2	Test Pulse Calibration . . . . .	69
4.4	Test Beam Analysis . . . . .	74
4.4.1	Test Beam Setup . . . . .	75
4.4.2	Analysis . . . . .	75
4.4.3	Results . . . . .	76
<b>5</b>	<b>Energy Estimators</b>	<b>79</b>
5.1	Motivation . . . . .	79
5.2	Calibration in the particle flow paradigm . . . . .	82
5.2.1	Digitisation Implementation . . . . .	84
5.2.2	MIP Scale Determination . . . . .	89
5.2.3	Electromagnetic and Hadronic Scale Setting . . . . .	92
5.3	Novel Energy Estimators . . . . .	96
5.3.1	HCal Hit Energy Truncation . . . . .	97
5.3.2	Software Compensation . . . . .	100
5.4	Timing Cuts . . . . .	107
<b>6</b>	<b>Calorimeter Optimisation Studies</b>	<b>111</b>
6.1	Introduction . . . . .	111
6.2	Electromagnetic Calorimeter Optimisation . . . . .	112
6.2.1	ECal Cell Size . . . . .	113
6.2.2	ECal Sampling Frequency . . . . .	115
6.2.3	ECal Active Material . . . . .	118

---

6.3	Hadronic Calorimeter Optimisation . . . . .	120
6.3.1	HCal Cell Size . . . . .	122
6.3.2	HCal Number of Layers . . . . .	125
6.3.3	HCal Sampling Frequency . . . . .	127
6.3.4	HCal Sampling Fraction . . . . .	130
6.3.5	HCal Absorber Material . . . . .	131
6.4	Global Detector Parameters . . . . .	135
6.4.1	The Magnetic Field Strength . . . . .	136
6.4.2	Inner ECal Radius . . . . .	137
7	<b>The sensitivity of CLIC to anomalous gauge couplings through vector boson scattering</b>	141
7.1	Motivation . . . . .	141
7.2	Event Generation, Simulation and Reconstruction . . . . .	145
7.3	Modelling of Anomalous Gauge Couplings . . . . .	146
7.4	Data Analysis . . . . .	150
7.4.1	Jet Finding . . . . .	150
7.4.2	Lepton Finding . . . . .	153
7.4.3	Discriminant Variables . . . . .	155
7.4.4	Jet Energy Resolution at CLIC . . . . .	156
7.5	Event Selection . . . . .	157
7.5.1	Preselection . . . . .	158
7.5.2	Multivariate analysis . . . . .	158
7.5.3	Event Selection Summary . . . . .	160
7.6	Effect of Anomalous Coupling/Fitting Methodology . . . . .	162
7.6.1	Sensitive Distribution . . . . .	163
7.6.2	$\chi^2$ Surface Definition . . . . .	163
7.6.3	Event Weight Interpolation Scheme . . . . .	165
7.7	Results . . . . .	167
7.7.1	Systematic Uncertainties . . . . .	167
7.8	Sensitivity at 3 TeV . . . . .	169
8	<b>Summary</b>	175
	<b>Bibliography</b>	179
	<b>List of figures</b>	191

<b>List of tables</b>	<b>205</b>
-----------------------	------------

*“Writing in English is the most ingenious torture  
ever devised for sins committed in previous lives.”*

— James Joyce



# Chapter 1

## Introduction

*"There, sir! that is the perfection of vessels!"*

— Jules Verne, 1828–1905

The Standard Model has proven to be one of the greatest accomplishments of modern day particle physics. It has have been used to make countless predictions of various physics processes across a wide range of energies that have proven to be consistent with experimental measurements. The final piece of the Standard Model to be discovered was the Higgs boson, which was found by the ATLAS [1] and CMS [2] experiments at the Large Hadron Collider (LHC) in 2012.

Despite the remarkable descriptive power of the Standard Model, there are a number of features in the universe that it does not provide a description for. How does gravity fit into the Standard Model? Why is there an excess of matter over antimatter in the observable universe? How does the "dark matter" predicted by astronomers couple with the particles in the Standard Model? What are the properties of the Higgs field in the Standard Model? While the LHC and previous generations of particle collider experiment have had enormous success in validating the Standard Model and searching for new physics, it is clear that there is more work to be done.

The linear collider experiments are proposals for the next generation of particle collider experiment. These experiments are  $e^+e^-$  colliders with a focus on precision measurements. The physics program for the linear collider is designed to complement and extend the work done at the LHC and to develop our understanding of particle physics. One of the primary goals of the linear collider experiments is to study the

Higgs field of the Standard Model. A detailed description of the Higgs field is likely to help in the description of "dark matter" as many extensions of the Standard Model Higgs field contain particles that fit the properties of "dark matter". The linear collider experiments will also provide a detailed description of the properties of the top quark. This will complement the Higgs study as the strongest couplings for the Higgs in the Standard Model occurs with the top quark. Another goal of the linear collider experiments is to provide high precision measurements of the electroweak sector in the Standard Model. As the electroweak sector is the only place in the Standard Model where CP violation can occur, a detailed description will help to determine why there is an excess of matter over antimatter in the universe. Furthermore, the linear collider will expand the descriptive reach for many Standard Model extensions such as supersymmetry (SUSY).

The linear collider experiments place emphasis on precision measurements. As well as searching for beyond Standard Model physics, precision measurements will guide the future direction of experimental particle physics. Precision measurements have helped to guide the course of particle physics experiments in the past; LEP electroweak data, which gave indirect information about the lightness of the Higgs boson, was used to build the physics case for the LHC. By colliding  $e^+ e^-$ , the experimental conditions found at the linear collider will be far cleaner than those at the LHC, which makes it easier to perform precision measurements. High precision measurements are made possible at the linear collider due to the use of particle flow calorimetry, which is a revolutionary technique in detector design that offers exceptional energy resolution for jets. This paradigm shift means the linear collider detectors are significantly different from those found in previous generations of particle colliders. As the detector design is continually evolving, the ongoing research in this area is vital for determining the overall success of these experiments.

This thesis is organised as follows. Chapter 2 contains a summary of the Standard Model as well as an outline of the physics of interest related to the analysis presented in chapter 7. Chapter 4 presents a study into a novel technology option for the Compact Linear Collider (CLIC) vertex detector. Chapter 5 contains numerous studies related to the treatment of energy deposits in the linear collider simulation. This begins with an outline of the calibration procedure for the linear collider detector simulation. This is followed by a number of novel software techniques aimed at improving the energy resolution of a calorimeter designed for particle flow calorimetry. Finally, the chapter concludes with a study of the timing requirements applied in the software trigger

that will be used at the linear collider experiment. Chapter 6 presents an optimisation study of the linear collider calorimeters. The starker contrast in detector design when comparing particle flow calorimeter and tradition calorimeter is the design of the calorimeters. As the linear collider experiments will be the first experiments purposefully built with particle flow calorimetry in mind, there is no precedence for the detector design. Therefore, these studies are vital for guiding detector design. Chapter 7 contains a study into anomalous gauge couplings that are sensitive to massive gauge boson quartic vertices at the CLIC experiment. This study is of particular interest as it provides a detailed probe of the electroweak symmetry breaking sector of the Standard Model as well as showing CLICs sensitivity to a possible extension to the Standard Model. The thesis concludes with a summary in chapter 8.

## 1.1 Future Linear Colliders

There are two proposed future linear collider experiments; the International Linear Collider (ILC) and the Compact LInear Collider (CLIC). These colliders are both  $e^+ e^-$  colliders with focus upon precision measurements, however, they operate at different collision energies, which presents each experiment with its own unique challenges. One benefit of a linear collider is that it is possible to stage the experiment at several different energies throughout the experiments lifetime

### 1.1.1 The International Linear Collider

The ILC, shown in figure 1.1, initially plans to operate at a centre-of-mass energy of 250 GeV to study the Higgs boson in detail through the Higgstrahlung process ( $e^+ e^- \rightarrow ZH$ ). This analysis of this process makes it possible to examine all the decays of the Higgs boson with high precision. The next phase of operation will increase the collision energy to 500 GeV. This will extend the study of the Higgs, making it possible to observe the Higgs coupling with the top quark and to determine self interactions of the Higgs. Furthermore, at this energy, it will be possible to search for evidence for SUSY and extended Higgs states. Finally, there is an option to increase the centre-of-mass up to 1 TeV, which would extend the search for SUSY and composite Higgs models.

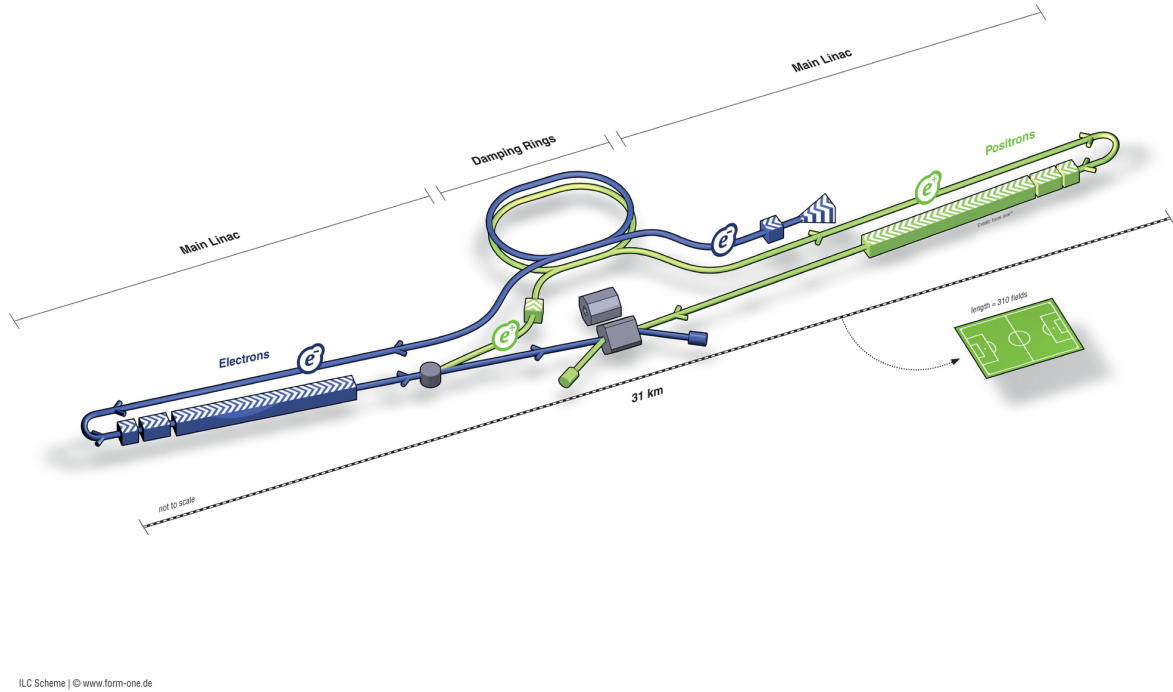


**Figure 1.1:** Schematic layout of the ILC, indicating all the major subsystems (not to scale). Figure taken from [3].

### 1.1.2 The Compact Linear Collider

The CLIC experiment, shown in figure 1.2, plans to operate with maximum collision energy of 3 TeV. CLIC will also operate at intermediate energy stages, however, these energies are to be determined by the ongoing work at the LHC. The large collision energy of CLIC gives it a greater physics reach for searching for extensions to the Standard Model, e.g. SUSY, that would be inaccessible at ILC-like energies [4]. Although the exact energies for the staging of the CLIC experiment are not certain, CLIC will operate at a low collision energy during staging,  $\sim 500$  GeV, to study the Higgs. The higher energy stages of the CLIC experiment will provide access to different channels for studying Higgs couplings, as shown by figure 1.3.

### Experimental Conditions at CLIC

The CLIC experiment will operate in a unique environment in comparison to either the ILC or previous generations of lepton colliders. It is vital that this is properly accounted for when determining the physics potential that CLIC has to offer. The

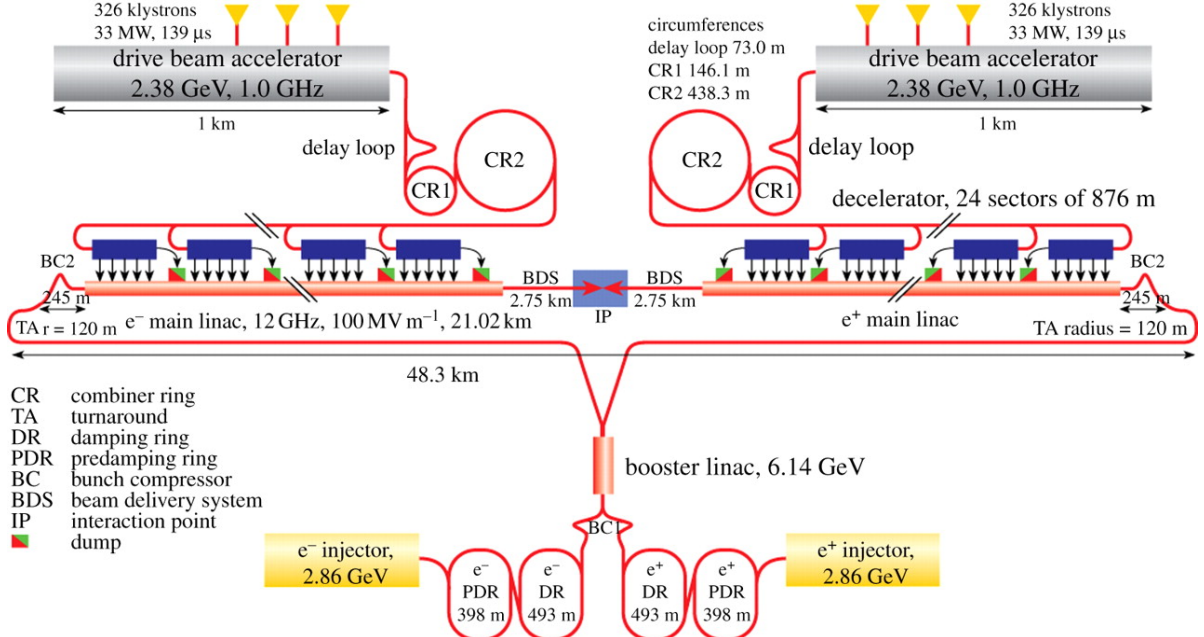


**Figure 1.2:** CLIC layout at 3 TeV. Figure taken from [5].

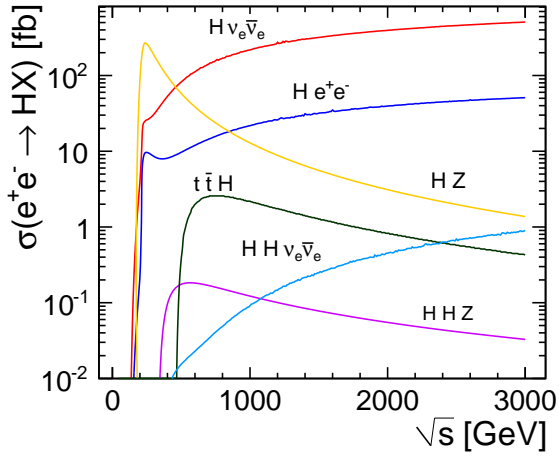


**Figure 1.3:** Cross section for production mechanisms of the Standard Model Higgs boson as a function of the collision energy. The cross sections were calculated assuming a Higgs mass of 120 GeV. Figure taken from [4].

following aspects of the CLIC experiment present the largest challenges to the physics potential:

- The high bunch charge density. The small beam size at the impact point produces very large electromagnetic fields. These fields can interact with the opposite beam

particles causing them to radiate photons in an effect known as beamstrahlung. Beamstrahlung acts to reduce the collision energy of the  $e^+e^-$  pairs.

- Beam related backgrounds. Beamstrahlung photons can subsequently interact to produce background events that must be accounted for. Dominant backgrounds of this form that cannot be easily vetoed in the reconstruction include incoherent pair production of  $e^+e^-$  and  $\gamma\gamma \rightarrow \text{Hadron}$ . While these backgrounds are also problematic for the ILC experiment, the lower collision energy means it has a much smaller impact on performance.
- Fast readout technology. The CLIC bunch train consists of 312 bunches with a repetition rate of 50 Hz. Each bunch is separated by 0.5 ns, therefore, it will be necessary to integrate over multiple bunch crossing when reading out the detectors. This places tight constraints on all detector electrical readout speeds and time resolutions.

## Beam-Related Backgrounds at CLIC

The primary sources of background for the CLIC experiment are as follows:

- $e^+e^-$  pair creation from the interaction of a beamstrahlung photons with the opposing beam. The different mechanisms for pair creation are as follows:
  - **Coherent pair production.** This mechanism involves the interaction of a real beamstrahlung photon with the electromagnetic field from the opposing beam.
  - **Trident pair production.** This mechanism involves the interaction of a virtual beamstrahlung photon with the electromagnetic field from the opposing beam.
  - **Incoherent pair production.** This mechanism involves the interaction of a real or virtual beamstrahlung photon with the individual particles in the opposing beam.
- $\gamma\gamma \rightarrow \text{Hadron}$  events from the interaction of real or virtual beamstrahlung photons with each other.
- Beam halo muons that arise from interactions of the beam particles during collimation. The dominant mechanisms producing beam halo muons are photon

conversions into muon pairs ( $\gamma e^- \rightarrow \mu^+ \mu^- e^-$ ) and annihilation of positrons with atomic  $e^-$  into muon pairs ( $e^+ e^- \rightarrow \mu^+ \mu^-$ ) [6].

Each of these has to be properly addressed to get a true measure of the physics potential at CLIC. Coherent and trident pair production is not a dominant source of background as they are produced at low transverse momenta, as figure 1.4 shows, and a simple cut would veto these backgrounds. This is not the case for incoherent pair production of  $e^+ e^-$ , which are dominant in the forward regions of the detector, and  $\gamma\gamma \rightarrow$  Hadron, which are dominant in the tracker and the calorimeters (with the exception of low radii in the calorimeter endcaps) [4, 7]. Beam halo muons are not a major source of background either as they can be easily removed during the reconstruction as they produce a clear signal in the detector. An algorithm was developed within the PandoraPFA framework for this purpose and it was found to be highly effective at removing the beam halo muons background [4].

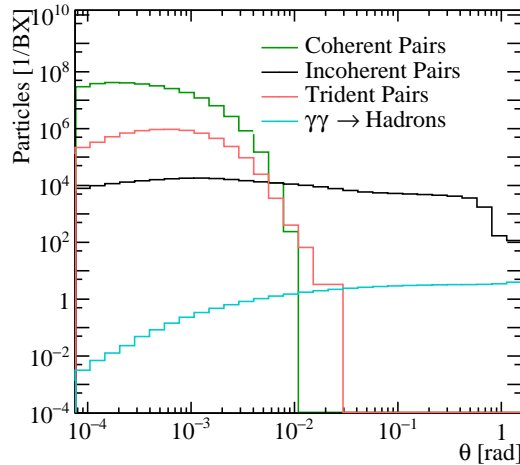


**Figure 1.4:** Angular distribution of number of particles for beam induced backgrounds for CLIC at a centre of mass energy of 3 TeV. Figure taken from [4].

$\gamma\gamma \rightarrow$  Hadron events are the most dominant source of background to consider at CLIC as these events deposit more energy throughout the detector than incoherent pair production of  $e^+ e^-$  events [4]. Although incoherent pairs are still a source of background, they will produce a second order effect in comparison to the  $\gamma\gamma \rightarrow$  Hadron events.



# Chapter 2

## Anomalous Gauge Coupling Theory

*“There, sir! that is the perfection of vessels!”*

— Jules Verne, 1828–1905

### 2.1 The Standard Model

The Standard Model is a non-abelian gauge theory of the  $SU(3) \times SU(2)_L \times U(1)$  symmetry group. It provides a description of three of the four fundamental forces of nature: the electromagnetic, weak and strong nuclear forces [8, 9]. The Standard Model contains a total of 24 fermion fields: six flavours of quark, each with three colours, and six leptons. A summary of the properties of these particles is given in table 2.1 and 2.2. As these fields,  $\psi$ , are spin- $\frac{1}{2}$ , they obey the Dirac equation:

$$\mathcal{L} = \bar{\psi}(i\vec{\partial} - m)\psi , \quad (2.1)$$

where  $\mathcal{L}$  is the Lagrangian density and  $m$  is a mass term. The derivative term,  $\vec{\partial} = \gamma^\mu \partial_\mu$ , represents a summation over the partial derivative,  $\partial^\mu = (\frac{\partial}{\partial t}, \frac{\partial}{\partial x}, \frac{\partial}{\partial y}, \frac{\partial}{\partial z})$ , of the field  $\psi$  and the gamma matrices,  $\gamma^\mu$ . Each of the gauge transformations of the Standard Model are defined by a unitary operator  $U$ , which acts to transform the vector space,  $\Psi$ , formed from a combination of fermion fields,  $\psi$ , in the following way:

$$\Psi \rightarrow \Psi' = U\Psi . \quad (2.2)$$

In the Standard Mode, the Lagrangian density describing the fermion fields is invariant under a  $SU(3)$ ,  $SU(2)_L$  and  $U(1)$  gauge transformations. The  $SU(2)_L$  gauge symmetry acts on doublets formed of pairs of left handed chiral components of the fermion fields,  $\psi_L = \frac{1}{2}(1 - \gamma_5)\psi$ , while the right handed components,  $\psi_R = \frac{1}{2}(1 + \gamma_5)\psi$ , transform trivially as singlets [10]. Similarly, the  $SU(3)$  symmetry acts on triplets formed of the fermion fields for each flavour of quark. All fields transform under the fundamental representation of  $U(1)$ . The invariance of the Standard Model Lagrangian to these gauge transformations is established by introducing 12 gauge fields, summarised in table 2.3, through the covariant derivative of the fermion fields:

$$\partial^\mu \rightarrow D^\mu = \partial^\mu + ig_1 Y B^\mu + ig_2 \mathbf{T} \cdot \mathbf{W}^\mu + ig_3 \mathbf{X} \cdot \mathbf{G}^\mu , \quad (2.3)$$

where  $B^\mu$  is the gauge field for the  $U(1)$  symmetry,  $\mathbf{W}^\mu$  ( $W_j^\mu, j = 1, 2, 3$ ) are the fields of the  $SU(2)_L$  symmetry and  $\mathbf{G}^\mu$  ( $G_j^\mu, j = 1, \dots, 8$ ) are the fields of the  $SU(3)$ .  $Y$  is the weak hypercharge, which is related to the chirality and flavour of the fermion it relates to. The three coefficients  $g_1, g_2$  and  $g_3$  are coupling constants related to the three gauged symmetry groups in the Standard Model. Mixing of the gauge fields for the  $U(1)$  and  $SU(2)$  symmetry of the form:

$$Z_\mu = \cos\theta_W W_\mu^3 - \sin\theta_W B_\mu , \quad (2.4)$$

$$A_\mu = \sin\theta_W W_\mu^3 + \cos\theta_W B_\mu , \quad (2.5)$$

$$W_\mu^\pm = \frac{1}{\sqrt{2}}(W_\mu^1 \mp iW_\mu^2) , \quad (2.6)$$

where:

$$\cos\theta_W = \frac{g_2}{g_1 + g_2} \text{ and } \sin\theta_W = \frac{g_1}{g_1 + g_2} , \quad (2.7)$$

gives the electroweak gauge bosons;  $W^\pm$ ,  $Z$  and  $\gamma$ . This mixing ensures that the  $W^\pm$  and  $Z$  bosons become massive, while the  $\gamma$  remains massless. The  $G_j^\mu$  fields are the eight massless gluons of the strong force.  $\mathbf{T}$  and  $\mathbf{X}$  are the generators for the  $SU(2)$  and  $SU(3)$  symmetries, which are typically chosen as:

$$T_i = \frac{1}{2}\tau_i , \quad (2.8)$$

$$X_i = \frac{1}{2}\lambda_i , \quad (2.9)$$

$$(2.10)$$

where  $\tau$  and  $\lambda$  are the Pauli and the Gell-Mann matrices respectively.

The gauge fields of the Standard Model,  $B_\mu$ ,  $\mathbf{W}_\mu$  and  $\mathbf{G}_\mu$ , transform under the gauge transformations as:

$$K_\mu \rightarrow K'_\mu = UK_\mu U^\dagger + \frac{i}{g}(\partial^\mu U)U^\dagger, \quad (2.11)$$

where  $K_\mu$  is any of  $B_\mu$ ,  $\mathbf{W}_\mu$  and  $\mathbf{G}_\mu$  and  $g$  is the coupling constants associated to the relevant gauged symmetry group. As the  $B_\mu$ ,  $\mathbf{W}_\mu$  and  $\mathbf{G}_\mu$  gauge fields are spin-1, they are described by the Proca action:

$$\mathcal{L} = -\frac{1}{4}F_i^{\mu\nu}F_{\mu\nu i} + \frac{1}{2}m_K^2K_{i\mu}K_i^\mu, \quad (2.12)$$

where:

$$F_i^{\mu\nu} = \partial^\mu K_i^\nu - \partial^\nu K_i^\mu - g f_{ijk} K_j^\mu K_k^\nu, \quad (2.13)$$

where  $f_{ijk}$  are the fully anti-symmetric structure constants of the group,  $K_i^\mu$  is the  $i^{th}$  gauge field of the group and  $m_K$  is a mass term for the gauge boson. The structure constants are defined from the commutation relations between generators of the symmetry group:

$$[T_i, T_j] = if_{ijk}T_k. \quad (2.14)$$

These structure constants govern the self-interactions for the gauge bosons. There is only one structure constant for the U(1) symmetry, which is zero, as the U(1) symmetry is abelian. The SU(2) symmetry structure constants are  $f_{ijk} = \epsilon_{ijk}$ , where  $\epsilon_{ijk}$  is the Levi-Civita tensor. Due to the symmetries that are present in the Standard Model,  $m_K = 0$  for all the gauge fields, however, it is clear that is is not the case. Therefore, to generate gauge boson mass terms a Higgs field is introduced that undergoes spontaneous symmetry breaking, as described in section 2.2.

Generation	Particle	Mass [MeV]	Spin	Q/e
1	$e^-$	$548.579909070 \pm 0.000000016$	1/2	-1
	$\nu_e$		-	0
2	$\mu^-$	$105.6583745 \pm 0.0000024$	1/2	-1
	$\nu_\mu$		-	0
3	$\tau^-$	$1776.86 \pm 0.12$	1/2	-1
	$\nu_\tau$		-	0

**Table 2.1:** The mass, spin and electric charge (Q) of the leptons found in the Standard Model [11]. Neutrino masses have not been included in the above table as precise measurements are yet to be made. However, oscillations between different neutrino flavour states have been observed, which indicates that the flavour and mass eigenstates differ and that the neutrinos have a non-zero mass. The current upper bound on neutrino mass measurements is 2 eV.

Generation	Particle	Mass [MeV]	Spin	Q/e
1	$u$	$2.2^{+0.6}_{-0.4}$	1/2	+2/3
	$d$	$4.7^{+0.5}_{-0.4}$	1/2	-1/3
2	$c$	$1270 \pm 30$	1/2	+2/3
	$s$	$98^{+8}_{-4}$	1/2	+2/3
3	$t$	$173210 \pm 510 \pm 710$	1/2	+2/3
	$b$	$4180^{+40}_{-30}$	1/2	-1/3

**Table 2.2:** The mass, spin and electric charge (Q) of the quarks found in the Standard Model [11]. Each of the particles in the above table corresponds to three fermion fields, one for each of the three colours of the SU(3) symmetry.

## 2.2 Higgs Physics

Mass terms are generated in the Standard Model by introducing a Higgs field that undergoes spontaneous symmetry breaking. This allows the gauge bosons, as well as the quarks and leptons, to obtain a mass, while still respecting the gauge symmetries found in the Standard Model.

Force	Particle	Mass [GeV]	Spin	Q/e
Electromagnetic	$\gamma$	0	1	0
Weak Nuclear	$W^\pm$	$80.385 \pm 0.015$	1	$\pm 1$
	Z	$91.1876 \pm 0.0021$	1	0
Strong Nuclear	$g$ ( $\times 8$ colours)	0	1	0
Higgs	H	$125.1 \pm 0.3$	0	0

**Table 2.3:** The mass, spin and electric charge (Q) of the gauge bosons found in the Standard Model [11]. The  $\gamma$  and  $g_s$  theoretically have zero mass, which is consistent with measurements. The upper bound on the  $\gamma$  mass has been measured at  $10^{-18}$  eV, while gluon masses of up to a few MeV have not been precluded. The upper bound on the magnitude of the charge of the  $\gamma$  is measured at  $10^{-35}$ .

### 2.2.1 Spontaneous Symmetry Breaking

To illustrate spontaneous symmetry breaking, consider a complex scalar field  $\psi$  with the Klein-Gordon Lagrangian:

$$\mathcal{L} = \partial^\mu \psi^* \partial_\mu \psi - m^2 |\psi|^2 = \partial^\mu \psi^* \partial_\mu \psi - V(\psi), \quad (2.15)$$

where  $\mathcal{L}$  the is Lorentz invariant Lagrangian density,  $\partial^\mu = (\frac{\partial}{\partial t}, \frac{\partial}{\partial x}, \frac{\partial}{\partial y}, \frac{\partial}{\partial z})$  is the partial derivative of the scalar field  $\psi$ ,  $m$  is a mass term and  $V(\psi)$  is the potential the field  $\psi$ . This Lagrangian density is invariant under the global symmetry  $\psi \rightarrow e^{i\alpha} \psi$ . By adding extra terms to the Lagrangian, which retain the invariance to this global symmetry, it is possible to modify the interactions of this scalar field. For example consider modifying the potential of the scalar field to the following:

$$V(\psi) = m^2 |\psi|^2 + \lambda |\psi|^4, \quad (2.16)$$

If  $m^2 > 0$ , the potential has a minima at zero, however, if  $m^2 < 0$  then the minima exists on a circle in the complex  $\psi$  plane, which is centred at  $(0, 0)$  and has radius  $v = \sqrt{-m^2/\lambda}$ . To quantise this theory it is necessary to expand about the minima of the potential. However, in the case of  $m^2 < 0$  there are an infinite number of choices of minima to expand about. Irrespective of the choice of minima used to expand the field about, the symmetry  $\psi \rightarrow e^{i\alpha} \psi$  is broken. Fluctuations about the minima along the degenerate direction leave the potential unchanged, which is a consequence of the breaking of the  $\psi \rightarrow e^{i\alpha} \psi$  symmetry; this is known as spontaneous

symmetry breaking. Goldstone's theorem [12] implies that, for Lorentz-invariant theories, spontaneous symmetry breaking always leads to the existence of a massless particles known as Goldstone bosons. For example, consider expanding the complex scalar  $\psi$  about the minima. In that case,  $\psi$  takes the form:

$$\psi = \frac{1}{\sqrt{2}}(v + \psi_1 + i\psi_2), \quad (2.17)$$

where  $\psi_1$  and  $\psi_2$  are real fields and  $v = \sqrt{-m^2/\lambda}$ . Applying this parameterisation to the Lagrangian yields a mass term of  $\sqrt{-m^2}$  for the  $\psi_1$  field. However, there is no corresponding mass term for the  $\psi_2$  field, which indicates that it is massless as predicated by Goldstone's theorem:

$$\mathcal{L} = \frac{1}{2}\partial^\mu\psi_1\partial_\mu\psi_1 + \frac{1}{2}\partial^\mu\psi_2\partial_\mu\psi_2 - m^2|\psi_1|^2 + \dots, \quad (2.18)$$

Spontaneous symmetry breaking is the origin of the gauge boson mass terms when applied to local symmetries instead of global ones. For example consider the global symmetry,  $\psi \rightarrow e^{i\alpha}\psi$ , that exists in equation 2.15. If this global symmetry is promoted to a local symmetry by letting  $\alpha \rightarrow \alpha(x)$  and  $\partial^\mu \rightarrow D^\mu = \partial^\mu + iA^\mu$ , where  $A^\mu$  is the gauge field that transforms as  $A^\mu \rightarrow A^\mu - \partial^\mu\alpha(x)$ , the Lagrangian becomes:

$$\mathcal{L} = (D^\mu\psi)^*(D_\mu\psi) - m^2|\psi|^2 - \lambda|\psi|^4. \quad (2.19)$$

If the  $\psi$  field is expanded about a non-zero minima in the potential, i.e.  $m^2 < 0$  and  $v = \sqrt{-m^2/\lambda}$ , as was done in equation 2.17, then a gauge boson mass term,  $+\frac{v^2}{2}A^\mu A_\mu$ , is generated from the  $(D^\mu\psi)^*(D_\mu\psi)$  term.

### 2.2.2 Electroweak Interactions

The electroweak sector of the Standard Model is that related to the  $SU(2)_L \times U(1)$  symmetry [13]. In this sector, spontaneous symmetry breaking must occur in such a way as to give three massive gauge bosons,  $W^\pm$  and  $Z$ , and one massless gauge boson, the  $\gamma$ . This can be achieved through a Higgs field,  $H$ , that transforms as a doublet under the  $SU(2)_L$  symmetry. The Lagrangian for this field is:

$$\mathcal{L}_{Higgs} = (D_\mu H)^\dagger D^\mu H - V(H). \quad (2.20)$$

The Higgs potential,  $V(H)$ , is:

$$V(H) = -\mu^2 H^\dagger H + \lambda(H^\dagger H)^2, \quad (2.21)$$

where  $\mu$  and  $\lambda$  are constants. The covariant derivative of this Higgs field must satisfy the  $SU(2)_L \times U(1)$  gauge symmetry meaning it takes the form:

$$D_\mu H = (\partial_\mu + ig_1 Y B_\mu + ig_2 \frac{\tau^i}{2} W_\mu^i) H, \quad (2.22)$$

where  $g_1$  and  $g_2$  are coupling constants for the  $U(1)$  and  $SU(2)_L$  gauged symmetries respectively,  $Y = \frac{1}{2}$  is the weak hypercharge of the Higgs and  $\tau^i$  are the Pauli matrices.  $B_\mu$  and  $W_\mu^i$  are the gauge fields for the  $U(1)$  and  $SU(2)_L$  gauged symmetries respectively.

Consider spontaneously breaking the symmetry in the Higgs sector by expanding the Higgs field about a non-zero vacuum expectation value (vev):

$$\langle H \rangle = \begin{pmatrix} 0 \\ \frac{v}{\sqrt{2}} \end{pmatrix}, \quad (2.23)$$

where the minima of the field is defined as:

$$\frac{v}{\sqrt{2}} = \sqrt{\frac{\mu^2}{2\lambda}}, \quad (2.24)$$

where  $v$  real. In that case, the kinematic term in the Higgs Lagrangian,  $D^\mu H^\dagger D_\mu H$ , contains mass terms for the gauge bosons:

$$D^\mu H^\dagger D_\mu H \subset \frac{v^2}{2} (ig_1 Y B^\mu + ig_2 \frac{\tau^i}{2} W^{i\mu}) (ig_1 Y B_\mu + ig_2 \frac{\tau^i}{2} W_\mu^i). \quad (2.25)$$

If there is mixing of the  $SU(2)_L$  and  $U(1)$  fields of the form:

$$Z_\mu = \cos\theta_W W_\mu^3 - \sin\theta_W B_\mu, \quad (2.26)$$

$$A_\mu = \sin\theta_W W_\mu^3 + \cos\theta_W B_\mu, \quad (2.27)$$

$$W_\mu^\pm = \frac{1}{\sqrt{2}} (W_\mu^1 \mp i W_\mu^2), \quad (2.28)$$

then the following gauge boson mass terms are generated:

$$\frac{(gv)^2}{4} W_\mu^+ W^{-\mu} + \frac{(g^2 + g'^2)v^2}{8} Z_\mu Z^\mu . \quad (2.29)$$

The gauge boson masses generated by spontaneous symmetry breaking of the Higgs field are:

$$\begin{aligned} m_W &= \frac{gv}{2} , \\ m_Z &= \frac{v\sqrt{g^2 + g'^2}}{2} = \frac{m_W}{\cos\theta_W} , \\ m_A &= 0 , \end{aligned} \quad (2.30)$$

where  $\theta_W$  is the Weinberg angle. This mixing produces a massless gauge boson, the  $\gamma$ , and three massive gauge bosons, the  $W^\pm$  and  $Z$ . By acquiring a non-zero vev, the Higgs field breaks the  $SU(2)_L \times U(1)$  symmetry that was present in the Lagrangian to the  $U(1)_{em}$  symmetry of electromagnetism.

The ratio of the masses of the  $W^\pm$  and  $Z$  bosons is predicted when spontaneous symmetry breaking occurs in the Higgs sector. This prediction sets the  $\rho$  parameter to unity, where the  $\rho$  parameter is defined as:

$$\rho = \frac{m_W^2}{m_Z^2 \cos^2\theta_W} = 1 . \quad (2.31)$$

This is a consequence of the Higgs potential containing custodial symmetry [11]. As the  $\rho$  parameter has been experimentally measured to be  $1.00040 \pm 0.00024$  [14], it is clear that any extension to the Standard Model should retain this result.

## Custodial Symmetry

The Standard Model Higgs field is defined by the Lagrangian:

$$\mathcal{L}_{Higgs} = (D_\mu H)^\dagger D^\mu H - V(H) , \quad (2.32)$$

where:

$$V(H) = -\mu^2 H^\dagger H + \lambda (H^\dagger H)^2 . \quad (2.33)$$

where  $\mu$  and  $\lambda$  are constants. By construction, the Higgs sector of the Standard Model is invariant under local  $SU(2)_L \times U(1)$  gauge transformations. However, a larger global symmetry also exists in this sector, which can be seen by considering the Higgs doublet [15]:

$$H = \begin{pmatrix} \psi^+ \\ \psi^0 \end{pmatrix} = \begin{pmatrix} \psi_1 + i\psi_2 \\ \psi_3 + i\psi_4 \end{pmatrix}. \quad (2.34)$$

All the terms in the Higgs potential involve  $H^\dagger H = \psi_1^2 + \psi_2^2 + \psi_3^2 + \psi_4^2$ , which is invariant under any rotation of these four components and hence under a  $SO(4)$  global symmetry. In general,  $SO(4) \cong SU(2) \times SU(2)$ , where  $\cong$  denotes an isomorphism. In the case of the Higgs sector  $SO(4) \cong SU(2)_L \times SU(2)_R$  where the  $SU(2)_L$  symmetry is the gauged symmetry of the Standard Model. This symmetry can be manifested using an alternative parameterisation [16] of the Higgs field :

$$\Phi = (i\tau_2 H, H) = \begin{pmatrix} \psi^{0*} & \psi^+ \\ -\psi^{+*} & \psi^0 \end{pmatrix}. \quad (2.35)$$

In this parametrisation the Higgs Lagrangian,  $\mathcal{L}_{Higgs}$ , becomes:

$$\mathcal{L}_{Higgs} = \frac{1}{2} \text{Tr}[(D_\mu \Phi)^\dagger D^\mu \Phi] + \mu^2 \text{Tr}[\Phi^\dagger \Phi] - \lambda \text{Tr}[\Phi^\dagger \Phi \Phi^\dagger \Phi], \quad (2.36)$$

which is invariant under transformations of the form:

$$\Phi \rightarrow U_L \Phi U_R^\dagger, \quad (2.37)$$

where  $U_L$  and  $U_R$  are transformations of the  $SU(2)_L$  and  $SU(2)_R$  symmetry groups respectively.

When the Higgs field acquires a non-zero vev the  $SU(2)_L \times SU(2)_R$  symmetry of the Higgs potential is broken to a  $SU(2)_C$  symmetry, which is known as custodial symmetry [17]. As  $SO(3) \cong SU(2)$ , symmetry breaking in the Higgs sector is equivalent to a  $SO(4)$  symmetry being broken to a  $SO(3)$  symmetry. This becomes clear when considering the form of the Higgs potential after symmetry breaking. Prior to symmetry breaking a  $SO(4)$  global symmetry is present, however, after expanding the Higgs about a non-zero vev, defined in equation 2.23, the terms in the Higgs potential involve  $H^\dagger H = (\psi_3 - v)^2 + \psi_1^2 + \psi_2^2 + \psi_4^2$ , which is only invariant to rotations between the  $\psi_1$ ,  $\psi_2$  and  $\psi_4$  fields, which is a  $SO(3)$  symmetry.

The Higgs field,  $H$ , transforms a singlet under this  $SU(2)_C$  custodial symmetry, while the  $SU(2)_L$  gauge boson fields,  $W_\mu^i$ , transform as a triplet. It is the transformation of the  $W_\mu^i$  fields under the  $SU(2)_C$  symmetry that enforces the relationship between the masses of the  $W^\pm$  and  $Z$  gauge bosons and that  $\rho$  should equal unity. It should be noted that the  $SU(2)_L \times SU(2)_R$  symmetry only exists in the Higgs sector of the Standard Model. The  $SU(2)_R$  symmetry is the Standard Model is broken by Yukawa couplings of the Higgs to quarks and leptons and by a non-zero coupling to the  $U(1)$  gauge symmetry of the Standard Model,  $g_1$ . However, this breaking of the  $SU(2)_R$  symmetry is weak, which means the deviations of  $\rho$  from unity are minimal [17].

## 2.3 Effective Field Theory

There are a number of features in the observable universe that cannot be accounted for using the Standard Model of particle physics. However, the Standard Model is a very good description of the interactions between particles at the energies being probed at modern particle collider experiments. Any underlying theory governing the interactions of particles must, therefore, behave like the Standard Model over these energies, or distance scales. Above such energies the theory will deviate from the Standard Model to account for the full underlying theory. Effective field theories (EFTs) work from this premise by assuming that the complete theory has a momentum scale,  $\Lambda$ , below which Standard Model behaviour is replicated [18, 19].

Quantum field theories must be renormalizable to ensure that non-infinite predictions of the coefficients in the Lagrangian can be made and tested [20]. Infinities arise from non-renormalizable theories due to divergent integrals from loop diagrams that assume the theory being applied is valid at all energy and length scales. Effective field theories act to avoid such problems by only integrating up to the momentum scale  $\Lambda$  and not above it. At the energy scale being considered, any infinities arising from the loop calculations in the EFT can be absorbed into a finite number of parameters. This methodology avoids the assumption that the theory in question is applicable to all energy scales and allows measurable predictions to be made.

As the Standard Model should be replicated at the low energy scale, it is appropriate when creating an EFT Lagrangian to append new operators to the Standard Model Lagrangian to account for areas of new physics. This gives the general form for an

EFT Lagrangian as [18]:

$$\mathcal{L}_{EFT} = \mathcal{L}_{SM} + \sum_{\text{dimension } d>4} \sum_i \frac{c_i^{(d)}}{\Lambda^{d-4}} \mathcal{O}_i^{(d)}, \quad (2.38)$$

where  $\mathcal{L}_{SM}$  is the Standard Model Lagrangian,  $c_i^{(d)}$  are free parameters,  $\mathcal{O}_i^{(d)}$  is the  $i^{th}$  unique operator with dimension  $d$  in the EFT and  $\Lambda$  is the EFT momentum scale. The sum runs over all unique operators with dimension greater than four. The presence of the  $\Lambda^{d-4}$  in the denominator is required to ensure correct dimensionality of the new terms being added to the Lagrangian.

New physics is introduced by the operators  $\mathcal{O}_i^{(d)}$ , but suppressed by the momentum scale  $\Lambda$ . It is assumed that  $\Lambda$  is large with respect to the momentum scales that have been examined at preexisting particle collider experiments, therefore, any new physics is suppressed. Under this assumption, new operators with dimension less than, or equal to, four can be vetoed from the EFT as their effects would be readily observed at preexisting particle collider experiments, due to the  $\Lambda^{4-d}$  coefficient. At energies below the momentum scale,  $\Lambda$ , it is possible to find the dominant new physics terms in the EFT and consider these as corrections to the Standard Model. Above this scale the EFT breaks down as operator  $\mathcal{O}_i^{(d)}$  in  $\mathcal{L}_{EFT}$  has a non-negligible coefficient. In the extremal limit,  $\Lambda \rightarrow \infty$ , the Standard Model is recovered as new physics is too far out of reach to have any impact on observables.

## 2.4 Electroweak Chiral Lagrangian

The introduction of a Higgs field undergoing spontaneous symmetry breaking is able to produce mass terms in the Lagrangian for the  $W^\pm$  and  $Z$  bosons. However, it is possible to introduce these terms by parameterising the Higgs field using the gauge boson fields of the  $SU(2)_L$  Standard Model symmetry [21]. In this approach, the pattern of spontaneous symmetry breaking mirrors that found in the Higgs sector of the Standard Model i.e. a global  $SU(2)_L \times SU(2)_R$  symmetry is broken to a  $SU(2)_C$  symmetry. This will ensure that the  $\rho$  parameter, introduced in section 2.2.2, retains a value of unity, which is consistent with experimental measurements. The Standard Model spontaneous symmetry breaking pattern can be replicated using a field,  $\Sigma(x)$ ,

which transforms under the  $SU(2)_L \times SU(2)_R$  global symmetries as:

$$\Sigma \rightarrow U_L \Sigma U_R^\dagger , \quad (2.39)$$

where  $U_L$  and  $U_R$  are transformations of the  $SU(2)_L$  and  $SU(2)_R$  symmetry groups respectively and  $\Sigma(x)$  is:

$$\Sigma(x) = \exp\left(\frac{-i}{v} \sum_{a=1}^3 \pi^a \tau^a\right) , \quad (2.40)$$

where  $\pi^a$  are the three would-be Goldstone bosons that exist when the  $SU(2)_L \times U(1)$  symmetry is broken to  $U(1)_{em}$  [22]. The  $SU(2)_L$  and  $U(1)$  symmetries of the Standard Model are gauged in the usual way by defining the covariant derivative of the  $\Sigma$  field:

$$\mathcal{D}_\mu \Sigma(x) = \partial_\mu \Sigma(x) + \frac{i g_2}{2} W_\mu^a \tau^a \Sigma(x) - \frac{i g_1}{2} B_\mu \tau^3 \Sigma(x) , \quad (2.41)$$

where  $g_2$  and  $g_1$  are coupling constants for the  $U(1)$  and  $SU(2)_L$  symmetries respectively and  $\tau^a$  are the Pauli spin matrices. The lowest order derivative term for this  $\Sigma$  field that could appear in the Lagrangian is:

$$\mathcal{L}_\Sigma = \frac{v^2}{4} \text{Tr}(\mathcal{D}^\mu \Sigma^\dagger \mathcal{D}_\mu \Sigma) = -\frac{v^2}{4} \text{Tr}(V_\mu V^\mu) , \quad (2.42)$$

where  $V_\mu = (\mathcal{D}_\mu \Sigma) \Sigma^\dagger$ . This term respects all the symmetries present in the Higgs sector of that Standard Model, including the custodial symmetry in the limit  $g_1 \rightarrow 0$ . Furthermore, by expanding this field about a non-zero vev, the  $SU(2)_L \times SU(2)_R$  global symmetry is broken to a  $SU(2)_C$  symmetry exactly as it is in the Standard Model. For example, if this field is expanded about the point  $\Sigma = \mathbb{1}$ , i.e. the unitary gauge, mass terms for the electroweak gauge bosons are generated that match those produced from spontaneous symmetry breaking of the Higgs field as described in section 2.2.1:

$$\frac{v^2}{4} \text{Tr}[V^\mu V_\mu] = -\frac{(gv)^2}{4} W_\mu^+ W^{-\mu} - \frac{(g^2 + g'^2)v^2}{8} Z_\mu Z^\mu \quad (2.43)$$

$$\begin{aligned} m_A &= 0 , \\ m_W &= \frac{gv}{2} , \\ m_Z &= \frac{v\sqrt{g^2 + g'^2}}{2} = \frac{m_W}{\cos\theta_W} , \end{aligned} \quad (2.44)$$

So far, all that has been done is a parameterisation of the Higgs field, however, it was shown by Longhitano [22] that there are several relevant operators involving the  $\Sigma$  field that are  $SU(2)_L \times U(1)$  invariant. As these operators obey the same symmetries as those found in the Standard Model they should be considered. This can be done using EFT approach, as discussed in section 2.3. Of the operators introduced by Longhitano, only two involve quartic massive gauge boson vertices and preserve the custodial symmetry [23]. They are:

$$\alpha_4 \text{Tr}[V^\mu V_\nu] \text{Tr}[V^\nu V_\mu] \text{ and } \alpha_5 \text{Tr}[V^\mu V_\mu]^2. \quad (2.45)$$

These terms contribute to the massive gauge boson quartic vertices shown in figure 2.1. The Standard Model already contains triple and quartic vertices involving the electroweak gauge bosons, shown in figure 7.1, and these are also present in this EFT approach. These vertices originate from the kinematic terms in the Proca action  $\mathcal{L}_{kin} = -\frac{1}{4}B_{\mu\nu}B^{\mu\nu} - \frac{1}{4}W_{\mu\nu}W^{\mu\nu}$ . Of the vertices showing sensitivity to  $\alpha_4$  and  $\alpha_5$ , only that shown in figure 2.1c is not present in the Standard Model.

Both terms shown in equation 2.45 contain dimension 8 operators [18] and, with respect to the EFT approach i.e. equation 2.38, their coefficients are proportional to  $\Lambda^{-4}$ , where  $\Lambda$  is the momentum scale of the new physics being modelled. In the limit that the momentum scale of new physics is beyond experimental reach, i.e.  $\Lambda \rightarrow \infty$ , these terms do not contribute to measurable observables and the Standard Model is recovered. It should be noted that in this case, the Standard Model has been parameterised using the  $\Sigma$  field, so in the limit  $\Lambda \rightarrow \infty$ , the gauge boson mass terms generated from  $\mathcal{L}_\Sigma$  do not vanish.

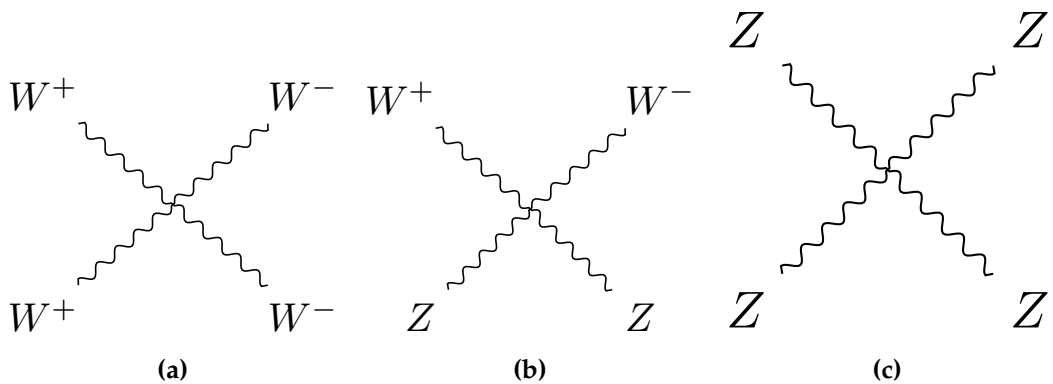


**Figure 2.1:** Gauge boson self-coupling vertices that are sensitive to the anomalous gauge couplings  $\alpha_4$  and  $\alpha_5$ .

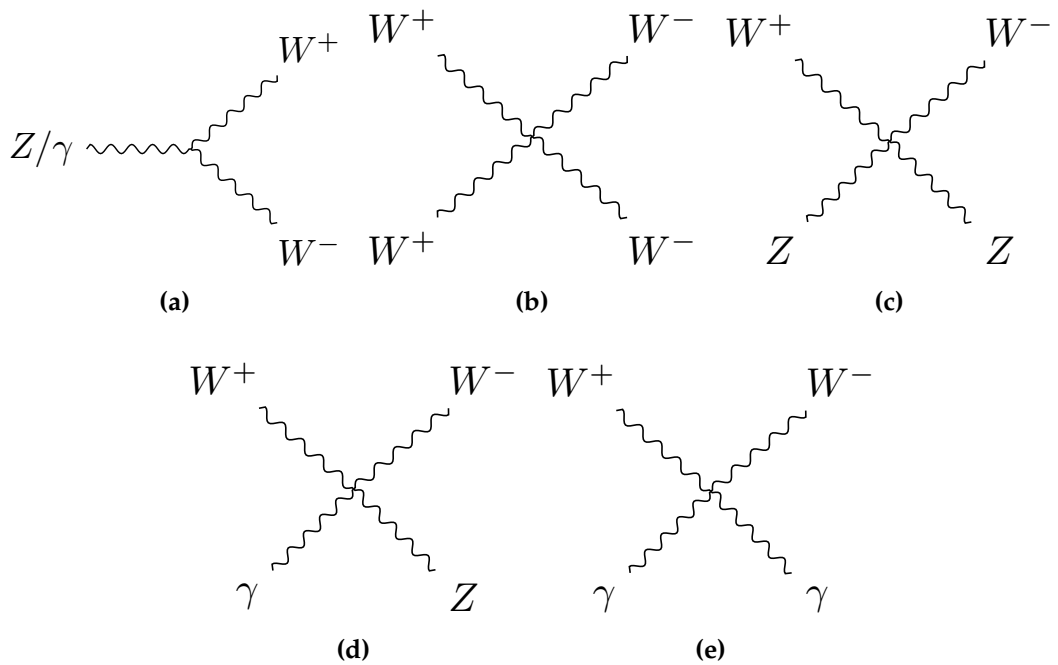


**Figure 2.2:** Gauge boson self-coupling vertices in the Standard Model.

A study into the sensitivity of the CLIC experiment to the anomalous gauge couplings  $\alpha_4$  and  $\alpha_5$  is presented in section 7.

# Chapter 3

## Particle Flow Calorimetry for Future Linear Colliders

*“I am fond of pigs. Dogs look up to us. Cats look down on us. Pigs treat us as equals.”*

— Winston Churchill

Particle flow calorimetry can provide extremely good jet energy resolutions for at a future linear collider. Jet energy resolution is crucial at the linear collider as many of the interesting processes will be characterised by multi-jet final states. Many of these multi-jet final states will be produced from the hadronic decays of W and Z bosons and one of the key goals of the future linear collider is to be able to separate these decays. Separation of these decays can be achieved, however, only by placing a tight requirement on the jet energy resolution;  $\sigma_E/E \lesssim 3.5\%$  for 50-500 GeV jets at the ILC and up to 1.5 TeV at CLIC [24]. The use of particle flow calorimetry will also be highly beneficial for quantifying final states of interest that involving charged leptons and missing momentum.

### 3.1 Particle Flow Calorimetry

The premise of particle flow calorimetry is to use the sub-detector that offers the best energy resolution to measure the energy of any given particle, which corresponds to energy measurements being made in the ECal for  $\gamma$ s, the HCal for neutral hadrons

and, crucially, the tracker for charged particles. The starker contrast of this approach to that of traditional calorimetry occurs in the measurement of the energy of charged particles. In particle flow calorimetry the energy of a charged particle is measured using the curvature of the path it transverses as it bends in a magnetic field, while in traditional calorimetry the energy would be measured using the calorimeters, predominantly the hadronic calorimeter (HCal). The tracker energy resolution for a single charged particle of energy  $E_{X^\pm}$  is  $\sim 10^{-4} \times E_{X^\pm}^2$ , while for the HCal it is  $\sim 0.55 \times \sqrt{E_{X^\pm}}$  [24]. The energy resolution offered by the tracker is significantly better than that offered by the HCal for energies up to  $\sim \mathcal{O}(300 \text{ GeV})$ . This means that particle flow calorimetry has the potential to offer a much better energy resolution for charged particles, below  $\sim \mathcal{O}(300 \text{ GeV})$ , than that of the traditional calorimetry approach. Particle flow calorimetry offers gains in performance for collision energies well beyond 300 GeV as the average long-lived particle energy for physics processes of interest is typically much less than 300 GeV. Furthermore, it also leads to a significant improvement in the measurement of jet energies as, after the decay of short-lived particles, approximately 60% of the energy of a jet is carried in the form of charged particles. The measurement of jet energies in the particle flow paradigm is summarised in table 3.1. The benefits to the energy resolution, for both charged particles and jets, offered by the particle flow approach to calorimetry is the driving factor behind why it is planned for used at the linear collider experiment.

Jet Component	Detector	Energy Fraction	Energy Resolution
Charged Particles ( $X^\pm$ )	Tracker	$\sim 0.6E_j$	$10^{-4} \times E_{X^\pm}^2$
Photons ( $\gamma$ )	ECal	$\sim 0.3E_j$	$0.15 \times \sqrt{E_\gamma}$
Neutral Hadrons ( $X^0$ )	HCal	$\sim 0.1E_j$	$0.55 \times \sqrt{E_{X^0}}$

**Table 3.1:** The approximate jet fractions and energy resolutions for charged particles ( $X^\pm$ ) of energy  $E_{X^\pm}$ , photons ( $\gamma$ ) of energy  $E_\gamma$  and neutral hadrons ( $X^0$ ) of energy  $E_{X^0}$ . Taken from [24].

Particle flow calorimetry is challenging to put into practice as it requires a precise reconstruction for all long-lived particles within a detector. Charged particle energy measurements are made using the curvature of the track they transverse as they bend in the magnetic field, but they also produce calorimetric energy deposits, as shown in figure 3.1. If both energy measurements are included, the energy of the charged particle

will be double counted. To avoid this, any calorimetric energy deposits associated to charged particle tracks must not be used when reporting the reconstructed energy. Furthermore, if the calorimetric energy deposits for a neutral particle are incorrectly associated to a track, the energy measurement for that neutral particle will be totally omitted. The combination of this double counting of charged particle energies and loss of neutral particle energies degrades the energy resolution. This is referred to as the 'confusion' contribution to the jet energy resolution. Particle flow calorimetry hinges on the event reconstruction being able to correctly associate all charged particle tracks to their corresponding calorimetric energy deposits. This can only be realised using calorimeters with fine segmentation so that it is possible to resolve individual particle showers. It also required sophisticated pattern recognition algorithms to reduce the effects of confusion.

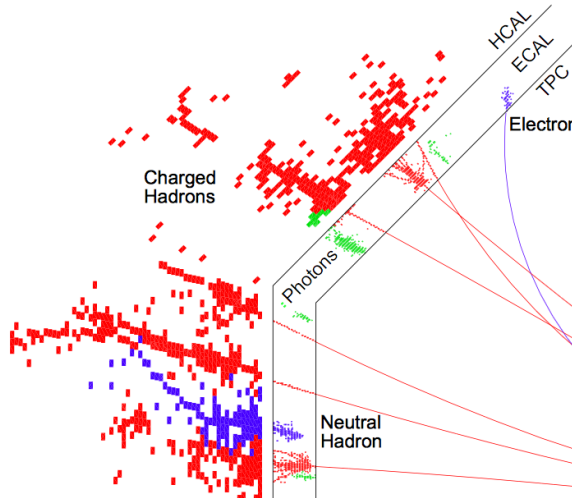


**Figure 3.1:** A typical simulated 250 GeV jet in the CLIC\_ILD detector, with labels identifying constituent particles. Image taken from [25].

## 3.2 International Large Detector

The current detector concepts for the linear collider experiments have been designed to make particle flow calorimetry possible. While there are a number of different concepts that are under consideration for both the ILC and CLIC one of the most prominent, and the focus of this work, is the International Large Detector (ILD). The ILD detector, shown in figure 3.2, achieves very high spatial resolution for all sub-detector systems thanks to its highly segmented calorimeters and central tracking

system, both of which are encompassed within a 3.5 T magnetic field. The sophisticated pattern recognition software that is needed for particle flow calorimetry is provided by PandoraPFA [24, 25].

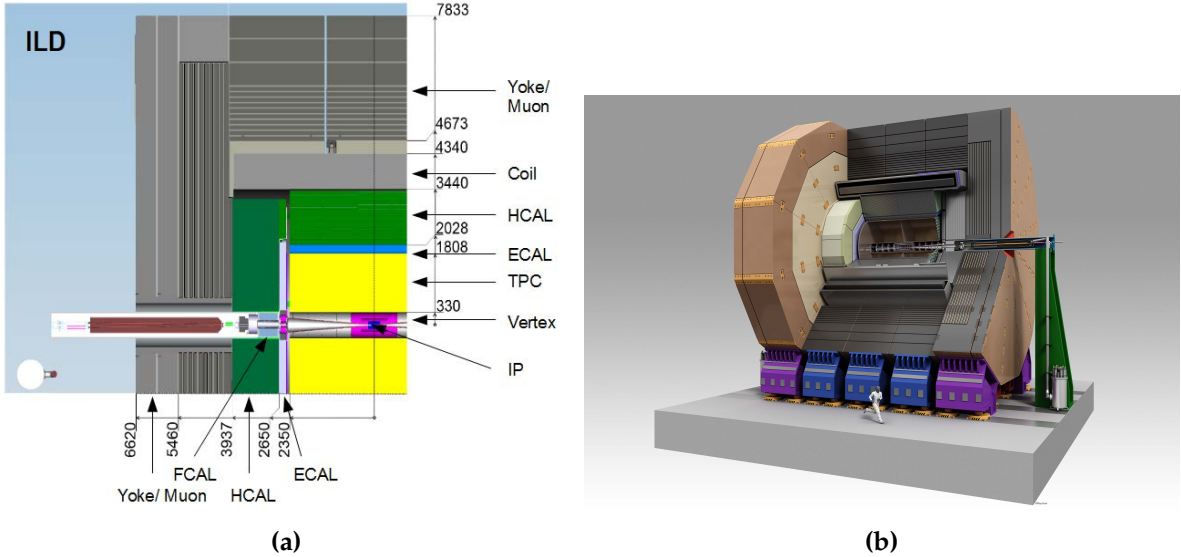


**Figure 3.2:** (a) Quadrant view of the ILD detector concept. The interaction point is in the lower right corner of the picture. Dimensions are in mm. (b) An artistic view of the ILD detector concept. Figures taken from [26].

### 3.2.1 Overview

The tracking system for the ILD detector consists of a vertex detector, a Time Projection Chamber (TPC) and a number of supplementary silicon detectors. The vertex detector is designed to give precise information about displaced vertices with respect to the impact point (IP), which is crucial for the study of short lived particles such as the D and B mesons. The vertex detector is located close to the IP and surrounding it is the TPC, which is the central tracker for ILD. The TPC provides detailed measurements of the trajectory of charged particle tracks passing through it, up to 224 measurements per track. This information is used for determining the curvature of the charged particle track and hence the momentum of the charged particle that transversed it. Finally, the purpose of the supplementary silicon detectors is to provide additional, high precision, spatial measurements to aid track fitting and extend coverage of the detector down to low polar angles.

The calorimetric system for ILD is comprised of an electromagnetic calorimeter (ECal), a hadronic calorimeter (HCal) and a number of forward calorimeters (FCal). The primary function of the ECal is to induce electromagnetic particles to shower within it and to measure the energy of these particle showers. Similarly, the HCal is designed to induce and measure the energy of hadronic particle showers. The ECal surrounds the tracking system in the ILD detector and is itself surrounded by the HCal. The function of FCal is to extend the coverage of the calorimeter system to low polar angles and to provide measurements of the luminosity of the colliding  $e^\pm$  beams.

The outermost elements of the ILD detector are the solenoid, iron yoke and muon system. The solenoid generates a magnetic field, which is essential for determining the energy of charged particles in the particle flow paradigm. The iron yoke is used to return the magnetic field generated by the solenoid. The yoke is instrumented by the muon system to provide additional information, which supplements the calorimetric energy measurements made by the ILD calorimeters.

### 3.2.2 Vertex Detector

The main goal of the ILD vertex detector is to achieve a resolution on the impact parameter of charged particle tracks of:

$$\sigma_b < 5 \oplus \frac{10}{p \sin(\theta)^{3/2}} \mu\text{m}, \quad (3.1)$$

where  $\sigma_b$  is the resolution on the track impact parameter,  $p$  is the momentum of the track and  $\theta$  is the angle between the track and the vertex detector plane. The first term in this parameterisation is the transverse impact parameters resolution and the second is a multiple-scattering term. This makes precisely tagging secondary vertices from charm and bottom mesons possible. Typically these mesons have relatively short proper lifetimes,  $\tau$ , such that  $c\tau \approx \mathcal{O}(300 \mu\text{m})$ . To achieve this impact parameter resolution, a spatial resolution of better than  $3 \mu\text{m}$  is required near the impact point (IP). Furthermore, a low material budget of less than 0.15 % of a radiation length per layer is required to ensure that few electromagnetic showers are initiated within the vertex detector. A low pixel occupancy is essential for determining the trajectory of individual tracks in the detector. Furthermore, consideration will have to be given to the mechanical structure of the detector, power consumption and cooling.

There are a number of different pixel technology options under consideration for the vertex detector for the ILD detector. This is an active area of ongoing research and development for the linear collider collaboration. The current design of the vertex detector consists of three concentric layers of double-sided ladders with the first layer contains 10 ladders, the second 11 ladders and the third 17 ladders as shown in figure 3.3. Each ladder has two silicon pixel sensors on each side and the ladder thickness is approximately 2 mm. The radii covered by the detector range from 16 mm to 60 mm from the IP.

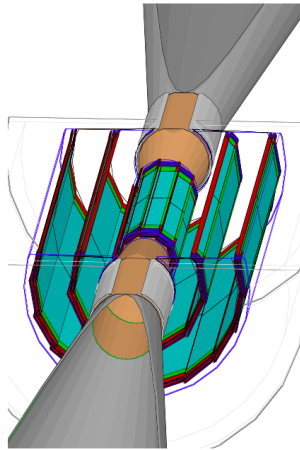


**Figure 3.3:** Vertex detector design for ILD. Figures taken from [27].

### 3.2.3 Time Projection Chamber

The central tracking system for the ILD detector is a TPC, which is shown in figure 3.4. The TPC consists of a cylindrical gas volume with a central electrode providing an axial electric field. When a charged particle passes through the TPC, it ionises the gas and the ionised molecules drift in the axial electric field. The direction of the electric field is chosen such that the electrons drift towards the endplates where they are collected. The position of the ionisation point can then be calculated using the drift time of the electrons in the TPC. Combining these TPC hits together makes reconstruction of the full charged particle track possible. TPCs have an advantage over silicon tracking in that they continuously track any charged particle passing through them, while silicon detectors are only sensitive within each silicon layer. This compensates for the worse single point resolution that TPCs have in comparison to silicon detectors and makes TPCs a viable option for the ILD detector. Furthermore, TPCs have a very low material

budget. This benefits calorimetry as it minimises energy losses prior to the particle energy entering the calorimeters, which means the calorimetric energy deposits give a better reflection of the true particle energy.

The ILD TPC has a point resolution of better than  $100 \mu\text{m}$  and a double hit resolution in  $\phi$  of less than 2 mm. The gas used for the TPC will be Ar:CH<sub>4</sub>:CO<sub>2</sub> (95:3:2) [28]. Several readout technology options, designed to measure the ionisation current, are currently under development. For all potential options it is envisaged that the readout pads would be  $\approx 1 \times 6\text{mm}^2$  giving a total of approximately  $10^6$  pads on each TPC endplate.

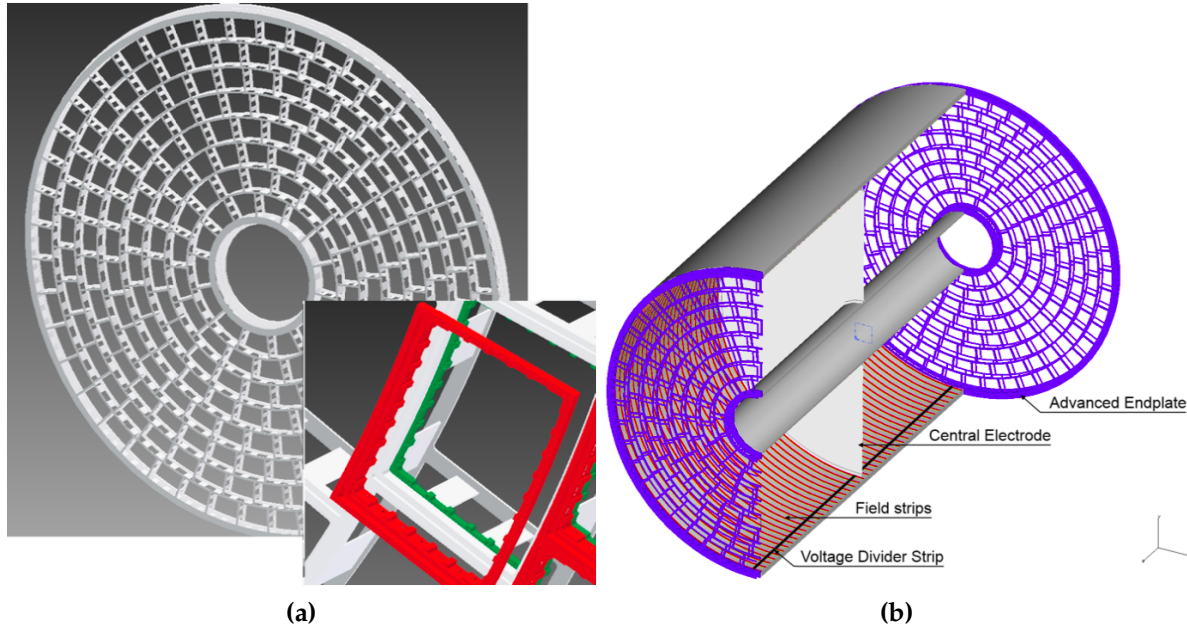


**Figure 3.4:** (a) Drawing of the proposed end-plate for the TPC. In the insert a back frame, which is designed to support the readout modules, is shown. (b) Conceptual sketch of the TPC system showing the main parts of the TPC (not to scale). The central electrode generates the axial electric field, the endplates collect the ionisation electrons, the field strips help to maintain a uniform electric field across the TPC and the voltage divider strips maintains the voltage difference between the anode and cathode. The field strips are held at fixed voltages such that they replicate the electric field produced by the electrodes. This reinforcing of the electric field configuration minimises non-uniformities in the electric field. The field cage of the TPC is not shown.

### 3.2.4 Supplemental Silicon Tracking System

There are four components that make up the supplemental silicon tracking system in ILD, shown in figure 3.5, which are:

- Silicon Inner Tracker (SIT) and Silicon External Tracker (SET). These are both barrel components, which are positioned immediately inside and outside the TPC. The SIT helps form associations between hits in the vertex detector and TPC, while the SET helps with extrapolation of TPC tracks into the calorimeter.
- Endplate of the TPC (ETD). This sensor is identical to the SET, but is positioned in front of the ECal endcap calorimeter. The ETD extends the coverage of the supplemental silicon tracking system envelope.
- Forward tracker (FTD). This detector consists of seven silicon disks that extend the coverage of the tracking down to small angles that are not covered by the TPC.

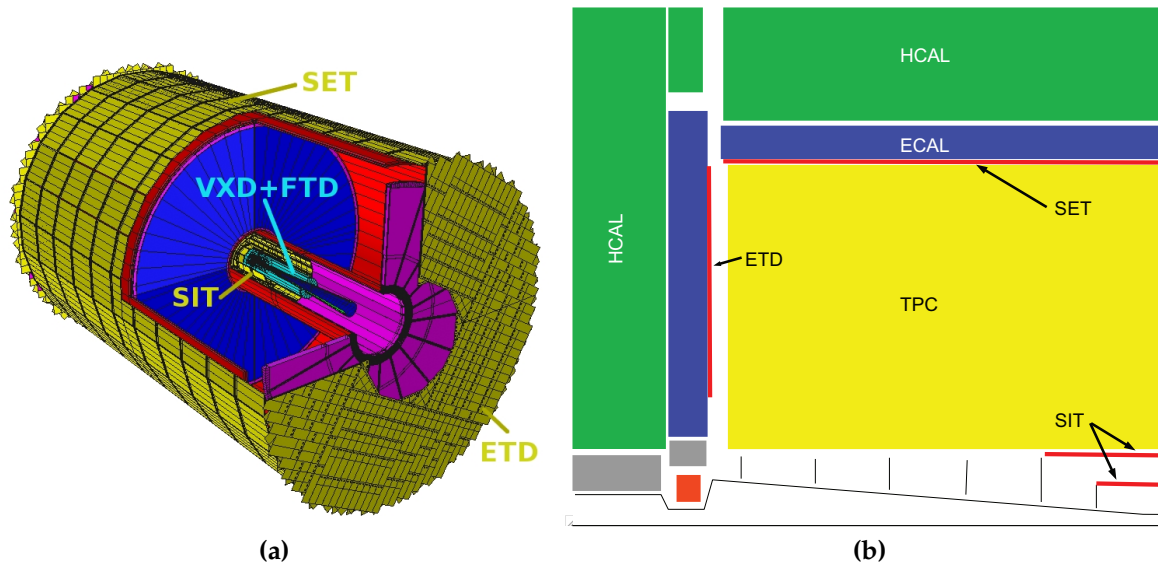


**Figure 3.5:** (a) A 3D detailed GEANT4 simulation description of the silicon system. (b) A quadrant view of the ILD silicon envelope made of the four components SIT, SET, ETD and FTD as included in the full MOKKA simulation. Figures taken from [26].

The coverage of the SIT, SET, ETD and FTD is given in table 3.2. These detectors are designed to give high precision space points that can be used in track fitting. Furthermore, the ETD and SET are of particular use for extrapolating the charged particle tracks into the calorimeters. This is key for particle flow calorimetry, which

Tracking System	Coverage [ $\cos\theta$ ]
SIT	0.910
SET	0.789
ETD	0.799 - 0.985
FTD	0.802 - 0.996

**Table 3.2:** Coverage of the supplementary silicon tracking systems in the ILD detector. In this table  $\theta$  is the polar angle with respect to the beam direction. Taken from [26].

relies upon correct association of charged particle tracks and clusters of calorimeter hits. Analogously to the vertex detector, these detectors require low material budget and low occupancy. The FTD, due to its proximity to the beam axis, is particularly prone to high occupancies.

The SIT, SET and ETD are silicon pixel sensors with  $50 \mu\text{m}$  pitch embedded in  $200 \mu\text{m}$  thick silicon. The FTD consists of seven silicon tracking disks, the first two being pixel detectors and the remaining five being strip detectors. The pixel detector disks are formed of 16 petals, as shown in figure 3.6. Within these petals the pixel size varies from  $26 \times 29 \mu\text{m}^2$  to  $26 \times 67 \mu\text{m}^2$ . Strip detectors are used for the outermost tracking disks as the occupancy considerations do not demand a high granularity detector i.e. a pixel detector. These detector disks will have a pitch of  $50 \mu\text{m}$ . The active sensor and readout ASIC design for each of these detectors is an active area of development for the linear collider.

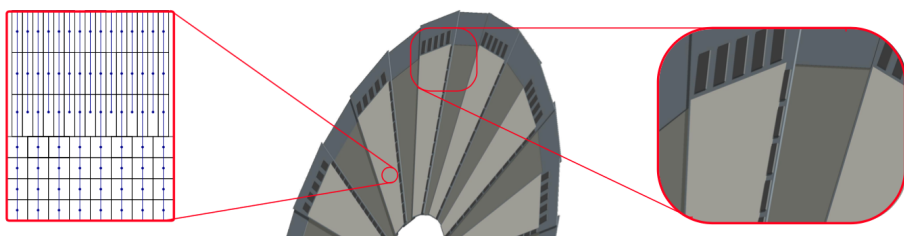


**Figure 3.6:** A half-disk for the FTD showing the petal concept. The rightmost zoom image shows a detail of the end-of-petal area that houses the read-out electronics. The leftmost image shows the region at  $R = 8 \text{ cm}$  where both the column width and the  $R$ -dimension of the pixels changes. Figures taken from [26].

### 3.2.5 Electromagnetic Calorimeter

The nominal ILD detector contains a finely segmented electromagnetic sampling calorimeter (ECal). The ILD ECal has been specifically designed with particle flow calorimetry in mind. To that extent the spatial resolution of particle showers within the ECal takes as much, if not more, precedence than the energy resolution.

There are a number of design requirements for the ECal:

- The ECal must be compact in size to reduce the overall cost of the detector.
- Fine segmentation of the ECal is required so that nearby particle showers can be separated. This is an essential requirement for particle flow calorimetry.
- Electromagnetic showers should be contained within the ECal.

Based on these requirements tungsten is used as the absorber material for the ILD ECal as it has a small radiation length ( $X_0$ ), a small Moli  re radius and a large ratio of radiation length to nuclear interaction length. A comparison of these properties for other ECal absorber material candidates is shown in table 3.3. The small radiation length in tungsten allows for a large number of radiation lengths,  $\approx 24X_0$ , to be compacted within a relatively short distance,  $\approx 20$  cm, in nominal ILD ECal. This is sufficient for containing all but the highest energy electromagnetic showers. The small Moli  re radius in tungsten will lead to compact electromagnetic showers. This makes separation of nearby showers easier. Finally, the large ratio of the radiation length to the nuclear interaction length in tungsten will lead to greater longitudinal separation between electromagnetic and hadronic showers again making shower identification easier.

The active material in the nominal ILD ECal is silicon, however, a scintillator strip option is also being considered. It contains a total of 30 readout layers, which is sufficient to provide a good energy resolution. The tungsten thickness for the innermost 20 layers is 2.1 mm, while for the final 10 layers it is 4.2 mm. This configuration of absorber material thickness is chosen to reduce the number of readout channels and hence the cost, while maintaining a high sampling rate for particle showers at the start of the ECal. It should be noted that this ECal offers no gains in terms of energy resolutions in comparison to preexisting particle collider experiments, as shown in table 3.4. This is the case as the focus of this calorimeter is split between imaging the particle showers and recording their energy as opposed to purely focusing on the

energy measurement. Each of the ECal layers is divided up into square cells, of side length 5 mm, which makes separation of nearby particle showers possible. This cell size was chosen as a balance between being able to resolve nearby particle showers and reducing the overall cost of the calorimeter, which scales with the number of readout channels. An optimisation study of the various ECal parameters for the ILD detector can be found in section 6.2.

Material	$\lambda_I$ (cm)	$X_0$ (cm)	$\rho_M$ (cm)	$\frac{\lambda_I}{X_0}$
Fe	16.8	1.76	1.69	9.5
Cu	15.1	1.43	1.52	10.6
W	9.6	0.35	0.93	27.4
Pb	17.1	0.56	1.00	30.5

**Table 3.3:** Comparison of the nuclear interaction length  $\lambda_I$ , radiation length  $X_0$  and Molière radius for iron, copper, tungsten and lead. Table taken from [24].

Experiment	ECal Energy Resolution $\frac{\sigma_E}{E}$
CMS [29]	$\sim \frac{2.8\%}{\sqrt{E(\text{GeV})}} \oplus 0.3\% \oplus \frac{12\%}{E(\text{GeV})}$
ATLAS [30]	$\sim \frac{10.1\%}{\sqrt{E(\text{GeV})}} \oplus 0.1\%$
LHCb [31]	$\sim \frac{9\%}{\sqrt{E(\text{GeV})}} \oplus 0.8\%$
ILC (ILD Silicon Option) [26]	$\sim \frac{16.6\%}{\sqrt{E(\text{GeV})}} \oplus 1.1\%$

**Table 3.4:** Comparison of the ECal energy resolutions for various experiments.

### 3.2.6 Hadronic Calorimeter

A finely segmented hadronic sampling calorimeter (HCal) is also present in the nominal ILD detector, which has been designed with particle flow calorimetry in mind.

The design requirements for the HCal mirror those of the ECal, which can be found in section 3.2.5, with one exception; the HCal is designed to contain hadronic showers as opposed to electromagnetic showers. Steel is used as the absorber material for the HCal as it has durable mechanical properties that allow the HCal to be constructed without the need of auxiliary supports. If required, auxiliary supports would create

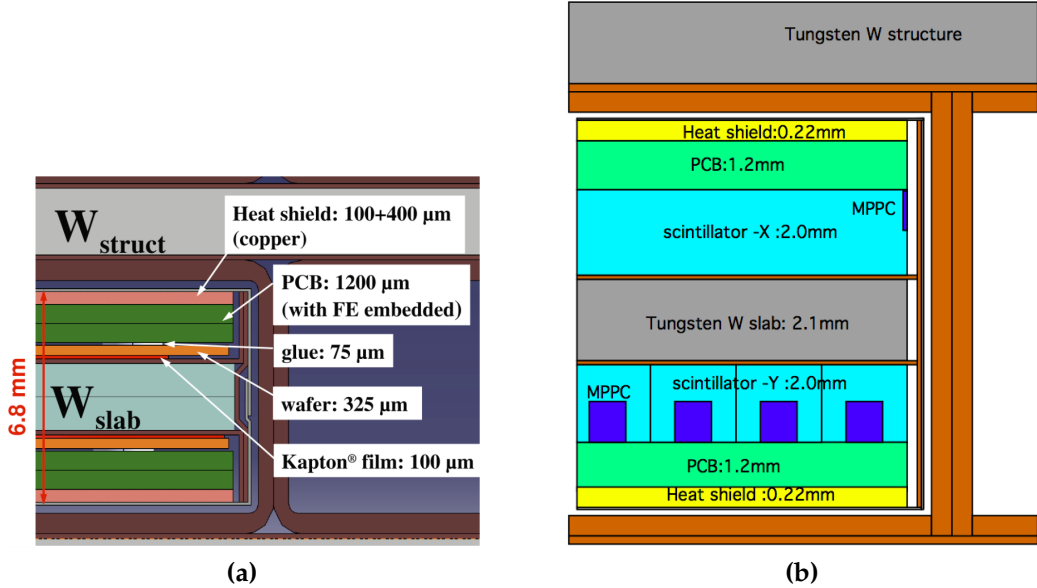


**Figure 3.7:** Cross section through ECal layer for (a) silicon and (b) scintillator option. Figures taken from [26].

dead regions in the detector that would harm performance. Furthermore, steel is relatively inexpensive and has a relatively small nuclear interaction length, meaning it is possible to achieve a compact calorimeter design at low cost. The nominal ILD HCal contains approximately  $6\lambda_I$ , which when combined with the  $1\lambda_I$  in the ECal is enough to contain the majority of hadronic showers at ILC like energies.

The active material in the nominal ILD HCal is scintillator. In total, the HCal contains 48 readout layers, which provides an extremely good energy resolution. This can be seen when comparing the HCal energy resolution between different experiments, as shown in table 3.5. An individual layer in the HCal is comprised of 20 mm of steel absorber material with 3 mm of scintillator active material. Each layer in the HCal is segmented into square cells, of side length 30 mm. This cell size was chosen as a balance between reducing the cost of the detector, which is proportional to the number of readout channels, and achieving the required spatial resolution to make particle flow calorimetry possible. The segmentation of the ILD HCal gives excellent spatial resolution and sufficiently good energy resolution to make the use of particle flow calorimetry a reality. An optimisation study of the various HCal parameters for the ILD detector can be found in section ??.

The ILD HCal is intrinsically non-compensating, which means that it has a different response to electromagnetic and hadronic showers. The origin of this different

response is the fundamentally different mechanisms governing the propagation of electromagnetic and hadronic showers. One key difference between the mechanisms is that hadronic showers have an invisible energy component, which occurs due to effects such as neutrons coming to rest in the detector and nuclear biding energy losses [32]. In general, this leads to a lower response from a calorimeter to a hadronic shower than an electromagnetic shower. A number of different software techniques have been developed for the linear collider experiment that attempt to correct this non-compensating response. For more details see chapter 5. The ILD ECal has a compensating response due to the use of tungsten as the absorber material [33], therefore, no additional treatment of energies is required.

Experiment	HCal Energy Resolution $\frac{\sigma_E}{E}$
CMS [34]	$\sim \frac{90\%}{\sqrt{E(\text{GeV})}} \oplus 4.8\%$
ATLAS [35]	$\sim \frac{52.1\%}{\sqrt{E(\text{GeV})}} \oplus 3.0\% \oplus \frac{1.6\%}{E(\text{GeV})}$
LHCb [31]	$\sim \frac{69\%}{\sqrt{E(\text{GeV})}} \oplus 9.0\%$
ILC (ILD Silicon Option) [26]	$\sim \frac{43.3\%}{\sqrt{E(\text{GeV})}} \oplus 1.8\%$

**Table 3.5:** Comparison of the HCal energy resolutions for various experiments.

### 3.2.7 Solenoid, Yoke and Muon System

Surrounding the ILD calorimeter system is solenoid that generates a 3.5 T magnetic field. The magnetic field produced by the coil is crucial for bending charged particles so that their momentum can be determined from the curvature of the path they transverse. Furthermore, the bending of charged particles leads to greater separation of calorimetric energy deposits between charged and neutral particles, which will reduce the effects of confusion when using particle flow calorimetry.

The magnetic field in the ILD detector is returned by an iron yoke that surrounds the solenoid. Iron is chosen for the yoke material as it has a very large permeability.

This yoke is instrumented by a muon system in the barrel and forward regions of the detector. The goal of this instrumentation is to identify muons escaping the calorimeters and to act as a tail catcher for the calorimeters. The muon system consists of 10 layers, spaced 140 mm apart, followed by 2 (3) layers spaced 600 mm apart in

the barrel (endcap) region of the detector, as shown in figure 3.8. There is also an additional sensitive layer for the barrel region placed immediately outside the HCal to help with association energy deposits between the calorimeters and the yoke. As the majority of particles at ILC like energies will be contained within the calorimeters, the energy and spatial resolution of the muon system are not critical to performance. It is for that reason that the number of layers is lower and the layer thicknesses wider in the yoke than in the calorimeters. The nominal ILD model uses 30 mm wide and 1 m long scintillator strips as the readout technology for the yoke.

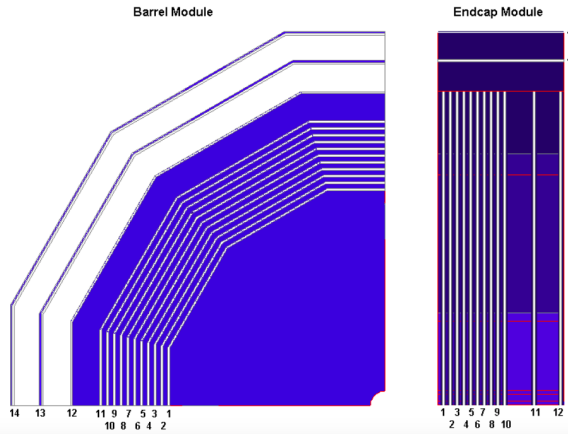


**Figure 3.8:** The sensitive layers of the ILD muon system. Figure taken from [26].

### 3.2.8 Forward Calorimetry

Forward calorimetry in the ILD detector consists of three additional sampling calorimeters:

- The LumiCal, which is located within the octagonal hole in the ECal endcap. This will give a precise measurement of the luminosity of the linear collider beam. The LumiCal uses Bhabha scattering,  $e^+ e^- \rightarrow e^+ e^- (\gamma)$ , as a gauge process for the luminosity measurement. Using this approach the luminosity can be measured with precision of less than  $10^{-3}$  at 500 GeV [28].
- The LHCAL, which is positioned within the square hole of the HCal endcap. This hadronic calorimeter is designed to extend the coverage of the HCal down to small polar angles.

- The BeamCal, which is located just in front of the final focusing quadrupole. This calorimeter will perform a bunch-by-bunch estimate of the luminosity based on the energy deposited in the calorimeter.

The layout of these calorimeters is shown in figure 3.9 and their coverage is summarised in table 3.6. Each of the forward calorimeters will have to deal with high occupancies due to the presence of background processes, e.g. beamstrahlung, which makes fast readout crucial. Furthermore, the BeamCal experiences a large flux of low energy electrons due to its proximity to the beam pipe, which results in a large radiation dose. This makes radiation hard sensors essential for the BeamCal.

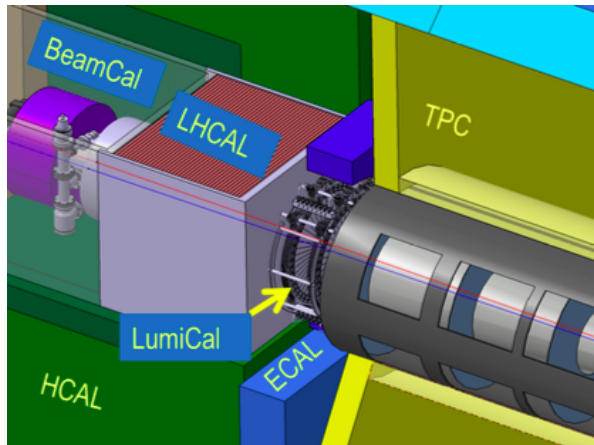


**Figure 3.9:** The very forward region of the ILD detector. LumiCal, BeamCal and LHCAL are carried by the support tube for the final focusing quadrupole, QD0, and the beam pipe. Figure taken from [26].

Forward Calorimeter	Polar Angle Coverage [mrad]
LumiCal	31 - 77
LHCAL	~ 29-122
BeamCal	5 - 40

**Table 3.6:** Coverage of the forward calorimeters in the ILD detector.

Each of these calorimeter is constructed using tungsten as the absorber material. The small Moli  re radius of tungsten ensures that narrow electromagnetic showers are formed within them, which makes separation and identification of showering particles easier.

The layout of these calorimeters is as follows:

- The LumiCal is a silicon tungsten sampling calorimeter that contains 30 readout layers. This gives the LumiCal a total depth of  $\approx 24X_0$ .
- The LHCAL is also a silicon tungsten sampling calorimeter, which contains 40 readout layers. The total depth of the LHCAL is  $\approx 4\lambda_L$ .
- The BeamCal is a tungsten based sampling calorimeter. The sensitive detector material for the BeamCal is an ongoing area of research as, due to the extremely high occupancy from the beam induced backgrounds, a very fast readout is required. The exact layer configuration of the BeamCal will depend upon the choice of sensitive detector material and hence is yet to be specified.

The segmentation within the layers, the cell size, in these forward calorimeters is yet to be fully optimised.

### 3.3 Simulation

Detector model simulation for all studies presented in this work was performed using MOKKA [36], a GEANT4 [37] wrapper providing detailed geometric descriptions of detector concepts for the linear collider. The MOKKA simulation of the ILD detector contains the following [26]:

- The vertex detector is simulated using silicon as the sensitive material. Support material and the cryostat are also included for additional realism.
- The supplementary silicon tracking systems are included. Again, material has been added to the simulation to represent the support material for these systems. Furthermore, an estimation has been made of the material budget for power and readout cables from the vertex detector, SIT and FTD and material has been added to the simulation to represent these. The material added to represent the power and readout cables comes in the form of an aluminium cylinder running inside the TPC field cage and around a cone around the beam pipe.
- The TPC is simulated as a cylindrical volume of a gas mixture surrounded by a field cage. A conservative estimate of the endplate is included in the simulation to account for the support structure, electronics and cooling pipes for the TPC.

- As well as including the silicon tungsten sampling calorimeter, the simulation of the ILD ECal contains additional material to represent the instrumented region of the sensor and a heat shield as shown in figure 5.5a.
- Simulation of the ILD HCal has a number of realistic features including detailed modelling of the electronics, detector gaps and the implementation of Birk’s law for the scintillator sensitive detector elements.
- The muon system, which is the instrumentation of the iron yoke, uses scintillator as the active material in the simulation. A square cell size of side length 30 mm is assumed. This is in contrast to the nominal ILD model, but as the tail-catcher plays a minimal role in event reconstruction at ILC like energies this difference should have negligible impact.
- The forward calorimeters, the LumiCal, LHCAL and BeamCal, are all included in the simulation. Tungsten is used as the absorber material for each of the calorimeters. The LumiCal and LHCAL use a silicon readout material, while the BeamCal uses a diamond readout.

## 3.4 CLIC ILD

The increased collision energy of the proposed CLIC accelerator means the use of the nominal ILD detector model would be inappropriate. Therefore, a new detector model, CLIC\_ILD [4], based upon the nominal ILD detector model was created to cope with the experimental conditions found at the CLIC experiment. The main differences between the nominal ILD detector and CLIC\_ILD are:

- The higher energies found at the CLIC experiment lead to more intense beam induced backgrounds, which is especially problematic for detectors close to the IP where the occupancies will be extremely high. For this reason the inner vertex detector in CLIC\_ILD is moved 15 mm further out from the IP.
- The HCal thickness is increased from  $6 \lambda_L$  to  $7.5 \lambda_L$ . This ensures that higher energy hadronic showers found at the CLIC experiment are contained within the calorimeters.
- The HCal absorber material for the barrel is tungsten as opposed to steel. This reduces the overall thickness of the HCal and keeps the coil size, one of the

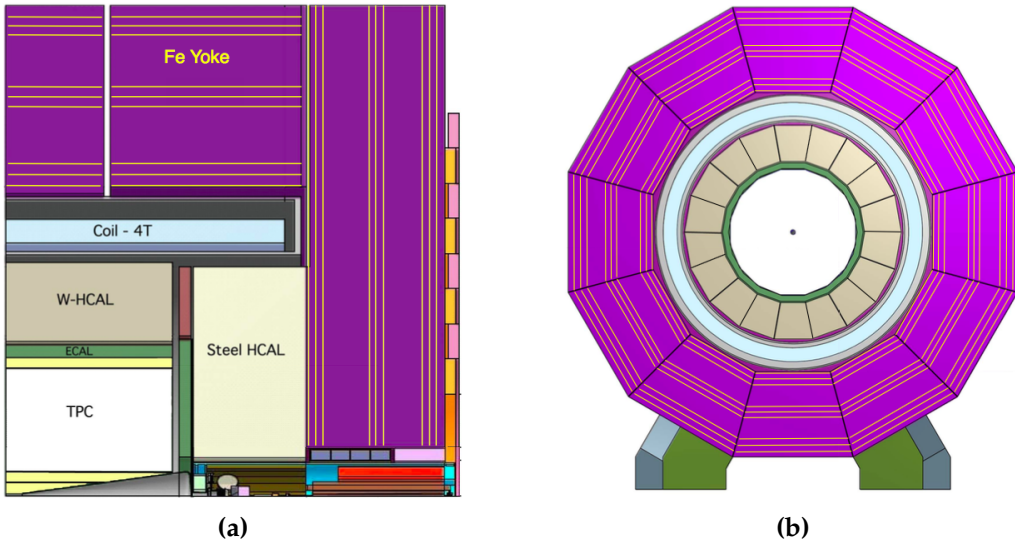


**Figure 3.10:** (a) Longitudinal (top quadrant) and (b) transverse cross section of the CLIC\_ILD detector. Figures taken from [4].

driving cost factors for the detectors, similar for the nominal ILD and CLIC\_ILD detectors. Steel is used as the absorber material for the HCal endcaps as there are no spatial requirements relating to the coil size and this will lower the detector cost. Furthermore, the shower development time in steel is faster than in tungsten making effective time stamping of energy deposits easier, which is crucial for the CLIC experiment for vetoing beam induced backgrounds.

- The magnetic field strength in the CLIC\_ILD detector is increased to 4 T. This was found to benefit the reconstruction, particularly at high energies, as it leads to greater separation of charged particle tracks. Furthermore, it was possible to achieve this increase in field strength using the nominal ILD coil design.
- The CLIC\_ILD detector contains masking, graphite layers placed in front of the BeamCal, to prevent particles produced by the beam-induced interactions from backscattering into the main detector. It is the increased collision energy that makes backscattering of particles a more problematic effect for the CLIC experiment than it is for the ILC experiment.

## 3.5 Particle Flow Reconstruction

Particle flow calorimetry relies upon correct associations being made between calorimetric energy deposits and charged particle tracks. Even with a finely segmented detector, such as the ILD detector described in section 3.2, correctly making these associations is a highly non-trivial task and must be done using advanced pattern recognition software. This is provided by the PandoraPFA particle flow algorithm [24,25]. PandoraPFA is applied in the linear collider reconstruction using MARLIN [38], a c++ framework specifically designed for the linear collider.

### 3.5.1 PandoraPFA

PandoraPFA takes as input calorimeter hits and charged particles tracks and produces as output reconstructed particles known as particle flow objects (PFOs). The pattern recognition in PandoraPFA is applied in eight main stages [24]:

1. Track selection. The input track collections are examined to determine whether  $V^0$  decays, two charged tracks originating from a point displaced from the IP, or kinks, where a charged particle has decayed into a single charged particle and a number of neutral ones, are present. Such information will be propagated in the reconstruction to the final PFO creation stage.
2. Calorimeter hit treatment. The treatment of calorimeter hits by PandoraPFA is of paramount importance to the work presented in chapters 5 and 6. Therefore, full details of the calorimeter hit selection procedure are presented here. This selection procedure is broken down into several steps:
  - The various collection of, post digitisation, calorimeter hits are passed into the Pandora framework and converted into Pandora calorimeter hits.
  - To minimise any dependency on the detector geometry each calorimeter hit is assigned to a pseudo-layer, which is representative of the hits position in the calorimeter. All further topological association algorithms work using the pseudo-layer definition, illustrated in figure 3.11.
  - A minimum ionising particle equivalent energy cut is applied to the calorimeter hits. If a calorimeter hit contains less than 0.5 (0.3) of the energy of

a normally incident MIP passing through the calorimeter cell in the ECal (HCal) then it is not used in the reconstruction.

- If a calorimeter hit is sufficiently far away from other hits, it is flagged as an isolated hit. Such hits are most likely due to low energy neutrons produced in hadronic showers, which can travel a significant distance from the original shower before depositing energy. Due to the distance they travel these hits are very difficult to associate to the correct particle shower. Furthermore, as such hits are unlikely to be the seed for a particle shower they are not used by the initial clustering algorithm.
  - Any calorimeter hit that contains an energy consistent with a MIP signal and where, at most, one Pandora calorimeter hit exists in the neighbouring cells within the same layer is flagged as a MIP consistent hit. This information is used in the identification of MIPs in the reconstruction.
  - The energy contribution for each calorimeter hits ultimately depends on whether the cluster the calorimeter hit has been associated to is deemed to have originated from an electromagnetic or hadronic particle shower. Different scale factors are applied to the energy for electromagnetic and hadronic showers to account for the non-compensating response of the calorimeters. These scale factors are used throughout the reconstruction, including the final reconstructed particle energy, once the particle shower type has been identified. For energy comparisons prior to the shower type being identified the uncorrected calorimeter hit energy is used. Further details on how these calibration constants are determined can be found in chapter 5.
3. Clustering. This begins by using the projection of the charged particle tracks onto the front face of the ECal as seeds for the initial clustering phase. Calorimeter hits are looped over on a per layer basis, working from the inner to the outer pseudo-layer, and if they fall within a cone of fixed dimensions surrounding a cluster direction they are associated to the cluster. If no association can be made to any preexisting calorimeter hit clusters then the calorimeter hit is used to seed a new cluster.
  4. Topological cluster merging. The initial clustering algorithm is designed to be conservative to avoid mixing together energy deposits from several particles. The fragments produced by the initial clustering are then merged together by various

algorithms whose logic is motivated by a number of well-motivated topological rules, such as those shown figure 3.12.

5. Statistical re-clustering. Comparisons between the cluster energy and any associated track momenta are made to determine whether they are consistent. If a large discrepancy is observed then statistical re-clustering is initiated. This involves running a number of differently configured algorithms to change the cluster configuration to determine if a new optimal configuration of tracks and clusters can be found.

This step relies upon the reported cluster energies being accurate. To ensure this is the case, a well defined calibration procedure is applied for all detector models considered in this work, for more details see chapter 5. At this point in the reconstruction, the energy resolution of the calorimeters impacts the way that the pattern recognition is performed. The better the energy resolution of the calorimeters, the fewer the number of mistakes that are made when pairing up clusters of calorimeter hits to charged particle tracks.

6. Photon identification and recovery. Topological likelihood data is used to identify clusters of calorimeter hits that are consistent with  $\gamma$ s. This is possible due to the clear transverse and longitudinal profiles observed for electromagnetic showers.
7. Fragment removal. Neutral clusters originating from a nearby charged particle cluster are identified and merged back into the parent charged particle cluster. These algorithms take into account the changes in the compatibility of the track and cluster associations when merging any neutral clusters into charged clusters.
8. Formation of particle flow objects. Finally, reconstructed particles are produced. The energy for charged particles is taken from the track momenta, while neutral particle energies are taken from the calorimeter cluster measurements. Furthermore, the different electromagnetic and hadronic scales are applied to the output neutral particle energies depending on whether the neutral cluster is consistent with a  $\gamma$ .

The application of the pattern recognition algorithms in PandoraPFA when combined with a highly segmented detector make particle flow calorimetry a reality. In turn this provides excellent jet energy resolution for studying many interesting physics processes at the linear collider experiment.

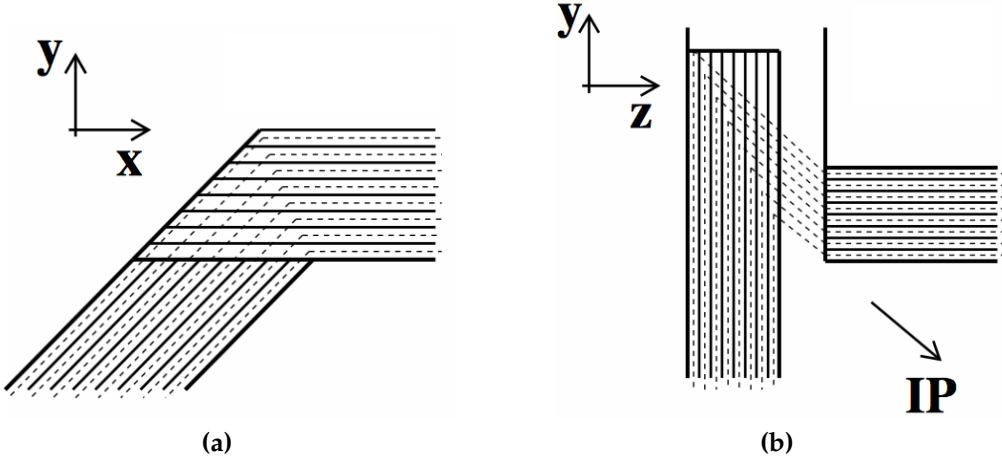


**Figure 3.11:** Schematic showing the definition of the pseudo-layer assignment for calorimeter hits. The solid lines indicate the positions of the physics ECal layers and the dashed lines show the definition of the virtual pseudo-layers. (a) The  $xy$ -view showing the ILD ECal stave structure. (b) The  $xz$  view showing a possible layout for the ECal barrel/endcap overlap region. The pseudo-layers are defined using projection back to the IP. Figures taken from [24].

## 3.6 Performance

The fundamental principle of particle flow calorimetry is to measure the energy of a particle passing through a detector in whichever sub-detector offers the best energy resolution. For particle collider experiments, this involves measuring the momenta of charged particles using the curvature of the track they create in the detector. This offers extremely good energy resolution in comparison to calorimetric energy measurements. As neutral particles produce no tracks, their energies must be measured using calorimetric energy deposits.

The application of particle flow calorimetry is extremely challenging as charged particles create both tracks and calorimetric energy deposits. If both of these energy measurements were included, the energy of all charged particles would be double counted. Therefore, to avoid this, any calorimetric energy deposits originating from charged particles are not included in the final energy measurement. However, this methodology makes it possible to double count and omit energy measurements if the origin of a calorimetric energy deposit is misidentified. For example:

- If a calorimetric energy deposit, made by a charged particle, is not associated to a track, the calorimetric energy deposit will be double counted: Firstly, when the

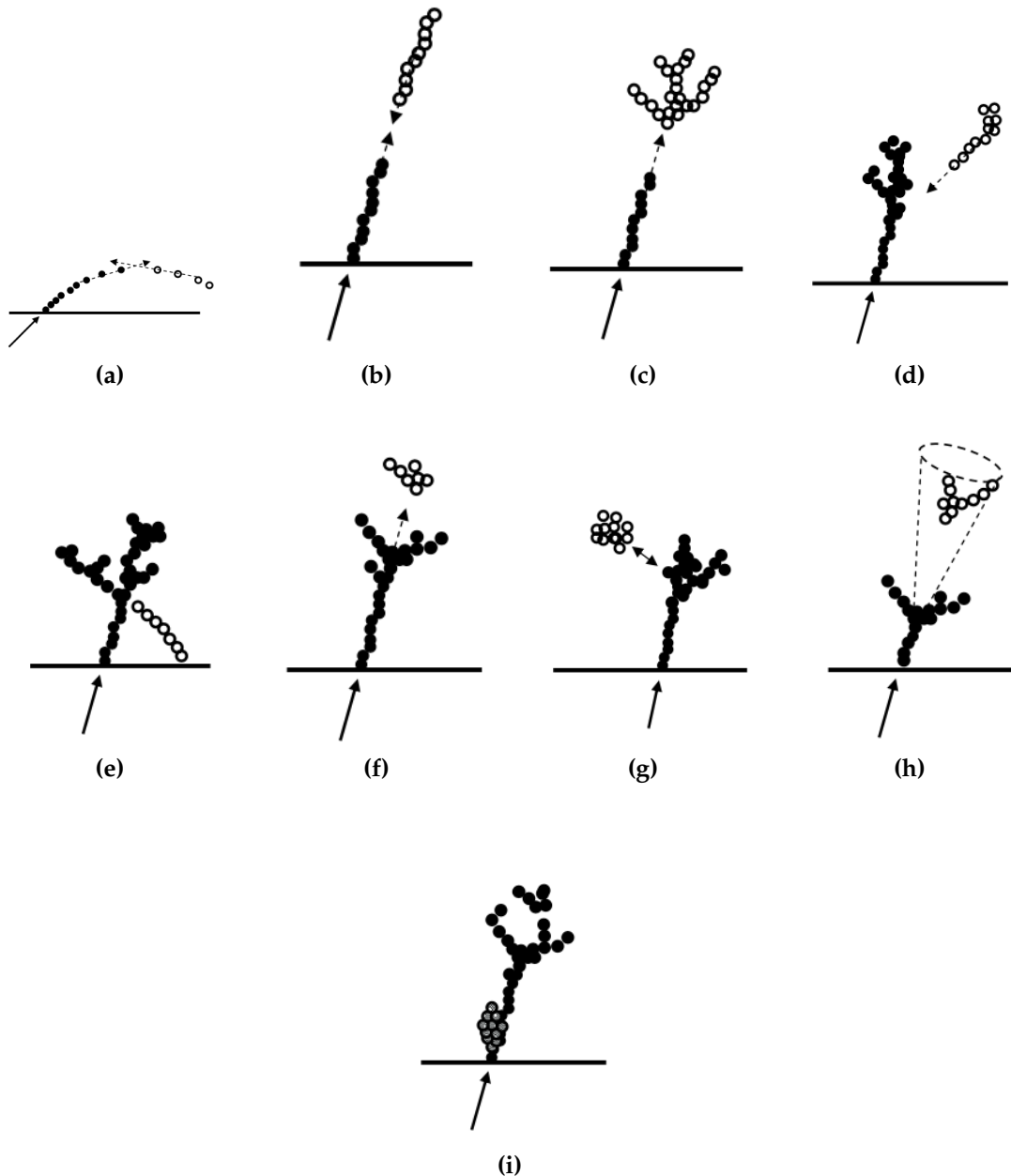


**Figure 3.12:** The main topological rules for cluster merging: (a) looping track segments; (b) track segments with gaps; (c) track segments pointing to hadronic showers; (d) track-like neutral clusters pointing back to a hadronic shower; (e) back-scattered tracks from hadronic showers; (f) neutral clusters which are close to a charged cluster; (g) a neutral cluster near a charged cluster; (h) cone association; and (i) recover of photons which overlap with a track segment. In each case the arrow indicates the track, the filled points represent the hits in the associated cluster and the open points represent hits in the neutral cluster. Figures taken from [24].

track energy is accounted for and secondly, when the calorimetric energy deposit is incorrectly reported as the energy of a neutral particle.

- If a calorimetric energy deposit, made by a neutral particle, is incorrectly associated to a track, that calorimetric energy deposit is not accounted for.

These effects, collectively known as "confusion", degrade the energy resolution of a particle flow detector. Therefore, it is crucial to make correct associations between charged particle tracks and their calorimetric energy deposits to minimise the effect of confusion. These associations can only be successfully made if the calorimeters used have fine segmentation, such as those found at the linear collider experiment, so that it becomes possible to separate the energy deposits from nearby showering particles. Even with this segmentation, making the association of charged particle tracks to calorimetric energy deposits is highly non-trivial. At the linear collider experiment, these associations are made using sophisticated pattern recognition algorithms, provided by PandoraPFA. The fine segmentation of the linear collider calorimeters allows PandoraPFA to reconstruct the four-momenta of all particles passing through the detector and to report the energy of all reconstructed particles using the energy measurement from the optimal sub-detector.

As many physics processes of interest at the linear collider involve multi-jet final states [39], good jet energy resolution is a crucial aspect of detector performance. As shown in chapter 7, the sensitivity of the linear collider experiment to areas of new physics can be determined using reconstructed jet energies. Furthermore, parameters derived from the energy measurements of jets are extremely useful for identification of physics channels of interest. Therefore, the primary metric used for this optimisation study is the jet energy resolution. Jet energy resolution in particular can benefit from the application of particle flow calorimetry as  $\approx 70\%$  of the energy of jets are carried in the form of charged particles. As particle flow aims to measure the energy of charged particles using the tracker, it has the potential to offer extremely large benefits when measuring jet energies in comparison to the traditional calorimetric approach.

### 3.6.1 Jet Energy Resolution

The jet energy resolution in these studies was determined through the simulation of off-shell mass Z boson events decaying to light quarks (u, d, s). PYTHIA version 6.4 [40], which had been trained on fragmentation data from the OPAL experiment [41],

was used to generate these events. The decay of tau leptons appearing in the day was simulated using TAUOLA [42]. Detector simulation and event reconstruction was carried out as described in sections 3.3 and 3.5 respectively.

As the Z boson in these events is produced at rest, the typical decays form two mono-energetic jets that are produced back to back as shown in figure 3.13. Only events where  $|\cos(\theta)| < 0.7$ , where  $\theta$  is the polar angle of the quarks, are used in the jet energy resolution calculation. This ensures little energy is lost down the beam axis. Using these events, the jet energy resolution was calculated as follows:

$$\frac{\text{RMS}_{90}(E_j)}{\text{Mean}_{90}(E_j)} = \frac{\text{RMS}_{90}(E_{jj})}{\text{Mean}_{90}(E_{jj})} \times \sqrt{2}, \quad (3.2)$$

where  $E_{jj}$  is the total reconstructed energy.  $\text{Mean}_{90}(E_{jj})$  and  $\text{RMS}_{90}(E_{jj})$  are the mean and root mean squared (RMS) of the  $E_{jj}$  distribution. These variables are calculated across the range of  $E_{jj}$  with the smallest RMS containing at least 90% of the data. This definition is used to remove the effect of outliers in the distribution [24]. If all associations between charged particle tracks and calorimeter clusters were correctly made, the reconstructed jet energy distribution would be Gaussian. However, the effect of confusion on certain events will distort this distribution and broaden the tails significantly. If the full range were to be used in the jet energy resolution calculation, the effect of these tails is overinflated. If the distribution of reconstructed jet energies is truncated to the narrowest range of the data containing at least 90% of the data, the effect of these tails can be negated. This removes events where confusion is dominant, which makes the jet energy resolution metric far more robust and representative of the bulk of the data.

An example of the application of this metric can be found in figure 3.14. In this example  $\text{RMS}(E_j)$ , the RMS calculated using the full range, is 5.8 GeV, while  $\text{RMS}_{90}(E_j)$ , the RMS using the reduced range, is 4.1 GeV. This corresponds to a reduction in the jet energy resolution from 4.1% to 2.9%, which clearly shows an overemphasis of the tails of the distribution when using the full jet energy range.

In the subsequent analysis a range of di-jet energies were considered ranging from the Z mass, 91 GeV, to the nominal running energy of the ILC, 500 GeV. Each event sample contained 10,000 events generated isotropically so that, given the polar angle cut, approximately 7,000 events contribute to the jet energy resolution calculation.

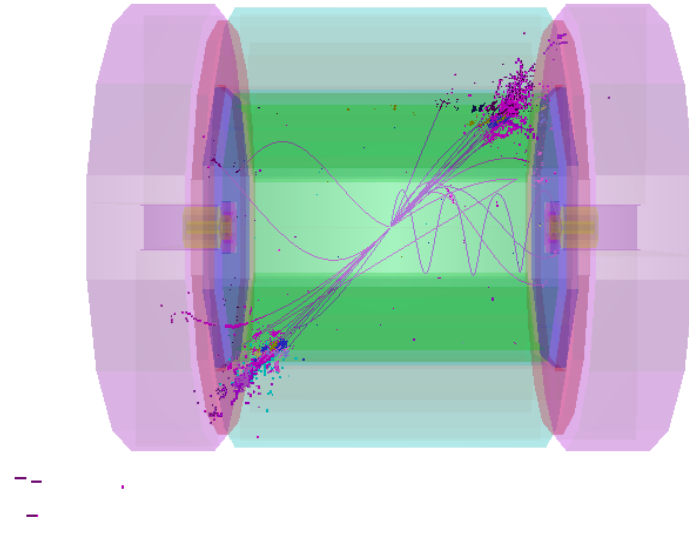


**Figure 3.13:** 500 GeV di-jet  $Z \rightarrow u\bar{d}s$  event display for nominal ILD detector.

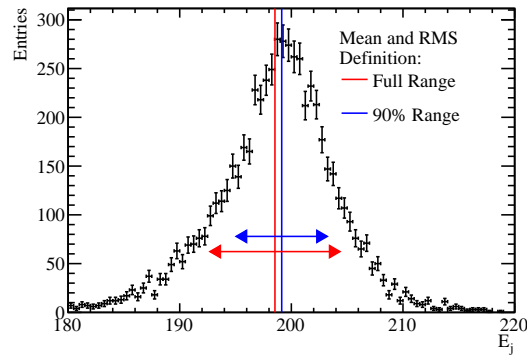


**Figure 3.14:** Definition of jet energy resolution. Reconstructed jet energy for 200 GeV di-jet  $Z \rightarrow u\bar{d}s$  events for nominal ILD detector.

### 3.6.2 Jet Energy Resolution Decompositions

It is possible to gain additional insight into the detector performance by cheating the pattern recognition, the clustering of calorimeter hits together and the creation of track to cluster associations, using MC information. Cheating the pattern recognition removes the effect of confusion as it ensures no errors are made when either clustering calorimeter hits together or when associating charged particle tracks to those calorimeter clusters. This allows the detector performance to be deconstructed into two terms;

one related exclusively to the intrinsic energy resolution of the detector and another related to the pattern recognition confusion. The additional information this provides is extremely useful for characterising changes to the overall detector performance.

The intrinsic energy resolution contribution to the jet energy resolution is determined by fully cheating the pattern recognition; in this case all confusion is negated. The total confusion is defined as the quadrature difference between the jet energy resolution using the standard reconstruction and this fully cheated reconstruction. Furthermore, it is possible to cheat the pattern recognition associated with individual types of particles. This is particularly useful for studies related to the ECal as, by cheating the photon pattern recognition, it is possible to isolate the confusion associated with photons. The photon confusion is defined as the quadrature difference between the jet energy resolution using the standard reconstruction and the reconstruction where the photon pattern recognition is cheated. Examples of the calculation of the various confusion terms defined above are given in table 3.7.

Reconstruction	Jet Energy Resolution [%]
Standard Reconstruction (No MC Information)	$a = 2.97 \pm 0.05$
Cheating Entire Reconstruction	$b = 1.69 \pm 0.02$
Confusion	$\sqrt{a^2 - b^2} = 2.45 \pm 0.05$
Cheating Photon Reconstruction	$c = 2.73 \pm 0.04$
Photon Confusion	$\sqrt{a^2 - c^2} = 1.18 \pm 0.06$

**Table 3.7:** Example calculation of the confusion contributions to the jet energy resolution. These jet energy resolutions are for 250 GeV jets using the nominal ILD detector model.

A common feature that is observed in these calibration studies is that as the intrinsic energy resolution of a calorimeter improves, the effect of confusion is reduced. This occurs as a better energy resolution means more precise comparisons can be made between the energy of a cluster of calorimeter hits and the momentum of any charged particle tracks associated to it. Comparisons such as these are made by PandoraPFA to determine whether the track cluster associations that have been made are consistent. If a large discrepancy is observed between the cluster energy and track momenta, the clustering of calorimeter hits is modified until a consistent association can be made. For more details on this comparison see chapter 3. This consistency check vastly reduces the number of errors made when clustering calorimeter hits and associating

charged particle tracks to those clusters i.e. the confusion. Therefore, improving the precision of this consistency check, by improving the energy resolution, reduces the effect of confusion.

### 3.6.3 Single Particle Energy Resolution

The energy resolution for individual particles is crucial for a number of physics studies of interest to the linear collider, such as  $\gamma$  energy resolutions in the study of anomalous triple and quartic gauge couplings [43–45]. Therefore,  $\gamma$  and  $K_L^0$  energy resolutions, alongside the jet energy resolution, will be considered in these optimisation studies. As both  $\gamma$  and  $K_L^0$  are uncharged, their energy measurements will be made using the calorimeters as opposed to the tracker.  $\gamma$ s are a natural choice of particle to consider as they are particularly relevant for several physics studies and, as they are largely contained within the ECal, they will be highly sensitive to changes in the ECal performance.  $K_L^0$ s were used as, analogously to  $\gamma$ s and the ECal, their energies are primarily measured using the HCal. In general, neutral hadron energy resolutions are less crucial to physics studies, however, they do make crucial contribution to the jet energy resolution that should not be overlooked. The reported  $\gamma$  energy resolutions were determined using events containing a single 100 GeV  $\gamma$ , while the  $K_L^0$  energy resolutions were determined using events containing a single 50 GeV  $K_L^0$ . These energies were chosen to be as large as possible, to maximise sampling of the calorimeter response, while minimising the affect of leakage of energy from the ECal to the HCal for the  $\gamma$  events and leakage of energy out of the rear of the HCal for the  $K_L^0$  events.

Detector simulation and event reconstruction for these  $\gamma$  and  $K_L^0$  events was carried out as described in sections 3.3 and 3.5 respectively.

The energy resolution for these single particle samples is determined using a Gaussian fit to the reconstructed energy distributions. To aid convergence, the fit was applied to the narrowest range of the reconstructed energy distribution containing at least 75% of the data. The single particle energy resolution is defined as the standard deviation divided by the mean of the fitted Gaussian. For each energy resolution calculation, a total of 10,000 events were used to populate the reconstructed energy distribution. For clarity, a cut of  $|\cos(\theta)| < 0.7$  was applied to veto events where particles travelled down the beam pipe or where they passed through the barrel/endcap

overlap region. An example of the reconstructed energy distributions for 100 GeV  $\gamma$ s and 50 GeV  $K_L^0$ s, alongside the Gaussian fits used to determine the energy resolutions, are shown in figure 3.15. The errors quoted on single particle energy resolutions are determined by propagating the errors reported from the Gaussian fit into the resolution calculation.

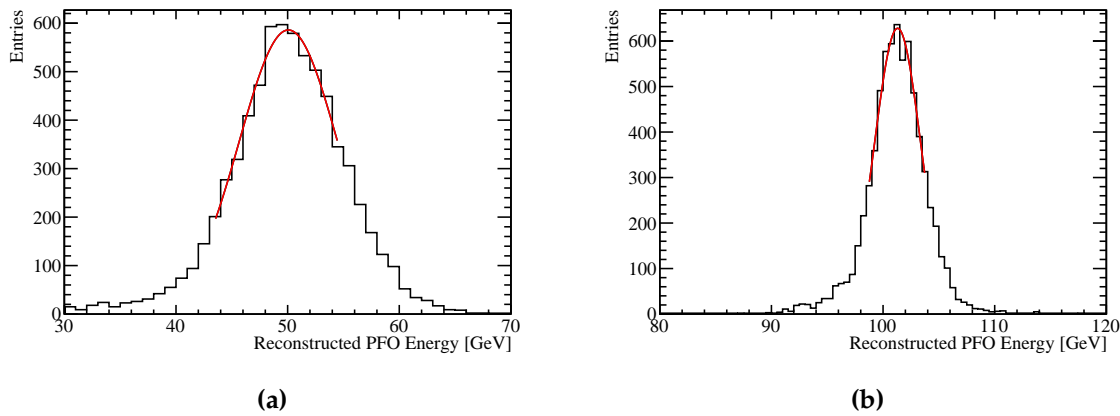


**Figure 3.15:** The reconstructed energy distribution for (a) 50 GeV  $K_L^0$  and (b) 100 GeV  $\gamma$  events. The red line shows a Gaussian fit used to parameterise the detector performance. The fit was applied to the truncated range of the reconstructed PFO energy distribution containing at least 75% of the data with the narrowest RMS. The nominal ILD model was used in this simulation.

### 3.7 Summary of ILD Detector Performance

The following section outlines the nominal ILD detector performance using the metrics outlined in section 3.6.

The reconstructed energy distributions for particles whose energies are measured using calorimeters will be Gaussian. This is the case for sampling calorimeters as the active material in each calorimeter hit essentially counts the number of charged particle tracks passing through it, or possibly the number of photons for scintillator options. An estimation of the total energy deposited in a calorimeter hit, including the absorber material, can be made based upon this number of tracks or photons. For more details on how this estimation is made see chapter 5. Finally, the energy of the entire particle shower is estimated by grouping together calorimeter hits and summing their

energy. As each calorimeter hit energy is an independent random measurement the particle shower energy will, by the central limit theorem, have a Gaussian distribution.

As each calorimeter hit involves counting a number of objects, charged particle tracks or photons, Poisson statistics governing the distribution of calorimeter hit energies. If the mean of the distribution of the energy of a cluster of calorimeter hits is  $\lambda = N$ , where  $N$  is the mean number of objects the are measured in the calorimeters, the standard deviation of that distribution is  $\sigma = \sqrt{\lambda} = \sqrt{N}$  and the energy resolution is  $\frac{\sigma}{\lambda} = \frac{1}{\sqrt{N}}$ . As the total shower energy,  $E_{Reco}$ , is proportional to  $N$  the energy resolution for a particle shower in an ideal calorimeter is proportional to  $\frac{1}{\sqrt{N}} = \frac{1}{\sqrt{E_{Reco}}}$ . Therefore, the energy resolution as a function of energy for an ideal calorimeter is  $\frac{\sigma_{Reco}}{E_{Reco}} = \frac{a}{\sqrt{E_{Reco}}}$ . In reality, it is typical to express the energy resolution of a calorimeter in the following form:

$$\frac{\sigma_{Reco}}{E_{Reco}} = \frac{a}{\sqrt{E_{Reco}}} \oplus b \oplus \frac{c}{E_{Reco}}, \quad (3.3)$$

where the  $b$  term is a constant term that accounts for a variety of instrumental effects that do not depend on energy, e.g. mechanical imperfections, and the  $c$  term accounts for electrical noise [46].  $\oplus$  denotes the quadrature sum.

Prototypes of the various ILD calorimeter options have been constructed and validated using test beam measurements. The energy resolution of the ILD ECal, determined from test beam measurements, was parameterised as  $\frac{16.6}{\sqrt{E_{Reco}}} \oplus 1.1\%$  for the silicon option and  $\frac{12.9}{\sqrt{E_{Reco}}} \oplus 1.2\%$  for the scintillator option [26]. The electrical noise was deemed sufficiently small that the  $c$  term in the parameterisation could be neglected in both cases. These results were determined using an  $e^-$  test beam with energies ranging up to  $\approx 40$  GeV. This parametrisation is compared to the full ILD detector simulation in figures 3.16a and 3.16b for the silicon and scintillator ECal options respectively. The test beam parameterisation of the energy resolution for the silicon ECal option is almost identical to the energy resolution observed in the full simulation. At very high energies,  $\approx 500$  GeV, the ECal is no longer sufficient to fully contain the  $\gamma$ s and so leakage of energy into the HCal leads to a minor degradation in the energy resolution. This accounts for the worse energy resolution seen in the full simulation when compared to an extrapolation of the test beam parameterisation

at high energies. The test beam parameterisation of the energy resolution for the scintillator ECal option is significantly better than that observed in the full simulation. This difference is most likely due to an imperfect implementation of the scintillator ECal within the full detector simulation. The  $\gamma$  energy resolutions seen in the full ILD simulation are similar for the silicon and scintillator ECal options.

Similarly, the energy resolution, determined from test beam measurements, for the nominal ILD HCal was parameterised as  $\frac{57.6}{\sqrt{E_{Reco}}} \oplus 1.6\%$  [47]. A comparison between this test beam parameterisation and the full ILD simulation, using the silicon ECal option, is shown in figure 3.16c. The test beam measurements were made using  $\pi^\pm$ s with energies ranging from 10 to 80 GeV, while the full ILD simulation used  $K_L^0$ s ranging from 10 to 100 GeV. For determining the test beam parameterisation, only showers starting in the HCal were considered to minimise the effect of errors associated with the ECal calibration, while all showers were considered in the full simulation. The deviation between the test beam parameterisation and the full simulation, which grows as the  $K_L^0$  energy increases, is most likely due to the treatment of energy deposits leaking out of the back of the HCal. A tail catcher was used in the test beam analysis that had a similar structure to the HCal, but with a much wider average absorber thickness. Energy deposits in this tail catcher were calibrated in a similar fashion to the HCal giving a very good energy resolution for these energy deposits. In the full simulation a muon chamber acts as the tail catcher, however, the calibration applied to it is less sophisticated than that applied to the test beam tail catcher data, which gives a worse energy resolution for those hits. Furthermore, energy deposits in the uninstrumented solenoid region in the full simulation could not be accounted for.

The jet energy resolutions as a function of jet energy using the full ILD simulation are shown in figure 3.16d. Alongside this, the intrinsic energy resolution and confusion contributions to the jet energy resolution are also presented. The jet energy resolution at low energies is dominated by the intrinsic energy resolution of the detector, while at high energies it is dominated by the effect of confusion. This is to be expected as the intrinsic energy resolution of the calorimeters is proportional  $\frac{1}{\sqrt{E_j}}$ , where  $E_j$  is the jet energy, which means that it will dominate the energy resolution at low energies. On the other hand, confusion, which is a measure of how easy it is to group calorimeter hits together into clusters and associate those clusters to charged particle tracks, will grow with increasing jet energy as the event topology becomes more dense. The total jet energy resolution for the ILD detector are sufficiently small,  $\frac{\sigma_{E_j}}{E_j} \lesssim 3.8\%$  [4, 24, 26], across the energy range considered to make separation of the hadronic decays of the

W and Z bosons possible, which is one of the key requirements for the future linear collider

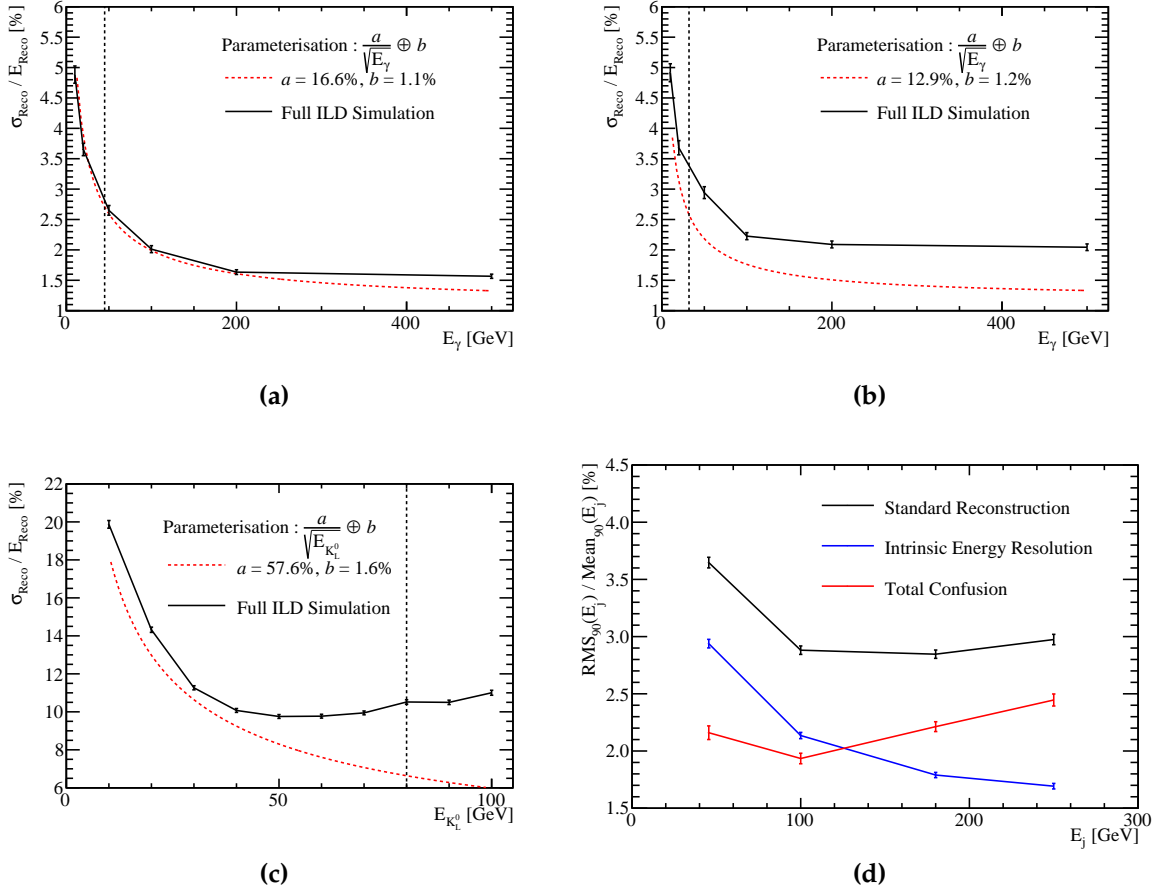


**Figure 3.16:** (a) The energy resolution as a function of  $\gamma$  energy for the silicon ECal option. The black markers indicate the energy resolutions for the full ILD simulation and the red dotted line shows the test beam parameterisation of the ECal energy resolution. (b) The energy resolution as a function of  $\gamma$  energy for the scintillator ECal option. The black markers indicate the energy resolutions for the full ILD simulation and the red dotted line shows the test beam parameterisation of the ECal energy resolution. (c) The energy resolution as a function of neutral hadron energy. The black markers indicate the energy resolutions for the full ILD simulation, with the silicon ECal option, which was determined using  $K_L^0$ s. The red dotted line shows the test beam parameterisation of the HCal energy resolution, which was determined using  $\pi^\pm$ s. (d) The jet energy resolution ( $\text{RMS}_{90}$ ) as a function of jet energy using the nominal ILD model, with the silicon ECal option. The intrinsic energy resolution and confusion contributions to the jet energy resolutions are also presented. The black dotted vertical line on the single particle energy resolutions shows the highest energy particles used in the test beam measurements.

# Chapter 4

## Capacitively Coupled Pixel Detectors for the CLIC Vertex Detector

*“There, sir! that is the perfection of vessels!”*

— Jules Verne, 1828–1905

### 4.1 Introduction

Identification of heavy-flavour quarks and tau-leptons at any of the currently proposed linear collider experiments will rely upon precise reconstruction of secondary displaced vertices that are produced when these particles decay. Furthermore, the ability to accurately associate any daughter tracks produced in such decays to the secondary vertices is essential. At CLIC, this can only be realised using a vertex detector with a very high spatial resolution, of approximately  $3\text{ }\mu\text{m}$ , and good geometric coverage, extending to low polar angles  $\theta$ . The vertex detector must also have a low material budget (less than 0.2 %  $X_0$  per layer) in order to prevent additional decay vertices from material interactions, and allow efficient track reconstruction despite the high presence of beam-induced background particles. Tracking in the vertex detector will be aided by the use of time-stamping of individual hits, to an accuracy of 10 ns, to identify particles produced from the physics event of interest.

As there are currently no technology options that fulfil all of the criteria for the CLIC vertex detector, the CLIC experiment has developed an extensive R&D program where

new technologies for the vertex detector are considered. High-voltage complementary metal-oxide-semiconductor (HV-CMOS) sensors, which are capacitively coupled to a separate readout application-specific integrated circuit (ASIC) are one such option. The performance of prototype detectors based upon this technology and the impact of mechanical tolerances present in their manufacture are presented in this chapter.

### 4.1.1 HV-CMOS

Pixel detectors can be broadly classified in two groups: hybrid detectors, where a separate sensor and readout chip are bonded together; and fully-integrated devices, where the collection diode is implanted in the same piece of silicon as the readout circuitry. Fully-integrated devices have traditionally not been suitable for applications with high timing requirements, due to the relatively slow charge collection time and limited on-pixel functionality. However, recent developments in CMOS technologies have led to new detector designs that may overcome some of these issues.

HV-CMOS is a processing technology whereby the n-MOS and p-MOS transistors forming the on-pixel electronics are placed entirely within a deep n-well, as shown in figure 4.1. By varying the voltage applied at the gate terminal, n-MOS and p-MOS transistors are able to control the current flowing between the source and drain terminals. The gate voltage produces an inversion layer between the source and drain terminals that acts as a conduit, allowing current to flow between the source and drain as shown in figure 4.2. The voltage at the gate, with respect to the body, controls the width of the inversion layer and hence the magnitude of this current. Logic operations can be performed directly on-pixel using various configurations of n-MOS and p-MOS transistors.

For the HV-CMOS, the deep n-well housing the on-pixel electronics acts as the charge collection diode as well as shielding the circuitry from the p-substrate. This shielding allows for the application of a moderate bias voltage to the sensor bulk that produces a depletion region, which facilitating fast charge collection via a drift current. In contrast, traditional monolithic active pixel sensors (MAPS) have a much smaller depletion region meaning charge collection occurs primarily through the slower mechanism of diffusion.

Furthermore, in conventional MAPS there is potential for competition for charge collection between the n-well collecting diode and the p-MOS transistors used to

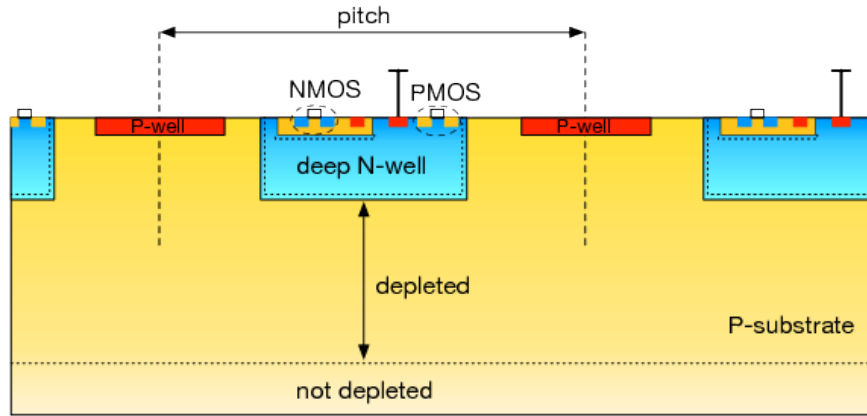


**Figure 4.1:** Schematic cross section of an HV-CMOS sensor: the deep n-well is the charge-collecting electrode and also contains additional CMOS circuitry such as a preamplifier. Image taken from [48].

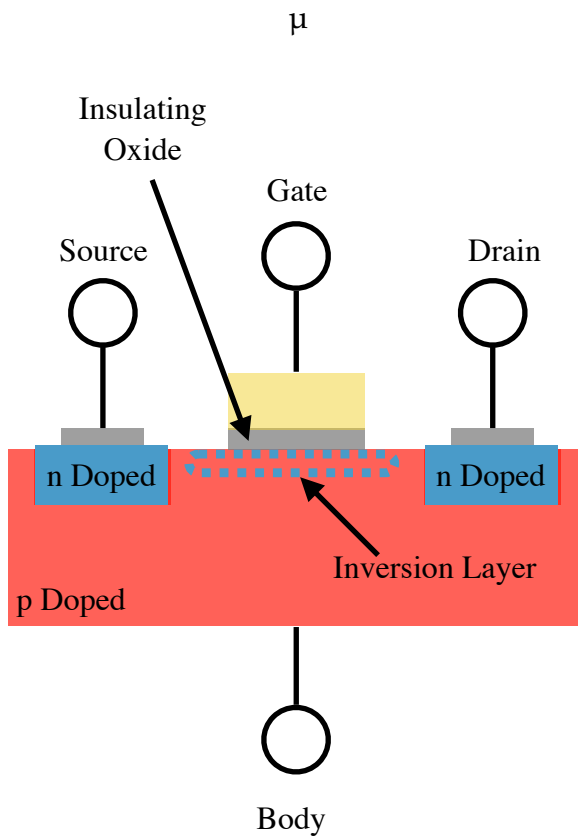


**Figure 4.2:** Schematic cross section of an n-MOS transistor. p-MOS transistors have a similar cross section where the n and p doped regions are switched.

perform logic operations as the p-MOS transistors are embedded within an n-well. This only occurs as the n-well collection diode is separated from the n-wells housing the p-MOS transistors. HV-CMOS technology does not suffer from this issue as the

deep n-well collecting diode houses the p-MOS transistors meaning charge is only collected at a single well in the sensor bulk.

HV-CMOS technology thus offers the possibility of fast charge collection with integrated on-pixel functionality, but several limitations still exist. As the on-pixel electronics have to be placed inside the deep n-well and the n-wells of neighbouring pixels have to be isolated from each other, there is a limited physical area of the pixel that can be used for transistor layout, which limits the available on-pixel functionality. In addition to this, it is not possible to implement full CMOS logic inside the deep n-well as coupling between p-MOS transistors and the collection diode will lead to noise injection at the charge collection node. While it is possible to embed p-MOS transistors within a p-well to shield them from the deep n-well, so-called "quadruple-well technology", to give access to full CMOS logic this option is not readily available for prototyping. By restricting the complexity of on-pixel electronics and using a separate readout ASIC, it is possible to overcome many of these issues. When coupled with the fast charge collection time and removal of competition in charge collection this makes HV-CMOS technology highly desirable for use in the CLIC vertex detector.

#### 4.1.2 CLIC ASICs

As HV-CMOS technology is such a promising option for use at the CLIC vertex detector, prototype devices based on this technology have been developed for testing. Two ASICs have been developed: the capacitively coupled pixel detector version 3 (CCPDv3), a sensor chip based on HV-CMOS technology, and the CLICpix, a readout chip providing additional on-pixel logic operations. The pixel pitch of the chips, both the CCPDv3 and the CLICpix, is 25  $\mu\text{m}$ , which should be sufficient to meet the requirements for the CLIC vertex detector. Each of the prototype ASICs consists of a matrix of  $64 \times 64$  pixels. The CCPDv3 is fabricated in a 180 nm HV-CMOS process, where 180 nm refers to the smallest size building block that can be used for creating the integrated circuits on a silicon wafer. This is comparable to device fabrication at the LHC, which typically uses a 130 and/or 250 nm CMOS processes [49, 50]. In comparison, the CLICpix is fabricated in a 65 nm process, which makes it possible to have more complex on-pixel circuitry incorporated into it than would be possible in previous generations of pixel detectors. A schematic of these devices can be found in figure 4.3.

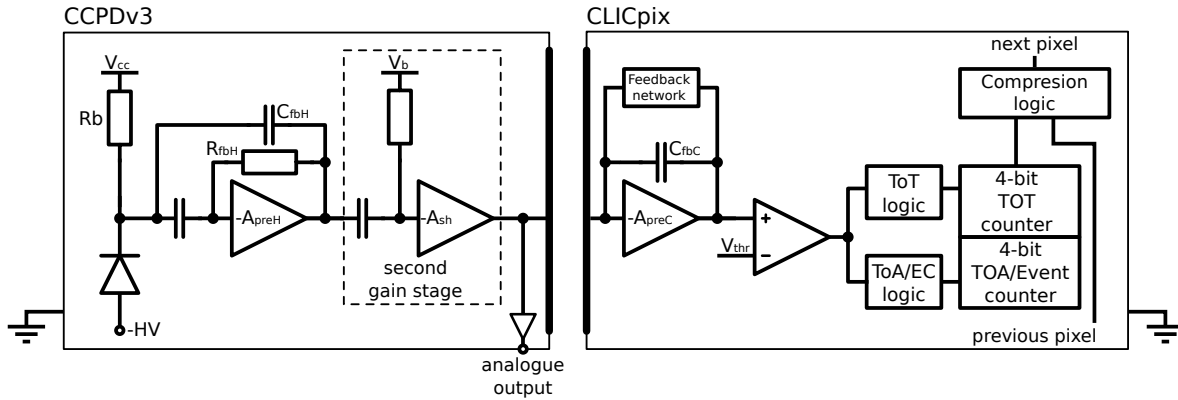


Figure 4.3: Schematic of CCPDv3 and CLICpix pixels.

## CLICpix

CLICpix is a hybrid pixel readout chip that has been developed for the CLIC vertex detector. Each CLICpix pixel contains a charge-integrating amplifier connected to a discriminator, as shown in figure 4.3. The discriminator remains high for as long as the input signal is over a given threshold, and this output is then used as the input for further logic operations. The additional logic operations record the time of arrival and magnitude of the collected charge, using a Time over Threshold (ToT) measurement. The ToT is stored in a 4-bit on-pixel counter.

The CLICpix operates using a shutter-based readout, where the entire matrix is kept active while the shutter is open and when closed the matrix is readout in its entirety. This is designed to match the expected beam structure for the CLIC experiment, as the accelerator will deliver bunch trains of  $e^+$  and  $e^-$  that are separated by 20 ms. Each bunch train contains 312 bunches with a spacing of 0.5 ns, giving a total train length of 156 ns. Furthermore, the shutter-based readout is well suited to power-pulsing, where the power to the front-end electronics is turned off between bunch crossings. This helps to significantly reduce the power consumption of the detector.

The threshold voltage, the voltage required for the discriminator to register an output, seen by each CLICpix pixel is slightly different due to variations in the manufacturing process. If these variations are not accounted for then the behaviour of the device across the matrix will not be uniform. To minimise the impact of these fluctuations, each CLICpix pixel contains a 4-bit local adjustment to the threshold voltage, which is calibrated to unify the response across the matrix. The threshold 'equalisation' is achieved by performing two threshold scans across the matrix, once

with all four bits set to 0 (no local threshold adjustment), and a second time with all four bits set to 1 (maximum local threshold adjustment). For each scan, the baseline voltage of each pixel is determined. By applying a linear interpolation between the 0000 and 1111 cases, each pixel can be tuned to a common point, such that all pixels respond at the same global threshold.

### 4.1.3 Capacitive Coupling

Solder bump-bonding is typically used to connect the sensor and readout ASIC in hybrid pixel detectors. This procedure uses small spheres of solder to connect each pixel on the sensor to the corresponding pixel on the readout ASIC. There are several drawbacks to the use of this procedure for pixel detectors: it is expensive and sets limits on the thickness of both ASICs that is required for mechanical stability. An alternative procedure for connecting the sensor and readout ASICs involves using a thin layer of glue to form a capacitive connection between the two. This procedure reduces the cost and material budget with respect to bump-bonding, making it highly desirable for use in the CLIC vertex detector. In order to make this viable, it is necessary to implement an amplifier in the CCPDv3 pixel, shown in figure 4.3, to boost the signal and overcome the intrinsically small coupling capacitance.

## 4.2 Device Fabrication

There are two issues related to device manufacture that have to be considered when using capacitive coupling to connect the sensor and readout ASIC: the uniformity of the glue layer and the spatial alignment of the sensor and readout pads. The former has been investigated in [CERN FABRICATION NOTE CITE], while the latter is the focus of this study. In order to characterise the impact on detector performance of any misalignment between the CCPDv3 and the CLICpix pads, a number of assemblies have been constructed that purposefully contain misalignments, as shown in figure 4.4. Table 4.1 contains a summary of the samples produced.

The full details of the glueing procedure can be found in [CERN FABRICATION NOTE CITE], along with a study of the absolute precision of the manufacturing procedure. For devices constructed in an identical fashion to those considered here,

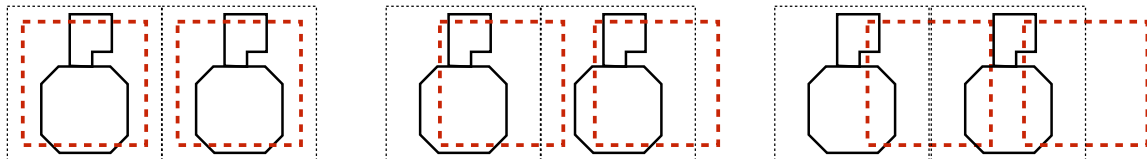


**Figure 4.4:** Alignment schematic of the CCPDv3 and CLICpix detectors studied. The red dotted line represents the CCPDv3 pad and the solid black line represents the CLICpix top metal layer. From left to right; centred pixels, 1/4 offset ( $6.25 \mu\text{m}$ ) and 1/2 offset ( $12.5 \mu\text{m}$ ).

Assembly	Alignment
SET 9	Centred
SET 10	$\frac{1}{4}$ Offset
SET 12	Centred
SET 13	Centred
SET 15	Centred
SET 16	$\frac{1}{2}$ Offset

**Table 4.1:** A list detailing the alignment of the CCPDv3 and CLICpix coupling pads for the devices considered in this study.

the glue layer thicknesses were less than  $1 \mu\text{m}$  and the precision on the pad positioning was less than  $2 \mu\text{m}$ .

### 4.3 Device Characterisation

A series of lab experiments were used to characterise the devices produced for this alignment study. The devices were also tested in realistic experimental conditions using the CERN SPS test beam. Due to the complexities of testing devices in a test beam, extensive lab test were performed first to characterise as many properties of the assemblies as possible. The lab experiments performed were as follows:

- **Radioactive source measurements.** The goal of this measurement is to measure the response of the CCPDv3 and CLICpix when a radioactive source is used to deposit charge within the CCPDv3 sensor.

- **Test pulse calibration of the CLICpix chip.** The goal of this measurement is to calibrate the response of the CLICpix sensor. This is achieved by examining the CLICpix response when injecting a quantity of charge directly into the input of the chip, which bypasses the CCPDv3 and glue layer.

### 4.3.1 Source Measurements

A radioactive source was used to deposit charge within the CCPDv3 sensor and the response of the CCPDv3 and CLICpix examined. The CCPDv3 sensor converts the deposited charge into a voltage, which in turn passes through the capacitive glue layer and into the CLICpix chip. Measurements were made of the output voltage produced by the CCPDv3 and the response of the CLICpix readout chip, in units of ToT. As the exact amount of charge deposited by the radioactive source is unknown, calibration of the CCPDv3 is not possible. Instead, this experiment focuses on examining the shape of the voltage produced by the CCPDv3 and determining the response of the CLICpix chip as a function of this voltage. As the CCPDv3 signal passes through the capacitively coupled glue layer before entering the CLICpix chip, this study characterises the properties of the gluing layer as well as the sensor and readout chips.

#### Experimental Setup

The radioactive material used in this study was Sr<sup>90</sup>. Sr<sup>90</sup> undergoes  $\beta^-$  decay to form Y<sup>90</sup>, which in turn undergoes  $\beta^-$  decay to form the stable isotope Z<sup>90</sup>. Each  $\beta^-$  decay produces an e<sup>-</sup> and a  $\bar{\nu}_e$ , and it is the e<sup>-</sup> that goes on to deposit charge in the CCPDv3 sensor. The Sr<sup>90</sup> source used had an activity of 29.6 MBq.

The radioactive source was positioned directly above the back-side of the CCPDv3 sensor, and measurements were made of both the ToT output from the CLICpix and the CCPDv3 analogue signal for individual pixels on the sensor. The CCPDv3 pulse shape was recorded on a fast sampling oscilloscope that was also used to trigger the CLICpix readout. The on-pixel event counter, which is located in the CLICpix chip, was used to veto events where multiple hits occurred within the active shutter period. The CCPDv3 sensor was biased to 60 V during this experiment. Examples of CCPDv3 output voltage pulses when using the Sr<sup>90</sup> source can be seen in figure 4.5. The analogue output has a baseline voltage of  $\approx$  1.15 V, with signal saturation occurring around a height of 700 mV.

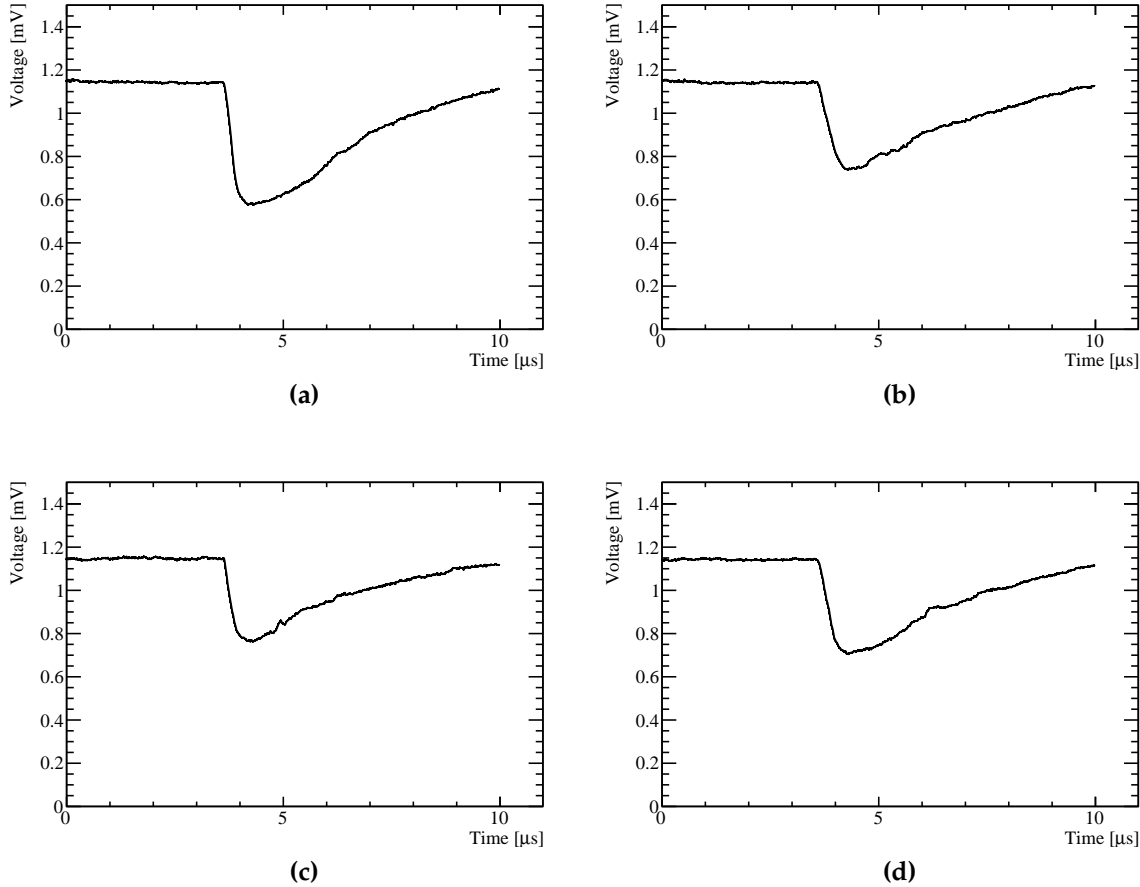


**Figure 4.5:** CCPDv3 voltage pulses produced using a radioactive source,  $\text{Sr}^{90}$ , to deposit charge in the sensor.

## Analysis

The quantities of interest related to the CCPDv3 output voltage are the pulse height, defined as the peak of the voltage pulse, and the rise time, defined as the time it takes for the CCPDv3 to reach the pulse height. For ease of analysis the baseline voltage is subtracted from the CCPDv3 output voltage and the pulse shape inverted before the following analysis is applied to extract the variables of interest.

The pulse height is defined using a Gaussian fit to the peak of the voltage pulse. This method is used to minimise the dependency of the pulse height on small fluctuations in the output voltage. The peak of the voltage pulse is defined as the region where the change in the CCPDv3 voltage output is greater than 90% of the maximum change in the CCPDv3 voltage output.

The rise time is defined as the time taken for the signal to go from 10% to 90% of the maximum change in the CCPDv3 voltage output. This definition makes the rise time metric more robust against fluctuations in the CCPDv3 voltage output.

Examples of the calculation of these metrics for a representative pulse is shown in figure 4.6. Due to the design of the CCPDv3 matrix, it is only possible to record the CCPDv3 voltage output for 15 pixels running along one edge of the  $64 \times 64$  matrix. Therefore, in the subsequent analysis data was taken for each of these accessible pixels and combined.

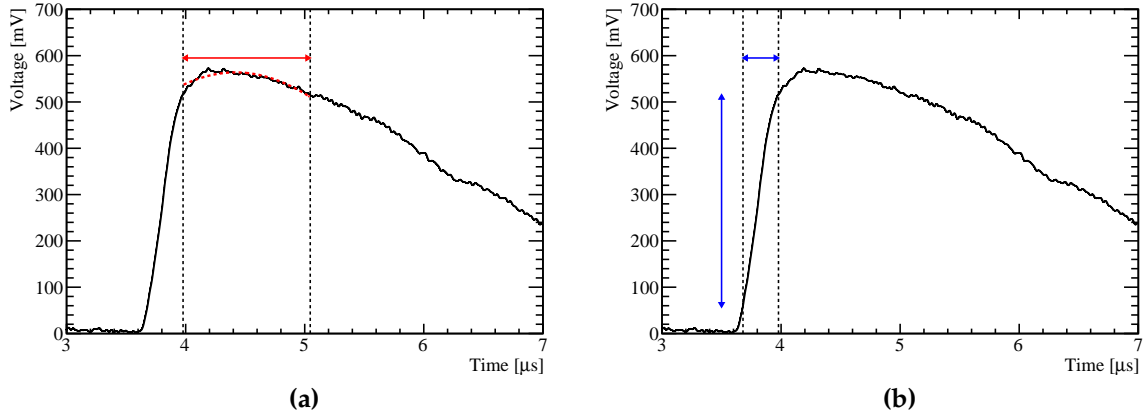


**Figure 4.6:** An example calculation of the pulse height and rise time for the CCPDv3 output voltage. In this example the black line show the CCPDv3 output voltage as a function of time where the baseline voltage has been subtracted and the pulse shape inverted. These voltage pulses were created using a radioactive source,  $\text{Sr}^{90}$ , to deposit charge in the sensor. (a) The definition of the pulse height. Pulse height is defined as the amplitude of a Gaussian function fitted across the peak of the voltage pulse. The peak of the voltage pulse is defined as the region where the voltage in excess of 90% of the raw pulse height, which is indicated in the figure by the red arrow. The red dotted line shows the Gaussian fit used to extract the pulse height. (b) The definition of rise time. Rise time is defined as the time taken for the CCPDv3 voltage to rise from 10% to 90% of the raw pulse height. The rise time, and change in CCPDv3 output voltage over this time, are shown in the figure by the blue arrows.

## Results - Rise Time vs Pulse Height

The mean rise time as function of pulse height for the CCPDv3 output voltage is shown in figure 4.7. This was determined by binning the measurements in pulse height and determining the mean rise time for measurements in each bin. The pulse

height was binned using a bin width of 4 mV ranging from 0 to 700 mV. A minimum of 10 measurements per bin were used for the calculation of the average rise time. The error bars on this figure show the standard error in the mean rise time. Data was only included in this analysis if the on-pixel event counter registered a single hit in the time window used to take data.

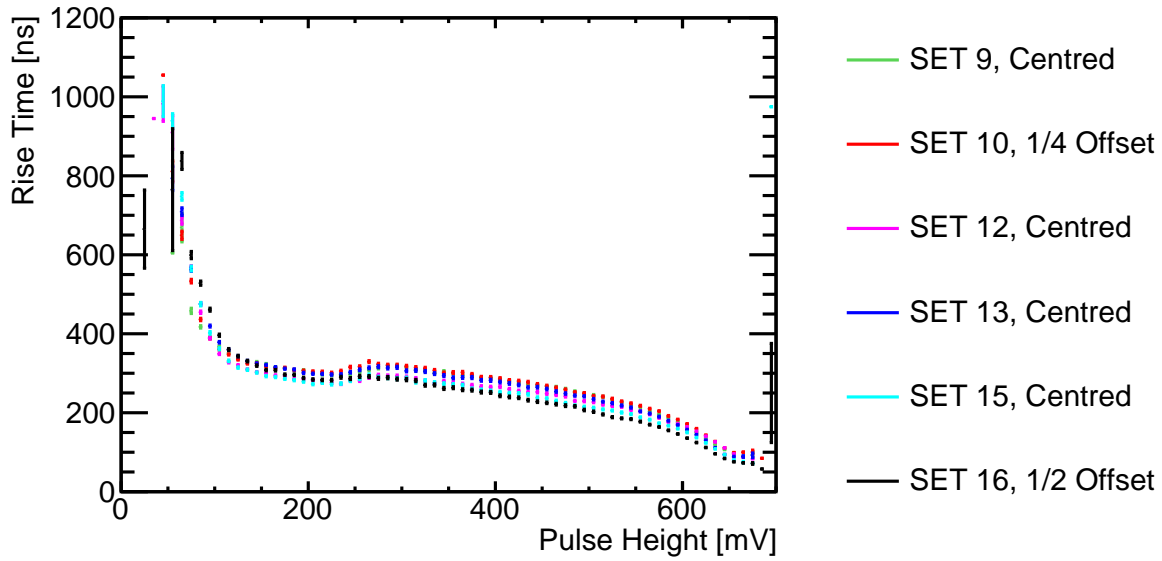


**Figure 4.7:** The CCPDv3 output voltage rise time as a function of pulse height.

The data in figure 4.7 shows that the rise time for the CCPDv3 front-end is approximately 300 ns across all samples. The rise time is largely independent of pulse height for all but the smallest signals. For very small pulse heights ( $< 100$  mV) rise times are significantly larger, which suggests that the deposited charge takes a longer time to be collected. This may be due to charge transport occurring via diffusion rather than drift. A gradual reduction in the rise time is observed as the total deposited charge, which is proportional to the pulse height, increases. This is expected as larger charge deposits in the sensor bulk lead to a greater rate of charge collection by the CCPDv3 and a smaller time taken for the pulse height to reach the peak. As the intrinsic performance of the CCPDv3 sensors in the devices tested is very similar, comparisons of the misaligned samples will be made more straightforward. As nearly identical intrinsic performance was observed for the CLICpix readout chips, as will be shown in section 4.3.2, any performance differences observed between these devices will be entirely due to the capacitive glue layer and the pad alignment.

## Results - ToT vs Pulse Height

The mean ToT measured in the CLICpix as a function of the CCPDv3 output voltage pulse height is shown in figure 4.8. Determination of the mean and error bars for the ToT as a function of pulse height measurement is identical to that described above for the rise time as a function of pulse height measurement.

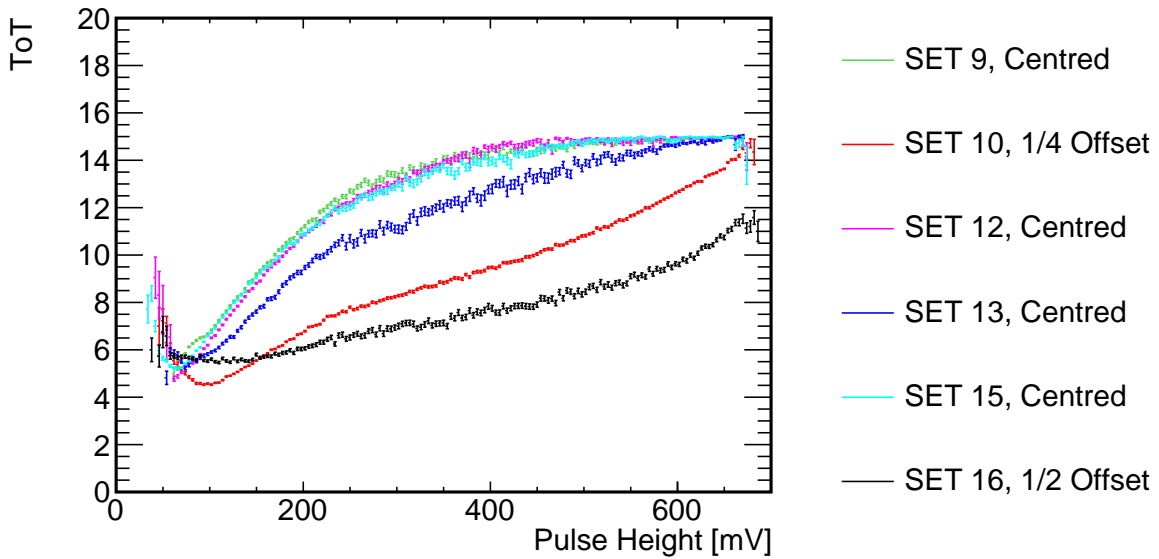


**Figure 4.8:** The mean ToT measured on the CLICpix ASIC as a function of CCPDv3 voltage pulse height.

For samples where the CCPDv3 and CLICpix are centred, the distribution of the mean ToT against pulse height shows that the ToT increases with pulse height up to values of approximately 400 mV and for larger pulse heights the mean ToT saturates at  $\approx 15$ . It is expected that the  $\frac{1}{4}$ - and  $\frac{1}{2}$ -offset samples will have a lower ToT than the centred samples due to the lower effective capacitance between the CCPDv3 and CLICpix pads. The greater the offset, the smaller the effective capacitance to the target CLICpix pad will be, and so the lower the recorded ToT. This is can be seen when comparing the centred samples to SET 10, the  $\frac{1}{4}$ -offset sample, and SET 16, the  $\frac{1}{2}$ -offset sample. In addition to the charge injected by the radioactive source there will also be background noise present from a variety of effects such as manufacturing defects in the silicon and thermal noise. This additional charge will increase the mean ToT recorded by the CLICpix and is the most likely reason as to why the mean ToT does not smoothly tend to zero as the pulse height decreases.

## Results - Cross Couplings

Capacitive coupling of the sensor to the readout ASIC can also lead to unwanted signals being induced on neighbouring pixels, due to non-zero stray capacitances. Cross-coupling is the transfer of signal from a sensor pad to the readout ASIC on an adjacent pad, which will occur if there is a non-negligible capacitance between the two pads. Signals are still transferred between the aligned sensor and readout pads, however, if the cross-capacitance is large enough unwanted additional hits in the neighbouring pads will be created. This issue is particularly relevant for this study as any misalignment between the sensor and readout pads will result in an increase in the cross-capacitance along the direction of the misalignment.

Any effects of cross-coupling can be studied using the same setup as was used in section 4.3.1 for the ToT against pulse height analysis, but by instead considering the ToT on the adjacent CLICpix pixel along the direction of the misalignment. The mean ToT on the adjacent pixel is shown as a function of the pulse height for all devices where the CCPDv3 and CLICpix are aligned in figure 4.9a and for the misaligned samples in figure 4.9b.

The distributions of the mean ToT on the adjacent CLICpix as a function of pulse height are governed largely by cross-coupling effects. These effects will make this distribution look similar in shape to that of the mean ToT in the target CLICpix as a function of pulse height, shown in figure 4.8. However, the gradient of the adjacent ToT distribution will be shallower than the adjacent ToT distribution as the cross-capacitance is smaller than the aligned capacitance. The exception to this is the  $\frac{1}{2}$ -offset sample where the cross-capacitance and aligned capacitance will be comparable. In addition to cross-coupling, this distribution will be effected by backgrounds from electrical noise and charge being deposited in the neighbouring HV-CMOS pixels.

For the centred samples, cross-coupling seems to have a small effect as the correlation between the adjacent ToT and pulse height is minimal. For the  $\frac{1}{4}$ -offset sample there is a stronger correlation between the adjacent ToT and pulse height, which indicates that cross-coupling is having a more dominant effect. The gradient of the adjacent ToT vs pulse height is, however, very shallow as the cross-capacitance for this device will be relatively small. A much stronger cross-capacitive effect can be seen in the  $\frac{1}{2}$ -offset sample, which is expected given it has a larger cross-capacitance than either the centred or  $\frac{1}{4}$ -offset sample. The adjacent ToT distribution for the

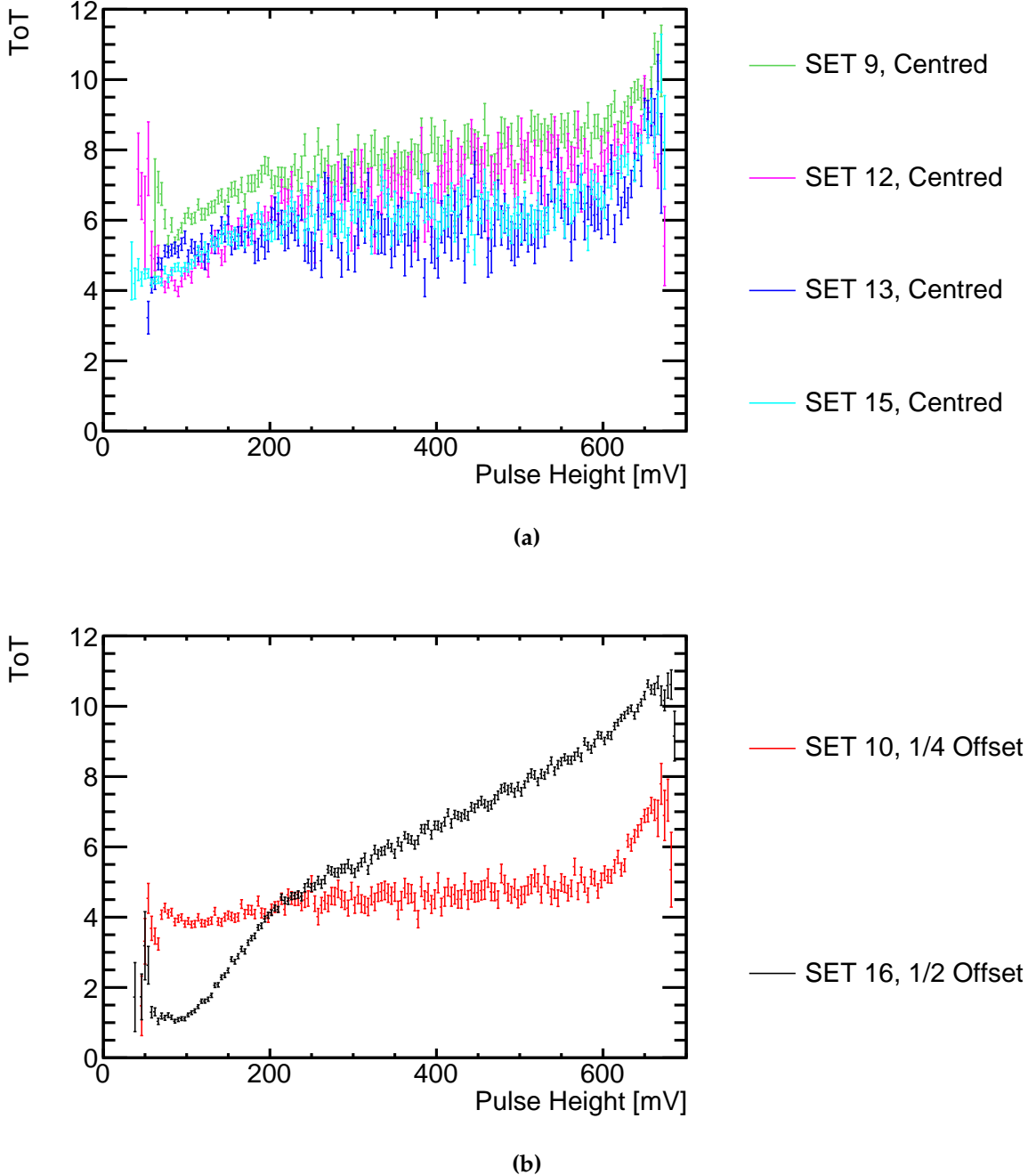


**Figure 4.9:** The mean ToT measured on the adjacent CLICpix pixel, along the direction of the offset, as a function of CCPDv3 voltage pulse height for (a) the centred and (b) the misaligned devices.

$\frac{1}{2}$ -offset sample almost mirrors the aligned ToT distribution in terms of both shape and width of the distribution. There are some small differences between the shape of the aligned and adjacent ToT vs pulse height distribution for the  $\frac{1}{2}$ -offset sample, but

this is understood to be from the column structure of the CLICpix readout ASIC, more details of which can be found in section 4.3.2. Overall, these results indicate that, as expected, the misalignment of between the CCPDv3 and CLICpix pads increases the effect of cross-coupling along the direction of the misalignment.

### 4.3.2 Test Pulse Calibration

In order to fully understand the charge transfer to the CLICpix, a calibration of the CLICpix front-end electronics response was performed. This was achieved by directly injecting a voltage pulse of fixed height directly into a capacitor help in each CLICpix pixel. This capacitor will then inject a known amount of charge into the pixel, and by varying the height of the pulse applied the response of the CLICpix to different amounts of charge can be quantified. This experiment extends the characterisation of the CLICpix chip beyond what was found using the radioactive source measurements, as applying the voltage directly to the CLICpix fully isolates the response of the chip from any effects relating to the glue layer or CCPDv3.

### Experimental Setup

To prevent any influence from neighbouring pixels during the testpulse measurements the matrix was pulsed in stages. Charge was injected into 1 out of every 16 pixels while masking the others to ensure issues related to power consumption were not encountered. This was repeated 15 more times using different mask configurations until the entire matrix had been sampled. This procedure was repeated 100 times to determine the average ToT response on a per-pixel level. The pulse height injected into the CLICpix was varied from 2 to 180 mV in steps of 2 mV in order to fully characterise the response up to saturation of the ToT output. An example of the mean ToT plotted against the injected pulse height is shown in figure 4.10.

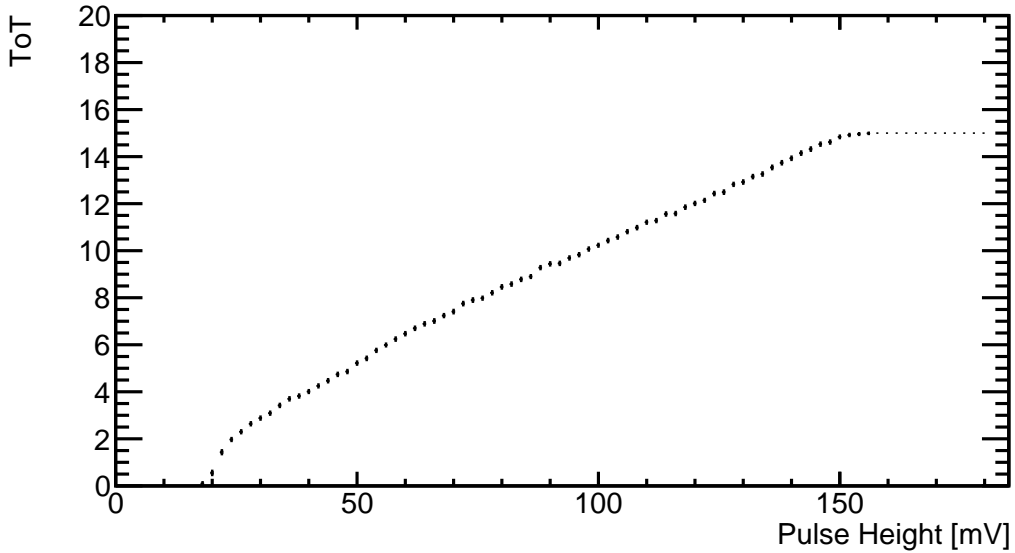


**Figure 4.10:** The CLICpix ToT as a function of injected pulse height. The black markers show the mean ToT and the error bars show the standard error.

## Analysis

The functional form of the ToT against pulse height plot will be described using a surrogate function [51], which is defined as:

$$y = ax + b - \frac{c}{x - t}, \quad (4.1)$$

where  $y$  is the ToT,  $x$  is the pulse height in mV and  $a$ ,  $b$ ,  $c$  and  $t$  are fit parameters. Application of the fit helps to condense the large amount of data recorded for an individual pixel down to a small number of parameters, which makes categorisation of the response of the CLICpix matrix more clear. At large pulse heights the linear relationship dominates while for low pulse heights the inversely proportional term dominates.  $c$  describes the curvature of the graph, while  $t$  determines the asymptote below which no signal is detected. Figure 4.11 shows an example of the application of this fit. As this function does not describe saturation of the ToT or the region below threshold, the fit is only applied on data points where the mean ToT is greater than 1 and less than 14.75.

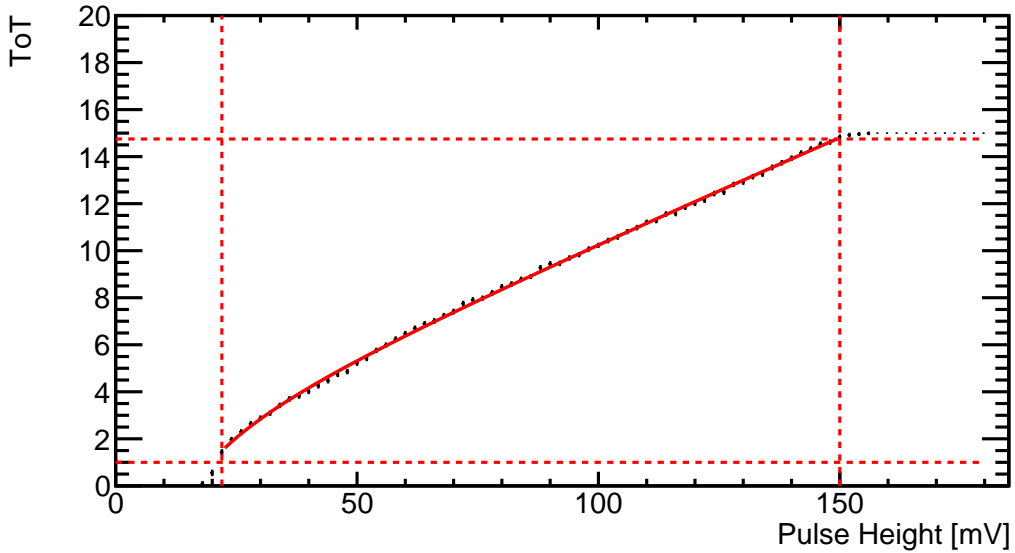


**Figure 4.11:** CLICpix ToT as a function of injected pulse height for a single pixel. The black markers are the mean ToT and the error bars are the standard error on the mean. The solid red line shows the surrogate function fit and the dotted red lines show the range where the fit was applied.

## Results

A known issue with the design of the CLICpix ASIC is the unwanted feedback capacitance between the discriminator output and amplifier input. This feedback leads to an additional fixed injected charge being measured for each recorded hit, due to the firing of the discriminator. The magnitude of this effect differs between even and odd columns across the CLICpix matrix due to slight differences in the physical layouts of alternating columns. By examining the distribution of the surrogate fit parameters, shown for SET 9 in figure 4.12, this effect can be seen.

The peaks at zero in the distribution of the  $a$  and  $b$  parameters, containing  $\approx 150$  entries, correspond to noisy and dead pixels. These damaged pixels will be found in the device due to problems occurring in the manufacturing process. The majority of the  $a$  and  $b$  parameters are centred around a single value, which indicates a similar response in the linear region of the surrogate function, however, the  $c$  and  $t$  parameters are centred around one of two values. When examining the distribution of these parameters as a function of position on the matrix, shown in figure 4.13 for a selected device, it can be seen that the structure is related to the column a given pixel is in. This

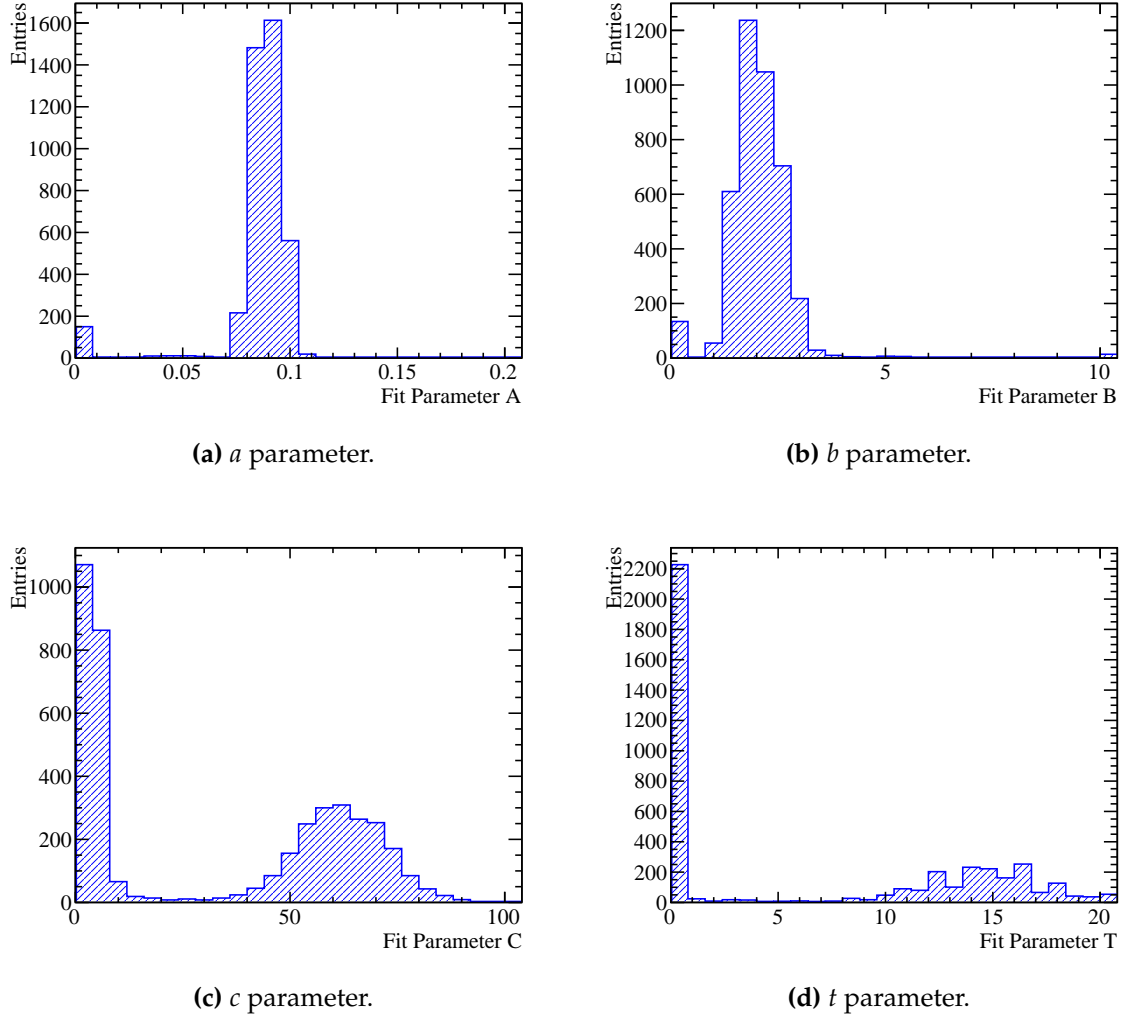


**Figure 4.12:** The distribution of the surrogate function parameters obtained when fitting the ToT as a function of injected pulse height for SET 9. (a), (b), (c) and (d) show the distribution of the  $a$ ,  $b$ ,  $c$  and  $d$  parameters respectively.

feature is present in all devices considered and the underlying cause, the unwanted feedback capacitance, will be remedied in the next generation of the CLICpix ASIC.

The matrix-averaged surrogate function fit parameters for all devices can be found in tables 4.2 and 4.3, for the even and odd columns respectively. The surrogate function for each device using these average parameters as input is shown in figure 4.14.

As figure 4.14 shows, the response of the CLICpix to the injected pulse height is largely uniform across all samples. For all devices the turn-on pulse height is  $\approx 10$  mV

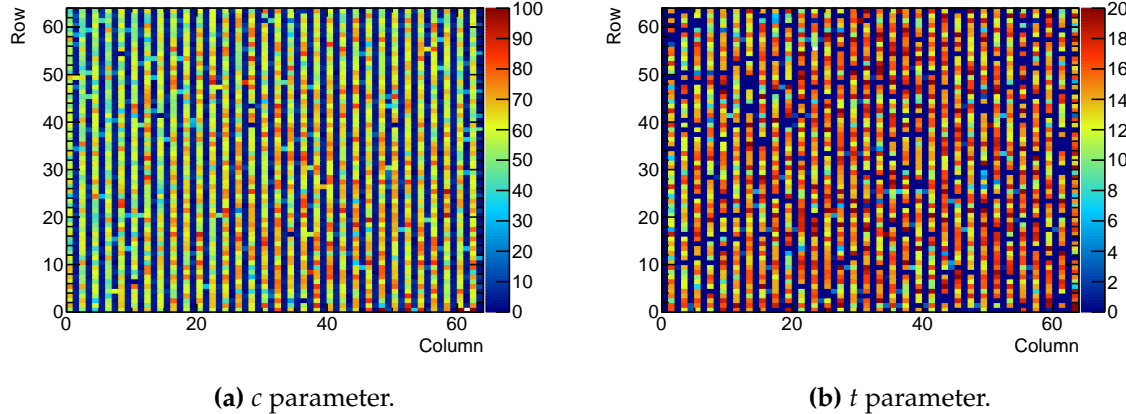


**Figure 4.13:** The distribution of selected surrogate function parameters obtained when fitting the ToT as a function of injected pulse height for SET 9 as a function of matrix position. (a) and (b) show the distribution of the  $c$  and  $t$  parameters respectively.

Assembly	$a$	$b$	$c$	$t$
SET 9	$0.0875 \pm 0.0005$	$2.41 \pm 0.03$	$5.1 \pm 0.1$	$12.79 \pm 0.15$
SET 10	$0.0769 \pm 0.0005$	$2.58 \pm 0.03$	$7.5 \pm 0.2$	$8.02 \pm 0.14$
SET 12	$0.0725 \pm 0.0005$	$2.87 \pm 0.04$	$12.1 \pm 0.3$	$7.86 \pm 0.22$
SET 13	$0.0708 \pm 0.0005$	$2.69 \pm 0.03$	$16.2 \pm 0.3$	$6.65 \pm 0.18$
SET 15	$0.0856 \pm 0.0005$	$2.34 \pm 0.03$	$5.1 \pm 0.2$	$12.51 \pm 0.13$
SET 16	$0.0746 \pm 0.0004$	$2.32 \pm 0.02$	$13.7 \pm 0.3$	$6.65 \pm 0.16$

**Table 4.2:** The average fit parameters for even columns of CLICpix sensor. The reported error was calculated using the standard error in the mean when averaging the fit parameters across the matrix.

and saturation, which occurs when the ToT output reaches the maximum value of 15, occurs at  $\approx 150$  mV. The differing column structure exists due to the unwanted feedback capacitance between the discriminator output and amplifier input. This unwanted feedback leads to a sharper rise in ToT for even-numbered columns than for odd-numbered columns, as in effect the even-numbered columns are operating at a lower threshold. This column structure is present in all devices considered. The uniformity of the response of the CLICpix ASICs observed in this study make comparisons between the misaligned samples clearer. These results show that any performance differences observed between the misaligned devices do not originate from the intrinsic behaviour of the CLICpix ASIC.

Assembly	$a$	$b$	$c$	$t$
SET 9	$0.0834 \pm 0.0003$	$1.72 \pm 0.01$	$61.0 \pm 0.3$	$0.25 \pm 0.09$
SET 10	$0.0759 \pm 0.0002$	$1.63 \pm 0.01$	$43.2 \pm 0.2$	$0.10 \pm 0.02$
SET 12	$0.0731 \pm 0.0003$	$1.92 \pm 0.02$	$51.5 \pm 0.3$	$0.36 \pm 0.12$
SET 13	$0.0713 \pm 0.0002$	$1.72 \pm 0.01$	$52.5 \pm 0.3$	$0.18 \pm 0.07$
SET 15	$0.0836 \pm 0.0003$	$1.52 \pm 0.02$	$52.7 \pm 0.3$	$0.42 \pm 0.08$
SET 16	$0.0727 \pm 0.0002$	$1.49 \pm 0.01$	$50.7 \pm 0.2$	$0.10 \pm 0.03$

**Table 4.3:** The average fit parameters for odd columns of CLICpix sensor. The reported error was calculated using the standard error in the mean when averaging the fit parameters across the matrix.

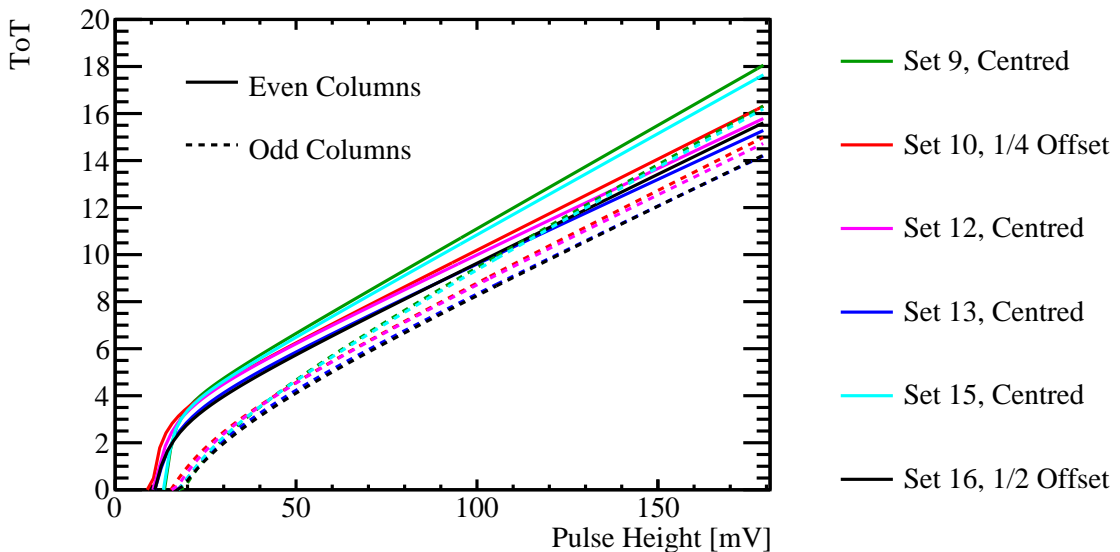


**Figure 4.14:** The average ToT response as a function of injected pulse height, which is represented using the surrogate function. Parameters for the surrogate function are obtained by fitting the ToT against pulse height curve for all pixels in the matrix. The results are divided into even and odd columns to account for the differing effective thresholds on alternate CLICpix columns.

## 4.4 Test Beam Analysis

Test beam measurements were used to characterise the behaviour of the prototype capacitively coupled pixel detectors. These measurements are particularly useful as they include information relating to the properties of the particles passing through the device under test (DUT). This information is crucial for calculating the efficiency of

the devices, which will ultimately determine whether the device is fit for use in the CLIC vertex detector.

The trajectory of any particles passing through the DUT was measured in the test beam setup using a telescope. The telescope consisted of several planes of pixel detectors mounted either side of the DUT. As low energy particles would be stopped by the telescope detector planes, telescopes can only be used to measure the trajectory of relatively high energy particles. This means that they cannot be used in lab based measurements, but can be used in test beams where high energy particles can be safely produced.

#### 4.4.1 Test Beam Setup

Test beam experiments were carried out in August and September 2015 on the H6 beam line in the CERN SPS North Area. The beam consisted of positively charged hadrons of momenta 120 GeV/c. Mean particle rates of  $500 \text{ kHz/cm}^2$  were observed during the 4.8 s spills at intervals of 25 s. The devices under test were mounted on an EUDET/AIDA telescope [52]. This telescope consisted of six planes of sensors, three on either side of the DUT, constructed of Mimosa pixel detectors. This telescope provided a resolution of  $1.6 \mu\text{m}$  on the intercept position between tracks passing through the device and the DUT mounted on it.

#### 4.4.2 Analysis

A number of cuts were applied to veto the effect of noisy pixels and tracks that underwent non-negligible multiple scattering. These effects would lead to discrepancies in the reported efficiencies of the devices, which are not representative of the true device performance. Any pixels identified on the DUT that were deemed to be noisy were removed from the analysis. A pixel was deemed noisy if it responded at a mean rate greater than  $5 \sigma$  in comparison to the average rate across the whole matrix. In addition to this, any tracks with an intercept on the DUT within half a pixel width of a noisy pixel were also rejected from the analysis. As tracks may undergo non-negligible multiple scattering, a  $\chi^2$  cut was used to remove less precisely reconstructed tracks. Furthermore, all tracks occurring within  $125 \mu\text{m}$  of each other were vetoed, in order to reduce the possibility of mis-association of clusters to tracks.

After the application of these cuts, the track position on the DUT was calculated using the measured particle trajectory through the telescope planes. This was followed by a search around the intercept position on the DUT to find an associated cluster. Clusters were associated to the track if they fell within 75  $\mu\text{m}$ , or 3 pixels, about the intercept position. If multiple clusters were associated to a track the cluster position was calculated as the ToT-weighted centre-of-gravity.

Alignment of the telescope planes was essential for ensuring that the correct trajectory of the particles passing through the setup could be determined. Furthermore, alignment of the DUT with respect to the telescope planes was critical for ensuring the correct track intercept position was found. With that in mind the six telescope planes were aligned by minimising the total track  $\chi^2$  with respect to the global alignment parameters. The tracks that were created in the alignment procedure are referred to as "rough tracks" as they are produced using the hits from sensor planes that may not be ideally aligned. The alignment proceeded one telescope plane at a time until all planes were accounted for. This procedure was iteratively repeated, updating the global alignment parameters to the optimal values found each time, until no further gains could be made. Once the telescope planes were aligned, the DUT was aligned in a similar manor, but this time minimising the summed square of track residuals. The residual is defined as the difference between the track intercept and associated cluster centre-of-gravity.

#### 4.4.3 Results

The metric used for characterising the device performance in the test beam is the single hit efficiency,  $\epsilon$ . This is defined as the number of tracks with associated clusters recorded by the DUT,  $n$ , divided by the number of reconstructed tracks passing through the DUT recorded by the telescope,  $m$ . The errors shown on the efficiency measurements are given by  $\sqrt{\frac{\epsilon(1-\epsilon)}{m}}$ , which follows from the variance of  $n$  given binomial statistics with mean  $\epsilon$ . The single hit efficiency as a function of threshold for all devices is shown in figure 4.15. The threshold, in units of number of electrons, is the size of the signal that must be injected into the CLICpix ASIC to generate a hit.

The data indicates that for all assemblies the single hit efficiency of the detector decreases when a higher amount of charge is required to generate a signal, which is to be expected. However, the efficiency of all samples, with the exception of the  $\frac{1}{2}$ -offset

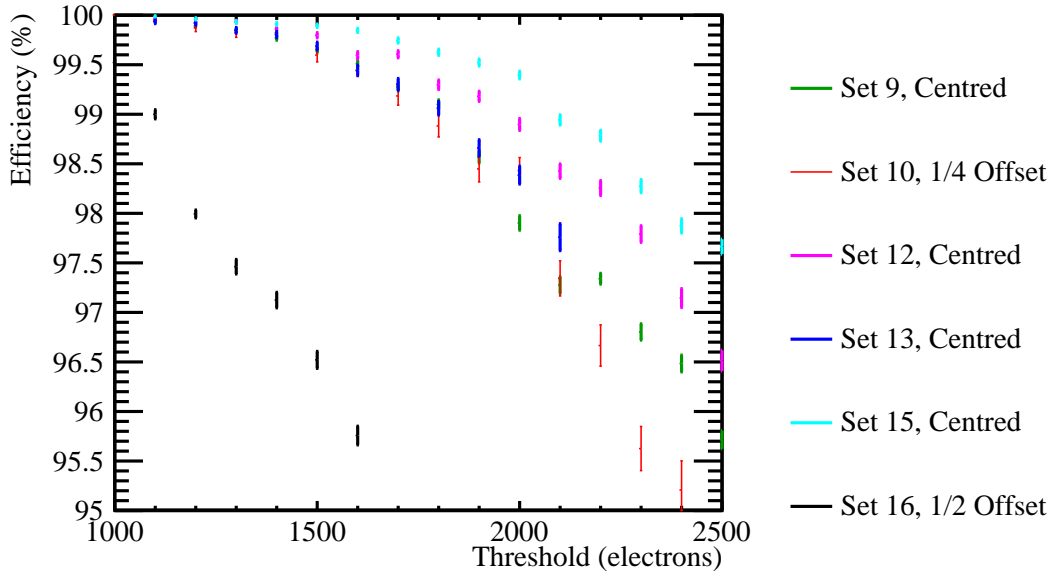


**Figure 4.15:** The efficiency of the devices considered as a function of the threshold applied.

sample, is still above 99% up to a threshold of 2000 electrons. This is encouraging behaviour as the larger the threshold that can be applied the lower the effects from noise will be. Reducing the effects from noise will aid tracking performance in the CLIC vertex detector, which is highly desirable. It is clear that the  $\frac{1}{2}$  offset sample, SET 16, has a much lower efficiency as a function of threshold in comparison to the other samples. For the same deposited charge in the CCPDv3 the  $\frac{1}{2}$ -offset sample will, due to the reduced capacitance, produce a smaller signal in the CLICpix than the centred samples. This is the cause of the reduced efficiency as a function of threshold in this sample. More encouragingly is the behaviour of the  $\frac{1}{4}$ -offset sample, SET 14, which in terms of performance is comparable to the aligned samples. There is a degradation in efficiency of the  $\frac{1}{4}$ -offset sample with respect to the aligned sample, which is to be expected given the reduced capacitance, however, it is relatively small. These results indicate that even with a relatively large misalignment between the CCPDv3 and CLICpix pads the device performance is not significantly affected, and therefore manufacturing tolerances of  $\frac{1}{4}$  of a pixel width would not be problematic if this device were used for the CLIC vertex detector.



# Chapter 5

## Energy Estimators

*“There, sir! that is the perfection of vessels!”*

— Jules Verne, 1828–1905

### 5.1 Motivation

The separation of energy deposits from charged and neutral particles in the calorimeters is crucial for achieving good energy resolutions in the particle flow paradigm. This is only possible if the energy estimators for those energy deposits are accurate. The ultimate goal of the calibration procedure outlined in this chapter is to obtain the best energy estimator for particles showering in the calorimeters. The energy estimator for a cluster of calorimeter hits is:

$$E_{\text{Cluster}} = \sum_{\text{ECal hits, } i} E_{\text{ECal}}^i + \sum_{\text{HCal hits, } i} E_{\text{HCal}}^i , \quad (5.1)$$

where  $E_{\text{ECal}}^i$  is the energy of ECal hit  $i$ ,  $E_{\text{HCal}}^i$  is the energy HCal hit  $i$  and  $\Sigma$  is the summation over all hits in a given calorimeter. This is a naive energy estimator that will act as a starting point for the development of more sophisticated procedures aimed at improving detector performance. However, before going further the calorimeter hit energies must be determined, which for a sampling calorimeter is non-trivial. Sampling calorimeters, such as those found at the linear collider, are comprised of alternating layers of active and absorber materials [46]; The absorber layers are

designed to initiate particle showers and propagate their development, while the active layers are designed to give a response that is proportional to the energy deposited within them. As the response of a sampling calorimeter gives a measure of the energy deposited in the active layers only, the energy deposited in the absorber medium has to be estimated based on the active layer energies. This estimation is made by assuming the energy deposited across a calorimeter hit, that is one active and one absorber layer, is uniform. Working under this assumption, the total calorimeter hit energy is proportional to the active layer hit energy. This estimation procedure is loosely referred to as digitisation and, in this way, the cluster energy estimator introduced above can be written as:

$$E_{\text{Cluster}} = \sum_{E\text{Cal hits}, i} \epsilon_{E\text{Cal}}^i \alpha_{E\text{Cal}} + \sum_{H\text{Cal hits}, i} \epsilon_{H\text{Cal}}^i \alpha_{H\text{Cal}}, \quad (5.2)$$

where  $\alpha_{E\text{Cal}}$  and  $\alpha_{H\text{Cal}}$  are digitisation constants for the ECal and HCal respectively,  $\epsilon_{E\text{Cal}}^i$  is the energy response in the active medium for ECal hit  $i$ ,  $\epsilon_{H\text{Cal}}^i$  is the energy response in the active medium for a HCal hit  $i$  and  $\sum$  is the summation over all hits in a given calorimeter. The first stage of the calibration procedure presented in this chapter covers the determination of these digitisation constants.

Once the basic energy estimator has been calibrated, it is possible to apply more advanced procedures designed to give a compensating calorimeter response [24]. A compensating calorimeter produces an identical response to a particle shower irrespective of whether the particle shower is electromagnetic or hadronic in nature. It is the atomic properties of the materials used in a calorimeter that determine whether a calorimeter is compensating. The primary cause of a difference in the response of a calorimeter to electromagnetic and hadronic showers is the invisible energy component that is found in hadronic showers. As this component cannot be measured by the calorimeter, the response is typically lower for hadronically showering particles than for electromagnetically showering particles. The invisible component exists due to a combination of effects such as neutrons stopping within the calorimeter and nuclear binding energy losses. If left unchecked, this difference would lead to a systematic loss of energy for hadronic showers that would harm detector performance.

There are two distinct routes available for negating this unwanted effect and achieving a compensating response from a calorimeter: The first is hardware compensation [53], whereby calorimeters are constructed using materials that yield extra energy in response to hadronic showers, and the second is software compensation [32],

whereby the uncompensated calorimetric energies for hadronic showers are modified at the software level. The linear collider lends itself to software compensation as the fine segmentation of the calorimeters and precise reconstruction of individual particles makes identification of hadronic showers, and modifying their energies, feasible. A basic form of software compensation included in the linear collider reconstruction is the modification of the electromagnetic cluster energy estimator to:

$$E_{EM\ Cluster} = \sum_{ECal\ hits,\ i} E_{ECal}^i \beta_{ECal}^{EM} + \sum_{HCal\ hits,\ i} E_{HCal}^i \beta_{HCal}^{EM}, \quad (5.3)$$

and the hadronic cluster energy to:

$$E_{Had\ Cluster} = \sum_{ECal\ hits,\ i} E_{ECal}^i \beta_{ECal}^{Had} + \sum_{HCal\ hits,\ i} E_{HCal}^i \beta_{HCal}^{Had}, \quad (5.4)$$

where the  $\beta$ s are scaling factors that are applied to the energy of clusters of calorimeter hits associated with electromagnetic and hadronic clusters in the ECal and HCal. This simple scaling of energies compensates the response of the calorimeters, which leads to better detector performance. Determination of these energy scale setting constants is the second stage of the calibration procedure that is presented in this chapter.

While this scaling of energies improves detector performance, it does not account for any changes to the  $\beta$  scaling factors as a function of the total energy deposited. An energy dependence in the scaling factors is expected as the mechanisms governing the propagation of hadronic showers are sensitive to the shower energy [54]. To account for this, more sophisticated software techniques have been developed that vary the calorimeter cluster energy estimator as a function of energy to achieve a compensating response across a wider range of energies. These techniques make use of the fine segmentation of the linear collider calorimeters to identify hadronic showers. These techniques also address the problem of spuriously high energy calorimeter hits that if left unchecked would damage the reconstruction. These high energy hits are caused by Landau fluctuations [55], which originate from high energy knock-on electrons appearing within particle showers [56]. In this chapter, following a description of the calibration procedure outlined above, is an explanation of these novel energy estimators and the impact they have on detector performance.

This chapter concludes with a study determining the impact on detector performance of timing cuts that are applied to the calorimeter hits. These cuts form part of the software trigger that will be used at the linear collider experiment. Details

regarding how all the detector performance metrics used in this chapter are calculated can be found in section ??.

### Hardware Compensation

A novel example of hardware compensation is the ZEUS calorimeter [53]. The ZEUS calorimeter was constructed using uranium as the absorber material. In response to neutral hadrons the uranium undergoes fission producing extra energy that increases the hadronic response of the calorimeter. The amount of uranium was carefully chosen to achieve a fully compensating calorimeter response i.e. identical calorimeter response to electromagnetic and hadronic showers. While hardware compensation is possible for the linear collider calorimeters, restrictions on calorimeter construction and the use of a large amount of radioactive material are highly undesirable.

### Calibration and detector optimisation

Optimising the detector at a future linear collider will be crucial to exploit the full physics potential available to it. An extensive optimisation of the calorimeters was performed and the results can be found in chapter 6.1. For each detector model considered, the calibration procedure outlined in section 5.2 was applied to ensure optimal energy estimators were used to quantify the detector performance. This made it possible to perform unbiased comparisons between detector models, which ensured reliability in the conclusions drawn from those studies.

## 5.2 Calibration in the particle flow paradigm

The calibration procedure described in the following section discusses how the digitisation constants,  $\alpha$ , and the scaling factors  $\beta$  that were introduced in section 5.1 are determined. In addition to this, minimum ionising particle (MIP) scale setting is included in the calibration procedure to ensure optimal detector performance is achieved.

The MIP scale is the average energy response, on a per hit level, of a calorimeter when a normally incident MIP passes through it. This energy scale is used by the

digitisation processor and PandoraPFA to apply noise vetoing cuts to the calorimeter hit energies. The digitisation processor will only create a calorimeter hit if the corresponding active layer energy exceeds a threshold energy, which is defined in units of MIPs. Similarly, PandoraPFA will only use a calorimeter hit in the reconstruction if the calorimeter hit energy exceeds a threshold energy, which is also defined in units of MIPs. Both of these cuts are designed to veto noise that would be present in a real detector. While noise is not explicitly added to the detector simulations, these thresholds are still applied to ensure the simulation better reflects the performance of a real detector. In addition to this, the MIP scale is used by the digitiser for simulating a number of realistic detector effects. This includes a truncation of the active layer calorimeter hit energies, which is set in units of MIPs. This truncation mimics saturation effects in the calorimeter readout technology. Setting the MIP scale is crucial for ensuring the noise vetoing cuts and realistic effects are correctly applied.

The MIP scale in the digitiser and PandoraPFA, while intrinsically linked, have to be calculated separately. The digitiser requires the MIP scale to be defined using the active layer hit energies while, PandoraPFA requires the definition from the full hit, the active and absorber layer, energies. It may be expected that the digitisation MIP scale could be related to the PandoraPFA MIP scale by the digitisation constants, however, this is not necessarily the case; additional cuts are applied to the full calorimeter hit energies that are not applied to the active layer hit energies e.g. timing cuts. Therefore, the conservative approach of independently recalculating the MIP scale for PandoraPFA was taken.

The  $\alpha$  and  $\beta$  constants are determined by tuning the mean of reconstructed energy distributions. A number of cuts are applied when populating these reconstructed energy distributions that ensure the relevant reconstructed energy is being tuned. The application of these cuts means that linear scaling of the  $\alpha$  and  $\beta$  constants does not lead to a linear shift in the mean of the reconstructed energy distributions. Therefore, when calibrating the  $\alpha$  and  $\beta$  constants an iterative approach is taken; the next iteration of the calibration constant is determined by repeating the reconstruction using the current iteration of the constant and adjusting the constant based on the mean of the reconstructed energy distribution.

## Ordering of Calibration Procedure

The calibration procedure is broadly split into four separate operations: determination of digitisation constants, determination of scaling factor constants and MIP scale setting in the digitiser and PandoraPFA. The ordering of each of these calibration steps is crucial as it is possible to get interference between the different stages if applied in an arbitrary order. With that in mind, the procedure order to minimise interference is as follows:

1. Setting the MIP scale setting in the digitiser. No dependancies on other calibration constants.
2. Setting the digitisation constants,  $\alpha$ s. This relies upon the MIP scale in the digitiser being set.
3. Setting the MIP scale setting in PandoraPFA. This relies upon correct calibration of calorimeter hit energies, therefore, the  $\alpha$ s must be calibrated first.
4. Setting the scaling factors,  $\beta$ s. This relies upon correct calibration of calorimeter hit energies and correct MIP scale setting in PandoraPFA.

## Photon Likelihood Data

Some of the algorithms in PandoraPFA make use of likelihood data to identify electromagnetic showers. This likelihood data consists of a series of probability density functions (PDFs) that describe a number of topological properties of PFOs. The data contained in these PDFs is related solely to the ECal, which means that every time the ECal is changed from that of the nominal ILD detector this likelihood data must be retrained. Should retraining be necessary it should be performed after the application of the calibration procedure as described in section 5.2. To ensure PandoraPFA gives optimal performance for jet reconstruction, the likelihood data is trained using off-shell mass Z boson events, at 500 GeV, decaying into light quarks (u, d, s).

### 5.2.1 Digitisation Implementation

This section discusses how the digitisation constants,  $\alpha$ , introduced in section 5.1 are determined. The digitisation constant for a given calorimeter depends upon

several factors such as the material properties of the active and absorber layers, the magnetic field strength and energy losses occurring within the gaps in the detector. Therefore, each calorimeter in the ILD detector model has a distinct constant that must be independently determined.

### ECal Digitisation Implementation

The procedure for determining the digitisation constants in the ECal involves simulation of single  $\gamma$  events at energy  $E_{MC} = 10$  GeV.  $\gamma$  events are ideal for calibration of the ECal as  $\gamma$ s are, at this energy, largely contained within the ECal, as shown in figure 5.1a. This makes them ideal for isolating the ECal digitisation calibration from that of the HCal digitisation calibration. Events are only used for calibrating the ECal digitisation if they are confined to the ECal. To that extent, cuts are applied ensuring that the sum of the reconstructed energy found outside the ECal is less than 1% of  $E_{MC}$  and that  $\cos(\theta) < 0.95$ , where  $\theta$  is the polar angle of the  $\gamma$ . The polar angle cut veto events where the  $\gamma$  goes down the beam pipe.  $\gamma$  conversions are also vetoed in this event sample at MC level. The impact of these cuts on the sum of ECal hit energies for the  $E_{MC} = 10$  GeV  $\gamma$  events is shown in figure 5.1b.

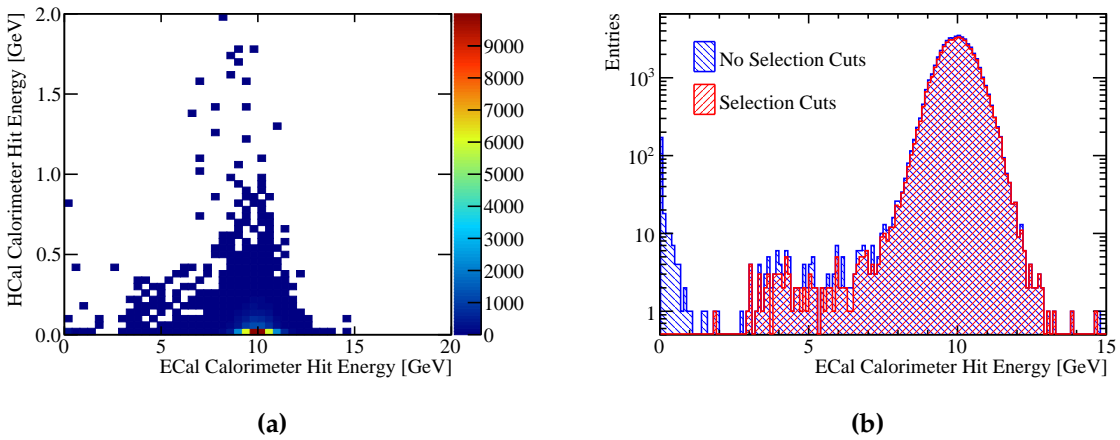


**Figure 5.1:** (a) The sum of calorimeter hit energies in ECal and HCal for 10 GeV  $\gamma$  events. (b) The sum of the ECal calorimeter hit energies for 10 GeV  $\gamma$  events with and without the selection cuts.

The calibration of the digitisation in the ECal is an iterative procedure, which begins with the simulation of single  $\gamma$  events using a trial calibration, with digitisation constant in the ECal  $\alpha_{\text{ECal}}^0$ . Next the distribution of the sum of calorimeter hit energies

within the ECal is produced for events passing the selection cuts, as shown in figure 5.1b. For an ideal calorimeter this distribution should be Gaussian, as described in chapter 6, therefore, a Gaussian fit is applied to this distribution and the mean,  $E_{\text{Fit}}$ , extracted. To remove the effect of any outliers in this distribution, the fit is applied to the range of data with the smallest root mean square that contains at least 90 % of the data. An example of such a fit is shown in figure 5.2. In the case of ideal calibration, the mean of this fit,  $E_{\text{Fit}}$ , would be equal  $E_{\text{MC}}$ . It is assumed that any difference between the two is due to the calibration, therefore, to correct this the digitisation constant from the trial calibration,  $\alpha_{\text{ECal}}^0$ , is rescaled by the ratio of the  $E_{\text{MC}}$  to  $E_{\text{Fit}}$ :

$$\alpha_{\text{ECal}}^0 \rightarrow \alpha_{\text{ECal}} = \alpha_{\text{ECal}}^0 \times \frac{E_{\text{MC}}}{E_{\text{Fit}}} , \quad (5.5)$$

This procedure is then repeated until the  $E_{\text{Fit}}$  falls within a specified tolerance. The tolerance applied here was  $|E_{\text{Fit}} - E_{\text{MC}}| < E_{\text{MC}} \times 5\%$ . The binning used for the fitted histogram is chosen such that the bin width is equal to the desired tolerance on  $E_{\text{Fit}}$  e.g.  $E_{\text{MC}} \times 5\% = 0.5 \text{ GeV}$ . This tolerance is somewhat loose, however, it is tight enough to ensure successful application of PFA. It should also be emphasised that the PFO energies used for downstream analyses have the electromagnetic and hadronic energy scale corrections applied, which are calibrated to a much tighter accuracy.

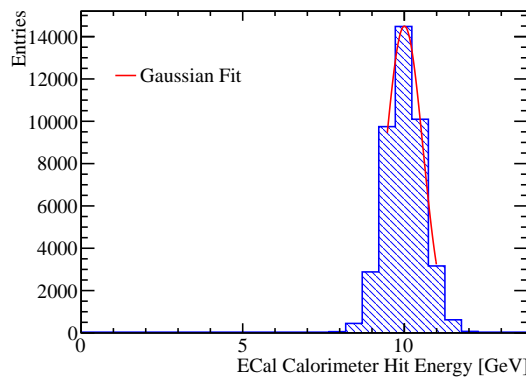


**Figure 5.2:** Gaussian fit to sum of the ECal calorimeter hit energies for 10 GeV  $\gamma$  events with selection cuts. The coarse binning reflects the tolerance on the digitisation constant calibration.

## HCal Digitisation Implementation

The calibration for the digitisation in the HCal proceeds in a similar manor to that described for the ECal with a few key differences. This calibration uses  $K_L^0$  events at  $E_{MC} = 20$  GeV as these neutral hadrons will deposit the bulk of their energy in the HCal. The higher energy, with respect to the ECal digitisation, is used to create larger particle showers that sample deeper into the HCal. As the  $K_L^0$ s must pass through the ECal before arriving at the HCal and, as the ECal contains  $\approx 1\lambda_I$ , some of the  $K_L^0$ s begin showering in the ECal, as shown by figure 5.3a. Such events are unsuitable for calibration of the HCal digitisation constants as rescaling  $\alpha_{HCal}^0$  would not lead to a linear change in  $E_{Fit}$ . These events are vetoed in the even selection by requiring events deposit less than less than 5% of  $E_{MC}$  outside of the HCal. In addition to this, the last layer of the HCal where energy is deposited is required to be in the innermost 90% of the HCal. This cut vetoes events that shower late in the HCal and deposit a significant amount of energy in the uninstrumented coil region of the detector. The impact of these cuts on the sum of HCal calorimeter hit energies for the  $E_{MC} = 20$  GeV  $K_L^0$  events is shown in figure 5.3b. There are two HCal digitisation constants used in the detector simulation, one applied for the barrel and another for the endcap. This is to account for differences in hadronic shower dynamics between the two, such as differing magnetic field configurations in the barrel and endcap. Both parameters are calibrated in the same manor, but have different cuts on  $\theta$ , the polar angle of the  $K_L^0$ . For the barrel region of the HCal events are selected if  $0.2 < \cos(\theta) < 0.6$ , while for the endcap events are selected if  $0.8 < \cos(\theta) < 0.9$ . These angular cuts are conservative to account for the transverse profile of the hadronic showers and ensure that they are confined to the relevant sub-detector. One further difference to the ECal digitisation procedure is that the target reconstructed energy for the  $K_L^0$  samples is the kinetic energy as opposed to the total energy. As the majority of the neutral hadrons appearing in jets are neutrons and their accessible energy is their kinetic energy, calibrating to the kinetic energy should give the best performance for jet reconstruction.

Using these cuts the calibration procedure for the digitisation of the HCal barrel and endcap proceeds in the same manor as was described for the ECal, the details of which can be found in section 5.2.1. Examples of the Gaussian fits applied to the sum of the calorimeter hit energies in the HCal barrel and endcap can be found in figure 5.4.

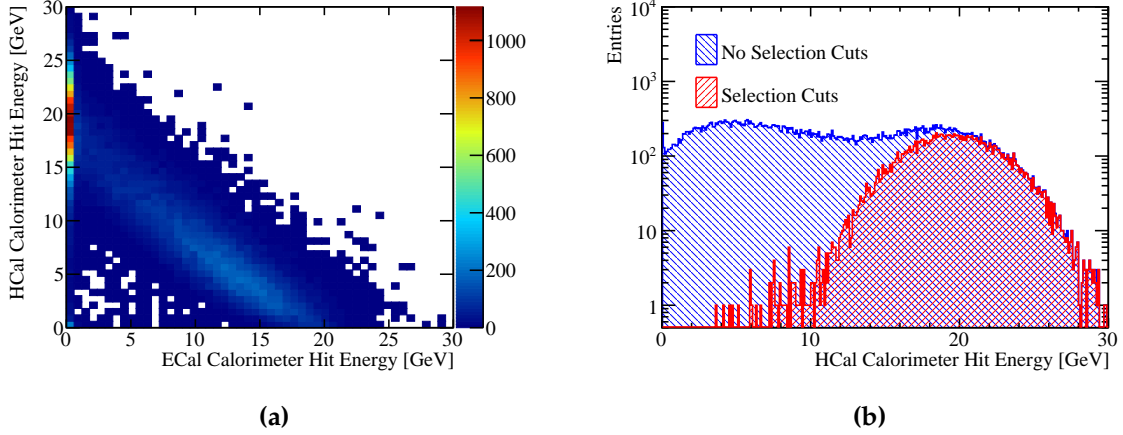


**Figure 5.3:** (a) Sum of calorimeter hit energies in ECal and HCal for 20 GeV  $K_L^0$  events. (b) Sum of the HCal calorimeter hit energies for a 20 GeV  $K_L^0$  events with and without the selection cuts.

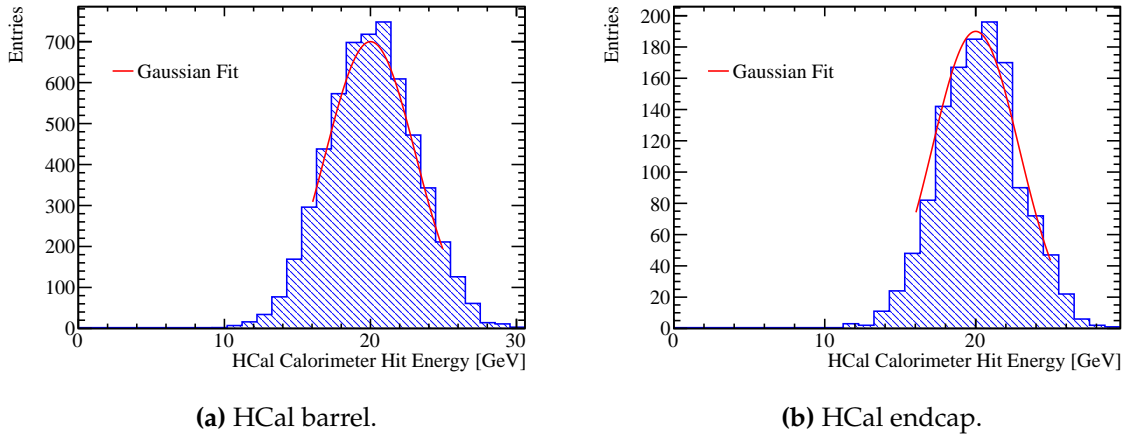


**Figure 5.4:** Gaussian fit to sum of the HCal calorimeter hit energies for 20 GeV  $K_L^0$  events with selection cuts.

## HCal Ring Digitisation Implementation

The HCal ring, illustrated in figure 5.5, also has an independent digitisation constant to account for any difference in the hadronic shower development between the ring, barrel and endcap. The procedure used to calibrate this constant has to differ from that presented in section 5.2.1 as it is unfeasible, due to the depth of the ring, to produce events that are wholly contained within it. Fortunately, the size of the HCal ring means it plays a minimal role in the reconstruction, so precise calibration is not crucial. To

ensure that the calibration is approximately correct for the HCal ring,  $\alpha_{\text{HCal ring}}$  is assumed to equal  $\alpha_{\text{HCal endcap}}$  multiplied by several factors designed to account for changes in the active layer thickness, absorber layer thickness and the MIP response between the HCal endcap and ring. In detail:

$$\alpha_{\text{HCal ring}} = \alpha_{\text{HCal endcap}} \times \frac{\langle \cos(\theta_{\text{endcap}}) \rangle}{\langle \cos(\theta_{\text{ring}}) \rangle} \times \frac{P_{\text{endcap}}}{P_{\text{ring}}} \times \frac{L_{\text{endcap}}^{\text{Absorber}}}{L_{\text{ring}}^{\text{Absorber}}} \times \frac{L_{\text{ring}}^{\text{Active}}}{L_{\text{endcap}}^{\text{Active}}}, \quad (5.6)$$

where  $\theta$  is the incident angle of the incoming particle to the calorimeter determined using the 20 GeV  $K_L^0$  events,  $L^{\text{Active}}$  is the active layer thickness and  $L^{\text{Absorber}}$  is the absorber layer thickness.  $P$  is the position of the MIP peak in the distribution of active layer hit energies, which has been corrected so that the MIP appears to enter the calorimeter at normal incidence, and is determined using 10 GeV  $\mu^-$  events. Details on how  $P$  is determined can be found in section 5.2.2.

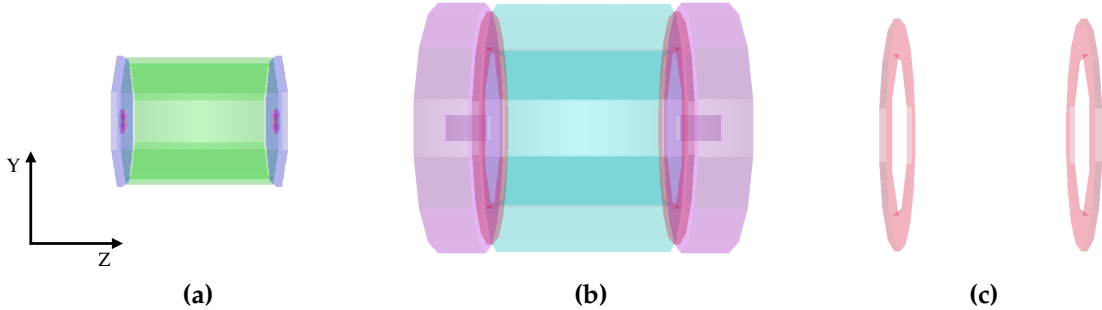


**Figure 5.5:** A PandoraPFA event display showing the nominal ILD calorimeters. (a) the ECal, (b) the full HCal and (c) the HCal ring.

### 5.2.2 MIP Scale Determination

The digitiser MIP scale was defined as the, non-zero, peak in the distribution of the active layer calorimeter hit energies for normally incident 10 GeV  $\mu^-$  [56], as shown in figure 5.6. This distribution is made for each calorimeter where the MIP scale needs to be determined. As the average energy deposited per hit in a given sub-detector is relevant for setting the MIP scale, as opposed to the total energy deposited in a sub-detector, no selection cuts are required. When populating the active layer energy distribution, a direction correction factor of  $\cos(\theta)$ , where  $\theta$  is the incident angle of the  $\mu^-$  to the calorimeter hit, was applied to the hit energy to generate the effect of having the  $\mu^-$  enter the calorimeter at normal incidence. The MIP scale was determined

separately for the ECal, HCal barrel, HCal endcap and HCal ring, however, only a single HCal MIP scale, taken as the HCal barrel, was required by the digitisation processor. The HCal endcap and ring MIP scales were calculated for the purposes of the HCal ring digitisation described in section 5.2.1. No MIP scale setting was required in the digitisation processor for the muon chamber.

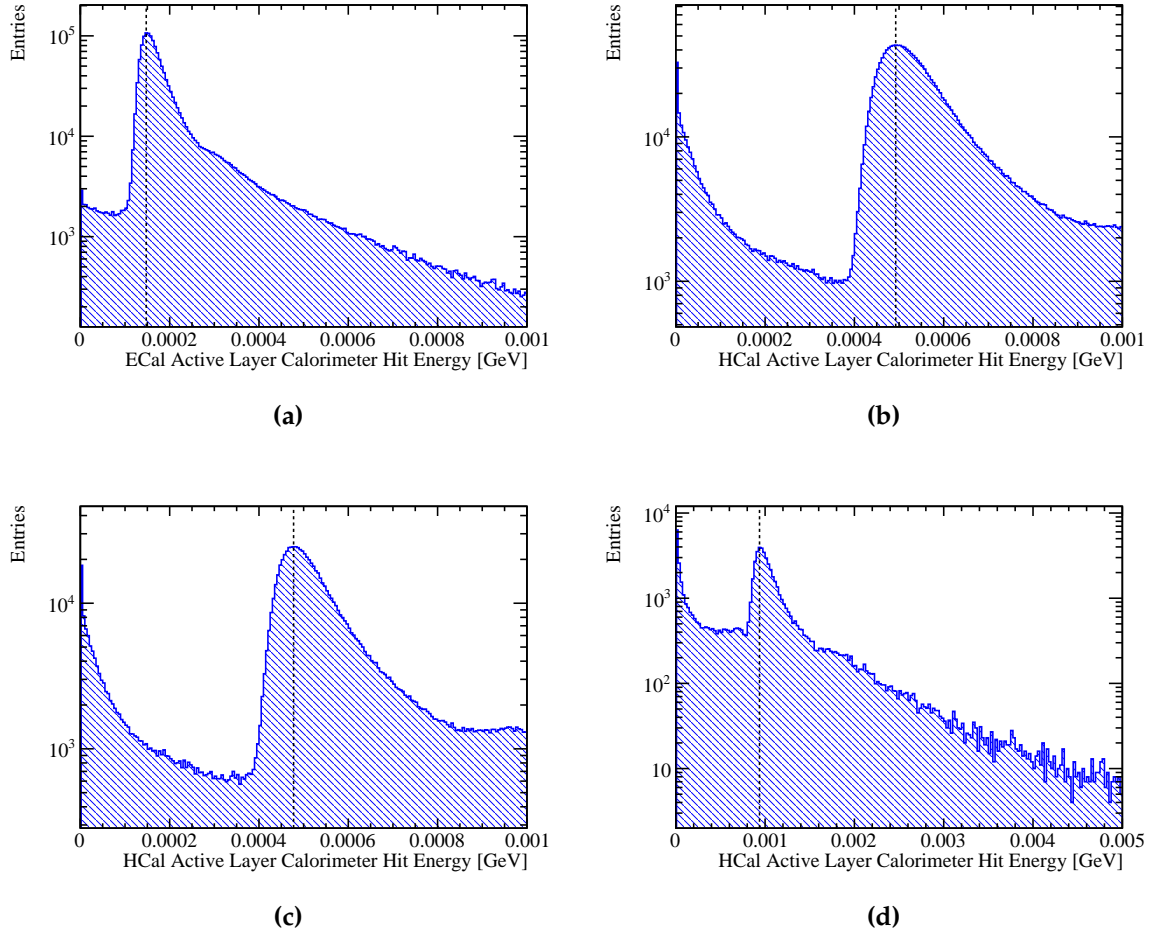


**Figure 5.6:** The active layer calorimeter hit energy distributions for (a) the ECal, (b) the HCal barrel, (c) the HCal endcap and (d) the HCal ring for 10 GeV  $\mu^-$  events.

A similar procedure was employed for calculation of the MIP peak in PandoraPFA. The distribution used to set the MIP scale in PandoraPFA is the distribution of the calorimeter hit energies, i.e. the active and absorber layer energies, as opposed to the active layer energies used for setting the MIP scale in the digitisation processor. Examples of the distributions used to set the MIP scale in PandoraPFA can be found in figure 5.7. There are few populated low calorimeter hit energy bins in these distributions as cuts are applied in the digitiser on the active layer energy. The

double peak structure observed in the ECal calorimeter hit energy distribution is expected given the ECal absorber material thickness doubling in the back 10 layers of the ECal. Further differences between the MIP scale setting in the digitiser and PandoraPFA are as follows: The MIP scale setting in PandoraPFA combines the HCal sub-detectors, the barrel, endcap and ring, together when creating the calorimeter hit energy distributions; PandoraPFA requires the MIP scale to be set in the muon chamber unlike the digitisation processor and, therefore, the muon chamber hit energy distribution must also be created.

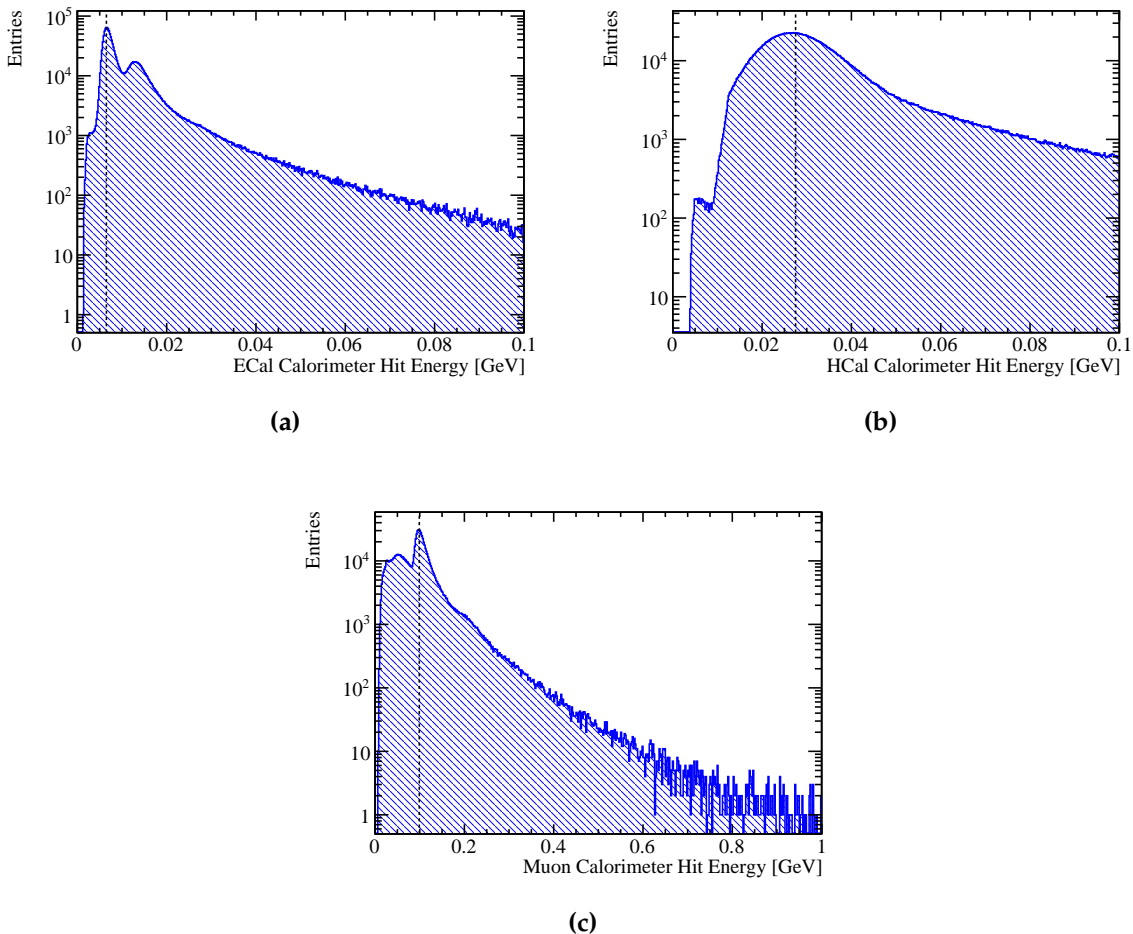


**Figure 5.7:** The calorimeter hit energy distributions for (a) the ECal, (b) the HCal and (c) the muon chamber for 10 GeV  $\mu^-$  events.

### 5.2.3 Electromagnetic and Hadronic Scale Setting

#### Electromagnetic scale setting

The electromagnetic scale in the ECal,  $\beta_{ECal}^{EM}$ , is determined using  $\gamma$  events at  $E_{MC} = 10$  GeV.  $\gamma$  events are ideal for setting the electromagnetic scale as they produce electromagnetic showers that are primarily confined to the ECal, which is shown by figure 5.1a. To ensure that the events used for this part of the calibration are largely confined to the ECal, a cut requiring less than 1% of the reconstructed energy to be found outside the ECal is applied. Furthermore, a cut requiring a single  $\gamma$  be reconstructed are added to veto events with pattern recognition failures.  $\gamma$  conversions are excluded at MC level to ensure energy measurements used in the calibration arise from the calorimeters and not the charged particle tracks. The impact of these cuts on the electromagnetic energy measured in the ECal for 10 GeV  $\gamma$  events is shown in figure 5.8a. In figure 5.8a, the peak with zero electromagnetic energy in the ECal is due to events traveling down the beam pipe and events with  $\gamma$  conversions. In  $\gamma$  conversion events the reconstructed energy is taken from the  $e^\pm$  tracks, which means the electromagnetic energy in the ECal will register as zero. The tail of events with low electromagnetic energy in the ECal occurs primarily due pattern recognition failures in  $\gamma$  conversion events. In such cases, some of the calorimetric energy deposits are not associated to the  $e^\pm$  tracks and instead form new  $\gamma$ s that contain only a small fraction of the true MC energy.

The fitting procedure follows that used for the ECal digitisation, described in section 5.2.1, whereby a trial calibration for the electromagnetic energy scale in the ECal,  $\beta_{ECal}^{EM0}$ , is assumed and the single  $\gamma$  events simulated. The distribution of the electromagnetic energy in the ECal is created and a Gaussian fit applied to the range of data with the smallest root mean square containing at least 90 % of the data. The mean of this fit,  $E_{Fit}$ , is then used to scale  $\beta_{ECal}^{EM0}$  in the following way:

$$\beta_{ECal}^{EM0} \rightarrow \beta_{ECal}^{EM} = \beta_{ECal}^{EM0} \times \frac{E_{MC}}{E_{Fit}} . \quad (5.7)$$

An example distribution and fit used in the calibration of the nominal ILD detector model can be found in figure 5.8b. This procedure is repeated using the updated  $\beta_{ECal}^{EM}$  until  $E_{Fit}$  falls within a specified tolerance. The tolerance applied here was  $|E_{Fit} - E_{MC}| < E_{MC} \times 0.5\%$ . The binning for the fitted histogram is chosen such that the bin width is equal to the desired target tolerance on  $E_{Fit}$  e.g.  $E_{MC} \times 0.5\% = 0.05$  GeV.

This tolerance is tighter than was applied for the digitisation as it is these energies that are used in downstream analyses.

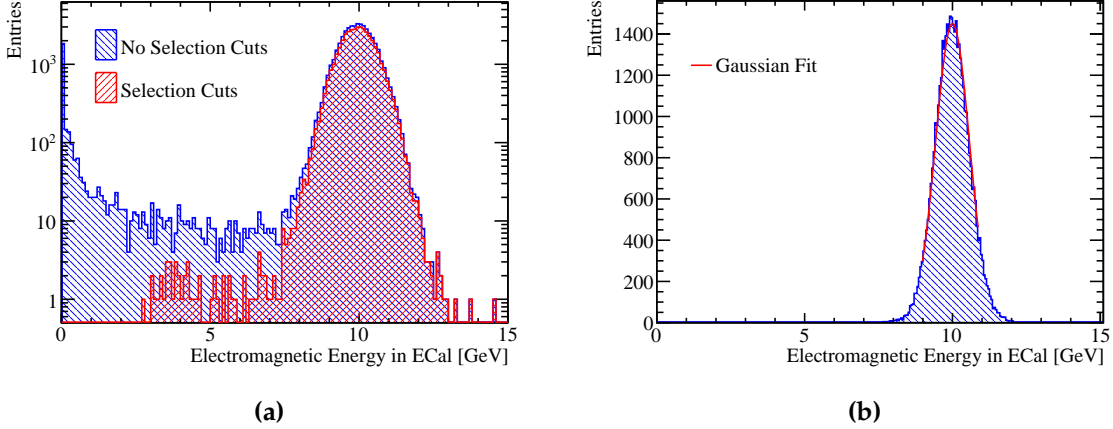


**Figure 5.8:** (a) The sum of the electromagnetic energy measured in the ECal for 10 GeV  $\gamma$  events with and without the selection cuts. (b) Gaussian fit to sum of the electromagnetic energy deposited in the ECal for 10 GeV  $\gamma$  events with selection cuts. The fine binning reflects the tolerance on the electromagnetic scale calibration constant in the ECal.

The electromagnetic scale in the HCal,  $\beta_{HCal}^{EM}$ , is chosen to be equal to the hadronic scale in the HCal,  $\beta_{HCal}^{Had}$ . The details of the determination of  $\beta_{HCal}^{Had}$  can be found in section 5.2.3. For the ILC and CLIC,  $\beta_{HCal}^{EM}$  is not a critical parameter in the reconstruction as  $\gamma$ s are largely contained within the ECal meaning little to no electromagnetic energy is measured in the HCal.

### Hadronic scale setting

The hadronic energy scale factors for the ECal and HCal,  $\beta_{ECal}^{Had}$  and  $\beta_{HCal}^{Had}$ , are determined using  $K_L^0$  events at  $E_{MC} = 20$  GeV. The hadronic scale in the ECal,  $\beta_{ECal}^{Had}$ , is important to detector performance as a non-negligible amount of hadronic energy will be measured in the ECal. As the ECal contains  $\approx 1\lambda_I$ , the hadronic scale in the ECal cannot be independently set as it is unfeasible to create a large sample of 20 GeV  $K_L^0$  events that are fully contained within it. Therefore, the hadronic scale in the ECal and HCal have to be set simultaneously.

For the reasons outlined in section 5.2.1, the target reconstructed energy for this sample is the kinetic energy,  $E_K$ , of the  $K_L^0$  as opposed to the total energy. To ensure

the events used are not affected by leakage of energy out of the back of the HCal, a cut is applied that vetoes events where energy is deposited in the outermost 10% of the HCal. In addition to this, a cut requiring a single neutral hadron to be reconstructed is applied to veto events with reconstruction failures. Finally, it is required that the total hadronic energy measured within the calorimeters fall within three  $\sigma$  of the kinetic energy of the  $K_L^0$ , where  $\sigma$  is defined to be  $55\% \times \sqrt{E_K}$  GeV. This definition for  $\sigma$  is approximately the energy resolution for neutral hadrons using the nominal ILD HCal [26]. This cut ensures that when fitting the two dimensional distribution of hadronic energy measured in the ECal and HCal outliers do not skew the fit. The impact of cuts is illustrated in figure 5.9.

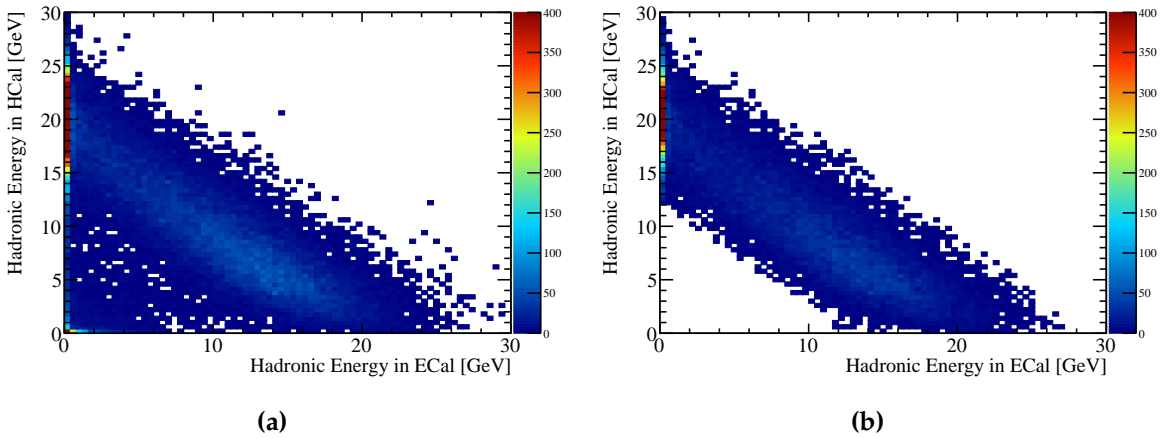


**Figure 5.9:** The distribution of hadronic energy measured in the ECal and HCal for 20 GeV  $K_L^0$  events (a) without selection cuts and (b) with selection cuts.

This part of the calibration procedure is again iterative and begins by assuming trial values,  $\beta_{ECal}^{Had0}$  and  $\beta_{HCal}^{Had0}$ , for the hadronic scale calibration factors  $\beta_{ECal}^{Had}$  and  $\beta_{HCal}^{Had}$ . Following this the 20 GeV  $K_L^0$  events are simulated and reconstructed using these scale factors. Then a linear fit is applied to the two dimensional distribution of the reconstructed hadronic energies measured in the ECal and HCal for events passing the selection cuts. The best fit is obtained by minimising  $\chi^2$  with respect to variables describing a linear fit to the distribution. In this case,  $\chi^2$  is defined as:

$$\chi^2(\delta_{ECal}^{Had}, \delta_{HCal}^{Had}) = \sum_i \frac{r_i}{\sigma_{r_i}}, \quad (5.8)$$

where  $r_i$  is the perpendicular distance in the two dimensional plane of hadronic energies measured in the ECal and HCal from the point  $(x_i, y_i)$  to a straight line

passing through the points  $(\delta_{E\text{Cal}}^{\text{Had}}, 0)$  and  $(0, \delta_{H\text{Cal}}^{\text{Had}})$ . In this definition,  $x_i$  and  $y_i$  are the hadronic energies measured in the ECal and HCal respectively for event  $i$ . The variables  $\delta_{E\text{Cal}}^{\text{Had}}$  and  $\delta_{H\text{Cal}}^{\text{Had}}$  describe a linear fit to the hadronic energy distribution, which are to be varied when minimising  $\chi^2$ . The explicit definition of  $r_i$  is given in equation 5.9, however it is best illustrated by considering figure 5.10. The uncertainty on  $r_i$  is given by  $\sigma_{r_i}$ , which is explicitly defined in equation 5.10. This uncertainty is calculated by propagating the uncertainties on  $x_i$  and  $y_i$ , which are assumed to be  $\sigma_{x_i/y_i} = 55\% \times \sqrt{x_i/y_i}$ , into the expression for  $r_i$ . The sum runs over all events,  $i$ , passing the selection cuts.

$$r_i = \frac{y_i \delta_{E\text{Cal}}^{\text{Had}} + x_i \delta_{H\text{Cal}}^{\text{Had}} - \delta_{E\text{Cal}}^{\text{Had}} \delta_{H\text{Cal}}^{\text{Had}}}{\sqrt{(\delta_{E\text{Cal}}^{\text{Had}})^2 + (\delta_{H\text{Cal}}^{\text{Had}})^2}}, \quad (5.9)$$

$$\sigma_i = \frac{(\sigma_{y_i} \delta_{E\text{Cal}}^{\text{Had}})^2 + (\sigma_{x_i} \delta_{H\text{Cal}}^{\text{Had}})^2}{\sqrt{(\delta_{E\text{Cal}}^{\text{Had}})^2 + (\delta_{H\text{Cal}}^{\text{Had}})^2}}, \quad (5.10)$$

The minimisation of  $\chi^2$  is done by stepping over a range of  $\delta_{E\text{Cal}}^{\text{Had}}$  and  $\delta_{H\text{Cal}}^{\text{Had}}$  centred

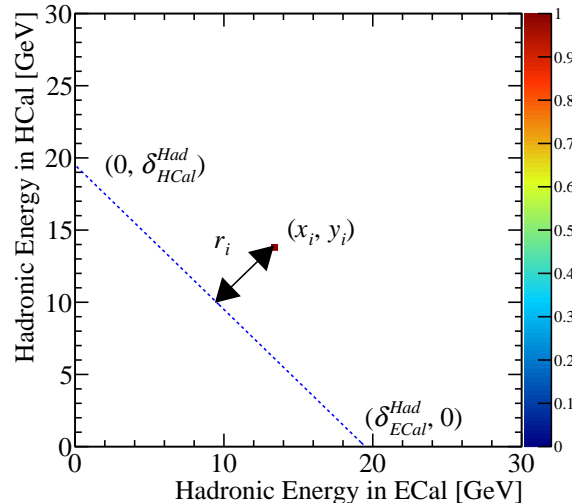


**Figure 5.10:** An example showing the definition of  $r_i$ , the variable used for the calculation of  $\chi^2(\delta_{E\text{Cal}}^{\text{Had}}, \delta_{H\text{Cal}}^{\text{Had}})$  in determining the hadronic energy scale factors. For an event that has been measured with hadronic energy  $x_i$  in the ECal and  $y_i$  in the HCal, the geometric interpretation of  $r_i$  is shown. The blue dotted line is defined as  $y_i = \delta_{H\text{Cal}}^{\text{Had}} - x_i \frac{\delta_{H\text{Cal}}^{\text{Had}}}{\delta_{E\text{Cal}}^{\text{Had}}}$ .

about the ideal value of  $E_K$  in search for the minimum  $\chi^2$ . Once the minima in  $\chi^2$  is found the trial calibration factors  $\beta_{E\text{Cal}}^{\text{Had}0}$  and  $\beta_{H\text{Cal}}^{\text{Had}0}$  are rescaled to correct for any deviation from the desired fit as follows:

$$\beta_{E\text{Cal}}^{\text{Had}0} \rightarrow \beta_{E\text{Cal}}^{\text{Had}} = \beta_{E\text{Cal}}^{\text{Had}0} \times \frac{E_K}{\Delta_{E\text{Cal}}^{\text{Had}}}, \quad (5.11)$$

$$\beta_{H\text{Cal}}^{\text{Had}0} \rightarrow \beta_{H\text{Cal}}^{\text{Had}} = \beta_{H\text{Cal}}^{\text{Had}0} \times \frac{E_K}{\Delta_{H\text{Cal}}^{\text{Had}}}, \quad (5.12)$$

where  $\Delta_{E\text{Cal}}^{\text{Had}}$  and  $\Delta_{H\text{Cal}}^{\text{Had}}$  are the values of  $\delta_{E\text{Cal}}^{\text{Had}}$  and  $\delta_{H\text{Cal}}^{\text{Had}}$  giving the minimum  $\chi^2$ . The step size used for minimising  $\chi^2$  with respect to  $\delta_{E\text{Cal}}^{\text{Had}}$  and  $\delta_{H\text{Cal}}^{\text{Had}}$  was chosen such that a single step would correspond to the final tolerance on  $\delta^{\text{Had}}$ , which in this case is  $\approx 0.1$  GeV. This procedure is then repeated using the updated hadronic scaling factors until  $\Delta_{E\text{Cal}}^{\text{Had}}$  and  $\Delta_{H\text{Cal}}^{\text{Had}}$  both fall within a specified final tolerance, which in this case it taken to be  $|\Delta_{E/H\text{Cal}}^{\text{Had}} - E_K| < E_K \times 0.5\% \approx 0.1$  GeV.

### 5.3 Novel Energy Estimators

This section describes the novel energy estimators that were introduced in section 5.1 with a view to improving the energy resolution for hadronic showers. Two techniques will be discussed; HCal hit energy truncation, which focuses on limiting the impact of Landau fluctuations, and software compensation, which focuses on achieving a compensating response from the calorimeters used in the simulation. Both of these techniques are implemented by introducing weights,  $\omega$ , to calorimetric energy deposits found in the HCal:

$$E_{\text{Cluster}} = \sum_{E\text{Cal hits}, i} E_{E\text{Cal}}^i + \sum_{H\text{Cal hits}, i} E_{H\text{Cal}}^i \omega^i(\rho^i). \quad (5.13)$$

Weights are only applied to calorimeter hits in the HCal as both techniques attempt to modify the energy of hadronic showers, which are primarily contained within the HCal. The weights,  $\omega^i$ , vary a function of the calorimeter hit energy density,  $\rho^i = \frac{E_{H\text{Cal}}^i}{V}$ , where  $V$  is the HCal hit volume. While the exact weight values depend on the implementation of the technique, a general feature present in both is that at large  $E_{H\text{Cal}}^i$  the weight is less than one. This limits the impact of spuriously high energy hits caused by Landau fluctuations that would otherwise harm detector performance. The

metrics used for quantifying detector performance when using these novel energy estimators are thoroughly defined in chapter 6.

### 5.3.1 HCal Hit Energy Truncation

#### Application

The first technique to be examined is a simple truncation of the hadronic energy recorded in any given HCal hit. This improves the energy estimators for hadronic clusters by limiting the impact of Landau fluctuations. In terms of  $\omega$  introduced in equation 5.13 the truncation corresponds to:

$$\omega(\rho) = \begin{cases} 1 & \text{if } \rho \times V < \kappa, \\ \frac{\kappa}{\rho \times V} & \text{otherwise,} \end{cases} \quad (5.14)$$

where  $\kappa$  is the value of the truncation and  $V$  is the volume of a HCal hit. This weight as a function of hit energy density is shown in figure 5.11.

#### Results: Energy Resolution

The application of these weights leads to an improvement in the energy resolution for neutral hadrons, which can be seen in figure 5.12a. However, a great deal of care has to be given to the truncation energy so that hits from typical hadronic shower development are not truncated, while the spuriously high energy hits are. Figure 5.12a indicates that a 1 GeV truncation is sufficient for dealing with the Landau fluctuations. For hit energy truncations greater than this, the energy resolution worsens as the effect Landau fluctuations are not accounted for. For hit energy truncations below 1 GeV, the truncation is too aggressive and hits from typical hadronic shower development are truncated. For completion the  $\gamma$  energy resolutions as a function of HCal hit energy truncation are shown in figure 5.12b. As expected the  $\gamma$  energy resolution is invariant to the HCal hit energy truncation as the  $\gamma$ s are largely contained within the ECal.

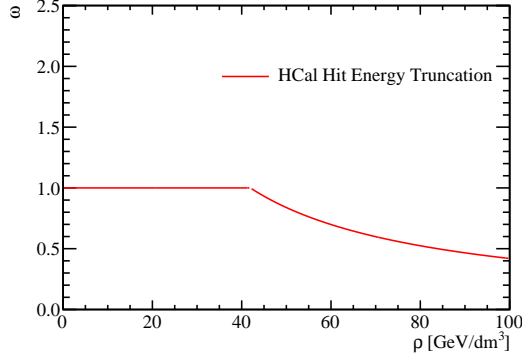


**Figure 5.11:** The weights,  $\omega$ , used in the HCal hit energy truncation as a function of the energy density of the HCal hit,  $\rho$ . The truncation shown here corresponds to a 1 GeV truncation in the nominal ILD HCal.

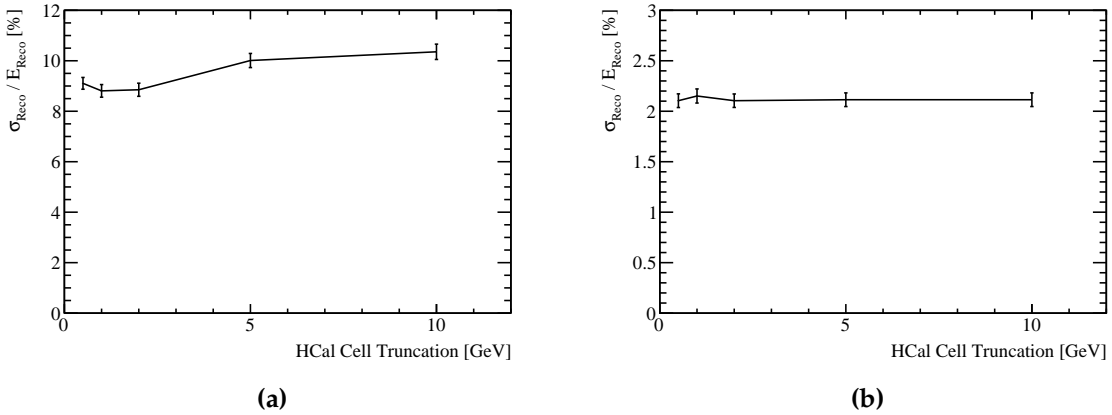


**Figure 5.12:** The energy resolution as a function of HCal cell truncation for (a) 50 GeV  $K^0_L$  events and (b) 100 GeV  $\gamma$  events using the nominal ILD detector model.

### Results: Jet Energy Resolution

There is an improvement in the jet energy resolution when applying a carefully chosen HCal hit energy truncation. Figure 5.13 shows the jet energy resolution as a function of jet energy for selected values of the HCal hit energy truncation. The trends in this plot are complex as the optimal cell truncation varies with the jet energy. At low energies a 0.5 GeV truncation gives the optimal performance, however, when the jet energies reach  $\approx 180$  GeV a 1 GeV truncation gives the optimal performance. This is to be expected based on the Landau fluctuations. The Landau distribution, governing the energy deposition for hadronic showers, is essentially a Gaussian with a high

energy tail and as the jet energy increases, the mean of the Gaussian increases and the definition of hit energies falling in the high energy tail changes.

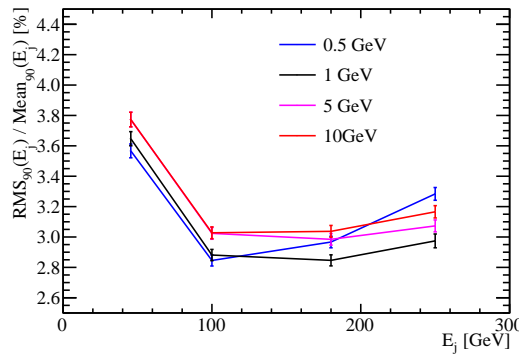


**Figure 5.13:** The jet energy resolution as a function of jet energy for various hadronic cell truncations. The results shown use the nominal ILD detector model.

While it is challenging to determine the optimal truncation to use for any given detector model, it is clear that applying an appropriate truncation produces significant improvement in detector performance. Therefore, for the optimisation studies presented in chapter 6 this form of novel energy estimator is applied. The optimal truncation for each detector model considered in that study was determined by performing the reconstruction using range of HCal hit energy truncations and quoting the optimal performance. The HCal hit energy truncations considered in the optimisation study were 0.5, 0.75, 1, 1.5, 2, 5 and 10 GeV. For the HCal cell size study the truncation used for the 10, 20, 30, 40, 50 and 100 mm cell size detector was 0.5, 0.75, 1, 1.5, 2 and 5 GeV respectively, for the tungsten HCal options the truncation used was 5 GeV and for all other options the truncation used was 1 GeV. This optimisation has a significant impact on detector optimisation, which can be seen by comparing the jet energy resolutions obtained when using the optimised cell truncation and a fixed 1 GeV truncation, shown in figure 5.14. Without this optimisation of hit energy truncation the significance of the HCal cell size is overinflated and could lead to a misinformed detector design choice.

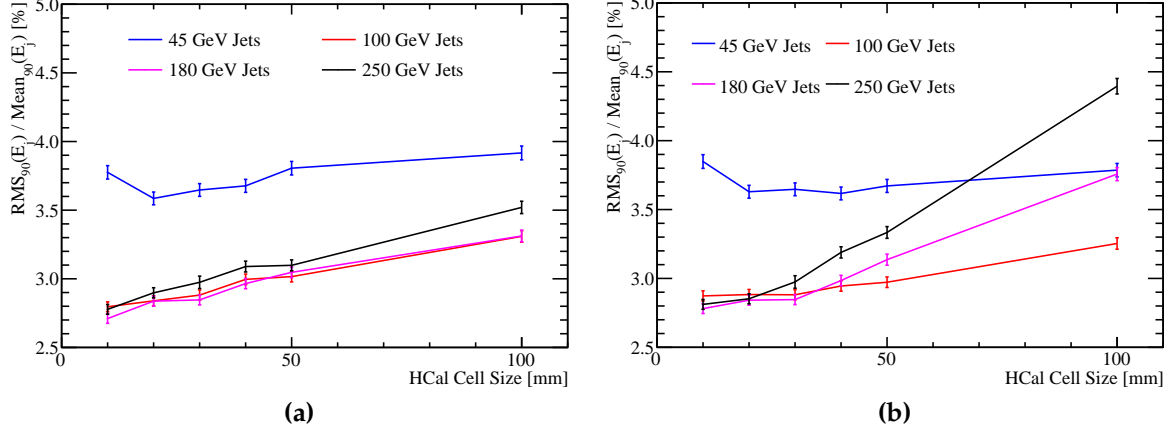


**Figure 5.14:** The jet energy resolution as a function of HCal cell size using a HCal hit energy truncation that is (a) optimised and (b) fixed at 1 GeV.

### 5.3.2 Software Compensation

#### Application

A particle shower produced when a hadron passing through a calorimeter has two components [54]; an electromagnetic shower core, which originates from the production and decay of  $\pi^0$ s and  $\eta$ s, and a hadronic shower component originating from all other interacting and decaying particles in the shower. By identifying each of these components in the reconstruction, it is possible to increase the energy of the hadronic hits to give a compensating response and decrease the energy of spuriously high energy hits that come from Landau fluctuations. The challenge of applying this approach is to identify whether a hit is likely to be hadronic or electromagnetic in nature. This is done based on the energy density of a hit, with high energy densities likely to be part of the electromagnetic core and low energy densities likely to be part of satellite hadronic hits around the shower core. An event display showing the energy density of a hadronic shower, where the electromagnetic core can be clearly seen, in a 500 GeV  $Z \rightarrow \text{uds}$  di-jet event can be found in figure 5.15.

An additional layer of sophistication in this approach is the weights that are applied vary as a function of the uncompensated cluster energy,  $E_{\text{Raw}}$ , as well as the hit energy density,  $\rho^i$ . This is to account for any changes to the distribution of calorimeter hit energy densities as the total shower energy is varied. For example, the fraction of hits in a hadronic shower that are electromagnetic in nature increases as the total

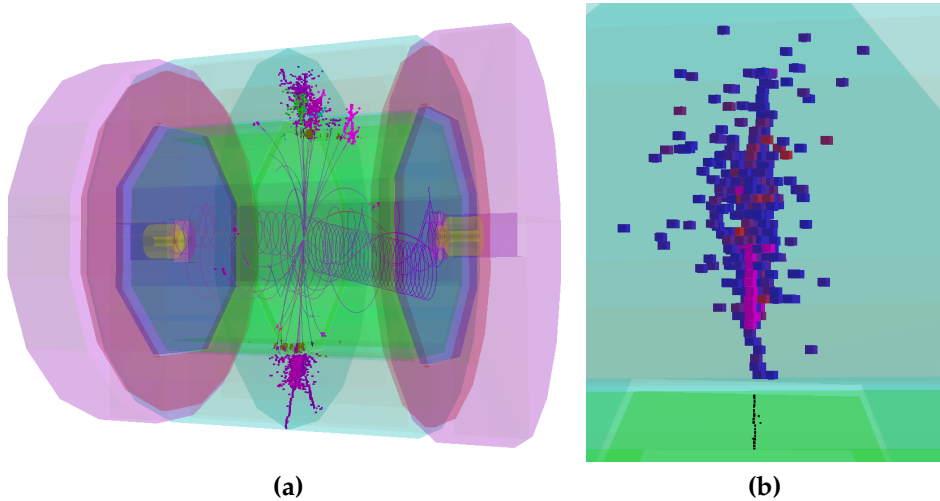


**Figure 5.15:** An event display for a 500 GeV  $Z \rightarrow \text{uds}$  di-jet event reconstructed using the nominal ILD detector. (a) The full event environment. (b) A single hadronic cluster from the same event where shading indicates the energy density in the HCal. High energy density cells are coloured red, while lower energy density cells are coloured blue. All ECal hits are shaded black. The high energy density electromagnetic core of the selected hadronic cluster is clearly visible.

energy of the hadronic shower increases [54]. Therefore, as the total shower energy increases a smaller fraction of hits will require weights greater than one as there are less fully hadronic hits in the shower than at low energies. The highly segmented calorimeters used at the linear collider experiment will give excellent spatial resolution for individual particle showers, which enables precise mapping of the calorimeter hits to different shower components. This allows the linear collider to employ this software compensation technique with greater effectiveness than was possible for previous collider experiments.

In terms of the parameterisation introduced in equation 5.13, the weights used for this technique are [47]:

$$\omega(E_{\text{Raw}}, \rho) = p_1(E_{\text{Raw}}) \times \exp(p_2(E_{\text{Raw}}) \times \rho) + p_3(E_{\text{Raw}}) \quad (5.15)$$

$$p_1 = p_{11} + p_{12} \times E_{\text{Raw}} + p_{13} \times E_{\text{Raw}}^2 \quad (5.16)$$

$$p_2 = p_{21} + p_{22} \times E_{\text{Raw}} + p_{23} \times E_{\text{Raw}}^2 \quad (5.17)$$

$$p_3 = \frac{p_{31}}{p_{32} + \exp(p_{33} \times E_{\text{Raw}})}, \quad (5.18)$$

where  $p_{ij}$  are trained parameters and:

$$E_{Raw} = \sum_{ECal\ hits,\ i} E_{ECal}^i + \sum_{HCal\ hits,\ i} E_{HCal}^i. \quad (5.19)$$

The parameters  $p_{ij}$  are determined by performing a  $\chi^2$  fit of the software compensated cluster energy to the MC energy for samples of  $K_L^0$  ranging from 10 to 100 GeV in steps of 10 GeV. Using the fitted parameters obtained for the nominal ILD detector,  $p_1$ ,  $p_2$  and  $p_3$  as a function of  $E_{Raw}$  is shown in figure 5.16 and  $\omega(E_{Raw}, \rho)$  as a function of  $\rho$  for selected values of  $E_{Raw}$  is shown in figure 5.17. Figure 5.17 shows that the high energy density hits are being reduced in energy to compensate for the effects of Landau fluctuations, while the low energy density hits are being increased in weight to compensate for the invisible energy component found in hadronic showers. Furthermore, the weights vary as a function of the raw hadronic shower energy to account for the changing energy density topology of hadronic showers with increasing shower energy.

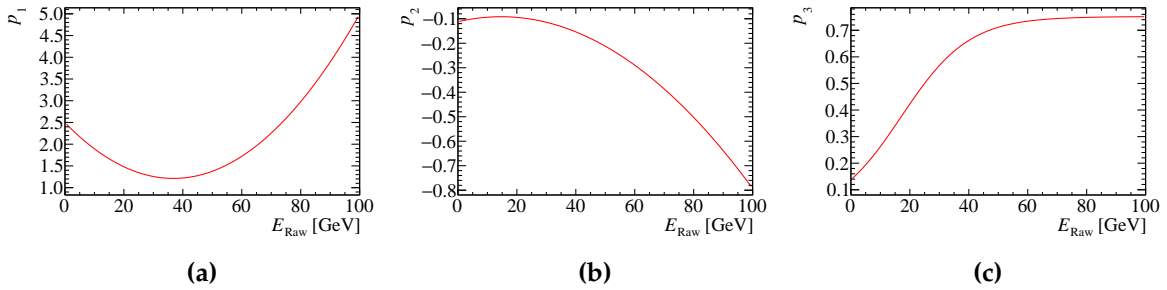


**Figure 5.16:** Parameters used in software compensation weight determination as a function of  $E_{Raw}$ .

This technique is applied in the PandoraPFA framework in the form of an energy correction function, which means whenever the energy of a cluster of hits is considered by PandoraPFA the software compensated energy is used. Applying software compensation in this way benefits the detector energy resolution in two ways; firstly, the intrinsic energy resolution of the detector improves and secondly, the confusion contribution to the energy resolution is reduced.

As software compensation only modifies the energy of HCal hits there is freedom to apply further energy corrections to the ECal hits. Applying the Clean Clusters logic, described in section 5.3.2, to the ECal hits alongside software compensation was found to be beneficial to the jet energy resolution. Therefore, the application of software

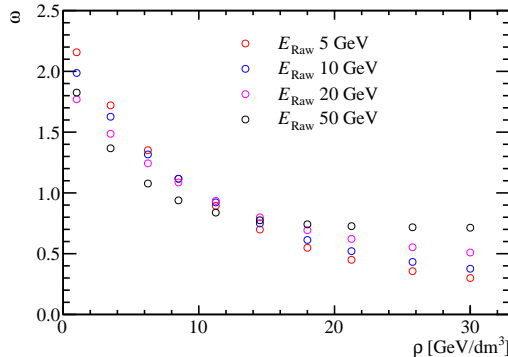


**Figure 5.17:** The software compensation weight applied to a calorimeter hit as a function of calorimeter hit energy density for various cluster energies.

compensation within PandoraPFA implicitly involves the application of the Clean Clusters logic to the ECal hits.

Software compensation was trained using a maximum  $K_L^0$  energy of 100 GeV, therefore, it is only applied to clusters where  $E_{\text{Raw}} < 100$  GeV as sensible behaviour outside this range cannot be ensured. While it would be possible to modify the energy range of the training sample to go to higher energies, hadronic clusters with energy greater than 100 GeV will be rare at the ILC like energies considered here.

### Context: Legacy Energy Corrections

Before examining the impact of software compensation on detector performance is it necessary to address the 'legacy' energy corrections that are used by default in PandoraPFA. The three energy correction that were in use prior to the development of software compensation are:

- **HCal hit energy truncation**, the details of which can be found in section 5.3.1.
- **Clean Clusters.** This algorithm checks to see whether the energy measured within a calorimeter hit is anomalously high. Anomalously high energy hits are defined as hits where the energy contained within the hit is greater than 10% of the energy of the cluster that the hit has been associated to. If a hit is deemed to have an anomalously high energy and if this energy is above a threshold (0.5 GeV) the hit energy used by PandoraPFA is modified. The updated hit energy is taken

as the average hit energy in the calorimeter layers immediately before and after the layer containing the high energy hit.

- **Scale Hot Hadrons.** This algorithm calculates the average number of MIP equivalent particles passing through each calorimeter hit in a cluster. If this number is larger than a given value, default 15 MIPs per hit, the cluster energy is rescaled to give a lower average number of MIPs per hit, default is 5 MIPs per hit.

Each of these energy corrections help to deal with the effects of spuriously high energy hits the origin of which is described in section 5.3.1. However, the algorithms are simplistic and software compensation is expected to give far better results than these ‘legacy’ options. The optimisation studies presented in section 6 use all three of these legacy options simultaneously, which was the default behaviour for PandoraPFA when the studies were undertaken. The new default behaviour in PandoraPFA is to use software compensation.

## Results: Energy Resolution

The energy resolution as a function of the MC energy for single  $K_L^0$  events is shown in figure 5.18 using various energy correction settings. When comparing the energy resolution given by software compensation to that obtained using no energy corrections, it can be seen that software compensation offers a gain of  $\approx 2\%$  in energy resolution across the energy range considered. The uniformity of this improvement is encouraging, indicating software compensation is achieving a compensating calorimeter response across this wide range of energies.

Comparing the performance of software compensation to the legacy corrections it can be seen that software compensation gives a better energy resolution across almost the entire range of energies considered. The only exception to this is around  $E_{K_L^0} \approx 50$  GeV where the performance of software compensation and the legacy corrections are comparable. By removing the hit truncation from the legacy options it is clear that the changes in energy resolution when using the legacy options are being driven by the hit truncation. This makes the trend in energy resolution observed using the legacy corrections clear as, at low  $K_L^0$  energies, very few hits are affected by the truncation so the performance is comparable to not using any energy corrections. At high  $K_L^0$  energies, the truncation is too aggressive and removes energy from hits that are not spuriously high leading to a worsening energy resolution. Between these two

extremes,  $E_{K_L^0} \approx 50$  GeV, the truncation works ideally and the improvement in energy resolution when using the legacy corrections is the largest.

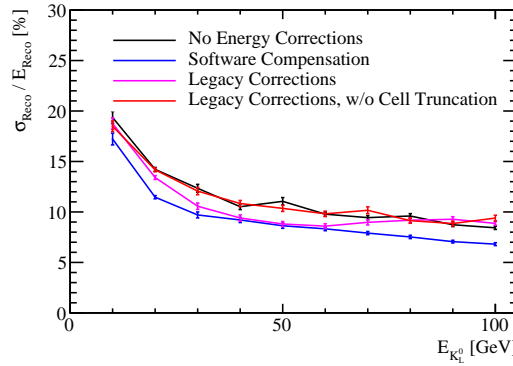


**Figure 5.18:** The energy resolution as a function of the MC energy for single  $K_L^0$  events using various energy correction settings. The detector model used was the nominal ILD detector model.

## Results: Jet Energy Resolution

The improvements in the intrinsic energy resolution of the detector observed when using software compensation will propagate into the reconstruction of jets. These effects are illustrated by examining the jet energy resolution as a function of jet energy, which is shown in figure 5.19. Again it is clear that software compensation is extremely beneficial to the detector performance as it gives a significant reduction in the jet energy resolution in comparison to using the legacy energy corrections.

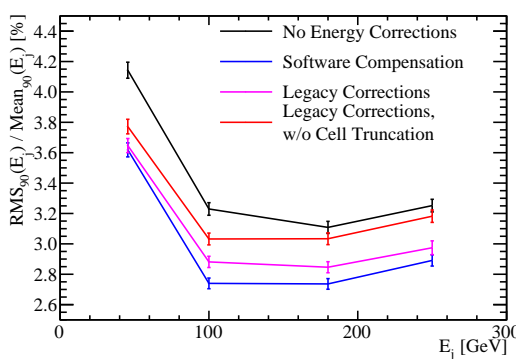


**Figure 5.19:** The jet energy resolution as a function of the jet energy for a variety of different energy correction options. These results were produced for the nominal ILD detector model.

Further light can be shed on these trends by examining the contributions to the jet energy resolutions from the intrinsic energy resolution and the pattern recognition confusion, which are shown in figure 5.20. The intrinsic energy resolution contribution shows that software compensation is significantly better than all other energy corrections options, which is to be expected from the energy resolution studies presented in section 5.3.2. Unlike the single particle study there is no jet energy for which the hit truncation matches the performance obtained using software compensation. This is due to the fact that the energy resolution when using the hit truncation is only comparable to the energy resolution using software compensation for a narrow range of hadronic cluster energies. As the jet contains a broad spectrum of hadronic cluster energies the performance obtained when using the hit truncation will always be worse than when using software compensation. When comparing the jet energy resolution for the legacy corrections is again apparent that the term driving the jet energy resolution is the hit truncation.

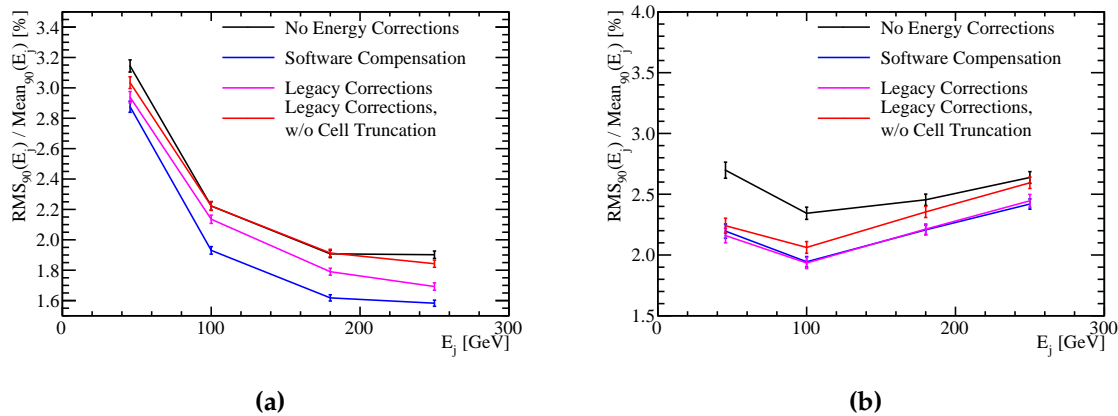


**Figure 5.20:** The contributions to the jet energy resolution as a function of the jet energy for a variety of different energy correction options. (a) is the intrinsic energy resolution of the detector and (b) is the total confusion term. The quadrature sum of both yields the standard reconstruction performance. These results were produced for the nominal ILD detector model.

The confusion contributions to the jet energy resolution when using software compensation and the legacy corrections are almost identical. This indicates that the improvement seen in the jet energy resolution when comparing software compensation and the legacy corrections, shown in figure 5.19, is being driven by the intrinsic energy resolution. The hit truncation and software compensation techniques both improve

the energy resolution of the hadronic clusters, however, software compensation is far more effective.

At low jet energies the Clean Clusters and Scale Hot Hadrons energy corrections are beneficial for reducing the confusion contribution, while the hit truncation is largely redundant. For high jet energies jets this trend is reversed. As the Clean Clusters and Scale Hot Hadrons energy corrections do not alter the intrinsic energy resolution of the detector, it is clear that they are compensating for failures in the pattern recognition, which occur primarily at low jet energies. By extracting the Clean Clusters logic, which is the driving term reducing the confusion contribution to the jet energy resolution at low jet energies, and embedding it within the software compensation energy correction, it is possible to obtain exceptional jet energy resolutions that will extend the physics reach of the linear collider detector.

## 5.4 Timing Cuts

The linear collider will operate using a trigger-less readout approach whereby the recorded data for each sub-detector is readout between collisions of  $e^+$  and  $e^-$  bunches. The train structure for ILC and CLIC, at their maximum operating energy, is shown in table 5.1. Event selection will proceed through the application of a software trigger. This involves the identification of any hard interactions, prior to full event reconstruction, and only putting data into the event reconstruction if it is measured within a chosen time window about these interactions. The recorded time of a calorimeter hit, which is cut on to make the time window for the software trigger, is corrected for straight time-of-flight to the IP. This ensures that the amount of time particle showers have to develop in the calorimeters is independent of their position in the detector. As the width of this time window changes, the amount of time particle showers have to develop changes, which will affect the performance of the detector.

For all choices of time window considered in this study the calibration procedure described in section 5.2 was applied. This ensure that the mean of the reconstructed energy distributions will be invariant to changes in the calorimeter timing window as the calibration procedure compensates for any energy losses incurred by truncating the particle shower development time.

	ILC 500 GeV	CLIC 3 TeV
Electrons per bunch [ $10^{10}$ ]	2.0	0.37
Bunches per train	2820	312
Train repetition rate [Hz]	5	50
Bunch separation [ns]	308	0.5

**Table 5.1:** The train structure for 500 GeV ILC and 3 TeV CLIC [4, 26].

### Results: Energy Resolution

The energy resolution for 100 GeV  $\gamma$  and 50 GeV  $K_L^0$  events as a function of the timing window applied to the calorimeter hits is shown, for the nominal ILD detector, in figure 5.21. The timing cut makes little difference to the energy resolution of the  $\gamma$  events, however, there is a significant decrease in the energy resolution for the neutral hadrons. This is to be expected as electromagnetic showers develop far more rapidly than their hadronic counterparts [54], which is shown in figure 5.22. Hadronic showers develop slowly as they often involve intermediate states that must decay to continue the propagation of the shower and as these states have non-zero lifetimes they slow the propagation of the shower. If a narrow calorimeter timing window is used, energy measurements from the hadronic shower will be lost and the energy resolution will degrade, which is what is observed.

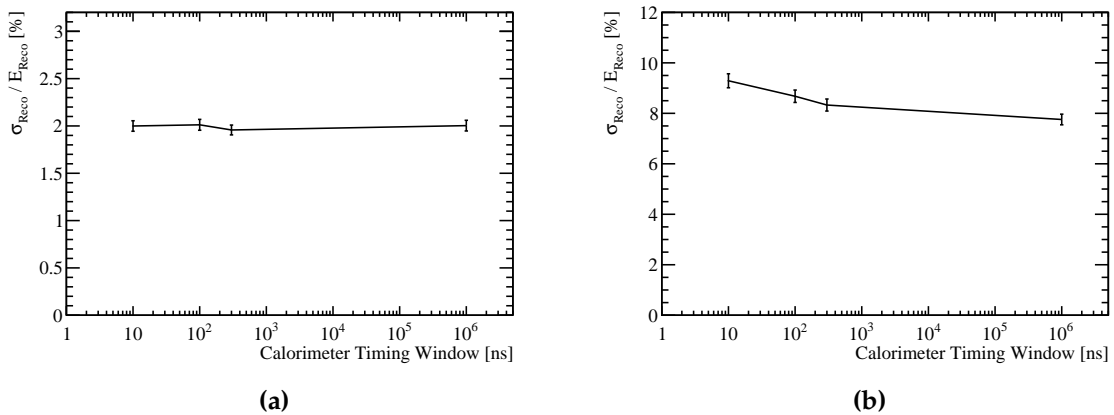


**Figure 5.21:** The energy resolution as a function of calorimeter timing window for (a) 100 GeV  $\gamma$  events and (b) 50 GeV  $K_L^0$  events using the nominal ILD detector model.

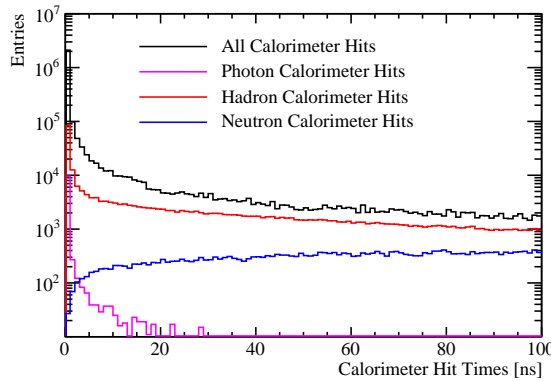


**Figure 5.22:** The distribution of the time of the calorimeter hits, corrected for time of flight to the impact point, for 91 GeV  $Z \rightarrow u\bar{d}s$  di-jet events.

### Results: Jet Energy Resolution

The jet energy resolution as a function of the jet energy for selected calorimeter time windows is shown in figure 5.23. As expected, the jet energy resolution will also be affected by the reduced neutral hadron energy resolution when the calorimeter timing window is reduced. The sole exception to this is the 250 GeV jets for the 100 ns time window whereby the jet energy resolution is slightly better than when using the 300 ns and semi-infinite time windows. As the magnitude of the changes to the jet energy resolution when varying the time window size are small in comparison to the absolute resolutions, this exception will most likely be due to a fluctuation in either the event sample used or in the application of the calibration procedure.

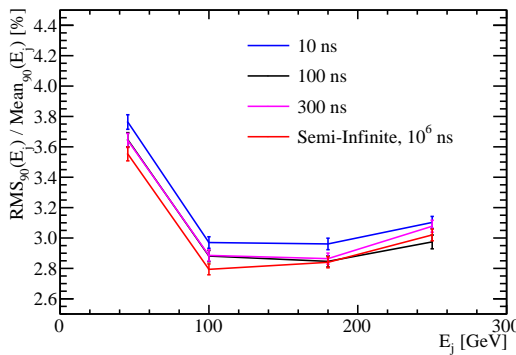


**Figure 5.23:** The jet energy resolution as a function of jet energy for various calorimeter timing cuts. The nominal ILD detector model was used for this study.

The time window applied to the calorimeter hits affects both the neutral hadron and jet energy resolutions with a larger timing window leading to better resolutions. It can be seen that applying an aggressive choice of time window, such as 10 ns, the jet energy resolution is degraded as many of the hadronic showers being sampled do not have time to fully develop. However, even using a 10 ns timing cut the jet energy resolutions are still sufficiently low to give excellent detector performance. Both the single particle and jet energy resolutions indicate that the majority of hadronic showers will have fully developed within 100 ns and that there are little gains to be made by extending the size of this window.

For results presented in this chapter and the optimisation studies found in chapter 6 a 100 ns timing window was applied across all models considered. As the choice of timing window has yet to be finalised for the linear collider this value was chosen as it represents something that could be achieved using the readout technology options presently available [57]. Furthermore, it adds additional realism to the detector simulation in comparison to omitting the effect of the calorimeter time window. The categorisation of changes to the detector performance when varying the calorimeter timing window presented here can be used to discern the impact of changing the timing window used for the optimisation studies at a later date if so desired.

# Chapter 6

## Calorimeter Optimisation Studies

*“The simple believes everything, but the prudent gives thought to his steps.”*

— Proverbs 14:15

### 6.1 Introduction

This chapter considered optimisation of the calorimeters used at the linear collider, with focus placed on obtaining the best energy resolution for jets. Parameters such as the number of layers, cell size and material choices for the calorimeters are investigated. This chapter concludes with an optimisation of several global detector parameters such as the magnetic field strength and the inner radius of the ECal. These parameters are not calorimeter specific, but affect the jet energy resolution obtained from particle flow.

The nominal detector model used in these optimisation studies is the ILD detector model, which is discussed in detail in section 3.2. A description of the metrics used to quantify detector performance in this chapter can be found in section 3.6. A summary of the performance of the nominal ILD detector model is given in section 3.7.

## 6.2 Electromagnetic Calorimeter Optimisation

The purpose of an electromagnetic calorimeter (ECal) is to measure the energy deposits from electromagnetic showers. The nominal ILD detector model ECal, summarised in table 6.1, is a silicon-tungsten sampling calorimeter. It contains 29 readout layers and 24 radiation lengths ( $X_0$ ), which is sufficient to contain all but the highest energy electromagnetic showers. The absorber thickness of the last nine layers is twice that of the first 20 layers to reduce the number of readout channels and cost of the calorimeter. This high sampling rate is crucial for the pattern recognition aspect of particle flow calorimetry, especially in the region where particle showers start developing, as shown in section 6.2.1.

Parameter	Default Value
Cell Size	$5 \times 5\text{mm}^2$ square cells
Number of Layers	29 readout layers
Active Material Choice	Silicon or Scintillator
Active Material Thickness	0.5 mm (Silicon) or 2 mm (Scintillator)
Absorber Material Choice	Tungsten
Absorber Material Thickness	20 layers of 2.1 mm followed by 9 layers of 4.2 mm

**Table 6.1:** The configuration of the ECal in the nominal ILD detector model. The parameters are given for the nominal silicon model as well as the alternative scintillator option.

The calorimeter performance was simulated for a number of detector models where the following detector parameters were varied:

- Cell size: This is a vital aspect of the detector in the particle flow paradigm as smaller cell sizes leads to better separation between nearby showering particles, which helps to minimise the effect of confusion. Modifying the cell size should have little effect on the intrinsic energy resolution of the detector.
- Sampling frequency: The sampling frequency in the ECal was varied by changing the number of layers in the ECal while simultaneously changing the thicknesses of the layers such that the total depth, in radiation lengths, was held constant. Increasing the number of layers in a sampling calorimeter means any particles showering within it are sampled more thoroughly. This leads to a reduction in the stochastic contribution to the energy resolution, as discussed in section 3.7.

Therefore, varying the number of layers is expected to change in intrinsic energy resolution of the calorimeter.

- Active material choice: The options under consideration for the active material choice are silicon or scintillator. As well as providing different intrinsic energy resolutions the readout mechanics of these two options are significantly different. There is no clear prior knowledge as to which should provide better performance.

### 6.2.1 ECal Cell Size

A number of different detector models were considered where the cell size in the ECal was varied about the nominal value of  $5 \times 5\text{mm}^2$  square cells. The granularities considered were  $3 \times 3\text{mm}^2$ ,  $5 \times 5\text{mm}^2$ ,  $7 \times 7\text{mm}^2$ ,  $10 \times 10\text{mm}^2$ ,  $15 \times 15\text{mm}^2$  and  $20 \times 20\text{mm}^2$  square cells for both the silicon and scintillator active material options.

The energy resolution, using 100 GeV  $\gamma$  events, as a function of the ECal cell size is shown in figure 6.2a for the silicon option and figure 6.2b for the scintillator option. As, at these energies, the  $\gamma$ s will be largely contained within the ECal, these results solely reflect the performance of the ECal. For both the silicon and scintillator ECal options the energy resolution does not depend strongly on the ECal cell size. This is to be expected as the number of layers, which is the main factor in determining the energy resolution of a sampling calorimeter, does not change when modifying the cell size. There are minor fluctuations in the energy resolution when varying the cell size, but these are mostly likely due to fluctuations in the energy response from calibration procedure applied to each detector models. For the scintillator ECal option there is a significant degradation in the energy resolution for the  $3 \times 3\text{mm}^2$  cell size model. The most likely cause of this is a "dead" region in the active material, which represents the readout multi pixel photon counter (MPPC) [27]. The MPPC occupies a fixed area of the cell, irrespective of cell size, and so the dead region of the cell fractionally increases as cell size is reduced. The larger this dead region, the worse the sampling of the electromagnetic showers in the ECal and the worse the resolution. While this effect will be present in all scintillator ECal options, it will only be significant for the small cell sizes when the dead region is fractionally the largest. This explains why degradation is seen only for the smallest cell size considered in the scintillator ECal option.

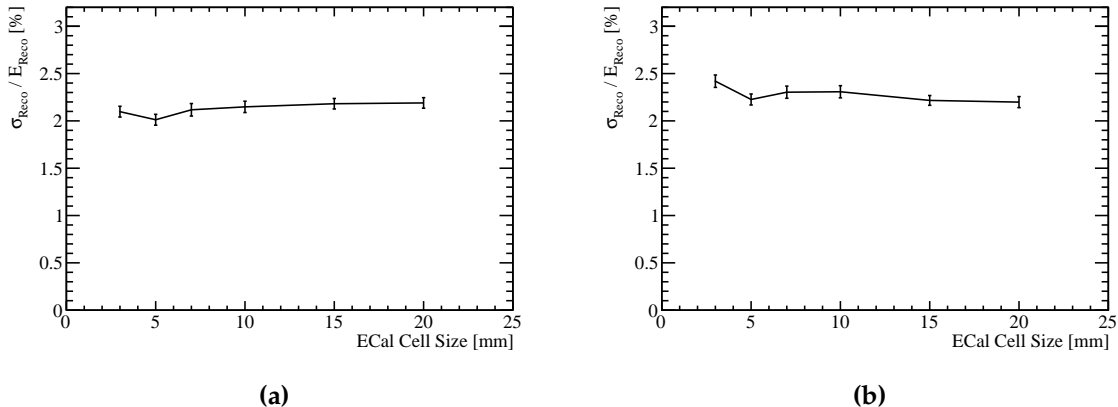


**Figure 6.1:** The energy resolution as a function of ECal cell size for 100 GeV  $\gamma s$  using the nominal ILD detector model with (a) the silicon and (b) the scintillator ECal option.

The separation of nearby particle showers within the calorimeter is fundamentally limited by the cell size. The smaller the cell size the easier it is to separate nearby particle showers and the better this separation the smaller the affect from confusion is. Therefore, it is expected that the jet energy resolution be sensitive to the ECal cell size even though the intrinsic energy resolution is not. The jet energy resolution as a function of ECal cell size is shown in figure 6.2a for the silicon option and figure 6.2b for the scintillator option. As expected there is a very strong dependancy on the ECal cell size, with smaller cell sizes leading to lower values of the jet energy resolution. The origin of this trend is best illustrated by considering the intrinsic energy resolution and confusion contributions to the jet energy resolution. These contributions are shown as a function of ECal cell size for 45 and 250 GeV jets, for both the silicon and scintillator ECal options, in figure 6.3. It is clear from these contributions that the intrinsic energy resolution of the detector does not change when varying the cell size, which agrees with both prior expectations of calorimeter behaviour and the single particle energy resolution study. The minor fluctuations seen in the energy resolution for the single particle study are washed out when considering the intrinsic energy resolution for jets, as only 30% of jet energy is carried in the form of  $\gamma s$ . Furthermore, it can be seen that the trend in jet energy resolution as a function of the ECal cell size is being driven purely by changes to the confusion contribution and, in particular, the confusion caused by the reconstruction of  $\gamma s$ . This is exactly what is to be expected given the ECal primarily measures  $\gamma s$  and shows that the performance of the ECal when varying the cell size is well understood.

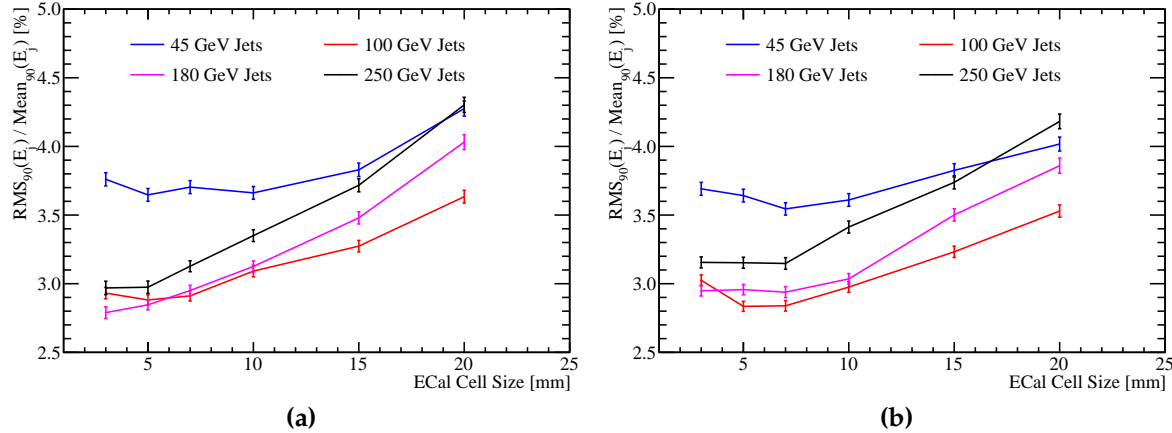


**Figure 6.2:** The jet energy resolution as a function of ECal cell size for various jet energies using the nominal ILD detector model with (a) the silicon and (b) the scintillator ECal option.

It is clear that the ECal cell size is extremely important for jet energy measurements, although it has little bearing on the intrinsic energy resolution of the ECal. To ensure separation of hadronic decays of W and Z bosons is possible at ILC like energies, an ECal cell size of least  $15 \times 15\text{ mm}^2$  is crucial. However, as reducing the ECal cell size beyond this leads to further improves the jet energy resolution choosing the smallest ECal cell size is desirable.

### 6.2.2 ECal Sampling Frequency

The detector performance was simulated where the number of layers in the ECal was varied, while keeping the total material budget ( $X_0$ ) approximately constant. This study was performed for both the silicon and scintillator active material options. In all cases tungsten was used for the ECal absorber material and the active layer thicknesses were not changed from those used in the nominal ILD ECal summarised in table 6.1. The different layouts for the ECals considered here are summarised in table 6.2.

The energy resolution, for 100 GeV  $\gamma$  events, as a function of the number of layers in the ECal is shown in figure 6.4a for the silicon option and in figure 6.4b for the scintillator option. As the number of layers is reduced the energy resolution increases, which is expected as more layers leads to greater sampling of the particle shower and a reduction in the stochastic contribution to the energy resolution.

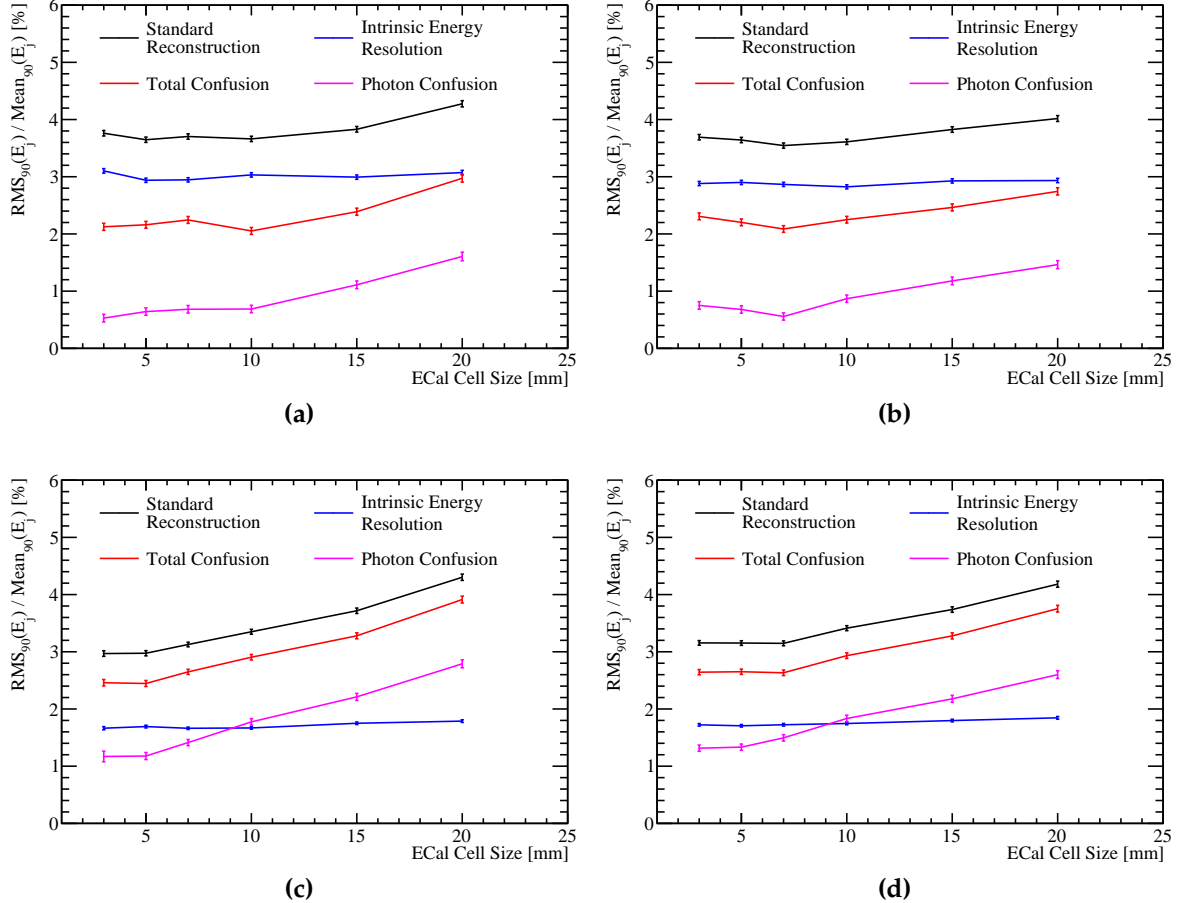


**Figure 6.3:** The contributions to the jet energy resolution as a function of ECal cell size using the nominal ILD detector model for (a) the silicon ECal option and 45 GeV jets, (b) the scintillator ECal option and 45 GeV jets, (c) the silicon ECal option and 250 GeV jets and (d) the scintillator ECal option and 250 GeV jets. The black curves correspond to the standard reconstruction, the blue curves to the intrinsic energy resolution contribution to the jet energy resolution, the red curves to the confusion contribution to the jet energy resolution and the magenta curves to the confusion contribution to the jet energy resolution related solely to  $\gamma$  reconstruction

When the number of layers in the ECal is increased, the intrinsic energy resolution of the ECal improves. This has the knock-on effect of reducing the confusion contribution to the jet energy resolution, which can be seen in figures 6.5a and 6.5b for the silicon and scintillator ECal options respectively. In both cases the jet energy resolution was found to improve when the number of layers in the ECal was increased. The magnitude of the change in jet energy resolution was dependent upon the jet energy, with a stronger dependency being observed for low energy jets. This is expected from the stochastic contribution to the energy resolution for a sampling calorimeter,

Total Number of Layers	$N_{Layers}$ Region 1	Absorber Thickness	$N_{Layers}$ Region 2	Absorber Thickness	Total Thickness
$N_{Layers}$ ECal		Region 1 [mm]		Region 2 [mm]	[ $X_0$ ]
30	20	2.10	9	4.20	22.77
26	17	2.40	8	4.80	22.60
20	13	3.15	6	6.30	22.47
16	10	4.00	5	8.00	22.31

**Table 6.2:** The longitudinal structure of the ECal models considered in the optimisation study. The radiation length of tungsten absorber is 3.504mm [58]. Note that a presampler layer contributes one extra layer to the cumulative number of layers.

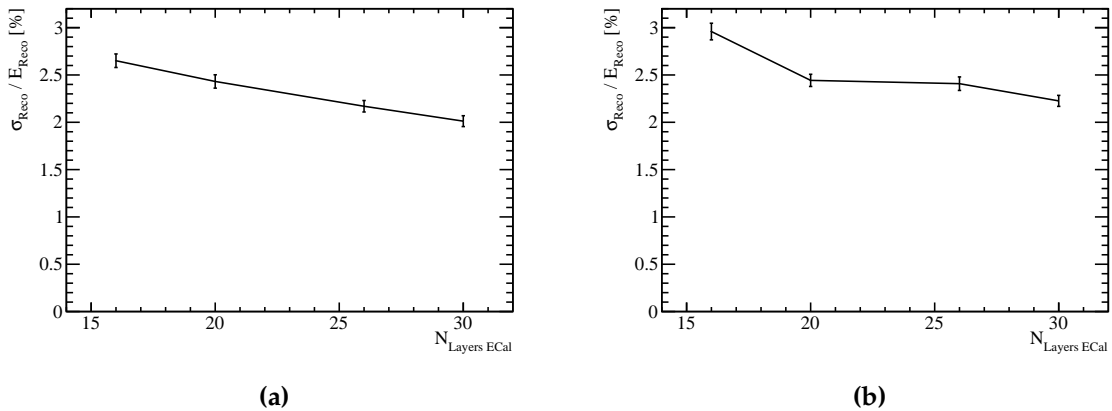


**Figure 6.4:** The energy resolution as a function of number of layers in the ECal for 100 GeV  $\gamma$ s using the nominal ILD detector model with (a) the silicon and (b) the scintillator ECal option.

which is  $\propto \frac{1}{\sqrt{E \times N_{Layers}}}$  where  $E$  is the reconstructed energy and  $N_{Layers}$  is the number of layers in the calorimeter. At high jet energies, the energy resolution in the ECal is small and changes to the stochastic term that occur when varying the number of layers are too fine to be resolved using jet energy resolution. While at low jet energies the stochastic term is larger making it possible to resolve the changes to it when varying the number of layers in the ECal. The jet energy resolution is less sensitive than the single  $\gamma$  energy resolution to changes in the number of ECal layers as only  $\approx 30\%$  of jet energy is carried in the form of  $\gamma$ s. The decomposition of the jet energy resolution into the intrinsic energy resolution and confusion contributions for 45 and 250 GeV jets are shown, for both the silicon and scintillator ECal options, in figure 6.6.

As expected, the improvement to the intrinsic energy resolution seen when increasing the number of layers in the ECal leads to the knock-on effect of lowering the confusion. However, significantly the magnitude of the change to the intrinsic energy resolution and confusion contributions to the jet energy resolution when varying the number of layers in the ECal are comparable in size. This shows that pattern recognition is as important for detector performance in the particle flow paradigm than intrinsic energy resolution.

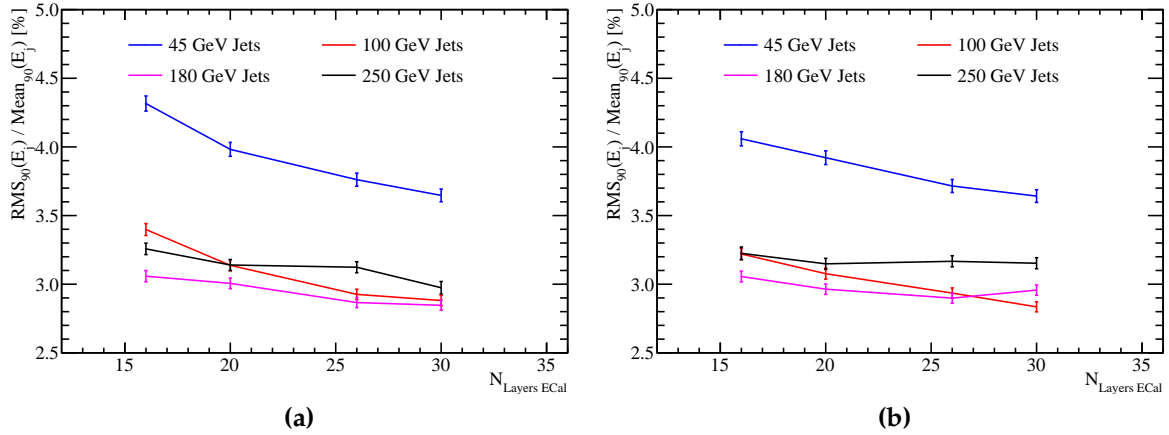


**Figure 6.5:** The jet energy resolution as a function of number of layers in the ECal for various jet energies using the nominal ILD detector model with (a) the silicon and (b) the scintillator ECal option.

Increasing the number of layers in the ECal is beneficial to the intrinsic energy resolution and the jet energy resolution, particularly for low jet energies. Separation of the W and Z hadronic decays should be possible for ILC like energies given there are at least 26 layers in the ECal, however, it is desirable to have as large a number of layers as possible to benefit single  $\gamma$  energy resolution.

### 6.2.3 ECal Active Material

In sections 6.2.1 and 6.2.2 the performance of the ECal was reported for both the silicon and scintillator options and to a large extent the performance of the two options was similar, but not identical:

- The intrinsic energy resolution of the silicon ECal option is better than that of a scintillator option for high energies, see figures 3.16a and 3.16b. This is most

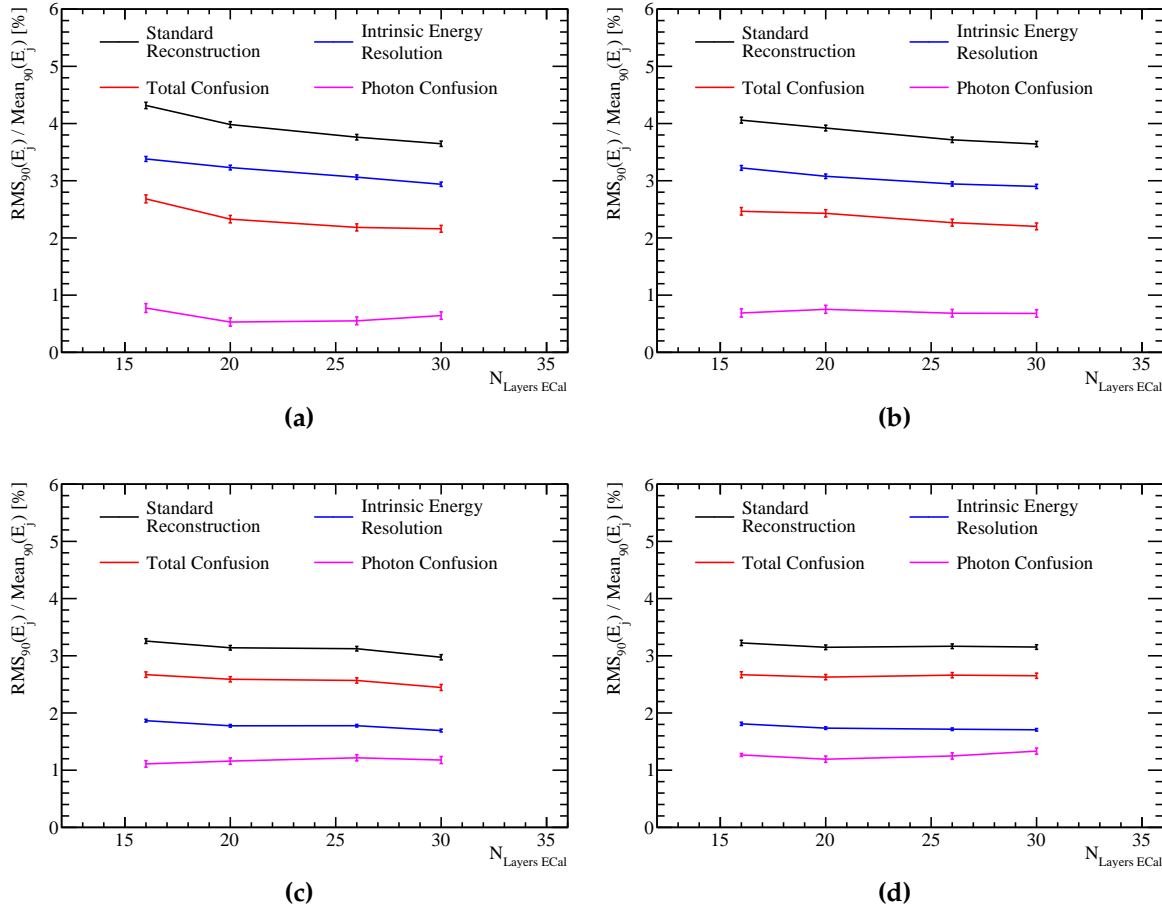


**Figure 6.6:** The contributions to the jet energy resolution as a function of number of layers in the ECal using the nominal ILD detector model for (a) the silicon ECal option and 45 GeV jets, (b) the scintillator ECal option and 45 GeV jets, (c) the silicon ECal option and 250 GeV jets and (d) the scintillator ECal option and 250 GeV jets. The black curves correspond to the standard reconstruction, the blue curves to the intrinsic energy resolution contribution to the jet energy resolution, the red curves to the confusion contribution to the jet energy resolution and the magenta curves to the confusion contribution to the jet energy resolution related solely to  $\gamma$  reconstruction.

likely due to the implementation of Birks' law [59] for scintillator active materials., which states:

$$\frac{d\mathcal{L}}{dx} \propto \times \frac{dE/dx}{1 + k_B dE/dx}, \quad (6.1)$$

where  $\frac{d\mathcal{L}}{dx}$  is the light yield per unit path length,  $dE/dx$  is the energy deposited per unit path length and  $k_B$  is a material property constant. For large energy deposits per unit length, such as those found in high energy  $\gamma$  events, the light yield

saturates causing a degradation in the energy resolution. Based on a comparison with the silicon ECal option performance, this effect starts to degrade the energy resolution for the scintillator option around 50 GeV. However, the degradation in energy resolution up to 100 GeV is relatively small.

- The "dead" region due to the presence of the MPPC in the simulation of the scintillator ECal option degrades performance of the detector for small transverse granularities, see figure 6.1.

In summary, the performance of the two options, in terms of energy and jet energy resolution, are similar, meaning no clear option is preferred. However, the silicon option is preferred when manufacture and implementation of the two models is compared. While constructing silicon wafers to fit a  $5 \times 5\text{mm}^2$  square cell size is achievable, this would be extremely challenging for scintillator tiles. To resolve this in actuality, the scintillator ECal option would have to use  $5 \times 45\text{mm}^2$  scintillator strips that are arranged in alternating directions in each ECal layer. By combining information from neighbouring layers it becomes possible to effectively achieve a  $5 \times 5\text{mm}^2$  square cell size.

### 6.3 Hadronic Calorimeter Optimisation

The purpose of an hadroinc calorimeter (HCal) is to measures the energy deposits from hadronic showers. The HCal in the default ILD detector model, summarised in table 6.3, is approximately 6 nuclear interaction lengths ( $\lambda_I$ ) deep. The ECal contributes approximately one  $\lambda_I$  giving a total of  $\approx 7\lambda_I$ , which is sufficient to contain jets at ILC like energies. The longitudinal structure of this model consists of 48 readout layers each containing a 3 mm active layer of scintillator and a 20 mm absorber layer of iron.

There are several readout approaches under consideration for the HCal including fully analogue, fully digital and semi-digital. The analogue readout measures the energy within each HCal cell using a continuous spectrum of measurements, while the digital readout only produces a response if the energy deposited within a calorimeter cell is above a given threshold. The semi-digital approach mirrors that of the digital approach, but has three responses each with a different energy threshold. While the energy resolution for digital calorimeters is not as good as that of analogue calorimeters, it is possible to construct smaller cell sizes using a digital readout. In

Parameter	Default Value
Cell Size	$30 \times 30\text{mm}^2$ square cells
Number of Layers	48 readout layers
Active Material Choice	Scintillator
Active Material Thickness	3 mm
Absorber Material Choice	Steel
Absorber Material Thickness	20 mm

**Table 6.3:** The configuration of the HCal in the nominal ILD detector model.

traditional calorimetry, a digital calorimeter would give a worse jet energy resolution than the analogue equivalent, however, that is not necessarily the case in particle flow calorimetry. If a digital calorimeter could be realised with a much small cell size than the analogue equivalent, then the affect of confusion in the digital calorimeter may be reduced so much that it compensates for any loss to intrinsic energy resolution. In the following studies optimisation of the analogue HCal is presented as this is the readout approach used in the nominal ILD detector model.

A number of options were simulated where the following parameters in the HCal were varied:

- Cell size: This is crucial for successful application particle flow calorimetry for making associations between clusters of calorimeter hits and charged particle tracks. It is expected that the intrinsic energy resolution be invariant to changes in the HCal cell size.
- Number of readout layers i.e. varying total depth of HCal: The number of layers in the HCal are varied, however, the thickness of those layers match those of the nominal ILD HCal design. This means the total depth of the HCal in  $\lambda_I$  is changing. It is expected that this study will determine the effect of leakage of energy out of the back of the HCal.
- Sampling frequency: This involves changing the of readout layers in the HCal while simultaneously changing the thicknesses of the active and absorber layers to keep the total number of  $\lambda_I$  in the HCal constant. As this modifies the sampling of particle showers in the HCal, this will affect the intrinsic energy resolution of the HCal.

- Sampling fraction: This is the ratio of the active medium thickness to the absorber medium thickness. This controls how particle showers within the calorimeter are sampled. In this study the total depth of the HCal in  $\lambda_I$  is held constant between detector models.
- Absorber material choice: Two options have been considered: steel and tungsten. This choice dictates the growth and propagation of hadronic showers and so plays a crucial role in calorimetry.

### 6.3.1 HCal Cell Size

The HCal cell size is an important detector parameter in the application of particle flow calorimetry. Smaller HCal cell sizes will lead to a finer spatial resolution that can be used to better separate charged and neutral particle calorimetric energy deposits. On the other hand, this will also lead to an increase in the number of readout channels that will raise the cost of the calorimeter. Therefore, it is highly desirable to achieve the optimal physics performance using the largest cell size possible. The nominal ILD HCal has a 30 mm square cell size and in this study the following square cell sizes were considered; 10 mm, 20 mm, 30 mm, 40 mm, 50 mm and 100 mm.

The energy resolution for 50 GeV  $K_L^0$  events as a function of cell size in the HCal is shown in figure 6.7. These  $K_L^0$  samples will deposit energy primarily within the HCal, making them appropriate events to consider when determining the performance of the HCal. However, a non-negligible amount of energy will also be deposited within the ECal. Therefore, these energy resolutions represent the intrinsic energy resolution of the ILD detector as a whole and not purely that of the HCal. It is clear that there is no strong dependency on the energy resolution of the  $K_L^0$  as a function of the HCal cell size. There are small fluctuations in the energy resolution that are most likely due to variations in applying the calibration procedure and the tuning of the optimal HCal cell truncation, described in section 5.3.1. The precision on the optimal cell truncation is worse for large HCal cell sizes as the truncations considered in the optimisation are focused around the optimal truncation for the nominal ILD HCal.

As a smaller HCal cell size will lead to better separation of charged and neutral hadron calorimetric energy deposits, it is expected that the confusion contribution to the jet energy resolution will be reduced by using smaller HCal cell sizes. The jet energy resolution as a function of cell size in the HCal shown in figure 6.8. At low

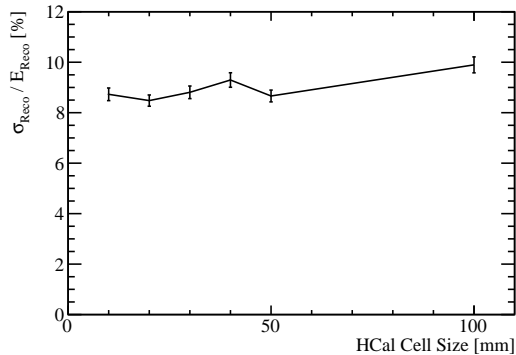


**Figure 6.7:** The energy resolution as a function of HCal cell size for 50 GeV  $K_L^0$  events using the nominal ILD detector model.

jet energies there is no strong dependency of the jet energy resolution on the HCal cell size, which is as expected from the  $K_L^0$  energy resolution study. For high energy jets there is a clear dependence, with lower HCal cell sizes leading to better jet energy resolutions. Examining the different contributions to the jet energy resolution, shown in figure 6.9 it can be seen that the intrinsic energy resolution contribution is largely invariant to changes in the HCal cell size. Instead it is the confusion contribution that drives the overall trend in the jet energy resolution. This is particularly clear at high jet energies where the confusion contribution to the jet energy resolution dominates that of the intrinsic energy resolution contribution. At high jet energies smaller HCal cell sizes clearly lead to a reduction in the effect of confusion. At low jet energies the trend in confusion is less clear, as the confusion contribution is less dominant, but a reduction in the effect of confusion with decreasing cell size is still visible for all but the smallest HCal cell size. The most likely cause of the increase in confusion for the smallest HCal cell size at low energies is tuning of the PandoraPFA algorithms to the nominal ILD HCal cell size. Furthermore, for both energies the photon confusion is largely invariant to changes in the HCal cell size. This indicates that the changes in confusion when varying the HCal cell size are due to pattern recognition improvements related to hadrons.

A comparison of the results from the ECal and HCal cell size optimisation studies shows that the jet energy resolution has a much stronger dependency on the ECal cell size than the HCal cell size. This is to be expected as in the particle flow paradigm  $\approx 30\%$  of jet energy is recorded in the ECal, while only  $\approx 10\%$  is recorded in the HCal meaning the potential effect of double counting and omitting energy deposits, i.e. confusion, is greater in the ECal than the HCal. Therefore, minimising confusion in

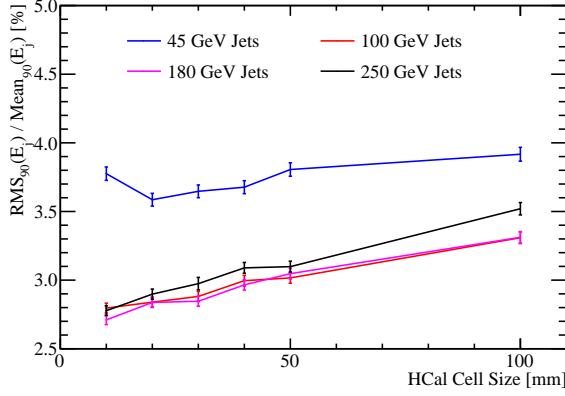


**Figure 6.8:** The jet energy resolution as a function of HCal cell size for various jet energies using the nominal ILD detector model.

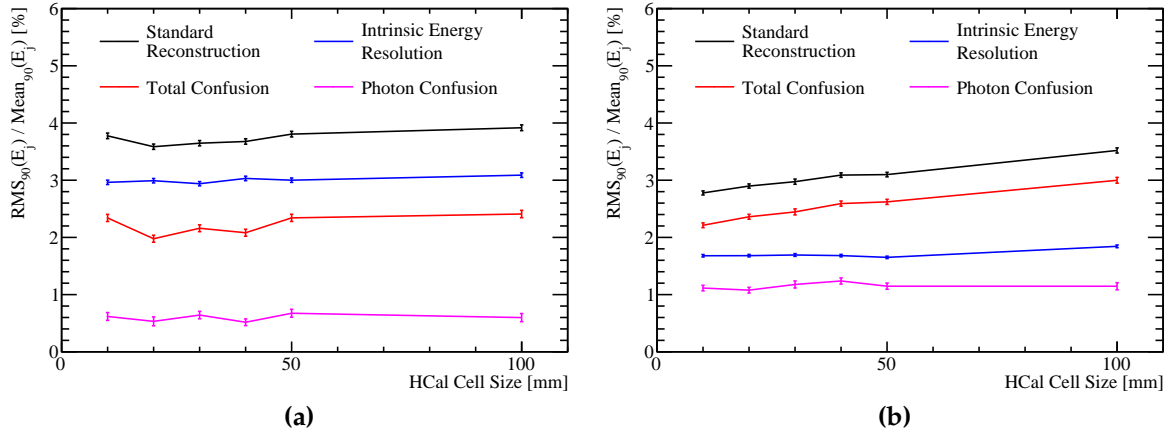


**Figure 6.9:** The contributions to the jet energy resolution as a function of HCal cell size using the nominal ILD detector model for (a) 45 GeV jets and (b) 250 GeV jets. The black curves correspond to the standard reconstruction, the blue curves to the intrinsic energy resolution contribution to the jet energy resolution, the red curves to the confusion contribution to the jet energy resolution and the magenta curves to the confusion contribution to the jet energy resolution related solely to  $\gamma$  reconstruction.

the ECal should be more crucial for the overall jet energy resolution, which is what is observed. Furthermore, as PandoraPFA groups calorimeter hits together using a cone clustering approach, identifying the start of a particle shower is key for determining how calorimeters hits are grouped together deeper into the calorimeters. In effect, this means the grouping of calorimeter hits in the HCal heavily relies upon information gathered in the ECal. Therefore, if the ECal performance is sufficiently good, even with coarse HCal cell sizes excellent performance can be achieved.

In summary, the confusion contribution to the jet energy resolution falls as the HCal cell size is reduced, while the intrinsic energy resolution of the detector is largely invariant to changes in the HCal cell size. As this dependency is relatively weak, even the use of 100 mm square HCal cell sizes would be enough to allow for separation of the hadronic decays of W and Z bosons at ILC like energies. However, as jet energy resolution does improve with decreasing cell sizes it is desirable to have as small a HCal cell size as possible.

### 6.3.2 HCal Number of Layers

A number of detector models were simulated where the total number of layers in the HCal was varied. In contrast to the sampling frequency study, the thickness of the HCal layers were not modified. Changing the number of layers in this way leads to a change in the total thickness of the calorimeter. It is expected that this study will determine what effects, if any, leakage of energy out of the back of the calorimeter will have on detector performance. The cost of the HCal is proportional to the number of readout channels, which is proportional to the number of layers used in the HCal. Therefore, minimising the number of layers, while retaining excellent physics performance is vital. For this study detector models were simulated with a HCal containing 36, 42, 48 (nominal), 54 and 60 layers.

It is expected that the energy resolution of the detector will improve when the number of layers in the HCal is increased as fewer events should suffer from the effects of leakage. Any improvements seen by increasing the number of layers in the HCal is expected only up to a point, as beyond this point the majority of hadronic showers will be fully contained making additional HCal layers redundant. The energy resolution as a function of number of layers in the HCal for 50 GeV  $K_L^0$  is shown in figure 6.10. The energy resolution becomes worse as the number of layers in the HCal is reduced below 48 layers, while above this point additional layers do not change the energy resolution. This indicates that the majority of hadronic showers at this energy are fully contained by a 48 layer HCal. However, as reducing the number of HCal layers to 36 only causes a small degradation in the neutral hadron energy resolution, it is feasible for the ILD to consider using a thinner HCal design.

The trend in the 50 GeV  $K_L^0$  energy resolution observed when varying the number of layers in the HCal is unlikely to be seen in the jet energy resolution as the trend weak

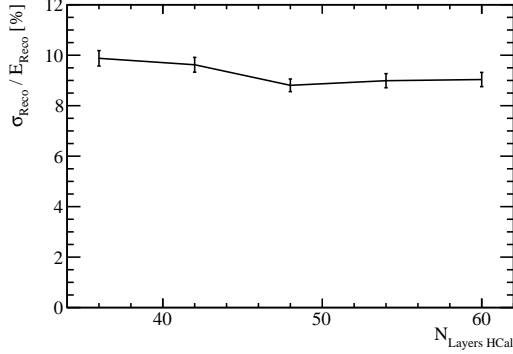


**Figure 6.10:** The energy resolution as a function of number of layers in the HCal for 50 GeV  $K_L^0$  events using the nominal ILD detector model.

and only a small fraction of jet energy is measured within the HCal. However, the confusion contribution to the jet energy resolution is expected to change as errors will be introduced, in the association of charged particle tracks to clusters of calorimeters hits, if part of the cluster energy has leaked from the back of the calorimeter. For example, if a particle shower from a charged particle suffers heavily from leakage there will be a large disparity between the track momentum and the energy it deposits within the calorimeter. In that case, PandoraPFA will be overly aggressive in associating other calorimeter energy deposits to this track to account for the energy that has leaked out of the calorimeter, which will increase the confusion. The jet energy resolution as a function of the number of layers in the HCal is shown in figure 6.11. As expected for low energy jets, where intrinsic energy resolution dominates, the jet energy resolution is invariant to the number of layers, while for high jet energies, where confusion dominates, a larger number of layers benefits the jet energy resolution. When examining the different contributions to the jet energy resolution, shown in figure 6.12, it becomes clear that the confusion contribution that drives the observed trends. The intrinsic energy resolution is largely invariant to changes to the number of HCal layers as only a small fraction of jet energy is recorded in the HCal. Furthermore, the photon confusion is invariant to changes in the number of HCal layers, indicating that the change in the confusion contribution are originating from pattern recognition involving hadrons.

In summary, even if the number of layers in the HCal were reduced by a factor of 25% the jet energy resolution would be sufficient for separating the hadronic decays of the W and Z bosons at ILC energies. However, it is clear that leakage of energy from the back of the HCal would negatively affect events at ILC like energies if the number

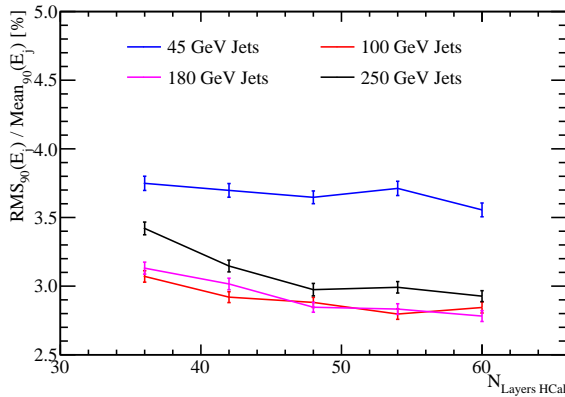


**Figure 6.11:** The jet energy resolution as a function of number of layers in the HCal for various jet energies using the nominal ILD detector model.

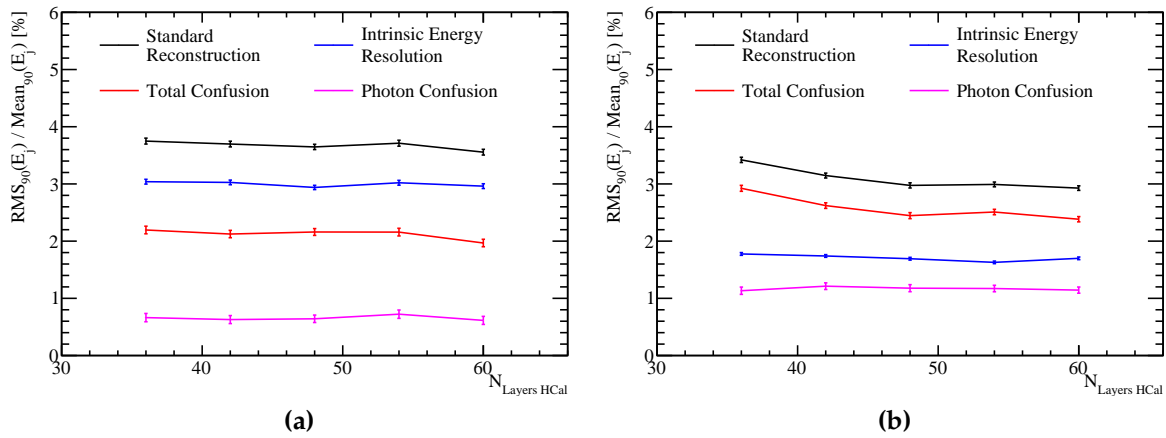


**Figure 6.12:** The contributions to the jet energy resolution as a function of number of layers in the HCal using the nominal ILD detector model for (a) 45 GeV jets and (b) 250 GeV jets. The black curves correspond to the standard reconstruction, the blue curves to the intrinsic energy resolution contribution to the jet energy resolution, the red curves to the confusion contribution to the jet energy resolution and the magenta curves to the confusion contribution to the jet energy resolution related solely to  $\gamma$  reconstruction.

of layers is reduced from the nominal value of 48 layers, therefore, it is desirable to have a minimum of 48 layers in the HCal.

### 6.3.3 HCal Sampling Frequency

Several detector models were simulated where the sampling frequency in the HCal had been modified from that found in the nominal ILD HCal. This sampling fraction

was altered by changing the number of layers in the HCal, while simultaneously changing the active and absorber layer thicknesses, to maintain the total depth of the HCal, in  $\lambda_I$ . For each model considered, the absorber material was steel, containing a total of  $5.72 \lambda_I$ , and the active material was scintillator, containing a total of  $0.19 \lambda_I$ . The ratio of the active to absorber layers thicknesses (the sampling fraction) in these models matched that found in the nominal ILD HCal. A summary of the detector models considered in this study can be found in table 6.4.

Number $N_{\text{Layers HCal}}$	Absorber Thickness [mm]	Active Thickness [mm]
60	16.00	2.40
54	17.78	2.67
48	20.00	3.00
42	22.86	3.43
36	26.67	4.00
30	32.00	4.80
24	40.00	6.00
18	53.33	8.00

**Table 6.4:** Cell size layout of various HCal models considered.

Increasing the number of layers in a sampling calorimeter, while leaving the total material budget unchanged, will lead to greater sampling of particles showering within it and a reduction the stochastic contribution to the energy resolution. Therefore, it is expected that the energy resolution will improve with increasing number of layers in the HCal. This is shown for 50 GeV  $K_L^0$  in figure 6.13, which clearly shows that the energy resolution of the calorimeter is strongly dependent upon the sampling frequency in the HCal. There are fluctuations in the energy resolution from fitting the reconstructed energy distribution to extract the mean and from the calibration of the detector, however, these are small and the underlying performance trend is still clear. The energy resolution does not exactly follow a  $\frac{1}{\sqrt{N_{\text{Readout Layers HCal}}}}$  relationship, but this is to be expected as this relationship only holds for the energy resolution of a single sampling calorimeter and these results are for the whole ILD detector, including the  $\approx 1\lambda_I$  in the ECal. Furthermore, this functional form neglects the constant term in the energy resolution described in section 3.7.

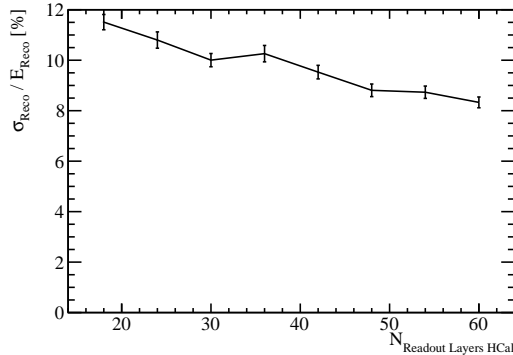


**Figure 6.13:** The energy resolution as a function of sampling frequency in the HCal for 50 GeV  $K_L^0$  events using the nominal ILD detector model.

The jet energy resolution as a function of sampling frequency in the HCal is shown in figure ???. It is clear that increasing the number of layers in the HCal leads to an improvement in the jet energy resolution. Figure 6.15 shows that both the intrinsic energy resolution and confusion are reduced with increasing sampling frequency. This is expected as increasing the sampling frequency of a calorimeter improves the intrinsic energy resolution, which has the knock-on effect of lowering the confusion contribution to the jet energy resolution as described in section 3.6.2.

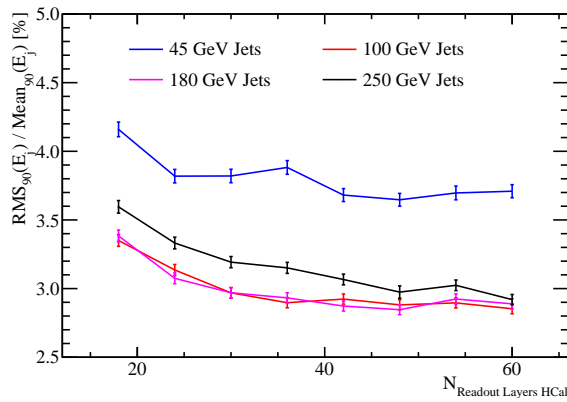


**Figure 6.14:** The jet energy resolution as a function of sampling frequency in the HCal for various jet energies using the nominal ILD detector model.

It is clear that a larger number of layers in the HCal benefits both the intrinsic energy resolution of the ILD detector as well as reducing the confusion contribution to the jet energy resolution. As there are few physics analyses that rely on the identification and categorisation of individual neutral hadrons, but there are many that rely on identification and categorisation of  $\gamma$ s, the intrinsic energy resolution of the HCal is

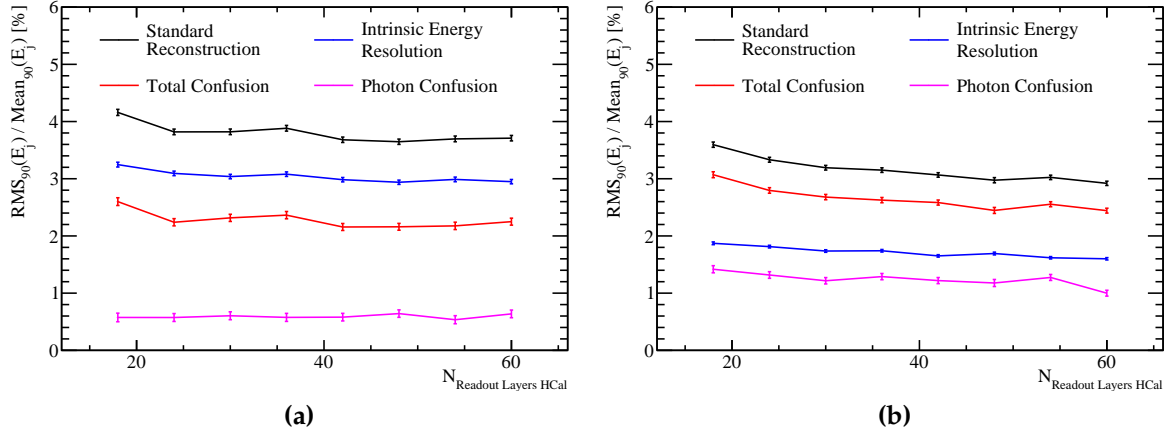


**Figure 6.15:** The contributions to the jet energy resolution as a function of sampling frequency in the HCal using the nominal ILD detector model for (a) 45 GeV jets and (b) 250 GeV jets. The black curves correspond to the standard reconstruction, the blue curves to the intrinsic energy resolution contribution to the jet energy resolution, the red curves to the confusion contribution to the jet energy resolution and the magenta curves to the confusion contribution to the jet energy resolution related solely to  $\gamma$  reconstruction.

less crucial from a physics perspective than that of the ECal. However, these studies show the HCal still has a crucial role to play in jet reconstruction in the particle flow paradigm and therefore cannot be neglected. To achieve a jet energy resolution of  $\frac{\sigma_E}{E} \lesssim 3.8\%$ , which is required to separate the W and Z hadronic decays, the ILD detector will require a minimum of 42 layers in the HCal. This sampling frequency is required particularly for low energy jets where the energy resolution is dominated by the intrinsic energy resolution of the detector.

### 6.3.4 HCal Sampling Fraction

The ILD detector performance was simulated where the ratio of the active to absorber layer thicknesses in the HCal were varied. In the nominal detector model the active scintillator layer thickness is 3 mm, while the absorber layer thickness is 20 mm giving a sampling fraction of 0.15. HCal models were simulated where this ratio was changed from 0.05 to 0.25 in steps of 0.05, while retaining the same number of interaction lengths in the absorber and active layers as is found in the nominal HCal model. If the active layer thickness becomes excessively small then it is possible that any signal produced in that layer would be insufficient to accurately estimate the energy deposited within

the surrounding absorber layers. However, no performance differences were observed for any of these detector models when considering the energy resolution for 50 GeV  $K_L^0$  events or the jet energy resolution for the 91, 200, 360 and 500 GeV  $Z \rightarrow u\bar{d}s$  di-jet events. This indicates the particle showers are sufficiently well sampled in all detector models considered and that thinning the active layer of the ILD HCal down to  $\sim 1$  mm would not harm the detector performance.

### 6.3.5 HCal Absorber Material

The nominal choice of absorber material is steel with tungsten providing a feasible alternative [33]. Although tungsten is more expensive than steel, it contains a larger number of nuclear interaction lengths per unit length. Therefore, using tungsten as opposed to steel as the absorber material would allow for a reduction in the size of the HCal, while retaining the same number of nuclear interaction lengths. Reducing the depth of the calorimeter would decrease the size of the solenoid required, which would offset some of the additional cost if tungsten were to be used.

The configuration for the steel and tungsten HCal options that were used in the full ILD simulation can be found in table 6.5. To isolate the effects of changing the absorber material, the total depth, in nuclear interaction lengths, was kept constant when comparing these two options. Furthermore, the sampling fraction was also held constant. The interaction of hadrons with the absorber material within the detector is simulated by GEANT4. A number of different physics lists exist within GEANT4 for the modelling of hadronic showers. The default model for high energy physics calorimetry is the QGSP\_BERT physics list, which uses the quark-gluon string model [60] with the precompound model of nuclear evaporation [61] (QGSP) for high energy interactions and the Bertini (BERT) cascade model [62] for intermediate energy interactions. For this study both the QGSP\_BERT and the QGSP\_BERT\_HP physics lists were used. The QGSP\_BERT\_HP list uses the high precision neutron package (NeutronHP) to deal with the transportation of neutrons from below 20 MeV to thermal energies. This added detail was thought to be necessary for a study involving tungsten due to the expected increase in shower development.

One of the dominant processes governing the energy deposition of hadronic showers in calorimeters is spallation [54]. Spallation begins with the collision of a high energy incident particle with an atomic nuclei from the calorimeter absorbing ma-

Parameter	Steel HCal Option	Tungsten HCal Option
Cell Size	$30 \times 30\text{mm}^2$ square cells	$30 \times 30\text{mm}^2$ square cells
Number of Layers	48 readout layers	48 readout layers
Absorber Material Thickness [mm]	20.0	12.0
Active Material Choice	Scintillator	Scintillator
Active Material Thickness [mm]	3.0	1.8

**Table 6.5:** The configuration of the steel and tungsten HCal options.

terial. This collision creates an internuclear cascade where a shower of high energy hadronic particles, e.g. protons, neutrons and pions, are produced within the nucleus. If these energies are large enough, some of these particles may escape the nucleus and form secondary particles in the hadronic shower. After this initial collision, the nuclei of the absorbing material are left in an excited state. Assuming the excited nuclei are sufficiently stable that they will not undergo fission, they will return to a stable state by ejecting energy in the form of particles in a process called evaporation. Evaporation of neutrons, which is the dominant form of evaporation, significantly delays the growth of hadronic showers as after the evaporation process some of these neutrons participate in neutron capture [57]. Neutron capture involves an absorber nuclei capturing a neutron and then emitting a  $\gamma$  as it returns to a stable state. The time taken for the neutron capture mechanism to proceed is limited by the lifetime of the unstable nuclei, which typically makes neutron capture one of the slowest mechanisms by which hadronic showers can propagate. As absorber materials with a large atomic number,  $Z$ , have a larger number of neutrons, it is expected that there will be an increase in the number of evaporation neutrons within hadronic showers developing in such materials. In turn this will lead to more neutron capture processes and a longer development time for the hadronic showers. This is what is observed when considering the shower development times using the tungsten ( $Z=74$ ) and steel (iron,  $Z=26$ ) HCal options as seen in figure 6.16.

The energy resolution for 50 GeV  $K_L^0$  events using the nominal ILD detector model with a steel and tungsten HCal absorber material can be found in table 6.6. The tungsten HCal option offers a slight improvement over steel in the energy resolution for these samples. This will be caused by differences in the atomic structure of the two materials, which will lead to different developments of the hadronic showers within them. For example, the energy losses to nuclear binding energies are smaller in

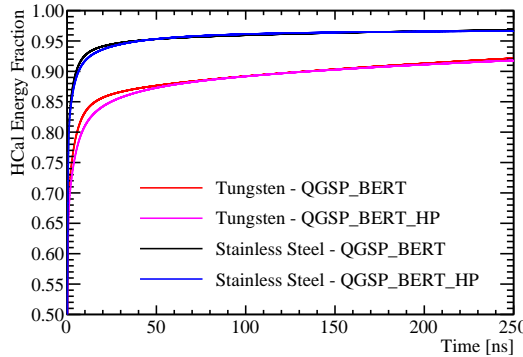


**Figure 6.16:** The fraction of the total calorimetric energy deposited in the HCal as a function of time for 25 GeV  $K_L^0$  events using the steel and tungsten HCal options. Results are shown for both the QGSP\_BERT and QGSP\_BERT\_HP physics lists. The calorimeter hit times have been corrected for straight line time of flight to the impact point.

tungsten than steel, as the atomic nuclei for tungsten is less stable than that of iron, therefore, less energy is needed to liberate nucleons in the shower development. This will lead to a larger signal in the tungsten calorimeter and a reduction in the energy resolution in comparison to steel. These results also indicated that the addition of the high precision neutron package did not alter the detector performance significantly for either option.

HCal Option	Energy Resolution [%]
Steel, QGSP_BERT	$8.8 \pm 0.2$
Steel, QGSP_BERT_HP	$9.0 \pm 0.3$
Tungsten, QGSP_BERT	$8.3 \pm 0.2$
Tungsten, QGSP_BERT_HP	$8.3 \pm 0.2$

**Table 6.6:** The energy resolution using the nominal ILD detector with various HCal options determined using 50 GeV  $K_L^0$  events.

It should be emphasised that in determining these results, the HCal cell truncation, as described in chapter 5, was separately tuned for the tungsten option. This was required as tungsten has a larger number of radiation lengths per unit length than steel, which leads to larger average cell energies meaning the truncation of cell energies required refining. As the HCal primarily measures hadronic showers, one may naively expect the number of radiation lengths in the HCal to be irrelevant to

performance, given both options have the same number of nuclear interaction lengths. However, this is not the case as all hadronic showers have an electromagnetic component generated by the decays of hadrons to  $\gamma$ s, e.g.  $\pi^0 \rightarrow \gamma\gamma$  and  $\eta \rightarrow \gamma\gamma$ . This leads to hadronic showers depositing more energy per calorimeter cell in a tungsten HCal when compared to a steel HCal.

The jet energy resolutions for selected jet energies are shown in table 6.7 for the various HCal options considered. These results indicate that steel outperforms tungsten as the absorber material for the HCal. Furthermore, as the jet energy increases, the magnitude of the difference in jet energy resolutions between the two options grows. This indicates the differences in jet energy resolution between the two options is driven by the confusion contribution as this contribution grows with increasing jet energy. Furthermore, as the  $K_L^0$  energy resolution was only slightly better for the tungsten option it is expected that the intrinsic energy resolution contribution to the jet energy resolution will not vary significantly between the two as only a small fraction of jet energy is measured in the HCal. The intrinsic energy resolution and confusion contributions to the jet energy resolution for 45 and 250 GeV jets are shown in table 6.8. As expected, the intrinsic energy resolution contribution to the jet energy resolution is nearly identical between the various options. The confusion contribution to the jet energy resolution is larger for the tungsten HCal option than for the steel HCal option. This is due to the PandoraPFA algorithms being tuned for the nominal (steel) ILD HCal dimensions, while the cells for the alternative tungsten option are thinner by a factor of approximately  $\frac{\lambda_I^{Steel}}{\lambda_I^{Tungsten}} \approx 1.7$ , where  $\lambda_I^x$  is the distance of one radiation length in material  $x$ . It is unfeasible to tune all of the PandoraPFA algorithms to each detector geometry, however, the breakdowns of the jet energy resolution indicate that even if this were done, the tungsten option would offer no advantage to the steel option in terms of intrinsic energy resolution. Once again, it was noted that the use of the QGSP\_BERT\_HP physics list, as opposed to QGSP\_BERT, made a minimal impact on these results.

In conclusion, there are no large differences in the intrinsic energy resolution of the ILD detector simulation, for either neutral hadrons or jets, when changing the HCal absorber material from steel to tungsten. The steel option HCal outperforms the tungsten option in terms of pattern recognition confusion, when using the default PandoraPFA settings, although this could be addressed should it become clear that tungsten were a preferred option. However, when examining the mechanical proper-

HCal Option	Jet Energy Resolution [%]			
	45 GeV	100 GeV	180 GeV	250 GeV
Steel, QGSP_BERT	$3.65 \pm 0.05$	$2.88 \pm 0.04$	$2.85 \pm 0.04$	$2.97 \pm 0.05$
Steel, QGSP_BERT_HP	$3.67 \pm 0.05$	$2.92 \pm 0.04$	$2.86 \pm 0.04$	$3.03 \pm 0.04$
Tungsten, QGSP_BERT	$3.78 \pm 0.05$	$3.12 \pm 0.04$	$3.15 \pm 0.04$	$3.43 \pm 0.04$
Tungsten, QGSP_BERT_HP	$3.80 \pm 0.05$	$3.08 \pm 0.04$	$3.24 \pm 0.04$	$3.41 \pm 0.04$

**Table 6.7:** The jet energy resolution using the nominal ILD detector with various HCal options for various jet energies.

HCal Option	Jet Energy Resolution [%]			
	45 GeV		250 GeV	
	Intrinsic	Confusion	Intrinsic	Confusion
Steel, QGSP_BERT	$2.93 \pm 0.04$	$2.16 \pm 0.06$	$1.69 \pm 0.02$	$2.45 \pm 0.05$
Steel, QGSP_BERT_HP	$2.98 \pm 0.04$	$2.15 \pm 0.06$	$1.65 \pm 0.02$	$2.53 \pm 0.04$
Tungsten, QGSP_BERT	$2.97 \pm 0.04$	$2.34 \pm 0.06$	$1.65 \pm 0.02$	$3.01 \pm 0.05$
Tungsten, QGSP_BERT_HP	$2.92 \pm 0.04$	$2.42 \pm 0.06$	$1.65 \pm 0.02$	$2.99 \pm 0.05$

**Table 6.8:** The contributions to the jet energy resolution using the nominal ILD detector with various HCal options for 45 and 250 GeV jet energies.

ties of steel and tungsten, it is clear that steel has a significant advantage over tungsten in terms of rigidity [4]. This means that fewer support structures would be required for the calorimeter leading to less dead material and better performance, which makes steel the more preferred option of the two.

## 6.4 Global Detector Parameters

The detector geometry and the magnetic field strength are major cost drivers for the ILD detector. Both will have an affect on the jet energy resolution and, for completeness, studies showing their impact on detector performance are presented here.

### 6.4.1 The Magnetic Field Strength

In the particle flow paradigm the momentum of charged particles is obtained through the curvature of the track they traverse as they bend in the magnetic field. Therefore, the magnetic field is an integral element for the successful application of particle flow calorimetry. Furthermore, the magnetic field deflects charged particles away from neutral particles in jets. The stronger the magnetic field, the larger the separation between the calorimetric energy deposits made by charged and neutral particles in jets, which reduces the effect of confusion. Therefore, it is expected that a stronger magnetic field will lead to better jet energy resolutions through a reduction of the confusion contribution to the jet energy resolution.

Detector models were simulated where the magnetic field was varied from 1 to 5 T in steps of 0.5 T and the jet energy resolutions for these detectors is shown in figure 6.17. For high energy jets there is a strong trend whereby a stronger magnetic field leads to a better jet energy resolution. While, at low jet energies the jet energy resolution is almost invariant to changes in the magnetic field.

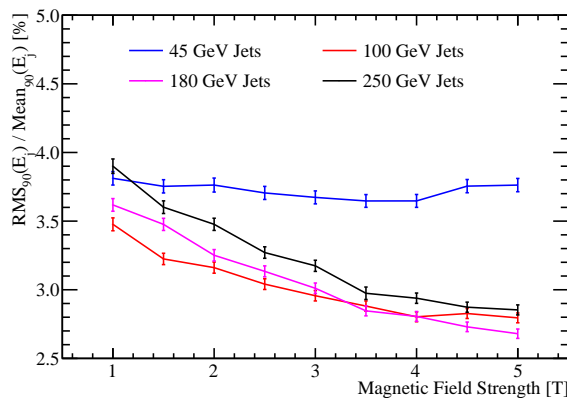


**Figure 6.17:** The jet energy resolution using the nominal ILD detector as a function of the magnetic field strength for various jet energies.

The jet energy resolution breakdowns into the various contributions are shown in figure 6.18 and as expected there is clear reduction in the confusion contribution to the jet energy resolution with increasing magnetic field strength. Furthermore, there is a reduction in intrinsic energy resolution with increasing magnetic field strength for low energy jets. At low energies, the radius of curvature of the helix charged particles traverse will be small. If the radius for a given particle is small enough, the particle will not enter the calorimeters. In this case, only if the track produced from this particle passes tight selection cuts, designed to ensure the track originates from the IP, will the

track be used in the reconstruction. Therefore, energy can and will be lost from events where particles are stuck within the tracker. Given the radii of curvature is inversely proportional to the magnetic field strength, the larger the magnetic field strength the more tracks will be confined to the tracker as is shown by figure 6.19. The more tracks that are confined to the tracker, the worse the intrinsic energy resolution becomes as inevitably some tracks fail the quality cuts. At high jet energies, low transverse momentum charged particles will still get trapped within the tracker, however, these contribute fractionally little energy to the total reconstructed energy. Therefore, the trend of worsening intrinsic energy resolution with increasing magnetic field strength is less pronounced as the jet energy grows. At very low magnetic field strengths and high jet energies, the intrinsic energy resolution actually degrades, due to an artefact in the determination of the intrinsic energy resolution. The intrinsic energy resolution is determined by associating a single MC particle to each calorimeter cell. At low magnetic field strengths and high jet energies, many of the MC particles will have overlapping energy deposits within the calorimeter cells and so associating a single MC particle per cell is inaccurate. This leads to imperfect association of charged particle tracks to calorimetric energy deposits, which worsens the intrinsic energy resolution. However, as this effect is second order small in comparison to changes in the confusion contribution the overall dependancy of detector performance on the magnetic field strength can be confidently quantified.

In summary, increasing the magnetic field strength is beneficial to detector performance as it reduces confusion from associating tracks to calorimetric energy deposits from charged particles. While there is a reduction in the intrinsic energy resolution for low transverse momentum jets with increasing magnetic field strength, this effect is largely offset by the change in confusion. While the nominal field of 3.5 T gives good performance increasing the field strength is a clear way of making gains in detector performance.

#### 6.4.2 Inner ECal Radius

Detector models were considered where the ECal inner radius was set to 1208, 1408, 1608, 1808 (nominal) and 2008 mm. For these models, all other detector parameters were identical to those found in the nominal ILD detector model.

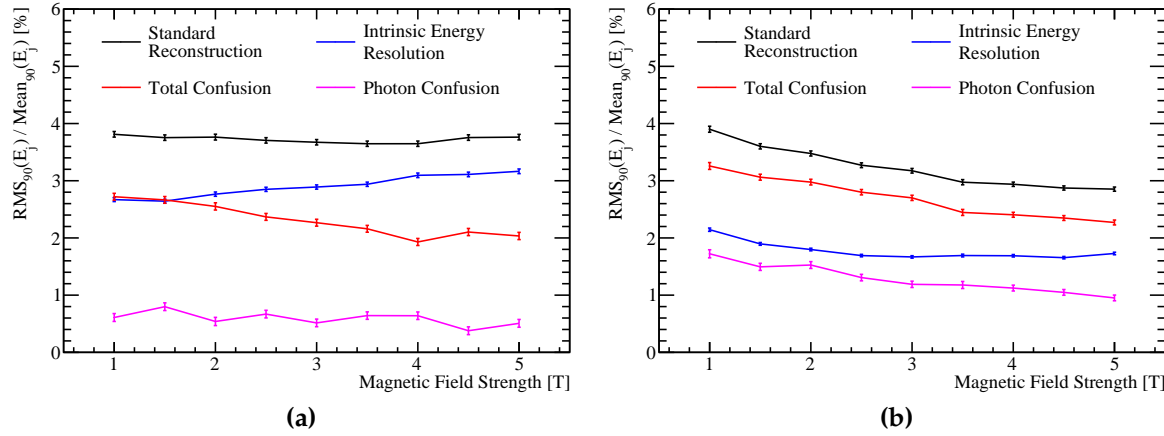


**Figure 6.18:** The contributions to the jet energy resolution as a function of the magnetic field strength using the nominal ILD detector model for (a) 45 GeV jets and (b) 250 GeV jets. The black curves correspond to the standard reconstruction, the blue curves to the intrinsic energy resolution contribution to the jet energy resolution, the red curves to the confusion contribution to the jet energy resolution and the magenta curves to the confusion contribution to the jet energy resolution related solely to  $\gamma$  reconstruction.

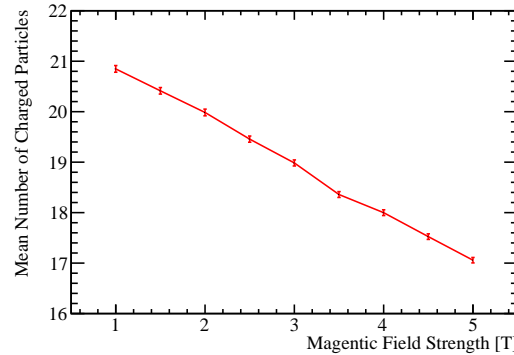


**Figure 6.19:** The mean number of reconstructed charged particles as a function of the magnetic field strength for 91 GeV  $Z \rightarrow u\bar{d}s\bar{s}$  di-jet events. The nominal ILD detector model was used and the pattern recognition has been fully cheated using the MC information.

Figure 6.20 shows the dependence of the jet energy resolution on the ECal inner radius. The simulations indicate that a large ECal inner radius was highly beneficial to detector performance, which is due to the increase in the time it takes for particles to reach the calorimeters. The longer it takes for the particles to reach the calorimeters the more the charged particles will bend in the magnetic field and the larger separation will be between calorimetric energy deposits from charged and neutral particles. This

larger this separation the smaller the effect of confusion. This conclusion is backed up by the decomposition of the jet energy resolution, shown in figure 6.21. These results explicitly show a reduction in confusion with increasing ECal inner radius. The intrinsic energy resolution of the detectors shows no strong dependence on the inner ECal radius. There is a small degradation in intrinsic energy resolution at low ECal inner radii, which is due to the association of a single MC particle per calorimeter cell when running the cheated pattern recognition as explained in section 6.4.1. Again, this effect has little bearing on the final conclusions as the change in intrinsic energy resolution across the detector models is a second order effect.

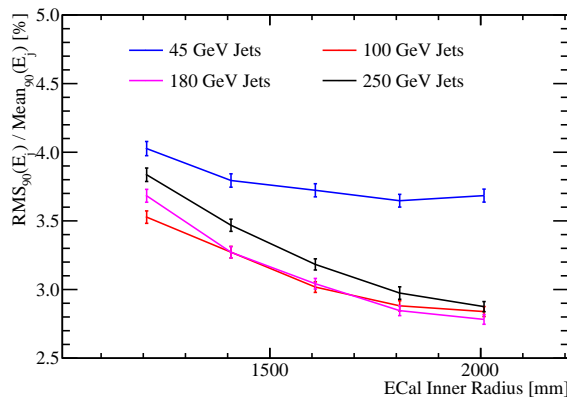


**Figure 6.20:** The jet energy resolution using the nominal ILD detector as a function of the ECal inner radius for various jet energies.

In conclusion, increasing the ECal inner radius benefits the jet energy resolution significantly. This trend is driven by changes to the confusion in associating calorimetric energy deposits to charged particle tracks.

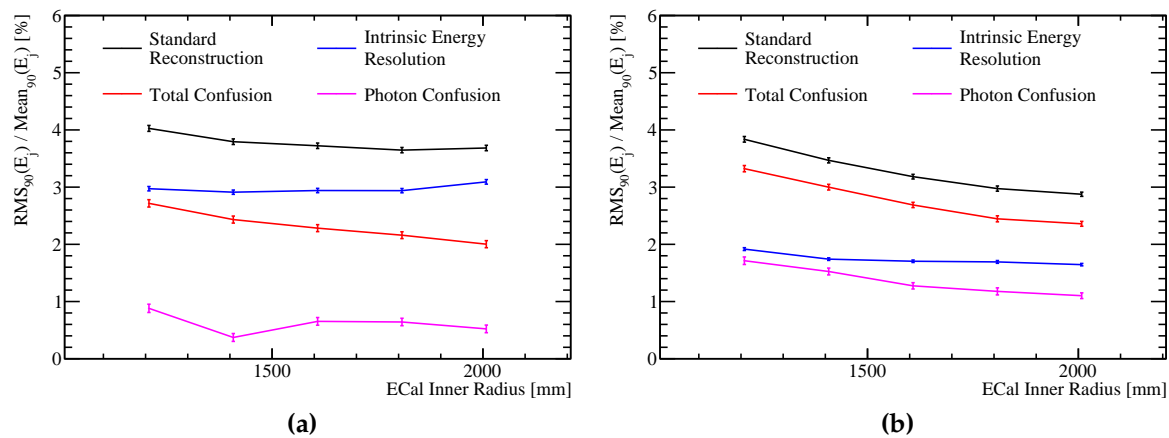


**Figure 6.21:** The contributions to the jet energy resolution as a function of the ECal inner radius using the nominal ILD detector model for (a) 45 GeV jets and (b) 250 GeV jets. The black curves correspond to the standard reconstruction, the blue curves to the intrinsic energy resolution contribution to the jet energy resolution, the red curves to the confusion contribution to the jet energy resolution and the magenta curves to the confusion contribution to the jet energy resolution related solely to  $\gamma$  reconstruction.

# Chapter 7

## The sensitivity of CLIC to anomalous gauge couplings through vector boson scattering

*“Kids, you tried your best, and you failed miserably. The lesson is, never try.”*

— Homer Simpson

### 7.1 Motivation

Vector boson scattering is the interaction of the form  $VV \rightarrow VV$  where  $V$  is any of the electroweak gauge bosons  $W^+$ ,  $W^-$ ,  $Z$  or  $\gamma$ . This is an interesting process to look at because it gives a detailed understanding of how the standard model Higgs is able to unitarise the otherwise unbounded cross section for longitudinal gauge boson scattering. Vector boson scattering also provides insights into beyond standard model physics that impacts the electroweak sector through the probing of anomalous triple and quartic gauge couplings. Presented in this section is an analysis into the sensitivity of CLIC to two of these anomalous quartic gauge couplings through the vector boson scattering process.

Triple and quartic gauge couplings lead to interactions of the form  $V \rightarrow VV$  and  $VV \rightarrow VV$  respectively. In the standard model there are five permissible vertices,

shown in figure 7.1, which arise from the kinematic term  $\mathcal{L}_{kin} = -\frac{1}{4}B_{\mu\nu}B^{\mu\nu} - \frac{1}{4}W_{\mu\nu}W^{\mu\nu}$ .

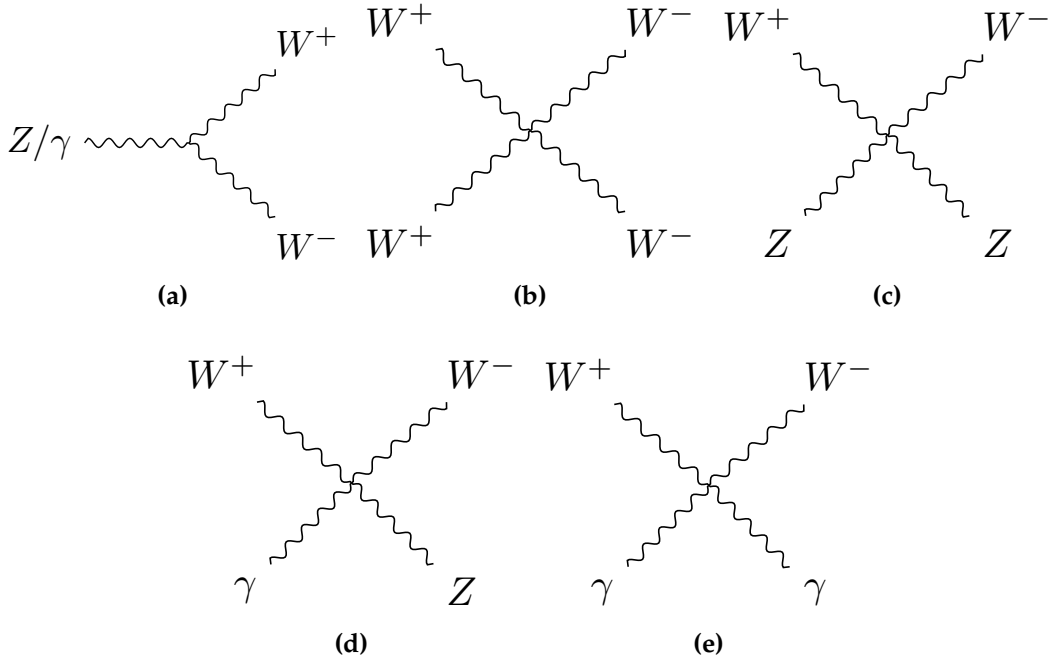


**Figure 7.1:** Gauge boson self-coupling vertices in the standard model.

Anomalous triple and quartic gauge couplings are introduced as parameters in effective field theories (EFTs). These couplings either modify the standard model triple and quartic gauge boson couplings or introduce new triple and quartic couplings that were previously forbidden. EFTs are a mathematical construct designed to introduce new physics in a manner that builds upon the standard model. They work under the assumption that new physics exists at an energy scale,  $\Lambda$ , that is much higher than the energy scales currently accessible to modern day particle physics experiments. In the limit  $\Lambda \rightarrow \infty$  the standard model should be reproduced as the new physics becomes kinematically inaccessible. Such theories are model independent, giving them a wide span in the search for new physics. A classic example of an EFT theory is the Fermi theory for beta decay [63]. The weak interaction occurring when a neutron decays into a proton, electron and anti-neutrino can, at energies much below the mass of the  $W$  boson, be treated as a four-point vertex with quartic coupling strength  $G_F$ , the Fermi Coupling constant as shown in figure 7.2.

This analysis examines the anomalous quartic gauge couplings  $\alpha_4$  and  $\alpha_5$ , which are introduced as part of an EFT described in chapter 2. They appear in the Lagrangian

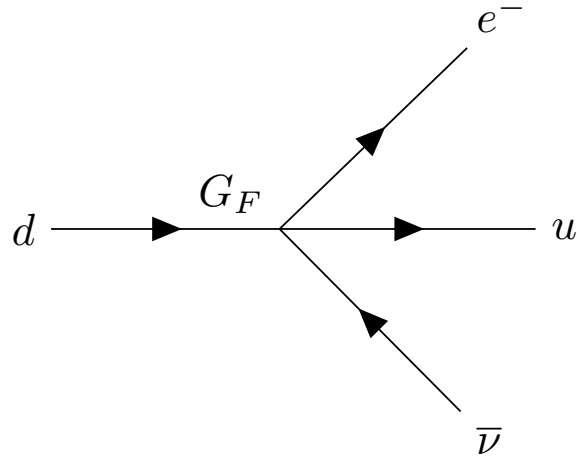


**Figure 7.2:** Four-point vertex proposed for explanation of beta decay by Fermi.

through the following terms:

$$\alpha_4 [\text{Tr}(V^\mu V_\mu)]^2 \text{ and } \alpha_5 \text{Tr}(V^\mu V_\nu) \text{Tr}(V^\nu V_\mu), \quad (7.1)$$

where  $V_\mu$  corresponds, in a carefully chosen gauge, to a linear combination of the massive gauge bosons  $W^+$ ,  $W^-$  and  $Z$ . These terms affect the coupling constants for the standard model vertices  $W^+W^- \rightarrow W^+W^-$  and  $W^+W^- \rightarrow ZZ$  as well as introducing the new vertex  $ZZ \rightarrow ZZ$ . Vector boson scattering is an appropriate process to consider for a study of the anomalous gauge couplings  $\alpha_4$  and  $\alpha_5$  as quartic gauge boson self-interaction vertices will be present in the dominant channels for such interactions. Example vector boson scattering Feynman diagrams showing sensitivity to quartic gauge boson self-interaction vertices are shown in figure 7.3.

As CLIC is purposefully deigned for high precision measurements it is ideal for a study into vector boson scattering. The application of Particle Flow Calorimetry with fine granularity calorimeters gives CLIC excellent jet energy resolution, which allows it to clearly characterise multi-jet final states. When considering the invariant mass of these paired up jets, the nominal jet energy resolution for CLIC allows for accurate separation of  $W$  and  $Z$  bosons, which will be invaluable for event selection. This precision also helps CLIC to characterise final states containing missing energy in the form of neutrinos. The cross sections for vector boson scattering processes are sufficiently large at the proposed running energies for CLIC to give a large signal sample size for this analysis. Finally, this study offers the potential to give results several orders of magnitude better than the complementary studies performed at the

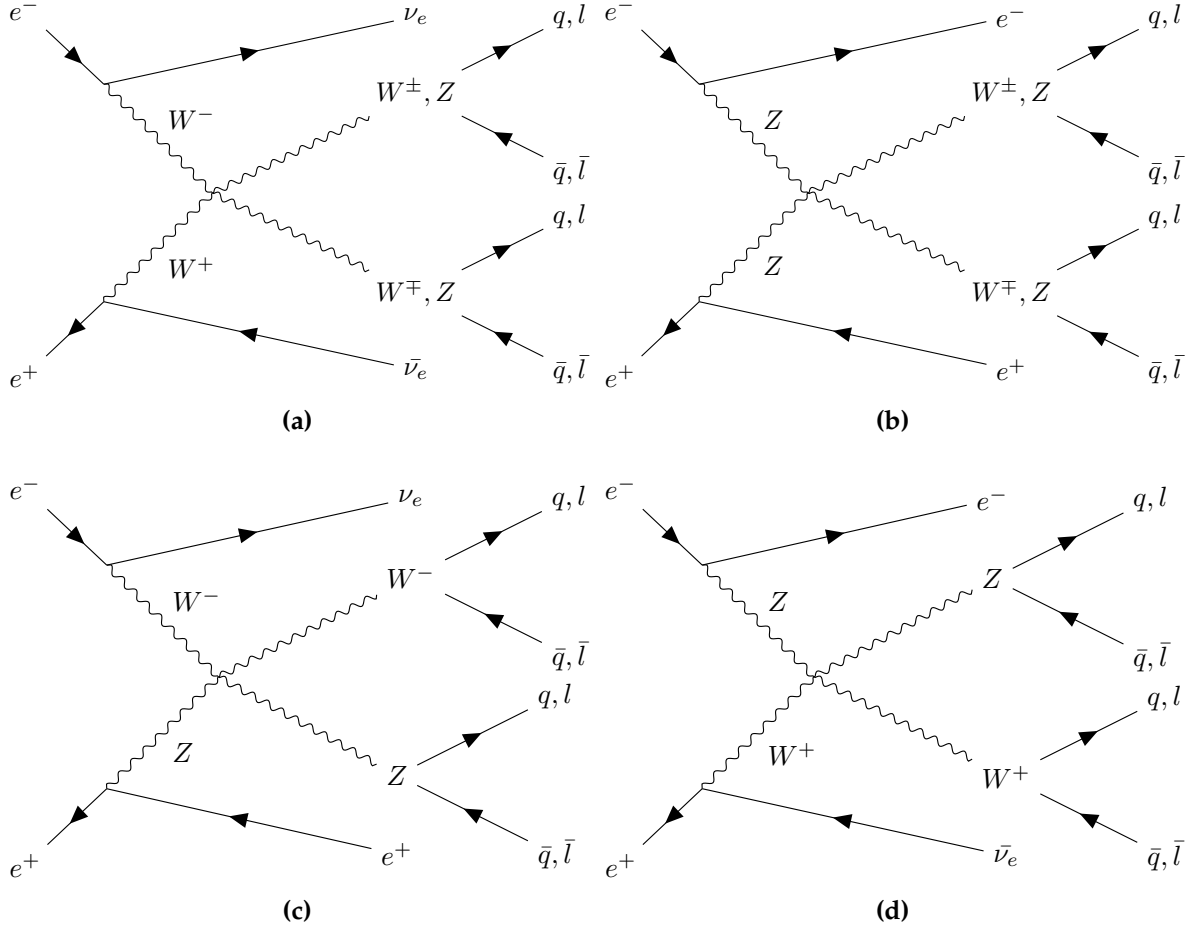


**Figure 7.3:** Example of vector boson scattering Feynman diagrams showing sensitivity to quartic gauge boson self-interaction vertices. The diagrams selected here are relevant for the CLIC experiment. In these diagrams  $q$  represents  $u, \bar{u}, d, \bar{d}, s, \bar{s}, c, \bar{c}, b$  or  $\bar{b}$ ;  $l$  represents  $e^\pm, \mu^\pm$  or  $\tau^\pm$ ; and  $\nu$  represents  $\nu_e, \bar{\nu}_e, \nu_\mu, \bar{\nu}_\mu, \nu_\tau$  and  $\bar{\nu}_\tau$ .

LHC. This is due to the reduction in hadronic backgrounds and the larger  $\sqrt{s}$  obtained when colliding leptons as opposed to protons. All of the above reasons make a strong case for performing this analysis at CLIC.

This study focuses on determining the sensitivity of CLIC to the anomalous gauge couplings based solely upon the vector boson scattering processes where the outgoing bosons decay purely hadronically. This decision was made as the hadronic channels are the dominant decay modes of the  $W$  and the  $Z$  boson, with branching fractions of the order of 70% for both [11], and given CLIC has excellent jet energy resolution. Therefore, the signal final states in this analysis are:  $\nu\nu qqqq$ ,  $l\nu qqqq$  and  $ll qqqq$ .

## 7.2 Event Generation, Simulation and Reconstruction

Events were generated for this analysis using Whizard [64, 65] version 1.95. Due to the presence of beamstrahlung photons in the CLIC beam, events were generated from collisions of  $e^+e^-$ ,  $e^+\gamma$ ,  $\gamma e^-$  and  $\gamma\gamma$ . The energy spectra used for all particles involved in these collisions took into account the effects of radiation in the form of beamstrahlung photons and the intrinsic energy spread of the CLIC beam. Furthermore, events involving the interaction between the electromagnetic field of the beam particles involving quasi-real photon mediators with low momenta, described by the Weizsäcker-Williams approximation or the Equivalent Photon Approximation (EPA), were generated using Whizard and included in this analysis. Fragmentation and hadronisation was implemented using PYTHIA 6.4 [40] that was tuned for OPAL  $e^+e^-$  collision data recorded at LEP [41]. The decays of tau leptons was simulated using TAUOLA [42]. The full list of events simulated for this analysis, along with their standard model cross section at 1.4 TeV can be found in table 7.1. The samples generated comprise all final states that would be relevant, either as signal or background processes, for an analysis involving the purely hadronic decay channels involved in a vector boson scattering process. In full they are:

- Vector boson scattering signal final states that are expected to show sensitivity to the anomalous couplings:  $e^+e^- \rightarrow \nu\nu qqqq$ ,  $e^+e^- \rightarrow l\nu qqqq$  and  $e^+e^- \rightarrow llqqqq$ .
- Four jet final states arising from  $e^+e^-$  interactions:  $e^+e^- \rightarrow qqqq$ .
- Two jet final states arising from  $e^+e^-$  interactions:  $e^+e^- \rightarrow \nu\nu qq$ ,  $e^+e^- \rightarrow l\nu qq$ ,  $e^+e^- \rightarrow llqq$  and  $e^+e^- \rightarrow qq$ .
- Four jet final states arising from the interactions of either  $e^+$  or  $e^-$  with a beamstrahlung photon:  $\gamma_{BS}e^- \rightarrow qqqqe^-$ ,  $e^+\gamma_{BS} \rightarrow qqqqe^+$ ,  $\gamma_{BS}e^- \rightarrow qqqq\nu$  and  $e^+\gamma_{BS} \rightarrow qqqq\nu$ .
- Four jet final states arising from the interactions of either  $e^+$  or  $e^-$  with the electromagnetic field of the opposing beam particle. These cross sections are calculated using the EPA approximation, which represents the electromagnetic field of the opposing beam particle as a series of photons, so the final states appear as interactions of  $e^+$  or  $e^-$  with photons:  $\gamma_{EPA}e^- \rightarrow qqqqe^-$ ,  $e^+\gamma_{EPA} \rightarrow qqqqe^+$ ,  $\gamma_{EPA}e^- \rightarrow qqqq\nu$  and  $e^+\gamma_{EPA} \rightarrow qqqq\nu$ .

- Four jet final states arising from the interaction of the electromagnetic fields of opposing beam particles using the EPA approximation:  $\gamma_{\text{EPA}} \gamma_{\text{EPA}} \rightarrow \text{qqqq}$ .
- Four jet final states arising from the interaction of the electromagnetic field of either  $e^+$  or  $e^-$  using the EPA approximation with a beamstrahlung photon:  $\gamma_{\text{EPA}} \gamma_{\text{BS}} \rightarrow \text{qqqq}$  or  $\gamma_{\text{BS}} \gamma_{\text{EPA}} \rightarrow \text{qqqq}$ .
- Four jet final states arising from the interaction of two beamstrahlung photons:  $\gamma_{\text{BS}} \gamma_{\text{BS}} \rightarrow \text{qqqq}$ .

In the above list q represents u,  $\bar{u}$ , d,  $\bar{d}$ , s,  $\bar{s}$ , c,  $\bar{c}$ , b or  $\bar{b}$ ; l represents  $e^\pm$ ,  $\mu^\pm$  or  $\tau^\pm$ ; and  $\nu$  represents  $\nu_e$ ,  $\bar{\nu}_e$ ,  $\nu_\mu$ ,  $\bar{\nu}_\mu$ ,  $\nu_\tau$  and  $\bar{\nu}_\tau$ .

The samples used in this analysis were simulated with the CLID\_ILD detector model [27]. Further details of this detector model can be found in chapter 3. The simulation was performed in MOKKA [36], a GEANT4 [37] wrapper providing detailed geometric descriptions of detector concepts for the linear collider. Events were reconstructed using MARLIN [38], a c++ framework designed for reconstruction at the linear collider. PandoraPFA [24,25] was used to apply Particle Flow Calorimetry in the reconstruction, the full details of which can be found in chapter 3.

The effect of the  $\gamma\gamma \rightarrow \text{Hadron}$  backgrounds, discussed in section 1.1.2, was incorporated into this analysis by overlaying  $\gamma\gamma \rightarrow \text{Hadron}$  events onto the signal and background event samples that were used. The overlaid backgrounds were added prior to reconstruction so that their impact on the reconstruction was fully accounted for. For a given event, the exact number of background events overlaid is drawn from a Poisson distribution with a mean of 3.2 (1.3) events per bunch crossing at 3 (1.4) TeV [4].

## 7.3 Modelling of Anomalous Gauge Couplings

It was necessary when generating samples that are sensitive to the anomalous gauge couplings  $\alpha_4$  and  $\alpha_5$  to use Whizard version 1.97, instead of the previously quoted version 1.95. This change was required as version 1.97 contained a unitarisation scheme that ensured cross sections for processes involving longitudinal gauge boson scattering were bound at the energies considered i.e. the TeV scale.

Final State	Cross Section 1.4 TeV [fb]
$e^+e^- \rightarrow \nu\nuqqqq$	24.7
$e^+e^- \rightarrow l\nuqqqq$	110.4
$e^+e^- \rightarrow llqqqq$	62.1
$e^+e^- \rightarrow qqqq$	1245.1
$e^+e^- \rightarrow \nu\nuqq$	787.7
$e^+e^- \rightarrow l\nu qq$	4309.7
$e^+e^- \rightarrow llqq$	2725.8
$e^+e^- \rightarrow qq$	4009.5
$\gamma_{\text{EPA}} e^- \rightarrow qqqqe^-$	287.1
$\gamma_{\text{BS}} e^- \rightarrow qqqqe^-$	1160.7
$e^+ \gamma_{\text{EPA}} \rightarrow qqqqe^+$	286.9
$e^+ \gamma_{\text{BS}} \rightarrow qqqqe^+$	1156.3
$\gamma_{\text{EPA}} e^- \rightarrow qqqq\nu$	32.6
$\gamma_{\text{BS}} e^- \rightarrow qqqq\nu$	136.9
$e^+ \gamma_{\text{EPA}} \rightarrow qqqq\nu$	32.6
$e^+ \gamma_{\text{BS}} \rightarrow qqqq\nu$	136.4
$\gamma_{\text{EPA}} \gamma_{\text{EPA}} \rightarrow qqqq$	753.0
$\gamma_{\text{EPA}} \gamma_{\text{BS}} \rightarrow qqqq$	4034.8
$\gamma_{\text{BS}} \gamma_{\text{EPA}} \rightarrow qqqq$	4018.7
$\gamma_{\text{BS}} \gamma_{\text{BS}} \rightarrow qqqq$	21406.2

**Table 7.1:** Cross sections of signal and background processes at 1.4 TeV. In the above table q represents u,  $\bar{u}$ , d,  $\bar{d}$ , s,  $\bar{s}$ , c,  $\bar{c}$ , b or  $\bar{b}$ ; l represents  $e^\pm$ ,  $\mu^\pm$  or  $\tau^\pm$ ; and  $\nu$  represents  $\nu_e$ ,  $\bar{\nu}_e$ ,  $\nu_\mu$ ,  $\bar{\nu}_\mu$ ,  $\nu_\tau$  and  $\bar{\nu}_\tau$ . The EPA and BS subscript on the incoming photon indicates whether the photon is generated from the equivalent photon approximation or beamstrahlung.

The sensitivity of an individual event to the anomalous gauge couplings is determined through an event weight. This weight is given by the ratio of the squares of the matrix element used in the cross section calculation, one matrix element using non-zero values of  $\alpha_4$  and  $\alpha_5$  and the other matrix element using the standard model values of  $\alpha_4$  and  $\alpha_5$ , i.e. 0. The weight varies as a function of  $\alpha_4$  and  $\alpha_5$  as well as varying on an event by event basis as the kinematics of the final state changes. Examples of the event weights as a function of  $\alpha_4$  and  $\alpha_5$  for selected events is shown in figure 7.4 for 1.4 TeV  $\nu\nuqqqq$  final state events.

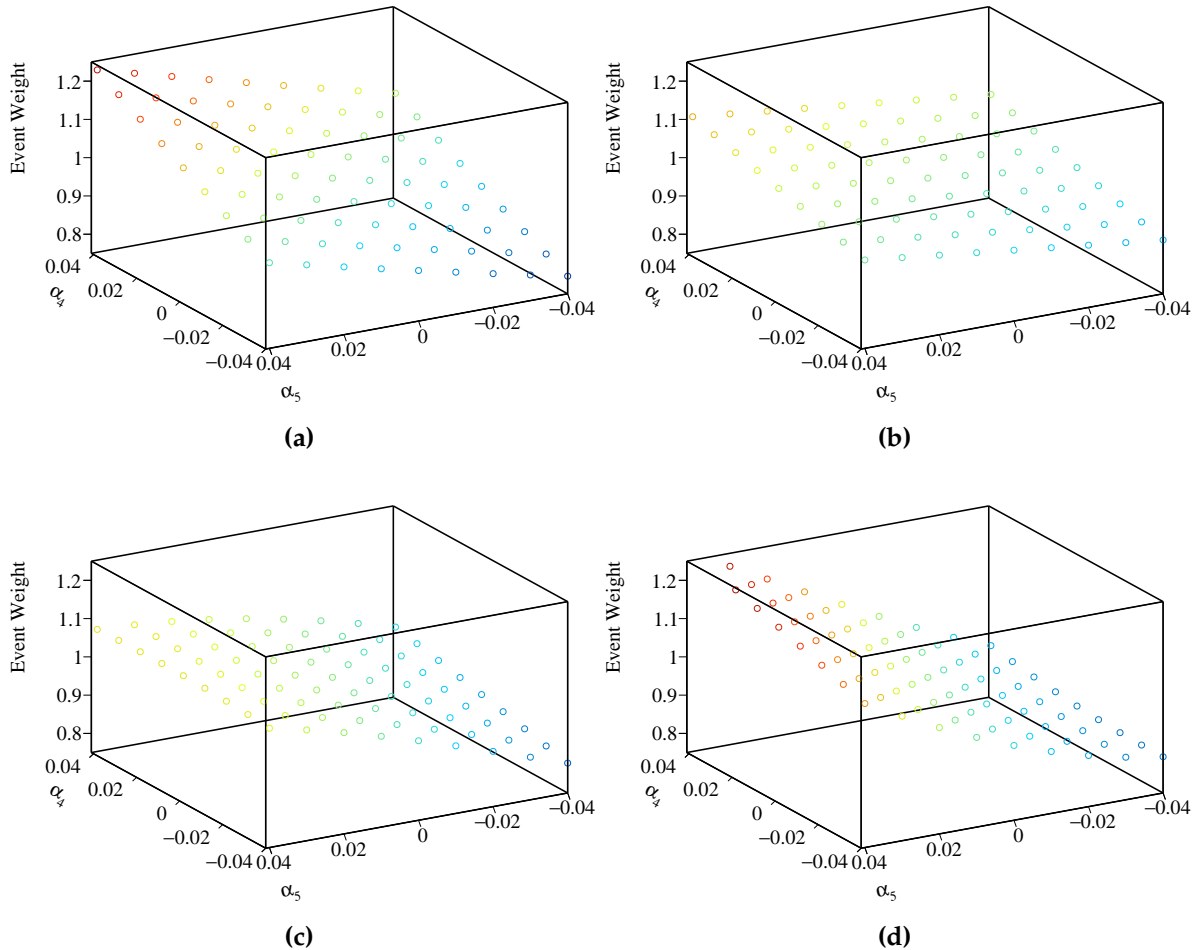


**Figure 7.4:** The event weight as a function of the anomalous couplings  $\alpha_4$  and  $\alpha_5$  for a selection of  $\nu\nu\text{qqqq}$  final state events at 1.4 TeV.

This reweighting procedure has many advantages over the alternative of generating new samples with fixed  $\alpha_4$  and  $\alpha_5$ , notably the absence of systematic errors arising from new event generation, simulation and reconstruction. Only final states showing a sensitivity to  $\alpha_4$  and  $\alpha_5$  require reweighting. To determine those states a comparison was made between the cross section using the standard model values of  $\alpha_4$  and  $\alpha_5$ , i.e. 0, and the same calculation using non-zero values of these couplings at 1.4 TeV. This comparison was performed on all of the generated samples listed in table 7.1 and the results for samples showing sensitivity to the couplings can be found in table 7.2.

The cross sections were found to differ when using non-zero values for the anomalous couplings in comparison to the standard model prediction only for the vector boson scattering signal final states  $\nu\nu\text{qqqq}$ ,  $\text{l}\nu\text{qqqq}$  and  $\text{ll}\text{qqqq}$ . In reality, non-zero

Final State	Cross Section [fb] ( $\alpha_4 = \alpha_5 = 0.00$ )	Cross Section [fb] ( $\alpha_4 = \alpha_5 = 0.05$ )	Percentage Change[%]
$e^+ e^- \rightarrow \nu\nu qqqq$	24.7	34.6	+40.1
$e^+ e^- \rightarrow l\nu qqqq$	115.3	113.0	-2.0
$e^+ e^- \rightarrow llqqqq$	62.1	68.6	+10.5

**Table 7.2:** Cross sections for selected processes showing the effect of the anomalous gauge couplings  $\alpha_4$  and  $\alpha_5$  at 1.4 TeV.

anomalous couplings would change the cross sections of all processes considered; however, the sensitivity would only arise from high order terms in the Lagrangian. Such terms would not be dominant in determining the cross section and so are omitted from the generator making certain final states appear invariant to changes in the anomalous couplings.

The cross section calculations show that the most sensitive final state to the anomalous gauge couplings is  $\nu\nu qqqq$ ; therefore, this analysis will focus entirely upon this final state. As the  $l\nu qqqq$  final state has a much reduced sensitivity in comparison to the  $\nu\nu qqqq$  state and as the  $llqqqq$  can be easily vetoed from the analysis, as will be shown in subsequent chapters, it is only necessary to consider the sensitivity of the  $\nu\nu qqqq$  final state. For the aforementioned reasons the  $l\nu qqqq$  and  $llqqqq$  final states will be treated as backgrounds that are invariant to changes in the anomalous couplings  $\alpha_4$  and  $\alpha_5$ .

In order to determine the anomalous gauge coupling sensitive event weights, it was necessary to use the anomalous gauge coupling model in Whizard, however, this enforced a unit CKM matrix. This has a negligible impact on this analysis as no significant differences were observed when comparing a variety of reconstructed level distributions for samples of  $\nu\nu qqqq$  generated with a standard model and a unit CKM matrix. Furthermore, flavour tagging of jets was not used in this analysis as it offered negligible gains when performing event selection, which means any differences in quark flavour due to the unit CKM matrix for the  $\nu\nu qqqq$  final state should be irrelevant.

## 7.4 Data Analysis

The focus of this section is to describe the post reconstruction procedure applied to the signal and background events, described in 7.2, to extract the relevant information needed for the sensitivity study.

### 7.4.1 Jet Finding

After the default reconstruction, described in chapter 3, two further processors are applied to remove any reconstructed particle flow objects (PFOs) originating from beam related backgrounds from the event. Further details on beam related backgrounds at CLIC can be found in section 1.1.2. The first processor, the CLICTrackSelection, is designed to veto poorly reconstructed tracks and to reject tracks where the time of arrival at the calorimeter when comparing a helix fit to the track and a straight line of flight differ by 50 ns. The latter would indicate the tracked particle does not create the calorimetric energy deposits that it has been associated to. The second processor, the CLICPfoSelector, applies cuts to the  $p_T$  and timing information of the PFOs. These cuts vary as a function of position in the detector and the reconstructed particle type to target regions of the detector where backgrounds are more prominent, primarily low  $p_T$  from  $\gamma\gamma \rightarrow \text{Hadrons}$  events. Three configurations of the CLICPfoSelector have been developed for the CLIC environment and were considered for this analysis. They are, in order of increasing background rejection, the Loose, Default and Tight selections. The full details of each can be found here [25].

After the application of the CLICTrackSelection and CLICPfoSelector the Marlin-FastJet processor, a wrapper for the FastJet [66] processor, was used to cluster the events into four jets. These jets are then paired up to form two candidate bosons. This pairing is performed on the assumption that the correct pairing is achieved when the difference between the invariant masses of the candidate bosons is a minima. In the case of the signal final state,  $\nu\nu qqqq$ , it is assumed that the four jets and two candidate bosons map onto the four quarks and the two outgoing bosons involved in the vector boson scattering process. The jet clustering was done using the longitudinally invariant  $k_t$  jet algorithm in exclusive mode. In contrast to the inclusive mode, the exclusive mode allows the user to request a fixed number of jets in the output from MarlinFastJet. The longitudinally invariant  $k_t$  algorithm proceeds as follows:

- For each pair of particles,  $i$  and  $j$ , the  $k_t$  distance,  $d_{ij}$ , and beam distance,  $d_{iB} = p_t^2$ , are calculated.  $d_{ij}$  is defined as:

$$d_{ij} = \min(p_{ti}^2, p_{tj}^2) \Delta R_{ij}^2 / R^2 \quad (7.2)$$

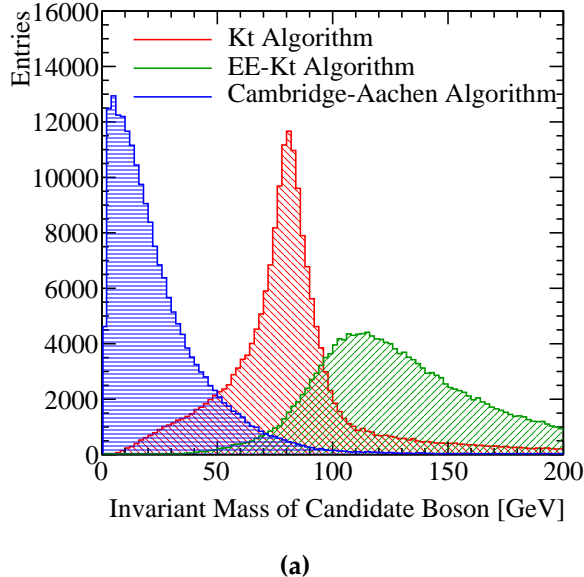
where  $\Delta R_{ij}^2 = (y_i - y_j)^2 + (\phi_i - \phi_j)^2$ ,  $p_t$  is the transverse momentum of the particle with respect to the beam axis,  $y_i$  is the rapidity of particle  $i$  and  $\phi_i$  is the azimuthal angle of particle  $i$ .  $R$  is a configurable parameter that typically is of the order of 1.

- The minimum distance,  $d_{\min}$ , of all the  $k_t$  and beam distances is found. If the minimum occurs for a  $k_t$  distance, particles  $i$  and  $j$  are merged, summing their 4-momenta. If the beam distance is the minima, particle  $i$  was declared to be part of the "beam" jet and the particle is removed from the list of particles and not included in the final jet output.
- This is repeated until the desired number of jets was created. Alternatively, in inclusive mode this would be repeated until no particles are left in the event.

Two other clustering algorithms were considered, but, as figure 7.5 shows, were found to be inappropriate for the experimental conditions at CLIC. These alternative algorithm choices are applied in the same manor as the longitudinally invariant  $k_t$  algorithm, however, they differ in the definition of  $d_{ij}$  and  $d_{iB}$ .

The first alternative jet algorithm considered was the  $k_t$  algorithm for  $e^+e^-$  colliders, the EE\_kt or Durham algorithm, where  $d_{ij} = 2\min(E_i^2, E_j^2)(1 - \cos\theta_{ij})$  and  $d_{iB}$  is not used.  $\theta_{ij}$  is the opening angle of particles  $i$  and  $j$  meaning that in the collinear limit  $d_{ij}$  corresponds to the relative transverse momenta of the particles. The major failure of this algorithm when applied to CLIC is the absence of  $d_{iB}$ , which leads to many beam related background particles being associated to jets. As figure 7.5 shows, the invariant mass of the paired jets, which should peak around the W and Z boson masses, is much larger than expected, due to the presence of the beam related backgrounds in the jets. Also this algorithm is not invariant to boosts along the beam direction making it inappropriate to use at CLIC as the beam induced backgrounds modify the nominal collision kinematics.

The second alternative jet algorithm considered was the Cambridge-Aachen jet algorithm where  $d_{ij} = \Delta R_{ij}^2 / R^2$  and  $d_{iB} = 1$ . This algorithm performed poorly as it does not accounts for the transverse momentum or the energy of the particles being



(a)

**Figure 7.5:** The reconstructed masses for different choices of jet algorithm for 1.4 TeV  $\nu\nu\text{qqqq}$  final state events. The masses are determined by forcing the events into 4 jets and then pairing the jet pairs to form candidate bosons. The jet pairing configuration is determined by pairing jets such that the mass differences between the two candidate bosons is a minimum. These samples should be dominated by vector boson scattering involving pairs of outgoing W bosons and so it is expected that a peak at the W boson mass,  $m_W = 80.385 \pm 0.015$  GeV [11], should be observed. As this does not occur for the Cambridge-Aachen algorithm or the EE\_kt algorithm they were deemed unsuitable for this analysis. In the case of the kt algorithm and the EE\_kt algorithm an R parameter of 0.7 was used.

clustered. In essence, this is a cone clustering algorithm with a cone radius defined through  $\Delta R_{ij} = R$ , which even for large R was found to discard too much energy in the event to be useful for this analysis. This can be seen in figure 7.5 where the invariant mass of the paired jets is much lower than expected. This algorithm is appropriate for events that contain highly boosted jets, however, at CLIC the jets are too disperse for this algorithm to be successful.

### Optimal Jet Finding Algorithm

Optimisation of the jet finding procedure was performed on both the PFO selection, described in section 7.8, and the value of the R parameter used in the longitudinally invariant  $k_t$  algorithm. The optimal configuration for the jet algorithm at 1.4 TeV was found to use default selected PFOs and an R parameter of 0.9.

The optimisation procedure involved performing the sensitivity study, described in section 7.6, using solely the  $\nu\nu\text{qqqq}$  signal final state. This led to the construction of a  $\chi^2$  surface from which confidence contours can be extracted in the  $\alpha_4$  and  $\alpha_5$  space. The  $\chi^2$  surface was constructed by comparing the distribution of the invariant mass of the visible system,  $M_{VV}$ , with and without the effect of the anomalous couplings  $\alpha_4$  and  $\alpha_5$ . The  $\chi^2$  surface for the optimal jet configuration at 1.4 TeV using the  $\nu\nu\text{qqqq}$  signal final state is shown in figure 7.6a. This methodology ensured that the optimisation was done with respect to the physics of interest without having to perform the jet reconstruction for the large number of background events for each jet algorithm configuration considered.

Confidence limits on the individual parameters  $\alpha_4$  and  $\alpha_5$  were determined by setting the corresponding coupling term to zero and examining the one dimensional  $\chi^2$  distribution. A fourth order polynomial was fitted to the minima of this distribution and the one sigma confidence limit defined using  $\Delta\chi^2$  of 1.  $\Delta\chi^2$  is defined as the change in  $\chi^2$  with respect to the minima in the  $\chi^2$  surface. Note that for the two dimensional  $\chi^2$  surface a one sigma confidence limit is given by a  $\Delta\chi^2$  of 2.28 due to the additional degree of freedom in the fit. The one dimensional  $\chi^2$  distribution for  $\alpha_4$  and  $\alpha_5$ , assuming  $\alpha_5 = 0$  and  $\alpha_4 = 0$  respectively, for the optimal jet configuration at 1.4 TeV using the  $\nu\nu\text{qqqq}$  signal final state is shown in figures 7.6b and 7.6c. Using these distributions the one sigma confidence limits on  $\alpha_4$  are -0.0038 to 0.0047 and on  $\alpha_5$  are -0.0027 to 0.0030.

#### 7.4.2 Lepton Finding

An isolated lepton finder was included in the analysis chain in an attempt to reject background final states containing leptons. As it is unlikely that isolated leptons will form via hadronisation, because all hadronisation products are boosted along the direction of the parent quark, it is likely that they originate from the primary interaction occurring at the IP. This makes the number of isolated leptons a powerful discriminating variable for discerning final states containing leptons.

The isolated lepton finder attempts to find whether a PFO is an electron or muon based on the calorimetric energy deposits. If the calorimetric energy deposits for a PFO are consistent with that of an electron or muon and there is a single associated track then cuts are placed on that associated track to determine whether the track

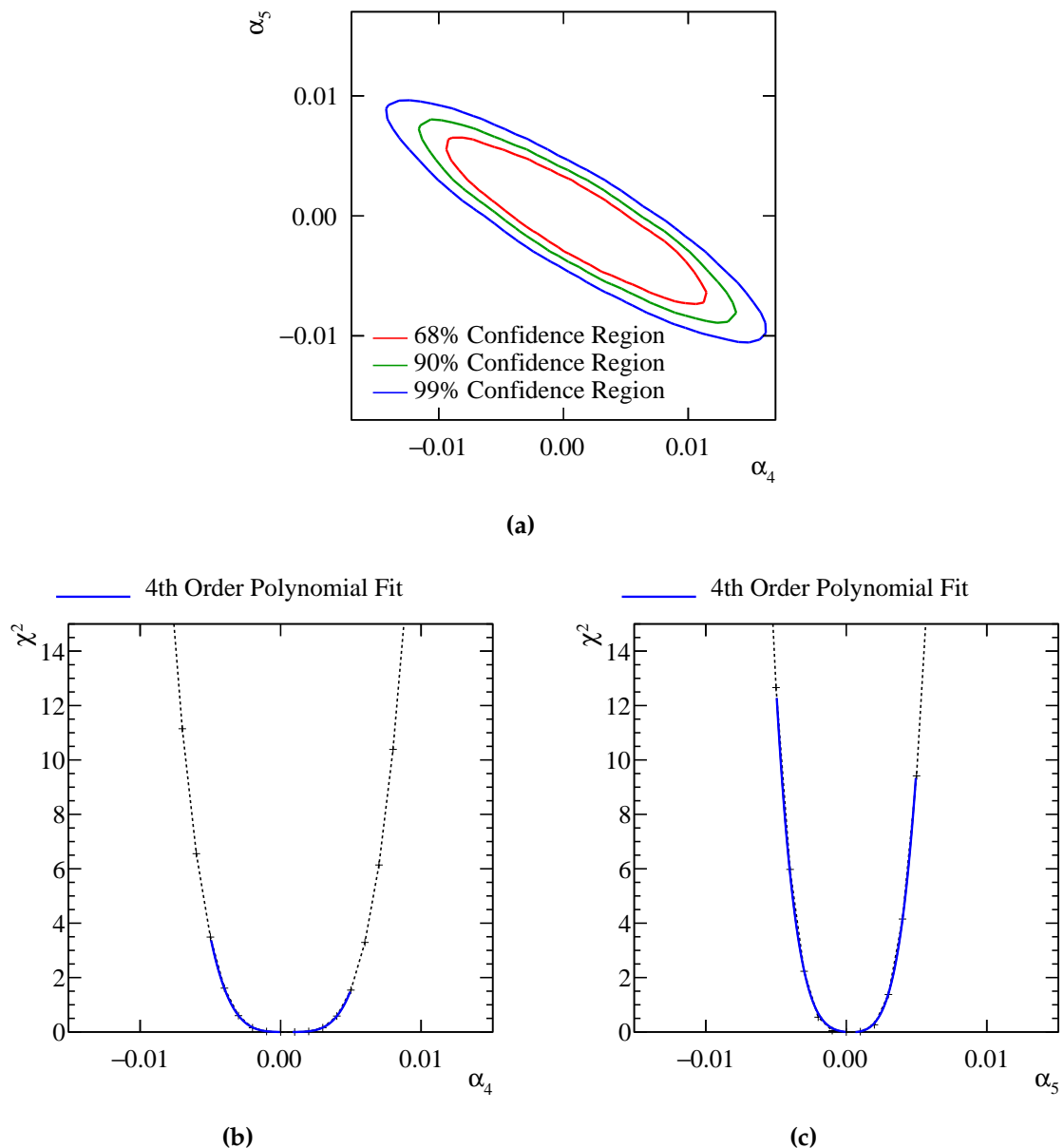


**Figure 7.6:**  $\chi^2$  sensitivity distributions from a fit to  $M_{VV}$  for the signal  $qqqq\nu\nu$  final state only at 1.4 TeV. These results use the optimal jet algorithm configuration of selected PFOs and an R parameter of 0.9 in the  $k_t$  algorithm. (a)  $\chi^2$  sensitivity contours in  $\alpha_4$  and  $\alpha_5$  space. (b)  $\chi^2$  as a function of  $\alpha_4$  assuming  $\alpha_5 = 0$ . (c)  $\chi^2$  as a function of  $\alpha_5$  assuming  $\alpha_4 = 0$ .

originates from the IP. If the track cuts deem the PFO to have originated from the IP, isolation cuts restricting the energy deposited in the calorimeters within a cone surrounding the PFO are applied to ensure the particles does not belong to a jet. If a PFO passes all of these criteria then it is counted as an isolated lepton. The efficiency of the lepton finder is summarised in table 7.3.

Final State	$\epsilon_{\text{Lepton Finding}}$
$e^+ e^- \rightarrow \nu\nu qqqq$	99.7
$e^+ e^- \rightarrow l\nu qqqq$	48.9

**Table 7.3:** The efficiency of isolated lepton finding at 1.4 TeV for the  $\nu\nu qqqq$  and  $l\nu qqqq$  final states. Efficiency here is defined as the fraction of events where no isolated leptons were found.

### 7.4.3 Discriminant Variables

The next stage of the analysis involved the calculation of a number of event-based variables that were found to be useful for this analysis. The variables that were calculated are as follows:

- **Particle level variables:**
  - Number of PFOs in each jet.
  - Energy of the highest energy PFO.
  - Energy of the highest energy electron.
  - Cosine of the polar angle of the highest energy track.
  - The number of isolated leptons found using the isolated lepton finder.
- **Candidate boson variables:**
  - Energy of the candidate bosons.
  - Invariant mass of the candidate bosons.
  - Acolinearity of the candidate boson pair, which is defined as 180 degrees minus the opening angle of the pair of bosons in the rest frame of the detector.

- **Event based variables:**

- The invariant mass of the visible system,  $M_{VV}$ .
- The vector sum of the transverse momentum of all PFOs in the event.
- Sphericity, defined through the sphericity tensor  $S^{ab}$ :

$$S^{ab} = \frac{\sum_i p_i^\alpha p_j^\alpha}{\sum_{i,\alpha=1,2,3} |p_i^\alpha|^2} \quad (7.3)$$

Where  $p_i$  are the components of the momenta of PFO  $i$  in the rest frame of the detector and the sum  $\sum_i$  runs over all particles in the event. Sphericity is defined as  $S = \frac{3}{2}(\lambda_2 + \lambda_3)$ , where  $\lambda_i$  are the eigenvalues of the sphericity tensor defined such  $\lambda_1 \geq \lambda_2 \geq \lambda_3$ . This provides a measure of how spherical the reconstructed event topology is with isotropic events having  $S \approx 1$ , while two jet events have  $S \approx 0$ .

- **Jet clustering parameter** variables,  $y_{ij}$  where  $i = 3, 4$  and  $j = i + 1$ . These are the smallest  $k_t$  distance found when combining  $j$  jets into  $i$  jets. The variable used in the multivariate analysis is  $-\log_{10}(y_{ij})$ .

#### 7.4.4 Jet Energy Resolution at CLIC

It is important to flag up the importance of the jet energy resolution that is extensively discussed in chapters ?? and 6. Many of the discriminant variables that are calculated for this analysis are dependant upon the jet energy resolution. In particular, all variables related to the candidate bosons, which are formed from pairing up jets, are totally dependent upon the measurement of jet energies.

The jet energy resolution as a function of the jet energy is shown in figure 7.7 for the  $\nu\nu qqqq$  final state, at 1.4 TeV, used in this analysis. The MC jet energy is obtained by pairing up quarks appearing in the final state to the reconstructed jets. In the calculation of the jet energy resolution presented here, the mean and RMS of the reconstructed jet energy are calculated over a narrower range than used in the previous chapters, 60% of the data with narrowest RMS as opposed to 90%. This is to account for the effects of jet finding and beam-induced background that are not present in the jet energy resolution studies presented in preceding chapters. The jet

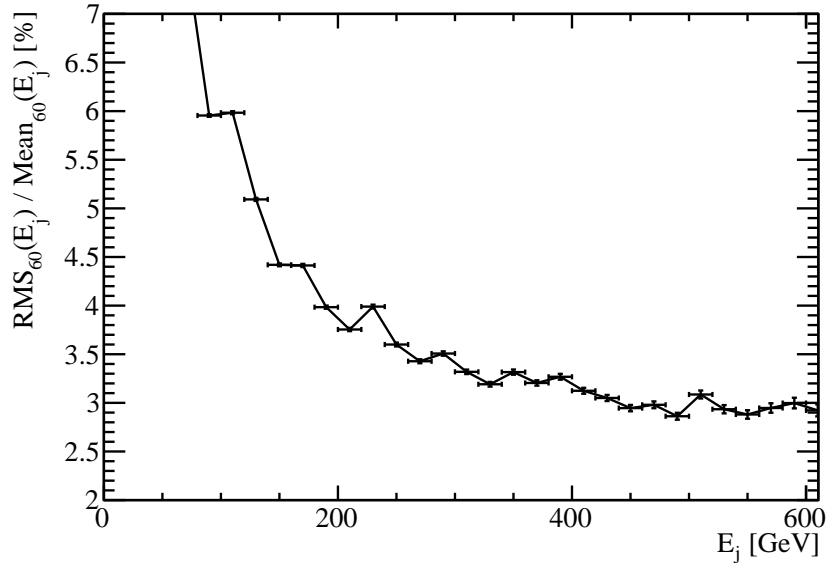


**Figure 7.7:** The jet energy resolution as a function of the jet energy for the  $\nu\nu\text{qqqq}$  final state at 1.4 TeV.

energy resolutions reported here are comparable to those quoted in earlier chapters from the standard reconstruction.

## 7.5 Event Selection

As described in section 7.3, the signal for this analysis is the  $\nu\nu\text{qqqq}$  final state, while the backgrounds consist of all two and four jet final states that could be confused with the signal after reconstruction. A complete list of signal and background final states used for this analysis, alongside their standard model cross sections, can be found in table 7.1. In an attempt to isolate the signal final state from the backgrounds an event selection procedure consisting of a set of preselection cuts followed by the application of a multivariate analysis (MVA), was applied. The full details of this procedure are given in the following section. All event numbers used in this analysis have been normalised, prior to event selection, to the correct luminosity for CLIC running at 1.4 TeV.

### 7.5.1 Preselection

A refined selection of the  $\nu\nu\text{qqqq}$  signal final state is achieved using MVA. However, to ensure efficiency in the training and application of that MVA a number of simple preselection cuts were developed to veto obvious background final states prior to the application of the MVA. These cuts were developed to reject as much background as possible, while retaining enough signal to make the analysis viable. Preselection cuts were applied to the transverse momentum of the system and the number of isolated leptons found in the event. The raw distributions of these variables is shown in figure 7.8 and based on these distributions the following cuts were applied:

- Transverse momentum of system  $> 100$  GeV. This cut is effective due to the presence of missing energy in the form of neutrinos in the signal final state.
- Number of isolated leptons in system  $= 0$ . This cut is effective as the signal final state does not contain leptons, while numerous background final states do.

The impact of these preselection cuts can be found in table 7.4 in section 7.5.3.

### 7.5.2 Multivariate analysis

Having established the preselection cuts a MVA was applied, using the TMVA toolkit [67], to refine the event selection. The signal and background final state samples were halved; one half sample was used to train the MVA and the remaining half sample was used in the subsequent analysis. The sample sizes for the signal and backgrounds were sufficiently large that halving them in this way had a negligible impact on the subsequent analysis. The following variables were used for training of the MVA:

- Number of PFOs in each jet.
- Energy of the highest energy PFO.
- Energy of the highest energy electron.
- Cosine of the polar angle of the highest energy track.
- Energy of the candidate bosons.
- Invariant mass of the candidate bosons.
- Acolinearity of the candidate boson pair.

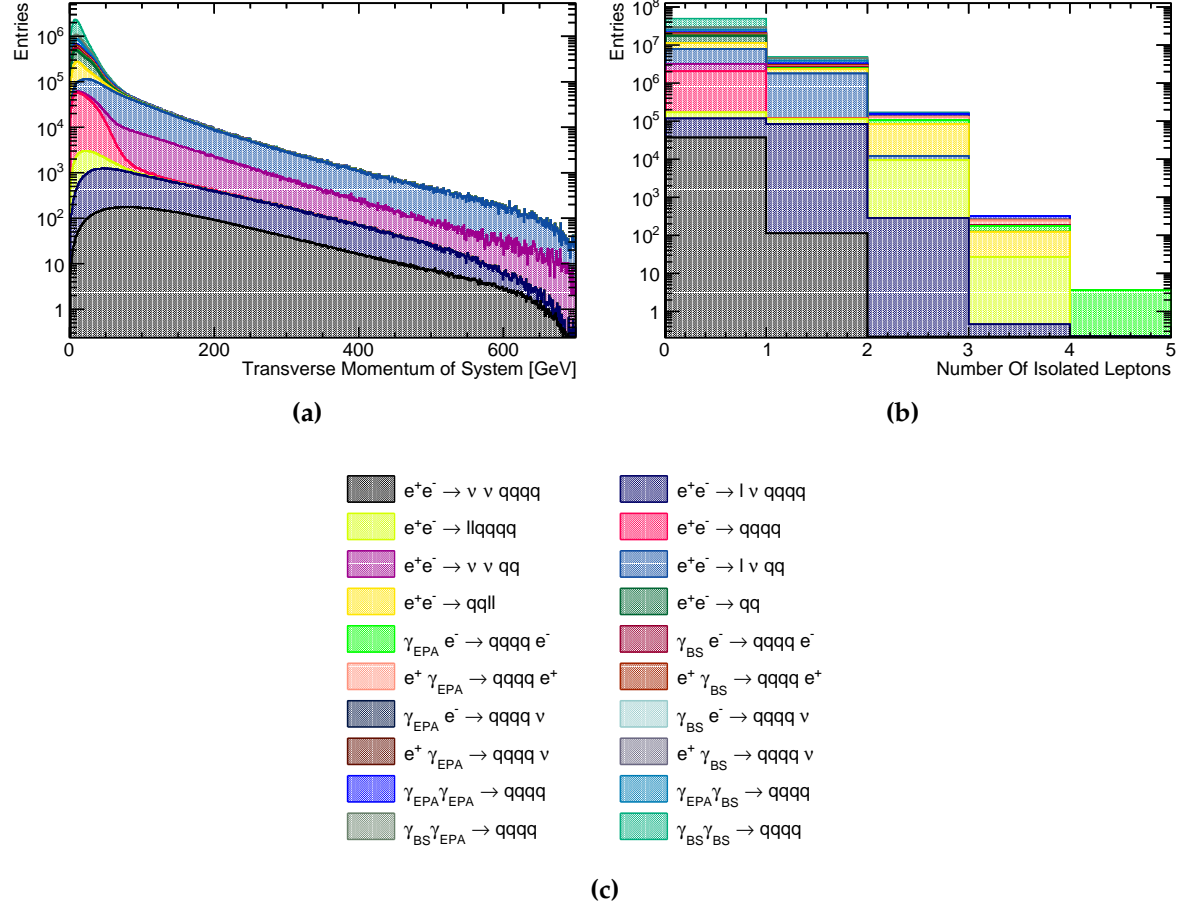


**Figure 7.8:** Distribution of variables cut on in the preselection at 1.4 TeV. (a) The transverse momentum of the visible system. (b) The number of isolated leptons in the system. (c) The legend for the preceding plots.

- The vector sum of the transverse momentum of all PFOS in the event.
- Sphericity.
- Jet clustering parameter variables,  $y_{ij}$  where  $i = 3, 4$  and  $j = i + 1$ . The variable used in the multivariate analysis is  $-\log_{10}(y_{ij})$ .

A variety of MVA options were considered and it was found that the optimal algorithm was the boosted decision tree (BDT) as shown by figure 7.9.

The BDT was further optimised by varying the number of trees used, the depth of the trees and the number of cuts applied and an optimal significance,  $S/\sqrt{(S+B)}$ , of 52.7 was obtained. In the determination of the significance  $S$  ( $B$ ) is the number of signal (background) events passing the preselection.

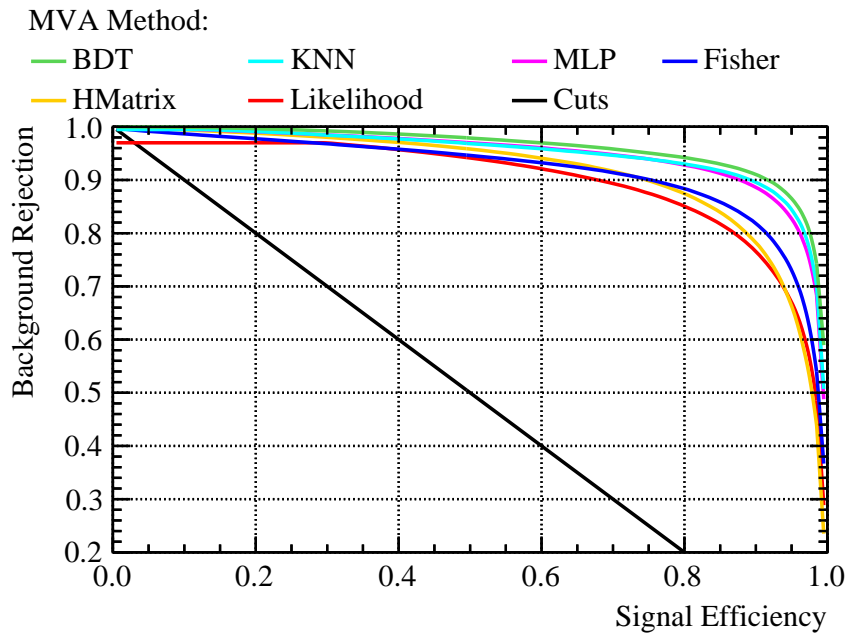


**Figure 7.9:** Background rejection as a function of signal efficiency for a variety of MVA options at 1.4 TeV.

### 7.5.3 Event Selection Summary

The event selection is summarised using the distribution of the invariant mass of the candidate bosons, which for the signal final state should peak around the W mass. This distribution is shown in figure 7.10 with no event selection, with the preselection cuts applied and with both preselections cuts and MVA applied. The event selection is also summarised using efficiencies shown in table 7.4.

As expected the dominant background processes after the MVA is applied are those that will look identical to the signal process, i.e.  $qqqq$  with missing energy. Two smaller sources of background are also present: two jet events with missing energy that are confused with four jet events with missing energy and events where a lepton is not properly reconstructed causing the event to look like four jets and missing energy.

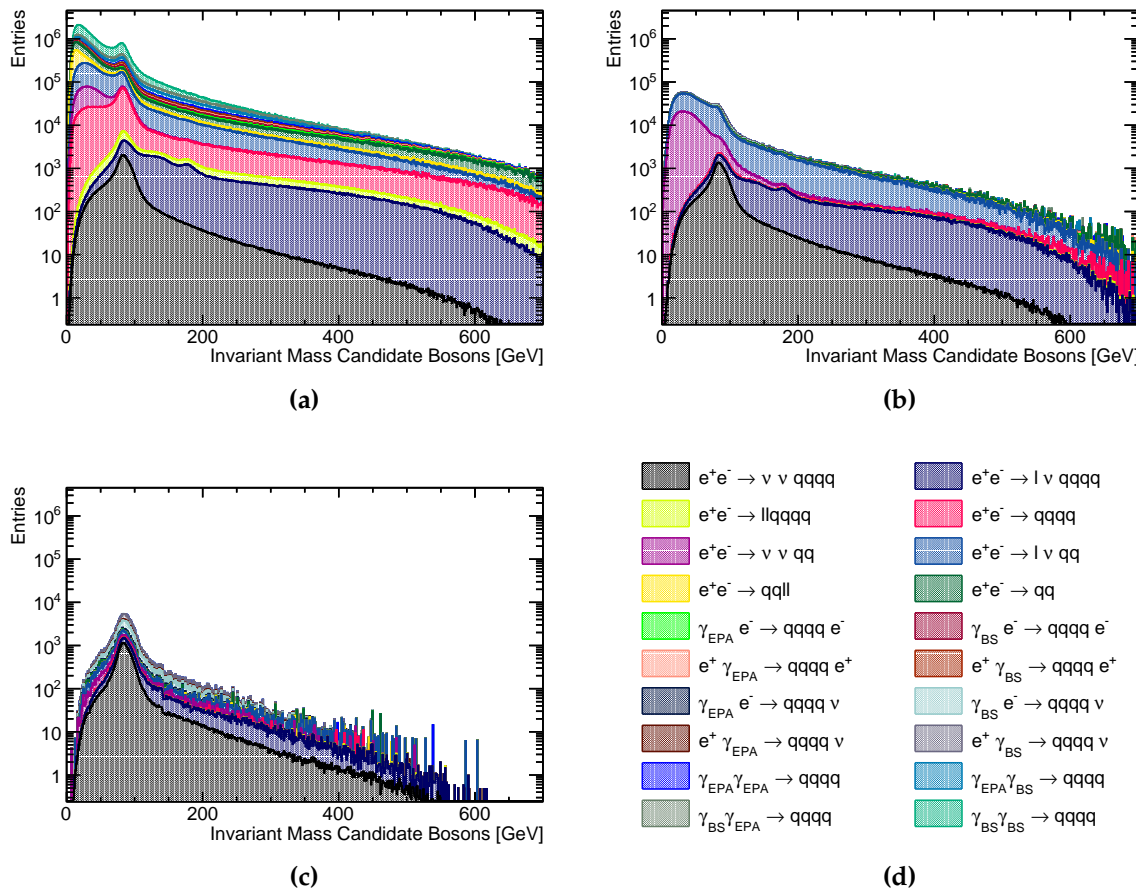


**Figure 7.10:** Impact of preselection and MVA on the reconstructed invariant mass of the bosons arising from jet pairing at 1.4 TeV. **(b)** No cuts applied. **(b)** Preselection cuts applied. **(c)** MVA with preselection applied. **(d)** The legend for the event selection plots.

Final State	$\epsilon_{\text{presel}}$	$\epsilon_{\text{BDT}}$	$N_{\text{BDT}}$
$e^+e^- \rightarrow \nu\nu qqqq$	64.1%	44.5%	16,470
$e^+e^- \rightarrow l\nu qqqq$	26.1%	5.2%	8,582
$e^+e^- \rightarrow llqqqq$	0.8%	0.1%	100
$e^+e^- \rightarrow qqqq$	0.3%	0.1%	1,698
$e^+e^- \rightarrow \nu\nu qq$	43.4%	0.5%	5,351
$e^+e^- \rightarrow l\nu qq$	19.1%	0.1%	9,319
$e^+e^- \rightarrow llqq$	0.1%	-	234
$e^+e^- \rightarrow qq$	0.6%	-	1,586
$\gamma_{\text{EPA}} e^- \rightarrow qqqqe^-$	0.2%	-	48
$\gamma_{\text{BS}} e^- \rightarrow qqqqe^-$	0.1%	-	42
$e^+ \gamma_{\text{EPA}} \rightarrow qqqqe^+$	0.3%	-	19
$e^+ \gamma_{\text{BS}} \rightarrow qqqqe^+$	-	-	65
$\gamma_{\text{EPA}} e^- \rightarrow qqqq\nu$	26.0%	9.0%	4,421
$\gamma_{\text{BS}} e^- \rightarrow qqqq\nu$	36.1%	15.0%	23,150
$e^+ \gamma_{\text{EPA}} \rightarrow qqqq\nu$	25.9%	9.2%	4,495
$e^+ \gamma_{\text{BS}} \rightarrow qqqq\nu$	36.4%	15.3%	23,410
$\gamma_{\text{EPA}} \gamma_{\text{EPA}} \rightarrow qqqq$	0.2%	-	81
$\gamma_{\text{EPA}} \gamma_{\text{BS}} \rightarrow qqqq$	0.1%	-	55
$\gamma_{\text{BS}} \gamma_{\text{EPA}} \rightarrow qqqq$	-	-	53
$\gamma_{\text{BS}} \gamma_{\text{BS}} \rightarrow qqqq$	-	-	0

**Table 7.4:** Selection summary at 1.4 TeV. The EPA and BS subscript on the incoming photon indicates whether the photon is generated from the equivalent photon approximation or beamstrahlung. Cells omitting the efficiency indicate an efficiency of less than 0.1%.

## 7.6 Effect of Anomalous Coupling/Fitting Methodology

This section describes the procedure used for constructing the  $\chi^2$  surface and the subsequent confidence contours used to determine the sensitivity of CLIC to the anomalous gauge couplings  $\alpha_4$  and  $\alpha_5$ .

### 7.6.1 Sensitive Distribution

The sensitivity of CLIC to the anomalous gauge couplings is determined through the use of a  $\chi^2$  fit to the distribution of  $M_{VV}$ , the invariant mass of the visible system. For a given event, the jet clustering and pairing proceeds as described in section ???. This leads to each event being clustered into four jets that are then paired up to give two candidate bosons. The distribution of  $M_{VV}$  proved to be highly sensitive to the anomalous gauge couplings, particularly for at large invariant masses, as shown in figure 7.11.

Two other distributions were considered for this sensitivity study, but proved to be less sensitive than  $M_{VV}$ :  $\cos\theta_{jets}^*$ , the angle between the boost direction and the back to back quark jets in the rest frame of the candidate bosons, and  $\cos\theta_{Bosons}^*$ , the angle between the boost direction and the back to back candidate bosons in the rest frame of the visible system. The sensitivity of these variables can be seen in figure 7.12. It should be noted that there are two entries, one from each candidate boson, in the  $\cos\theta_{jets}^*$  distribution per event. To negate the effect of correlation between these two variables when performing the  $\chi^2$  fit, a two dimensional fit of  $\cos\theta_{jets}^*$  variable was applied where a distinction between candidate bosons was made based on their energy. No such effect was present for the  $\cos\theta_{Bosons}^*$  variable as there is only a single pair of candidate bosons per event.

### 7.6.2 $\chi^2$ Surface Definition

The  $\chi^2$  surface is defined through the following equation:

$$\chi^2 = \sum_i \frac{(O_i - E_i)^2}{E_i}, \quad (7.4)$$

where  $O_i$  is the observed,  $\alpha_4 = \alpha_5 = 0$ , and  $E_i$  the expected,  $\alpha_4 \neq 0$  and  $\alpha_5 \neq 0$ , bin content for bin  $i$  in the distribution of  $M_{VV}$ .  $\Sigma_i$  is the sum over the bins of the  $M_{VV}$  distribution. The distribution of  $M_{VV}$  was binned using 14 bins. The first bin spanned the invariant mass range between 0 and 200 GeV, this was followed by 11 bins of width 100 GeV ranging from 200 to 1300 GeV and finally the last bin contained all invariant masses above 1300 GeV. The expanded bin widths were chosen at the tails of the

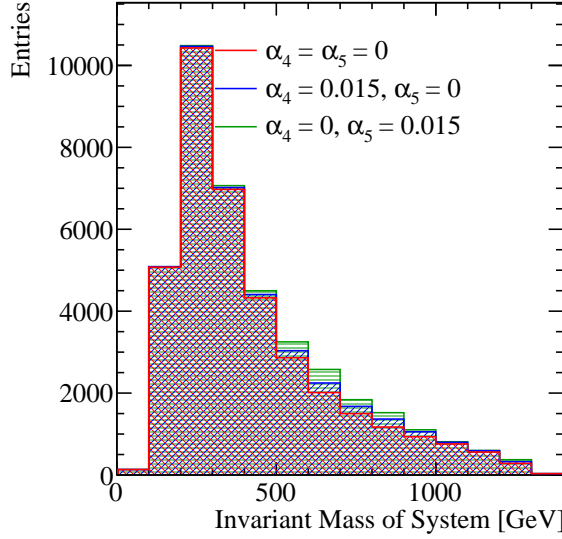


**Figure 7.11:** The sensitivity of  $M_{VV}$  to the anomalous gauge couplings  $\alpha_4$  and  $\alpha_5$  at 1.4 TeV. The jet algorithm used was the longitudinally invariant kt algorithm with an R parameter of 0.9 and Selected PFOs were used. This distribution is for the  $\nu\nu\text{qqqq}$  signal final state only.

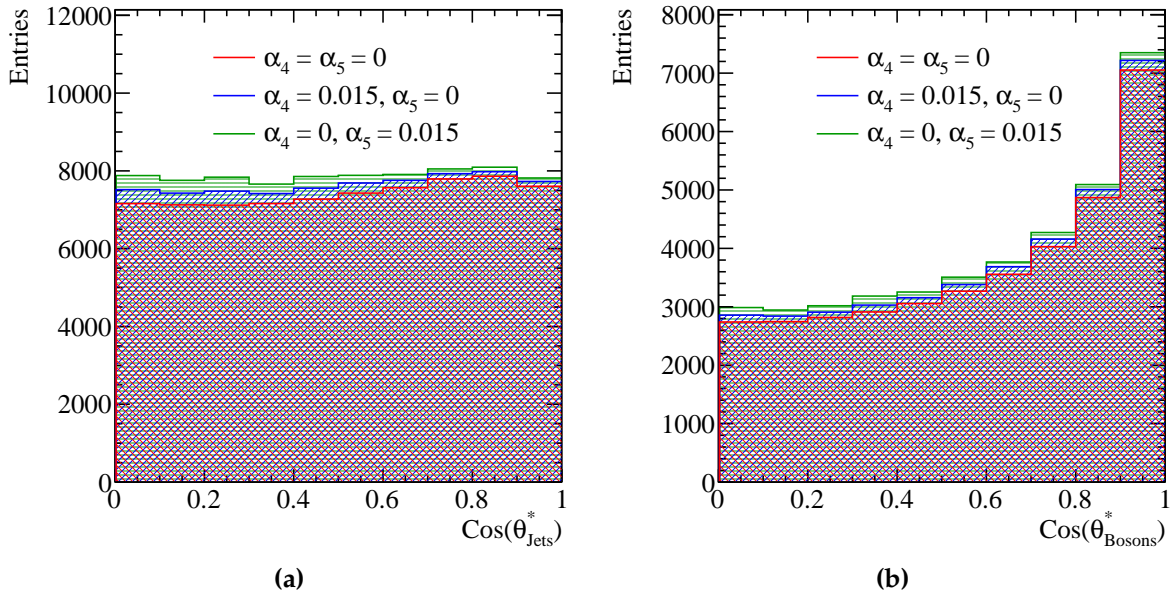


**Figure 7.12:** The sensitivity of various variables to the anomalous gauge couplings  $\alpha_4$  and  $\alpha_5$  at 1.4 TeV. The jet algorithm used was the longitudinally invariant kt algorithm with an R parameter of 0.9 and Selected PFOs were used. This distribution is for the  $\nu\nu\text{qqqq}$  signal final state only. (a) shows the distribution of  $\cos\theta_{\text{jets}}^*$  and (b) shows the distribution of  $\cos\theta_{\text{Bosons}}^*$ .

distribution to ensure the bin contents are sufficiently large to give a reliable estimate the likelihood function using the  $\chi^2$  parameter. This choice of binning minimises the effect of large bin by bin fluctuations arising from individual events with large event weights.

Confidence limits describing the sensitivity of the CLIC experiment to the anomalous gauge couplings were found by examining this  $\chi^2$  surface in  $\alpha_4$  and  $\alpha_5$  space. Deviations about the minima of this surface, which by construction occurs at  $\alpha_4 = \alpha_5 = 0$ , yield confidence limits that indicate the probability of observing a particular value of  $\alpha_4$  and  $\alpha_5$ . The confidence limits used in subsequent sections, 68%, 90% and 99%, are defined using fixed deviations from the minima of  $\chi^2$  contours of 2.28, 4.61 and 9.21 respectively. These numbers arise from the integral of the two dimensional  $\chi^2$  function.

It proved useful to consider the sensitivities to the individual parameters  $\alpha_4$  and  $\alpha_5$  independently. This was done by projecting out the  $\alpha_4 = 0$  or  $\alpha_5 = 0$  one dimensional  $\chi^2$  distribution from the two dimensional  $\chi^2$  distribution as discussed in section 7.4.1. The sensitivity to individual parameters was then extracted using confidence limits arising from the integral of the one dimensional  $\chi^2$  function i.e. 68% confidence limit occurs for  $\chi^2 = 0.989$ . In subsequent chapters these are the sensitivities quoted for individual anomalous gauge couplings.

### 7.6.3 Event Weight Interpolation Scheme

As described in section 7.3, event weights are used to determine the sensitivity of CLIC to the anomalous gauge couplings. These event weights are extracted on an event by event basis for the signal final state  $\nu\nu\text{qqqq}$  from the generator Whizard. To achieve a smooth  $\chi^2$  distribution a fine sampling of the  $M_{VV}$  distribution in the  $\alpha_4$  and  $\alpha_5$  space is needed. However, as extracting the event weights is highly CPU intensive, it is unfeasible to produce a finely sampled grid of event weights on an event by event basis by calling the generator. To resolve this issue, an interpolation scheme was applied to determine the event weights within a sampled region of the  $\alpha_4$  and  $\alpha_5$  space. This allows for an infinite sampling of the  $M_{VV}$  distribution in the space of  $\alpha_4$  and  $\alpha_5$  within the sampled region, without having to call the generator an infinite number of times.

A bicubic interpolation scheme, cubic interpolation along two dimensions, was applied to the event weights that were extracted from the generator. This procedure is best illustrated by figure 7.13, which shows the interpolated event weight surface superimposed with the raw event weights from the generator for several  $\nu\nu\text{qqqq}$  events at 1.4 TeV. This interpolation scheme produces a smooth and continuous surface that is sufficiently accurate for the fitting procedure applied in this analysis. At 1.4 TeV event weights were produced from the generator, Whizard, by stepping along  $\alpha_4$  and  $\alpha_5$  in steps of 0.01 ranging from -0.07 to 0.07, as shown in figure 7.4. These range proved to be sufficient for the contours of interest for the CLIC sensitivity analysis at these energies.

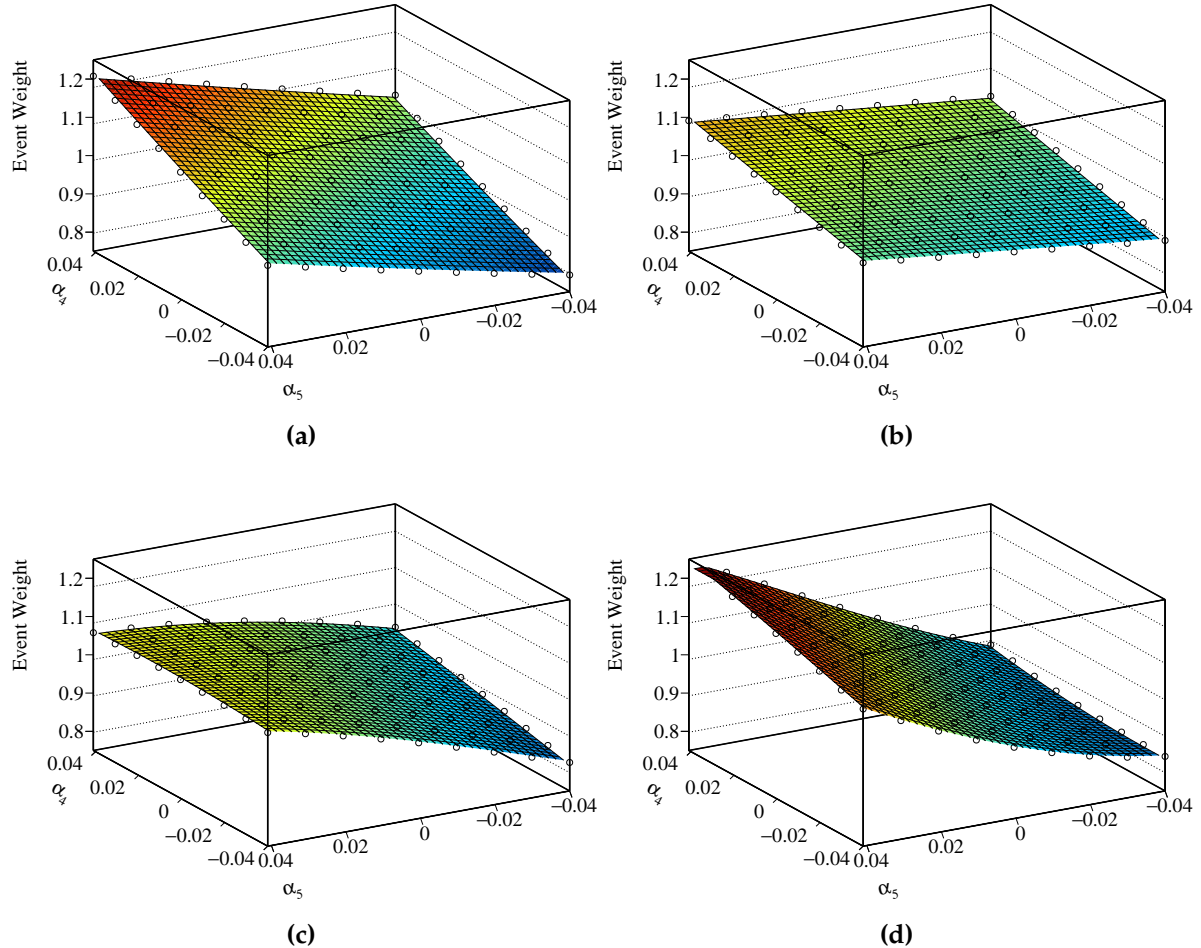


**Figure 7.13:** A selection of plots showing how the event weight changes when varying the anomalous couplings  $\alpha_4$  and  $\alpha_5$  for 1.4 TeV  $\nu\nu\text{qqqq}$  final state events. The hollow circles show the event weight produced from the generator, while the surface shown is found using bicubic interpolation between those points.

## 7.7 Results

The sensitivity of the CLIC experiment to the anomalous gauge couplings  $\alpha_4$  and  $\alpha_5$  at 1.4 TeV is shown in figure 7.14a. This result shows the sensitivity after the application of preselection and MVA purposed to remove the included background channels. These contours yield the one  $\sigma$  confidence limit on the measurement of  $\alpha_4$  to the range -0.0082, 0.0116 and similarly for the measurement of  $\alpha_5$  to the range -0.0055, 0.0078.

### 7.7.1 Systematic Uncertainties

A source of systematic error in this experiment is the uncertainty on the cross sections for the signal and background final states. Based on the selection efficiencies given in table 7.4, the  $\chi^2$  fit procedure is applied on a distribution that primarily consists of the background final states  $qqqq\nu$  arising from the interaction of  $e^+$  and  $e^-$  with beamstrahlung photons. Therefore, uncertainties in the cross section for these backgrounds should be considered. A detailed study of the accuracy of the relevant cross section calculations has yet to be performed for CLIC and so a wide spectrum in the uncertainty of these cross sections is considered here.

This systematic is included in the  $\chi^2$  through the use of a nuisance parameter, whereby the cross section for the  $\gamma_{\text{BS}}e^\pm \rightarrow qqqq\nu$  backgrounds are allowed to fluctuate. The magnitude of the fluctuation of the cross section,  $r$ , is moderated by an additional penalty term in the  $\chi^2$  as follows:

$$\chi^2(r) = \sum_i \frac{(O_i - E_i(r))^2}{E_i(r)} + \frac{(r - 1)^2}{\sigma_r^2}, \quad (7.5)$$

where  $O_i$  is the observed,  $\alpha_4 = \alpha_5 = 0$ , bin content for bin  $i$  in the distribution of  $M_{VV}$  with no background fluctuations.  $E_i(r)$  is the expected,  $\alpha_4 \neq 0$  and  $\alpha_5 \neq 0$ , bin content for bin  $i$  in the distribution of  $M_{VV}$  with the  $\gamma_{\text{BS}}e^\pm \rightarrow qqqq\nu$  background cross sections fluctuated by the factor  $r$ .  $\sum_i$  is the sum over the bins of the  $M_{VV}$  distribution.  $\sigma_r$  is the width of the distribution of  $r$ , which indicates the uncertainty on the measurement of the background cross sections. The  $\chi^2$  surface is constructed in the space of  $\alpha_4$  and  $\alpha_5$  by minimising  $\chi^2(r)$  at each point. The 68% confidence contour is

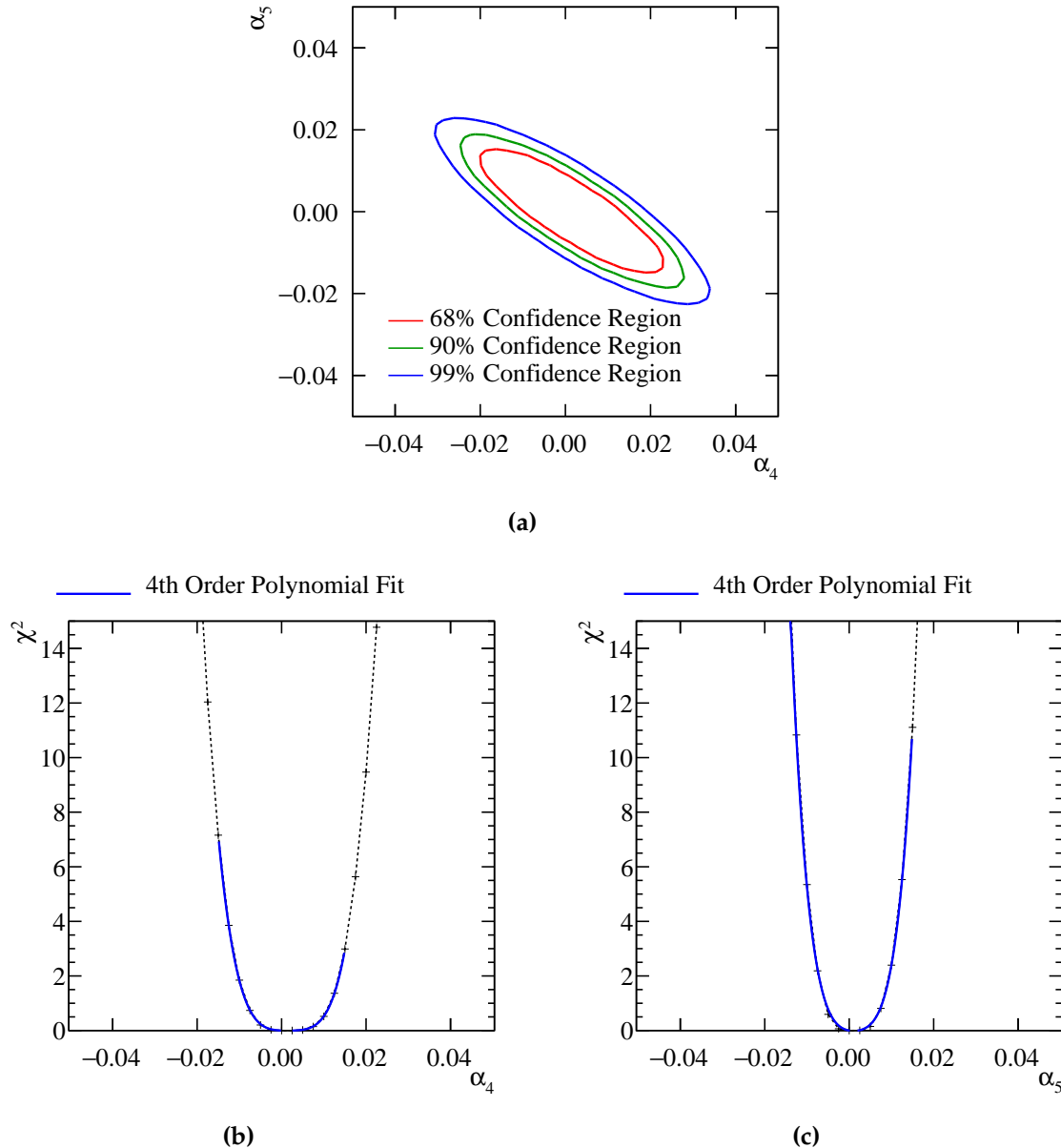


**Figure 7.14:**  $\chi^2$  sensitivity distributions from a fit to  $M_{VV}$  at 1.4 TeV. Results include the effect of backgrounds after the application of a series of preselection cuts and MVA. (a)  $\chi^2$  sensitivity contours in  $\alpha_4$  and  $\alpha_5$  space. (b)  $\chi^2$  as a function of  $\alpha_4$  assuming  $\alpha_5 = 0$ . (c)  $\chi^2$  as a function of  $\alpha_5$  assuming  $\alpha_4 = 0$ .

shown with the inclusion of this nuisance parameter for various values of  $\sigma_r$  in figure 7.15.

Minimal changes in sensitivity are observed when allowing the backgrounds to fluctuate even up to the 50% level. This can be understood by considering the shape

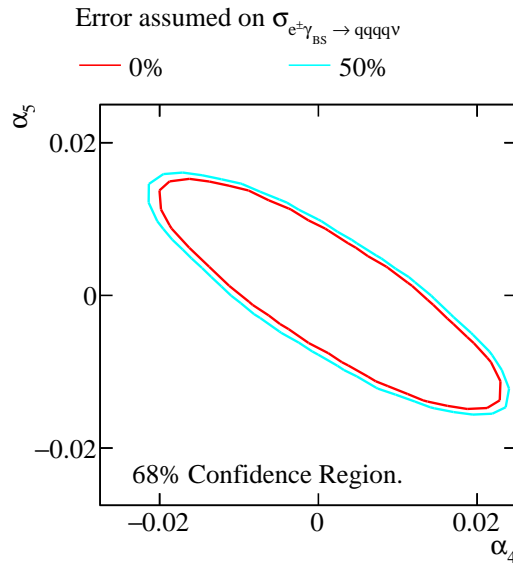


**Figure 7.15:** 68% sensitivity contour including systematic errors, of varying magnitudes, in dominant background cross sections.

of the  $M_{VV}$  distribution for the signal, with and without the effect of anomalous couplings, and the  $\gamma_{BS} e^\pm \rightarrow qqqqV$  backgrounds, which is shown in figure 7.16. These distribution shows that anomalous couplings primarily affect events with large invariant masses, while these backgrounds peak at low invariant masses. Therefore, by fluctuating the cross-section for the background processes it is not possible to gain a significantly better match between the observed and expected bin contents in the  $M_{VV}$  distribution. This is encouraging as despite these backgrounds dominating the fit being used to determine the sensitivity of CLIC to the anomalous gauge couplings, precise knowledge of their cross-section is not essential.

## 7.8 Sensitivity at 3 TeV

The anomalous gauge coupling sensitivity study described in this chapter was reproduced for CLIC operating at 3 TeV. The procedure for the 3 TeV analysis largely mirrors that of the 1.4 TeV analysis, therefore, in this section only the differences between the analyses are highlighted.

The signal and background final states for the 3 TeV analysis were identical to those used for the 1.4 TeV analysis as described in section 7.2. The cross sections at 3 TeV for those signal and background final states can be found in table 7.5.

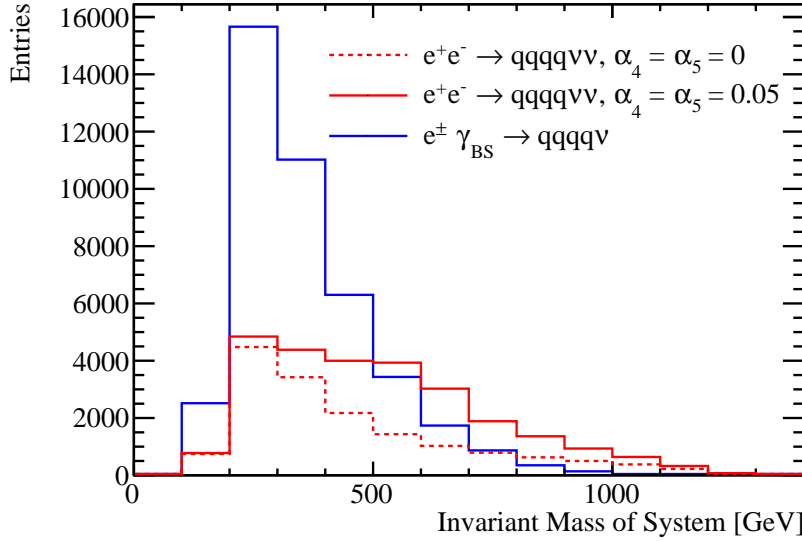


**Figure 7.16:** Distributions of  $M_{VV}$  for the  $\nu\nu\text{qqqq}$ , with and without the effect from anomalous couplings, and the combined dominant background processes  $\gamma_{\text{BS}}e^\pm \rightarrow \text{qqqq}\nu$ .

The data analysis and event selection procedures used at 3 TeV mirrored those used at 1.4 TeV. Descriptions of both can be found in sections 7.4 and 7.5 respectively.

Jet finding was performed using the longitudinally invariant  $k_t$  algorithm as described in section . Optimisation of the jet algorithm configuration, which uses pure signal only as described in section 7.4.1, found the optimal configuration at 3 TeV to be tight selected PFOs and an R parameter of 1.1. As the cross section for the  $\gamma\gamma \rightarrow \text{Hadrons}$  increases with energy the impact of these backgrounds is more problematic at 3 TeV than 1.4 TeV [25]. Therefore, it is to be expected that the optimal PFO selection at 3 TeV is more aggressive, tight selected PFOs, at vetoing these backgrounds than at 1.4 TeV, selected PFOs, which is what is observed.

As opposed to training the MVA using 50% of the signal and background samples, as was done for the 1.4 TeV analysis, the 3 TeV analysis trained the MVA using 10% of the signal and background samples. This change was made to increase the sample size going forward to the sensitivity study to minimise the impact of a small number of events with very large anomalous coupling event weights that would otherwise skew the  $M_{VV}$  distribution and bias the fit applied to it. No such effect was seen at 1.4 TeV where the sensitivity to anomalous couplings is much lower than at 3 TeV. The sample sizes were sufficiently large that training on 10% of the total sample was sufficient to achieve good MVA performance.

Final State	Cross Section 3 TeV [fb]
$e^+e^- \rightarrow \nu\nuqqqq$	71.5
$e^+e^- \rightarrow l\nuqqqq$	106.6
$e^+e^- \rightarrow llqqqq$	169.3
$e^+e^- \rightarrow qqqq$	546.5
$e^+e^- \rightarrow \nu\nuqq$	1317.5
$e^+e^- \rightarrow l\nu qq$	5560.9
$e^+e^- \rightarrow llqq$	3319.6
$e^+e^- \rightarrow qq$	2948.9
$\gamma_{\text{EPA}} e^- \rightarrow qqqqe^-$	287.8
$\gamma_{\text{BS}} e^- \rightarrow qqqqe^-$	1268.6
$e^+ \gamma_{\text{EPA}} \rightarrow qqqqe^+$	287.8
$e^+ \gamma_{\text{BS}} \rightarrow qqqqe^+$	1267.3
$\gamma_{\text{EPA}} e^- \rightarrow qqqq\nu$	54.2
$\gamma_{\text{BS}} e^- \rightarrow qqqq\nu$	262.5
$e^+ \gamma_{\text{EPA}} \rightarrow qqqq\nu$	54.2
$e^+ \gamma_{\text{BS}} \rightarrow qqqq\nu$	262.3
$\gamma_{\text{EPA}} \gamma_{\text{EPA}} \rightarrow qqqq$	402.7
$\gamma_{\text{EPA}} \gamma_{\text{BS}} \rightarrow qqqq$	2423.1
$\gamma_{\text{BS}} \gamma_{\text{EPA}} \rightarrow qqqq$	2420.6
$\gamma_{\text{BS}} \gamma_{\text{BS}} \rightarrow qqqq$	13050.3

**Table 7.5:** Cross sections of signal and background processes at 3 TeV. In the above table q represents u,  $\bar{u}$ , d,  $\bar{d}$ , s,  $\bar{s}$ , c,  $\bar{c}$ , b or  $\bar{b}$ ; l represents  $e^\pm$ ,  $\mu^\pm$  or  $\tau^\pm$ ; and  $\nu$  represents  $\nu_e$ ,  $\bar{\nu}_e$ ,  $\nu_\mu$ ,  $\bar{\nu}_\mu$ ,  $\nu_\tau$  and  $\bar{\nu}_\tau$ . The EPA and BS subscript on the incoming photon indicates whether the photon is generated from the equivalent photon approximation or beamstrahlung.

The event selection for the 3 TeV analysis is summarised in table 7.6.

Due to the increased sensitivity of the signal sample at 3 TeV, the stepping along  $\alpha_4$  and  $\alpha_5$  to extract the event weights from the generator was much finer than that used for the 1.4 TeV analysis. At 3 TeV event weights were taken from the generator in steps of 0.00025 ranging from 0.0065 to -0.0065. Bicubic interpolation was again used to make a continuous surface for the event weights. These event weight surfaces were then used to construct the  $M_{VV}$  distribution and the  $\chi^2$  surface used to determine the reported sensitivities.

Final State	$\epsilon_{\text{presel}}$	$\epsilon_{\text{BDT}}$	$N_{\text{BDT}}$
$e^+ e^- \rightarrow \nu\nu qqqq$	74.4%	46.0%	65,740
$e^+ e^- \rightarrow l\nu qqqq$	40.0%	12.0%	25,660
$e^+ e^- \rightarrow llqqqq$	7.5%	1.1%	3,570
$e^+ e^- \rightarrow qqqq$	3.7%	0.3%	3,224
$e^+ e^- \rightarrow \nu\nu qq$	50.5%	1.2%	30,510
$e^+ e^- \rightarrow l\nu qq$	32.0%	0.4%	48,320
$e^+ e^- \rightarrow llqq$	1.4%	-	1,028
$e^+ e^- \rightarrow qq$	1.4%	0.1%	3,268
$\gamma_{\text{EPA}} e^- \rightarrow qqqqe^-$	6.6%	0.8%	4,736
$\gamma_{\text{BS}} e^- \rightarrow qqqqe^-$	4.6%	0.7%	13,660
$e^+ \gamma_{\text{EPA}} \rightarrow qqqqe^+$	6.5%	0.8%	4,686
$e^+ \gamma_{\text{BS}} \rightarrow qqqqe^+$	4.7%	0.7%	13,310
$\gamma_{\text{EPA}} e^- \rightarrow qqqq\nu$	45.6%	17.2%	18,610
$\gamma_{\text{BS}} e^- \rightarrow qqqq\nu$	55.9%	26.7%	110,900
$e^+ \gamma_{\text{EPA}} \rightarrow qqqq\nu$	45.9%	17.3%	18,750
$e^+ \gamma_{\text{BS}} \rightarrow qqqq\nu$	56.5%	27.4%	113,700
$\gamma_{\text{EPA}} \gamma_{\text{EPA}} \rightarrow qqqq$	5.3%	0.7%	5,531
$\gamma_{\text{EPA}} \gamma_{\text{BS}} \rightarrow qqqq$	3.5%	0.4%	16,640
$\gamma_{\text{BS}} \gamma_{\text{EPA}} \rightarrow qqqq$	3.5%	0.4%	15,900
$\gamma_{\text{BS}} \gamma_{\text{BS}} \rightarrow qqqq$	0.6%	-	4,124

**Table 7.6:** Selection summary at 3 TeV. The EPA and BS subscript on the incoming photon indicates whether the photon is generated from the equivalent photon approximation or beamstrahlung. Cells omitting the efficiency indicate an efficiency of less than 0.1%.

The sensitivity of the CLIC experiment to the anomalous gauge couplings  $\alpha_4$  and  $\alpha_5$  at 3 TeV is shown in figure 7.17a. This result shows the sensitivity after the application of preselection and MVA, described in sections 7.5.1 and 7.5.2, purposed to remove the included background channels. These contours yield the one  $\sigma$  confidence limit on the measurement of  $\alpha_4$  to the range -0.0010 to 0.0011 and similarly for the measurement of  $\alpha_5$  the range is -0.0007 to 0.0007.

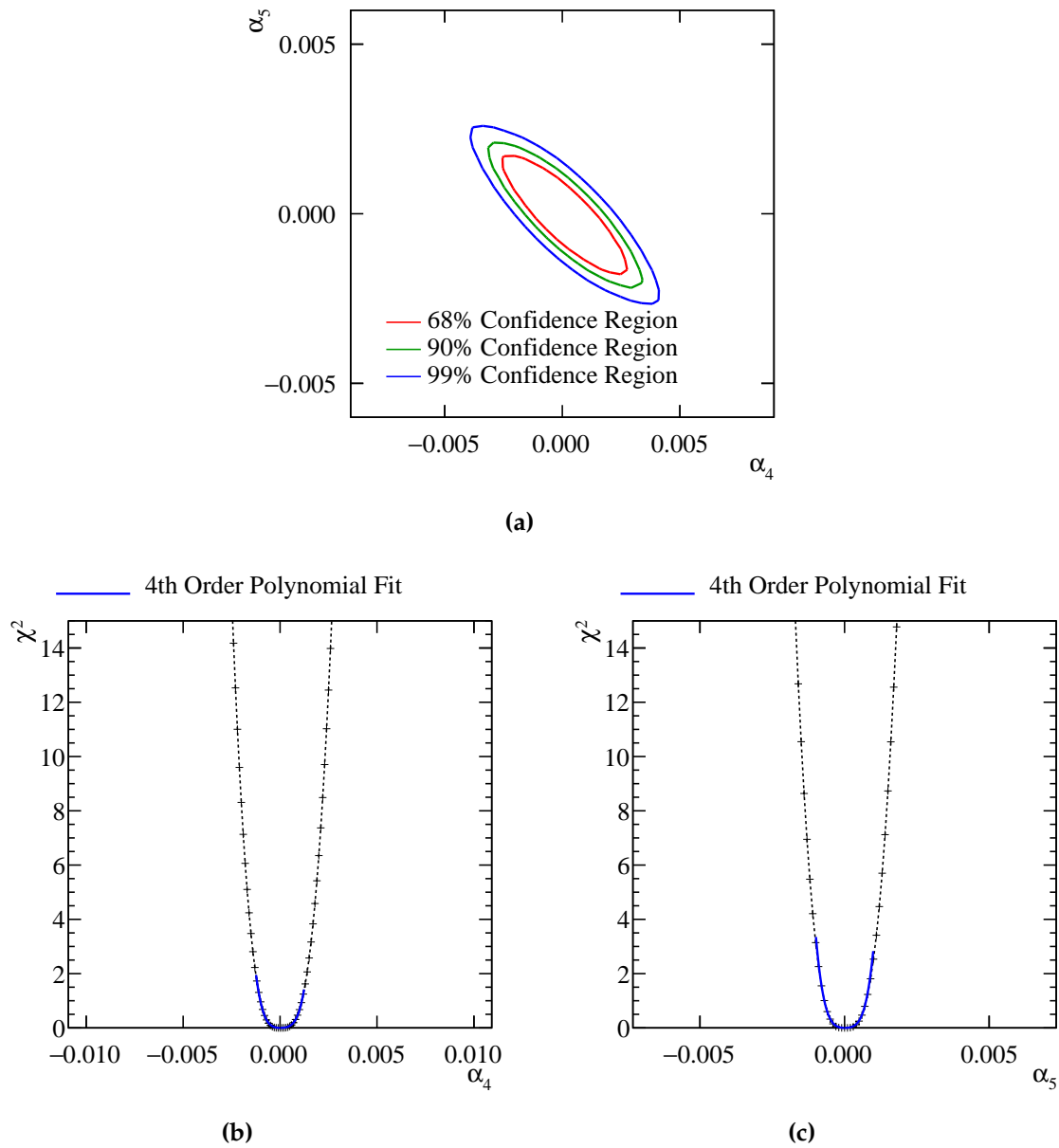


**Figure 7.17:**  $\chi^2$  sensitivity distributions from a fit to  $M_{VV}$  at 3 TeV. Results include the effect of backgrounds after the application of a series of preselection cuts and MVA. (a)  $\chi^2$  sensitivity contours in  $\alpha_4$  and  $\alpha_5$  space. (b)  $\chi^2$  as a function of  $\alpha_4$  assuming  $\alpha_5 = 0$ . (c)  $\chi^2$  as a function of  $\alpha_5$  assuming  $\alpha_4 = 0$ .



# Chapter 8

## Summary

*“There, sir! that is the perfection of vessels!”*

— Jules Verne, 1828–1905

The work presented in this thesis has made significant contributions to the future linear collider experiments in terms of detector design, event reconstruction and demonstration of physics potential.

A number of capacitively coupled pixel detectors were prototyped and tested, using both lab and test beam measurements, to determine whether they were viable for use in the CLIC vertex detector. The performance of these prototyped devices was extremely good. As an offset between the sensor and readout ASICs could be accidentally introduced to the devices during the manufacturing procedure, a number of devices were examined that contained a known offset. Even devices containing an offset of up to  $\frac{1}{4}$  of a pixel were found to have comparable performance to the ideally aligned devices. Although modifications would be required for the final design of the sensor and readout ASICs to fully optimise performance, the technique of capacitive coupling of sensor to readout ASICs was found to be viable for use at the future linear collider experiments.

An optimisation study of the calorimeter design for use at the future linear collider was performed. This study clarified those detector parameters that are crucial for achieving outstanding performance in the particle flow paradigm. Furthermore, this work has made it possible to make informed decisions about the detector design that minimise the cost, while retaining outstanding jet energy resolutions. Reliability in

the conclusions drawn from this study could only be achieved by employing the calibration procedure that was developed for the linear collider simulation.

Development of novel software techniques, which make full use of the segmentation of the linear collider calorimeters, led to a significant improvement in the energy resolution of the linear collider detector. This improvement would be extremely expensive to obtain if it were achieved by modifying the design of the calorimeters, therefore, as well as extending the physics reach of the detector, a significant cost reduction was made.

The final study presented determined the sensitivity of the CLIC experiment to the anomalous gauge couplings  $\alpha_4$  and  $\alpha_5$  through the vector boson scattering process. The signal final state  $\nu\nu qqqq$  was selected for this analysis based on the relative sensitivities of final states showing sensitivity to these couplings. Background processes were then selected based on whether they could be confused with the signal. An event selection procedure was applied to separate the signal and backgrounds. The significance obtained from this event selection was 52.7 (90.6) for CLIC running at 1.4 (3) TeV. Finally, a  $\chi^2$  fit was applied to the distribution of the invariant mass of the system to determine the sensitivity of the CLIC experiment to the anomalous gauge couplings. The sensitivity manifested itself in the form of event weights for the signal final state. Using this procedure the one  $\sigma$  confidence limits on the couplings, assuming the corresponding coupling is zero, were found to be:

$$-0.0082 < \alpha_4 < 0.0116, \quad (8.1)$$

$$-0.0055 < \alpha_5 < 0.0078, \quad (8.2)$$

at 1.4 TeV and:

$$-0.0010 < \alpha_4 < 0.0011, \quad (8.3)$$

$$-0.0007 < \alpha_5 < 0.0007, \quad (8.4)$$

at 3 TeV. These limits significantly improve on the measurements made at the LHC, Run 1, by a factor of approximately 10 (100) at 1.4 (3) TeV [68]. This is a large gain in sensitivity indicating just one aspect of the physics capabilities of the linear collider. This study adds further weight to the argument for the construction of a linear collider.

# Colophon

This thesis was made in L<sup>A</sup>T<sub>E</sub>X 2 <sub>$\epsilon$</sub>  using the “hepthesis” class [69].



# Bibliography

- [1] Georges Aad et al. Observation of a new particle in the search for the Standard Model Higgs boson with the ATLAS detector at the LHC. *Phys. Lett.*, B716:1–29, 2012.
- [2] Serguei Chatrchyan et al. Observation of a new boson at a mass of 125 GeV with the CMS experiment at the LHC. *Phys. Lett.*, B716:30–61, 2012.
- [3] Ties Behnke, James E. Brau, Brian Foster, Juan Fuster, Mike Harrison, James McEwan Paterson, Michael Peskin, Marcel Stanitzki, Nicholas Walker, and Hitoshi Yamamoto. The International Linear Collider Technical Design Report - Volume 1: Executive Summary. 2013.
- [4] Lucie Linssen, Akiya Miyamoto, Marcel Stanitzki, and Harry Weerts. Physics and Detectors at CLIC: CLIC Conceptual Design Report. 2012.
- [5] M Aicheler, P Burrows, M Draper, T Garvey, P Lebrun, K Peach, N Phinney, H Schmickler, D Schulte, and N Toge. A Multi-TeV Linear Collider Based on CLIC Technology. 2012.
- [6] B. Pilicer, Helmut Burkhardt, Laurent Gatignon, Andrea Latina, Ercan Pilicer, Daniel Schulte, Ilhan Tapan, and Rogelio TomÃ¡s. Study of Muon Backgrounds in the CLIC Beam Delivery System. In *Proceedings, 6th International Particle Accelerator Conference (IPAC 2015): Richmond, Virginia, USA, May 3-8, 2015*, page TUPTY032, 2015.
- [7] AndrÃ¡s Sailer. *Radiation and Background Levels in a CLIC Detector due to Beam-Beam Effects*. PhD thesis, CERN, 2012-05-09.
- [8] David J. Griffiths. *INTRODUCTION TO ELEMENTARY PARTICLES*. 1987.
- [9] Michael E. Peskin and Daniel V. Schroeder. *An Introduction to quantum field theory*. 1995.

- [10] Steven Weinberg. A Model of Leptons. *Phys. Rev. Lett.*, 19:1264–1266, 1967.
- [11] J. Beringer et al. Review of Particle Physics (RPP). *Phys. Rev.*, D86:010001, 2012.
- [12] Jeffrey Goldstone, Abdus Salam, and Steven Weinberg. Broken Symmetries. *Phys. Rev.*, 127:965–970, 1962.
- [13] John Ellis. Higgs Physics. In *Proceedings, 2013 European School of High-Energy Physics (ESHEP 2013): Paradfurdo, Hungary, June 5-18, 2013*, pages 117–168, 2015.
- [14] K. A. Olive et al. Review of Particle Physics. *Chin. Phys.*, C38:090001, 2014.
- [15] R. Keith Ellis, W. James Stirling, and B. R. Webber. QCD and collider physics. *Camb. Monogr. Part. Phys. Nucl. Phys. Cosmol.*, 8:1–435, 1996.
- [16] J. R. Andersen et al. Discovering Technicolor. *Eur. Phys. J. Plus*, 126:81, 2011.
- [17] Christophe Grojean. New approaches to electroweak symmetry breaking. *Phys. Usp.*, 50:1–35, 2007. [Usp. Fiz. Nauk177,3(2007)].
- [18] Celine Degrande, Oscar Eboli, Bastian Feigl, Barbara JÄd'ger, Wolfgang Kilian, Olivier Mattelaer, Michael Rauch, JÄijrgen Reuter, Marco Sekulla, and Doreen Wackerlo. Monte Carlo tools for studies of non-standard electroweak gauge boson interactions in multi-boson processes: A Snowmass White Paper. In *Proceedings, 2013 Community Summer Study on the Future of U.S. Particle Physics: Snowmass on the Mississippi (CSS2013): Minneapolis, MN, USA, July 29-August 6, 2013*, 2013.
- [19] Christopher Arzt. Reduced effective Lagrangians. *Phys. Lett.*, B342:189–195, 1995.
- [20] Ben Gripaios. Lectures on Effective Field Theory. 2015.
- [21] Maria J. Herrero and Ester Ruiz Morales. The Electroweak chiral Lagrangian as an effective field theory of the standard model with a heavy Higgs. In *Workshop on Electroweak Symmetry Breaking Budapest, Hungary, July 11-13, 1994*, pages 37–54, 1994.
- [22] Anthony C. Longhitano. Low-Energy Impact of a Heavy Higgs Boson Sector. *Nucl. Phys.*, B188:118–154, 1981.
- [23] A Belyaev, Oscar J P ÄL'boli, M ConcepcíÄsn GonzÄález-GarcíÄa, J K Mizukoshi, S F Novaes, and I E Zacharov. Strongly interacting vector bosons at the CERN LHC: Quartic anomalous couplings. Strongly Interacting Vector Bosons at the

- LHC: Quartic Anomalous Couplings. *Phys. Rev. D*, 59(hep-ph/9805229. FTUV-98-34. IFIC-98-35. IFT-P-98-21. IFUSP-P-1306. 1):15022. 12 p, May 1998.
- [24] M. A. Thomson. Particle Flow Calorimetry and the PandoraPFA Algorithm. *Nucl. Instrum. Meth.*, A611:25–40, 2009.
- [25] J. S. Marshall, A. MÄijnnich, and M. A. Thomson. Performance of Particle Flow Calorimetry at CLIC. *Nucl. Instrum. Meth.*, A700:153–162, 2013.
- [26] Halina Abramowicz et al. The International Linear Collider Technical Design Report - Volume 4: Detectors. 2013.
- [27] Toshinori Abe et al. The International Large Detector: Letter of Intent. 2010.
- [28] Toshinori Abe et al. The International Large Detector: Letter of Intent. 2010.
- [29] Serguei Chatrchyan et al. Energy Calibration and Resolution of the CMS Electromagnetic Calorimeter in  $pp$  Collisions at  $\sqrt{s} = 7$  TeV. *JINST*, 8:P09009, 2013. [JINST8,9009(2013)].
- [30] M. Aharrouche et al. Energy linearity and resolution of the ATLAS electromagnetic barrel calorimeter in an electron test-beam. *Nucl. Instrum. Meth.*, A568:601–623, 2006.
- [31] Pascal Perret. First Years of Running for the LHCb Calorimeter System. *PoS*, TIPP2014:030, 2014.
- [32] Huong Lan Tran, Katja KrÄijger, Felix Sefkow, Steven Green, John Marshall, Mark Thomson, and Frank Simon. Software compensation in Particle Flow reconstruction. 2017.
- [33] M. Chefdeville et al. Shower development of particles with momenta from 15 GeV to 150 GeV in the CALICE scintillator-tungsten hadronic calorimeter. *JINST*, 10(12):P12006, 2015.
- [34] Howard S. Budd. CMS central hadron calorimeter. *Nucl. Phys. Proc. Suppl.*, 54B:191–197, 1997. [,191(2001)].
- [35] A. Airapetian et al. ATLAS calorimeter performance Technical Design Report. 1996.
- [36] P. Mora de Freitas and H. Videau. Detector simulation with MOKKA / GEANT4: Present and future. In *Linear colliders. Proceedings, International Workshop on physics*

- and experiments with future electron-positron linear colliders, LCWS 2002, Seogwipo, Jeju Island, Korea, August 26-30, 2002, pages 623–627, 2002.*
- [37] S. Agostinelli et al. GEANT4: A Simulation toolkit. *Nucl. Instrum. Meth.*, A506:250–303, 2003.
  - [38] F. Gaede. Marlin and LCCD: Software tools for the ILC. *Nucl. Instrum. Meth.*, A559:177–180, 2006.
  - [39] H. Abramowicz et al. Higgs Physics at the CLIC Electron-Positron Linear Collider. 2016.
  - [40] Torbjorn Sjostrand, Stephen Mrenna, and Peter Z. Skands. PYTHIA 6.4 Physics and Manual. *JHEP*, 05:026, 2006.
  - [41] G. Alexander et al. A Comparison of b and u d s quark jets to gluon jets. *Z. Phys.*, C69:543–560, 1996.
  - [42] Z. Was. TAUOLA the library for tau lepton decay, and KKMC / KORALB / KORALZ / ... status report. *Nucl. Phys. Proc. Suppl.*, 98:96–102, 2001. [,96(2000)].
  - [43] Serguei Chatrchyan et al. Measurement of the  $W\gamma$  and  $Z\gamma$  inclusive cross sections in  $pp$  collisions at  $\sqrt{s} = 7\text{TeV}$  and limits on anomalous triple gauge boson couplings. *Phys. Rev.*, D89(9):092005, 2014.
  - [44] Georges Aad et al. Measurement of  $W^+W^-$  production in  $pp$  collisions at  $\sqrt{s}=7\text{TeV}$  with the ATLAS detector and limits on anomalous WWZ and WW $\tilde{\chi}$  couplings. *Phys. Rev.*, D87(11):112001, 2013. [Erratum: *Phys. Rev.*D88,no.7,079906(2013)].
  - [45] Serguei Chatrchyan et al. Search for  $WW\gamma$  and  $WZ\gamma$  production and constraints on anomalous quartic gauge couplings in  $pp$  collisions at  $\sqrt{s} = 8 \text{ TeV}$ . *Phys. Rev.*, D90(3):032008, 2014.
  - [46] C. W. Fabjan and F. Gianotti. Calorimetry for particle physics. *Rev. Mod. Phys.*, 75:1243–1286, 2003.
  - [47] C. Adloff et al. Hadronic energy resolution of a highly granular scintillator-steel hadron calorimeter using software compensation techniques. *JINST*, 7:P09017, 2012.
  - [48] M. Benoit et al. Testbeam results of irradiated ams H18 HV-CMOS pixel sensor

- prototypes. 2016.
- [49] Roel Aaij, Bernardo Adeva, Marco Adinolfi, Ziad Ajaltouni, Simon Akar, Johannes Albrecht, Federico Alessio, Michael Alexander, Suvayu Ali, Georgy Alkhazov, Paula Alvarez Cartelle, Antonio Augusto Alves Jr, Sandra Amato, Silvia Amerio, Yasmine Amhis, Liupan An, Lucio Anderlini, Guido Andreassi, Mirco Andreotti, Jason Andrews, Mario Anelli, Robert Appleby, Flavio Archilli, Philippe d'Argent, Joan Arnau Romeu, Alexander Artamonov, Marina Artuso, Elie Aslanides, Giulio Auriemma, Marouen Baalouch, Igor Babuschkin, Sebastian Bachmann, John Back, Alexey Badalov, Clarissa Baesso, Sophie Baker, Vladislav Balagura, Wander Baldini, Alessandro Balla, Alexander Baranov, Roger Barlow, Colin Barschel, Sergey Barsuk, William Barter, Fedor Baryshnikov, Mateusz Baszczyk, Varvara Batozskaya, Baasansuren Batsukh, Vincenzo Battista, Aurelio Bay, Leo Beaucourt, John Beddow, Franco Bedeschi, Ignacio Bediaga, Andrew Beiter, Lennaert Bel, Violaine Bellee, Nicoletta Belloli, Konstantin Belous, Ivan Belyaev, Eli Ben-Haim, Giovanni Bencivenni, Sean Benson, Sarah Beranek, Alexander Berezhnoy, Roland Bernet, Alessandro Bertolin, Christopher Betancourt, Federico Betti, Marc-Olivier Bettler, Martinus van Beuzekom, Iaroslava Bezshyiko, Simone Bifani, Pierre Billoir, Alex Birnkraut, Alexander Bitadze, Andrea Bizzeti, Thomas Blake, Frederic Blanc, Johan Blouw, Steven Blusk, Valerio Bocci, Thomas Boettcher, Alexander Bondar, Nikolay Bondar, Walter Bonivento, Igor Bordyuzhin, Alessio Borgheresi, Silvia Borghi, Maxim Borisjak, Martino Borsato, Francesco Bossu, Meriem Boubdir, Themistocles Bowcock, Espen Eie Bowen, Concezio Bozzi, Svende Braun, Thomas Britton, Jolanta Brodzicka, Davide Brundu, Emma Buchanan, Christopher Burr, Albert Bursche, Jan Buytaert, Sandro Cadeddu, Roberto Calabrese, Marta Calvi, Miriam Calvo Gomez, Alessandro Camboni, Pierluigi Campana, Daniel Hugo Campora Perez, Lorenzo Capriotti, Angelo Carbone, Giovanni Carboni, Roberta Cardinale, Alessandro Cardini, Maurizio Carletti, Paolo Carniti, Laurence Carson, Kazuyoshi Carvalho Akiba, Gianluigi Casse, Lorenzo Cassina, Lucia Castillo Garcia, Luigi Casu, Marco Cattaneo, Giovanni Cavallero, Riccardo Cenci, David Chambon, Matthew Charles, Philippe Charpentier, Georgios Chatzikonstantinidis, Maximilien Chefdeville, Shanzhen Chen, Shu-Faye Cheung, Veronika Chobanova, Marcin Chrzaszcz, Alexsei Chubykin, Paolo Ciambrone, Xabier Cid Vidal, Gregory Ciezarek, Mauro Citterio, Peter Clarke, Marco Clemencic, Harry Cliff, Joel Closier, Victor Coco, Simone Coelli, Julien Cogan, Eric Cogneras, Violetta Cogoni, Lucian Cojocariu, Paula Collins, Albert Comerma-Montells, Andrea Contu, Andrew Cook, George Coombs, Samuel Coquereau, Gloria Corti, Marco Corvo,

Cayo Mar Costa Sobral, Benjamin Couturier, Greig Cowan, Daniel Charles Craik, Andrew Crocombe, Melissa Maria Cruz Torres, Samuel Cunliffe, Robert Currie, Carmelo D'Ambrosio, Franciole Da Cunha Marinho, Elena Dall'Occo, Jeremy Dalseno, Pieter David, Adam Davis, Kristof De Bruyn, Stefano De Capua, Michel De Cian, Jussara De Miranda, Leandro De Paula, Marilisa De Serio, Patrizia De Simone, Cameron Thomas Dean, Daniel Decamp, Mirko Deckenhoff, Luigi Del Buono, Moritz Demmer, Adam Dendek, Denis Derkach, Olivier Deschamps, Francesco Dettori, Biplab Dey, Angelo Di Canto, Pasquale Di Nezza, Hans Dijkstra, Francesca Dordei, Mirco Dorigo, Alvaro Dosil SuÁarez, Anatoliy Dovbnya, Karlis Dreimanis, Laurent Dufour, Giulio Dujany, Kevin Dungs, Paolo Durante, Rustem Dzhelyadin, Agnieszka Dziurda, Alexey Dzyuba, Nicolas DÃ'lÃ'lage, Sajan Easo, Marcus Ebert, Ulrik Egede, Victor Egorychev, Semen Eidelman, Stephan Eisenhardt, Ulrich Eitschberger, Robert Ekelhof, Lars Eklund, Scott Ely, Sevda Esen, Hannah Mary Evans, Timothy Evans, Antonio Falabella, Nathanael Farley, Stephen Farry, Robert Fay, Davide Fazzini, Giulietto Felici, Dianne Ferguson, Gerard Fernandez, Antonio Fernandez Prieto, Fabio Ferrari, Fernando Ferreira Rodrigues, Massimiliano Ferro-Luzzi, Sergey Filippov, Rosa Anna Fini, Marco Fiore, Massimiliano Fiorini, Miroslaw Firlej, Conor Fitzpatrick, Tomasz Fiutowski, Frederic Fleuret, Klaus Fohl, Marianna Fontana, Flavio Fontanelli, Dean Charles Forshaw, Roger Forty, Vinicius Franco Lima, Markus Frank, Christoph Frei, Paolo Fresch, Jinlin Fu, Wolfgang Funk, Emiliano Furfaro, Christian FÃd'rber, Abraham Gallas Torreira, Domenico Galli, Stefano Gallorini, Silvia Gambetta, Miriam Gandelman, Paolo Gandini, Yuanning Gao, Luis Miguel Garcia Martin, JuliÃ¡n GarcÃa PardiÃšas, Jordi Garra Tico, Lluis Garrido, Philip John Garsed, David Gascon, Clara Gaspar, Maurizio Gatta, Laura Gavardi, Giulio Gazzoni, David Gerick, Evelina Gersabeck, Marco Gersabeck, Timothy Gershon, Philippe Ghez, Sebastiana GianÃњ, Valerie Gibson, Olivier GÃúran Girard, Lavinia-Helena Giubega, Konstantin Gizdov, Vladimir Gligorov, Dmitry Golubkov, Andrey Golutvin, Alvaro Gomes, Igor Vladimirovich Gorelov, Claudio Gotti, Ekaterina Govorkova, Ricardo Graciani Diaz, Luis Alberto Granado Cardoso, Eugenii GraugÃls, Elena Graverini, Giacomo Graziani, Alexandru Grecu, Roman Greim, Peter Griffith, Lucia Grillo, Barak Raimond Gruberg Cazon, Oliver GrÃijnberg, Evgeny Gushchin, Yury Guz, Thierry Gys, Carla GÃúbel, Thomas Hadavizadeh, Christos Hadjivasilou, Guido Haefeli, Christophe Haen, Susan Haines, Brian Hamilton, Xiaoxue Han, Stephanie Hansmann-Menzemer, Neville Harnew, Samuel Harnew, Jonathan Harrison, Mark Hatch, Jibo He, Timothy Head, Arno Heister, Karol Hen-

nessy, Pierre Henrard, Louis Henry, Eric van Herwijnen, Miriam Heřšová, Adlánne Hicheur, Donal Hill, Christoph Hombach, P H Hopchev, Zachary Huard, Wouter Hulsbergen, Thibaud Humair, Mikhail Hushchyn, David Hutchcroft, Marek Idzik, Philip Ilten, Richard Jacobsson, Paweł Jalocha, Eddy Jans, Abolhassan Jawahery, Feng Jiang, Malcolm John, Daniel Johnson, Christopher Jones, Christian Joram, Beat Jost, Nathan Jurik, Sergii Kandybei, Matthias Karacson, James Mwangi Kariuki, Sarah Karodia, Matthieu Kecke, Matthew Kelsey, Matthew Kenzie, Tjeerd Ketel, Egor Khairullin, Basem Khanji, Chitsanu Khurewathanakul, Thomas Kirn, Suzanne Klaver, Konrad Klimaszewski, Tatsiana Klimkovich, Serhii Kolieiev, Michael Kolpin, Ilya Komarov, Patrick Koppenburg, Alena Kosmyntseva, Sofia Kotriakhova, Anastasiia Kozachuk, Mohamad Kozeiha, Leonid Kravchuk, Katharina Kreplin, Michal Kreps, Pavel Krokovny, Florian Kruse, Wojciech Krzemien, Wojciech Kucewicz, Marcin Kucharczyk, Vasily Kudryavtsev, Axel Kevin Kuonen, Krzysztof Kurek, Tengiz Kvaratskheliya, Daniel Lacarrere, George Lafferty, Adriano Lai, Christoph Langenbruch, Thomas Latham, Cristina Lazzeroni, Renaud Le Gac, Jeroen van Leerdam, Alexander Leflat, Jacques Lefrançois, Regis Lefèvre, Florian Lemaitre, Edgar Lemos Cid, Olivier Leroy, Tadeusz Lesiak, Blake Leverington, Tenglin Li, Yiming Li, Zhuoming Li, Tatiana Likhomanenko, Rolf Lindner, Federica Lionetto, Xuesong Liu, David Loh, Angelo Loi, Iain Longstaff, Jose Lopes, Donatella Lucchesi, Miriam Lucio Martinez, Haofei Luo, Anna Lupato, Eleonora Luppi, Oliver Lupton, Alberto Lusiani, Xiao-Rui Lyu, Frederic Machefert, Florin Maciuc, Oleg Maev, Kevin Maguire, Sneha Malde, Alexander Malinin, Timofei Maltsev, Giulia Manca, Giampiero Mancinelli, Peter Michael Manning, Jan Maratas, Jean François Marchand, Umberto Marconi, Carla Marin Benito, Matthieu Marinangeli, Pietro Marino, József Marks, Davide Marras, Giuseppe Martellotti, Morgan Martin, Maurizio Martinelli, Diego Martinez Santos, Fernando Martinez Vidal, Danielle Martins Tostes, Laure Marie Massacrier, Andrzej Massafferri, Rosen Matev, Abhijit Mathad, Zoltan Mathe, Clara Matteuzzi, Andrea Mauri, Emilie Maurice, Brice Maurin, Alexander Mazurov, Michael McCann, Andrew McNab, Ronan McNulty, Brian Meadows, Frank Meier, Dmytro Melnychuk, Marcel Merk, Andrea Merli, Emanuele Michielin, Diego Alejandro Milanes, Marie-Noelle Minard, Dominik Stefan Mitzel, Andrea Mogini, Josue Molina Rodriguez, Igancio Alberto Monroy, Stephane Monteil, Mauro Morandin, Piotr Morawski, Michael Joseph Morello, Olga Morgunova, Jakub Moron, Adam Benjamin Morris, Raymond Mountain, Franz Muheim, Mick Mulder, Manuel Mussini, Dominik Mäßller, Janine Mäßller, Katharina Mäßller, Vanessa

MÃijller, Paras Naik, Tatsuya Nakada, Raja Nandakumar, Anita Nandi, Irina Nasteva, Matthew Needham, Nicola Neri, Sebastian Neubert, Niko Neufeld, Max Neuner, Thi Dung Nguyen, Chung Nguyen-Mau, Simon Nieswand, Ramon Niet, Nikolay Nikitin, Thomas Nikodem, Alla Nogay, Alexey Novoselov, Daniel Patrick O'Hanlon, Agnieszka Oblakowska-Mucha, Vladimir Obraztsov, Stephen Ogilvy, Rudolf Oldeman, Gerco Onderwater, Juan Martin Otalora Goicochea, Adam Otto, Patrick Owen, Maria Aranzazu Oyanguren, Preema Rennee Pais, Antimo Palano, Matteo Palutan, Antonios Papanestis, Marco Pappagallo, Luciano Pappalardo, Cheryl Pappenheimer, William Parker, Christopher Parkes, Giovanni Passaleva, Alessandra Pastore, Mitesh Patel, Claudia Patrignani, Alex Pearce, Antonio Pellegrino, Gianni Penso, Monica Pepe Altarelli, Stefano Perazzini, Pascal Perret, Luca Pescatore, Konstantinos Petridis, Alessandro Petrolini, Aleksandr Petrov, Marco Petruzzo, Eduardo Picatoste Olloqui, Boleslaw Pietrzyk, Małgorzata Pikies, Davide Pinci, Alessandro Pistone, Alessio Piucci, Vlad-Mihai Placinta, Stephen Playfer, Maximo Plo Casasus, Tuomas Poikela, Francesco Polci, Marco Poli Lener, Anton Poluektov, Ivan Polyakov, Erica Polycarpo, Gabriela Johanna Pomery, Sébastien Ponce, Alexander Popov, Dmitry Popov, Bogdan Popovici, Stanislav Poslavskii, CÃldric Potterat, Eugenia Price, Jessica Prisciandaro, Claire Prouve, Valery Pugatch, Albert Puig Navarro, Giovanni Punzi, Chen Qian, Wenbin Qian, Renato Quagliani, Bartolomiej Rachwal, Jonas Rademacker, Matteo Rama, Miguel Ramos Pernas, Murilo Rangel, Iurii Raniuk, Fedor Ratnikov, Gerhard Raven, Federico Redi, Stefanie Reichert, Alberto dos Reis, Clara Remon Alepuz, Victor Renaudin, Stefania Ricciardi, Sophie Richards, Mariana Rihl, Kurt Rinnert, Vicente Rives Molina, Patrick Robbe, Ana Barbara Rodrigues, Eduardo Rodrigues, Jairo Alexis Rodriguez Lopez, Pablo Rodriguez Perez, Alexey Rogozhnikov, Stefan Roiser, Alexandra Paige Rollings, Vladimir Romanovskiy, Antonio Romero Vidal, John William Ronayne, Marcello Rotondo, Matthew Scott Rudolph, Thomas Ruf, Pablo Ruiz Valls, Juan Jose Saborido Silva, Elnur Sadykhov, Naylya Sagidova, Biagio Saitta, Valdir Salustino Guimaraes, David Sanchez Gonzalo, Carlos Sanchez Mayordomo, Brais Sanmartin Sedes, Roberta Santacesaria, Cibran Santamarina Rios, Marco Santimaria, Emanuele Santovetti, Alessandro Saputi, Alessio Sarti, Celestina Satriano, Alessia Satta, Daniel Martin Saunders, Darya Savrina, Stefan Schael, Margarete Schellenberg, Manuel Schiller, Heinrich Schindler, Maximilian Schlupp, Michael Schmelling, Timon Schmelzer, Burkhard Schmidt, Olivier Schneider, Andreas Schopper, HF Schreiner, Konstantin Schubert, Maxime Schubiger, Marie Helene Schune, Rainer Schwemmer, Barbara Sciascia, Adal-

berto Sciubba, Alexander Semennikov, Antonino Sergi, Nicola Serra, Justine Serrano, Lorenzo Sestini, Paul Seyfert, Mikhail Shapkin, Illya Shapoval, Yury Shcheglov, Tara Shears, Lev Shekhtman, Vladimir Shevchenko, Benedetto Gianluca Siddi, Rafael Silva Coutinho, Luiz Gustavo Silva de Oliveira, Gabriele Simi, Saverio Simone, Marek Sirendi, Nicola Skidmore, Tomasz Skwarnicki, Eluned Smith, Iwan Thomas Smith, Jackson Smith, Mark Smith, Lais Soares Lavra, Michael Sokoloff, Paul Soler, Bruno Souza De Paula, Bernhard Spaan, Patrick Spradlin, Srikanth Sridharan, Federico Stagni, Marian Stahl, Sascha Stahl, Pavol Steffko, Slavomira Stefkova, Olaf Steinkamp, Simon Stemmle, Oleg Stenyakin, Holger Stevens, Sabin Stoica, Sheldon Stone, Barbara Storaci, Simone Stracka, Maria Elena Stramaglia, Mihai Straticiuc, Ulrich Straumann, Liang Sun, William Sutcliffe, Krzysztof Swientek, Vasileios Syropoulos, Marek Szczechowski, Tomasz Szumlak, Stephane T'Jampens, Andrey Tayduganov, Tobias Tekampe, Giulia Tellarini, Frederic Teubert, Eric Thomas, Jeroen van Tilburg, Matthew James Tilley, Vincent Tisserand, Mark Tobin, Siim Tolk, Luca Tomassetti, Diego Tonelli, Stig Topp-Joergensen, Francis Toriello, Rafael Tourinho Jadallah Aoude, Edwige Tournefier, Stephane Tourneur, Karim Trabelsi, Murdo Traill, Minh TĂcм Tran, Marco Tresch, Ana Trisovic, Andrei Tsaregorodtsev, Panagiotis Tsopelas, Alison Tully, Niels Tuning, Artur Ukleja, Andrey Ustyuzhanin, Ulrich Uwer, Claudia Vacca, Vincenzo Vagnoni, Andrea Valassi, Sebastien Valat, Giovanni Valenti, Maarten Van Dijk, Ricardo Vazquez Gomez, Pablo Vazquez Regueiro, Stefania Vecchi, Maarten van Veghel, Jaap Velthuis, Michele Veltri, Giovanni Veneziano, Aravindhan Venkateswaran, Tobias Anton Verlage, Maxime Vernet, Mika Vesterinen, Joao Vitor Viana Barbosa, Benoit Viaud, Daniel Vieira, Maria Vieites Diaz, Harald Viemann, Xavier Vilasis-Cardona, Marcela Vitti, Vladimir Volkov, Achim Vollhardt, Balazs Voneki, Alexey Vorobyev, Vitaly Vorobyev, Christian VoĂ§, Jacco de Vries, Carlos VĂazquez Sierra, Roland Waldi, Charlotte Wallace, Ronan Wallace, John Walsh, Jianchun Wang, David Ward, Heather Mckenzie Wark, Nigel Watson, David Websdale, Andreas Weiden, Mark Whitehead, Jean Wicht, Guy Wilkinson, Michael Wilkinson, Mark Richard James Williams, Matthew Williams, Mike Williams, Timothy Williams, Fergus Wilson, Jack Wimberley, Michael Andreas Winn, Julian Wishahi, Wojciech Wislicki, Mariusz Witek, Guy Wormser, Stephen Wotton, Kenneth Wraight, Kenneth Wyllie, Yuehong Xie, Zhou Xing, Zhirui Xu, Zhenwei Yang, Zishuo Yang, Yuezhe Yao, Hang Yin, Jiesheng Yu, Xuhao Yuan, Oleg Yushchenko, Kristian Alexander Zarebski, Mikhail Zavertyaev, Liming Zhang, Yanxi Zhang, Alexey Zhelezov, Yangheng Zheng, Xianglei Zhu,

- Valery Zhukov, and Stefano Zucchelli. Expression of Interest for a Phase-II LHCb Upgrade: Opportunities in flavour physics, and beyond, in the HL-LHC era. Technical Report CERN-LHCC-2017-003, CERN, Geneva, Feb 2017.
- [50] A Dominguez, D Abbaneo, K Arndt, N Bacchetta, A Ball, E Bartz, W Bertl, G M Bilei, G Bolla, H W K Cheung, M Chertok, S Costa, N Demaria, Daniel Dominguez Vazquez, K Ecklund, W Erdmann, K Gill, G Hall, K Harder, F Hartmann, R Horisberger, W Johns, H C Kaestli, K Klein, D Kotlinski, S Kwan, M Pesaresi, H Postema, T Rohe, C SchÄdfer, A Starodumov, S Streuli, A Tricomi, P Tropea, J Troska, F Vasey, and W Zeuner. CMS Technical Design Report for the Pixel Detector Upgrade. Technical Report CERN-LHCC-2012-016. CMS-TDR-11, Sep 2012. Additional contacts: Jeffrey Spalding, Fermilab, Jeffrey.Spalding@cern.ch Didier Contardo, Universite Claude Bernard-Lyon I, didier.claude.contardo@cern.ch.
- [51] Niloufar Alipour Tehrani, Samir Arfaoui, Mathieu Benoit, Damiano Celeste, Dominik Dannheim, Florentina Pfleger, and Sophie Redford. Calibration of ultra-thin hybrid pixel detector assemblies with Timepix readout ASICs. Sep 2015.
- [52] I Rubinskiy. An EUDET/AIDA Pixel Beam Telescope for Detector Development. (AIDA-CONF-2015-035), Jun 2011.
- [53] M. Derrick, D. Gacek, N. Hill, B. Musgrave, R. Noland, E. Petereit, J. Repond, R. Stanek, and K. Sugano. Design and construction of the ZEUS barrel calorimeter. *Nucl. Instrum. Meth.*, A309:77–100, 1991.
- [54] R. Wigmans. Calorimetry: Energy measurement in particle physics. *Int. Ser. Monogr. Phys.*, 107:1–726, 2000.
- [55] L. Landau. On the energy loss of fast particles by ionization. *J. Phys.(USSR)*, 8:201–205, 1944.
- [56] H. Bichsel, Donald E. Groom, and S. R. Klein. Passage of particles through matter. 2004.
- [57] C. Adloff et al. The Time Structure of Hadronic Showers in highly granular Calorimeters with Tungsten and Steel Absorbers. *JINST*, 9:P07022, 2014.
- [58] C. Patrignani et al. Review of Particle Physics. *Chin. Phys.*, C40(10):100001, 2016.
- [59] J. B. Birks. *The theory and practice of scintillation counting*. Pergamon Press Oxford,

- 1964.
- [60] G. Folger and J. P. Wellisch. String parton models in GEANT4. *eConf*, C0303241:MONT007, 2003.
  - [61] *Geant4 Physics Reference Manual, Section IV, Chapter 28*.
  - [62] M. P. Guthrie, R. G. Alsmiller, and H. W. Bertini. Calculation of the capture of negative pions in light elements and comparison with experiments pertaining to cancer radiotherapy. *Nucl. Instrum. Meth.*, 66:29–36, 1968.
  - [63] E. Fermi. An attempt of a theory of beta radiation. 1. *Z. Phys.*, 88:161–177, 1934.
  - [64] Wolfgang Kilian, Thorsten Ohl, and Jurgen Reuter. WHIZARD: Simulating Multi-Particle Processes at LHC and ILC. *Eur. Phys. J.*, C71:1742, 2011.
  - [65] Mauro Moretti, Thorsten Ohl, and Jurgen Reuter. O'Mega: An Optimizing matrix element generator. 2001.
  - [66] Matteo Cacciari, Gavin P. Salam, and Gregory Soyez. FastJet User Manual. *Eur. Phys. J.*, C72:1896, 2012.
  - [67] Andreas Hoecker, Peter Speckmayer, Joerg Stelzer, Jan Therhaag, Eckhard von Toerne, and Helge Voss. TMVA: Toolkit for Multivariate Data Analysis. *PoS*, ACAT:040, 2007.
  - [68] Daniel R. Green, Patrick Meade, and Marc-Andre Pleier. Multi-Boson Interactions at the Run 1 LHC. *Submitted to: Rev. Mod. Phys.*, 2016.
  - [69] Andy Buckley. The hephthesis L<sup>A</sup>T<sub>E</sub>X class.



# List of figures

1.1	Schematic layout of the ILC, indicating all the major subsystems (not to scale). Figure taken from [3]. . . . .	4
1.2	CLIC layout at 3 TeV. Figure taken from [5]. . . . .	5
1.3	Cross section for production mechanisms of the Standard Model Higgs boson as a function of the collision energy. The cross sections were calculated assuming a Higgs mass of 120 GeV. Figure taken from [4]. . . . .	5
1.4	Angular distribution of number of particles for beam induced backgrounds for CLIC at a centre of mass energy of 3 TeV. Figure taken from [4]. . . . .	7
2.1	Gauge boson self-coupling vertices that are sensitive to the anomalous gauge couplings $\alpha_4$ and $\alpha_5$ . . . . .	21
2.2	Gauge boson self-coupling vertices in the Standard Model. . . . .	22
3.1	A typical simulated 250 GeV jet in the CLIC_ILD detector, with labels identifying constituent particles. Image taken from [25]. . . . .	25
3.2	(a) Quadrant view of the ILD detector concept. The interaction point is in the lower right corner of the picture. Dimensions are in mm. (b) An artistic view of the ILD detector concept. Figures taken from [26]. . . . .	26
3.3	Vertex detector design for ILD. Figures taken from [27]. . . . .	28

3.4 (a) Drawing of the proposed end-plate for the TPC. In the insert a back frame, which is designed to support the readout modules, is shown. (b) Conceptual sketch of the TPC system showing the main parts of the TPC (not to scale). The central electrode generates the axial electric field, the endplates collect the ionisation electrons, the field strips help to maintain a uniform electric field across the TPC and the voltage divider strips maintains the voltage difference between the anode and cathode. The field strips are held at fixed voltages such that they replicate the electric field produced by the electrodes. This reinforcing of the electric field configuration minimises non-uniformities in the electric field. The field cage of the TPC is not shown. . . . .	29
3.5 (a) A 3D detailed GEANT4 simulation description of the silicon system. (b) A quadrant view of the ILD silicon envelope made of the four components SIT, SET, ETD and FTD as included in the full MOKKA simulation. Figures taken from [26]. . . . .	30
3.6 A half-disk for the FTD showing the petal concept. The rightmost zoom image showers a detail of the end-of-petal area that houses the read-out electronics. The leftmost image shows the region at $R = 8$ cm where both the column width and the $R$ -dimension of the pixels changes. Figures taken from [26]. . . . .	31
3.7 Cross section through ECal layer for (a) silicon and (b) scintillator option. Figures taken from [26]. . . . .	33
3.8 The sensitive layers of the ILD muon system. Figure taken from [26]. . . . .	36
3.9 The very forward region of the ILD detector. LumiCal, BeamCal and LHCAL are carried by the support tube for the final focusing quadruple, QD0, and the beam pipe. Figure taken from [26]. . . . .	37
3.10 (a) Longitudinal (top quadrant) and (b) transverse cross section of the CLIC_ILD detector. Figures taken from [4]. . . . .	39

---

3.11 Schematic showing the definition of the pseudo-layer assignment for calorimeter hits. The solid lines indicate the positions of the physics ECal layers and the dashed lines show the definition of the virtual pseudo-layers. (a) The $xy$ -view showing the ILD ECal stave structure. (b) The $xz$ view showing a possible layout for the ECal barrel/endcap overlap region. The pseudo-layers are defined using projection back to the IP. Figures taken from [24]. . . . .	43
3.12 The main topological rules for cluster merging: (a) looping track segments; (b) track segments with gaps; (c) track segments pointing to hadronic showers; (d) track-like neutral clusters pointing back to a hadronic shower; (e) back-scattered tracks from hadronic showers; (f) neutral clusters which are close to a charged cluster; (g) a neutral cluster near a charged cluster; (h) cone association; and (i) recover of photons which overlap with a track segment. In each case the arrow indicates the track, the filled points represent the hits in the associated cluster and the open points represent hits in the neutral cluster. Figures taken from [24]. . . . .	44
3.13 500 GeV di-jet $Z \rightarrow u\bar{d}s$ event display for nominal ILD detector. . . . .	47
3.14 Definition of jet energy resolution. Reconstructed jet energy for 200 GeV di-jet $Z \rightarrow u\bar{d}s$ events for nominal ILD detector. . . . .	48
3.15 The reconstructed energy distribution for (a) 50 GeV $K_L^0$ and (b) 100 GeV $\gamma$ events. The red line shows a Gaussian fit used to parameterise the detector performance. The fit was applied to the truncated range of the reconstructed PFO energy distribution containing at least 75% of the data with the narrowest RMS. The nominal ILD model was used in this simulation. . . . .	51

3.16 (a) The energy resolution as a function of $\gamma$ energy for the silicon ECal option. The black markers indicate the energy resolutions for the full ILD simulation and the red dotted line shows the test beam parameterisation of the ECal energy resolution. (b) The energy resolution as a function of $\gamma$ energy for the scintillator ECal option. The black markers indicate the energy resolutions for the full ILD simulation and the red dotted line shows the test beam parameterisation of the ECal energy resolution. (c) The energy resolution as a function of neutral hadron energy. The black markers indicate the energy resolutions for the full ILD simulation, with the silicon ECal option, which was determined using $K_L^0$ s. The red dotted line shows the test beam parameterisation of the HCal energy resolution, which was determined using $\pi^\pm$ s. (d) The jet energy resolution (RMS <sub>90</sub> ) as a function of jet energy using the nominal ILD model, with the silicon ECal option. The intrinsic energy resolution and confusion contributions these the jet energy resolutions are also presented. The black dotted vertical line on the single particle energy resolutions shows the highest energy particles used in the test beam measurements. . . . .	54
4.1 Schematic cross section of an HV-CMOS sensor: the deep n-well is the charge-collecting electrode and also contains additional CMOS circuitry such as a preamplifier. Image taken from [48]. . . . .	57
4.2 Schematic cross section of an n-MOS transistor. p-MOS transistors have a similar cross section where the n and p doped regions are switched. . . . .	57
4.3 Schematic of CCPDv3 and CLICpix pixels. . . . .	59
4.4 Alignment schematic of the CCPDv3 and CLICpix detectors studied. The red dotted line represents the CCPDv3 pad and the solid black line represents the CLICpix top metal layer. From left to right; centred pixels, 1/4 offset (6.25 $\mu\text{m}$ ) and 1/2 offset (12.5 $\mu\text{m}$ ). . . . .	61
4.5 CCPDv3 voltage pulses produced using a radioactive source, Sr <sup>90</sup> , to deposit charge in the sensor. . . . .	63

4.6 An example calculation of the pulse height and rise time for the CCPDv3 output voltage. In this example the black line show the CCPDv3 output voltage as a function of time where the baseline voltage has been subtracted and the pulse shape inverted. These voltage pulses were created using a radioactive source, Sr <sup>90</sup> , to deposit charge in the sensor. (a) The definition of the pulse height. Pulse height is defined as the amplitude of a Gaussian function fitted across the peak of the voltage pulse. The peak of the voltage pulse is defined as the region where the voltage in excess of 90% of the raw pulse height, which is indicated in the figure by the red arrow. The red dotted line shows the Gaussian fit used to extract the pulse height. (b) The definition of rise time. Rise time is defined as the time taken for the CCPDv3 voltage to rise from 10% to 90% of the raw pulse height. The rise time, and change in CCPDv3 output voltage over this time, are shown in the figure by the blue arrows. . . . .	64
4.7 The CCPDv3 output voltage rise time as a function of pulse height. . . . .	65
4.8 The mean ToT measured on the CLICpix ASIC as a function of CCPDv3 voltage pulse height. . . . .	66
4.9 The mean ToT measured on the adjacent CLICpix pixel, along the direction of the offset, as a function of CCPDv3 voltage pulse height for (a) the centred and (b) the misaligned devices. . . . .	68
4.10 The CLICpix ToT as a function of injected pulse height. The black markers show the mean ToT and the error bars show the standard error. . . . .	70
4.11 CLICpix ToT as a function of injected pulse height. . . . .	71
4.12 The distribution of the surrogate function parameters obtained when fitting the ToT as a function of injected pulse height for SET 9. (a), (b), (c) and (d) show the distribution of the $a$ , $b$ , $c$ and $d$ parameters respectively. . . . .	72
4.13 The distribution of selected surrogate function parameters obtained when fitting the ToT as a function of injected pulse height for SET 9 as a function of matrix position. (a) and (b) show the distribution of the $c$ and $t$ parameters respectively. . . . .	73

4.14 The average ToT response as a function of injected pulse height, which is represented using the surrogate function. Parameters for the surrogate function are obtained by fitting the ToT against pulse height curve for all pixels in the matrix. The results are divided into even and odd columns to account for the differing effective thresholds on alternate CLICpix columns. . . . .	74
4.15 The efficiency of the devices considered as a function of the threshold applied. . . . .	77
5.1 (a) The sum of calorimeter hit energies in ECal and HCal for 10 GeV $\gamma$ events. (b) The sum of the ECal calorimeter hit energies for 10 GeV $\gamma$ events with and without the selection cuts. . . . .	85
5.2 Gaussian fit to sum of the ECal calorimeter hit energies for 10 GeV $\gamma$ events with selection cuts. The coarse binning reflects the tolerance on the digitisation constant calibration. . . . .	86
5.3 (a) Sum of calorimeter hit energies in ECal and HCal for 20 GeV $K_L^0$ events. (b) Sum of the HCal calorimeter hit energies for a 20 GeV $K_L^0$ events with and without the selection cuts. . . . .	88
5.4 Gaussian fit to sum of the HCal calorimeter hit energies for 20 GeV $K_L^0$ events with selection cuts. . . . .	88
5.5 A PandoraPFA event display showing the nominal ILD calorimeters. (a) the ECal, (b) the full HCal and (c) the HCal ring. . . . .	89
5.6 The active layer calorimeter hit energy distributions for (a) the ECal, (b) the HCal barrel, (c) the HCal endcap and (d) the HCal ring for 10 GeV $\mu^-$ events. . . . .	90
5.7 The calorimeter hit energy distributions for (a) the ECal, (b) the HCal and (c) the muon chamber for 10 GeV $\mu^-$ events. . . . .	91
5.8 (a) The sum of the electromagnetic energy measured in the ECal for 10 GeV $\gamma$ events with and without the selection cuts. (b) Gaussian fit to sum of the electromagnetic energy deposited in the ECal for 10 GeV $\gamma$ events with selection cuts. The fine binning reflects the tolerance on the electromagnetic scale calibration constant in the ECal. . . . .	93

5.9	The distribution of hadronic energy measured in the ECal and HCal for 20 GeV $K_L^0$ events with and without selection cuts. . . . .	94
5.10	An example showing the definition of $r_i$ , the variable used for the calculation of $\chi^2(\delta_{ECal}^{Had}, \delta_{HCal}^{Had})$ in determining the hadronic energy scale factors. . . . .	95
5.11	The weights, $\omega$ , used in the HCal hit energy truncation as a function of the energy density of the HCal hit, $\rho$ . The truncation shown here corresponds to a 1 GeV truncation in the nominal ILD HCal. . . . .	98
5.12	The energy resolution as a function of HCal cell truncation for (a) 50 GeV $K_L^0$ events and (b) 100 GeV $\gamma$ events using the nominal ILD detector model. . . . .	98
5.13	The jet energy resolution as a function of jet energy for various hadronic cell truncations. The results shown use the nominal ILD detector model. . . . .	99
5.14	The jet energy resolution as a function of HCal cell size using a HCal hit energy truncation that is (a) optimised and (b) fixed at 1 GeV. . . . .	100
5.15	An event display for a 500 GeV $Z \rightarrow u\bar{d}s$ di-jet event reconstructed using the nominal ILD detector. (a) The full event environment. (b) A single hadronic cluster from the same event where shading indicates the energy density in the HCal. High energy density cells are coloured red, while lower energy density cells are coloured blue. All ECal hits are shaded black. The high energy density electromagnetic core of the selected hadronic cluster is clearly visible. . . . .	101
5.16	Parameters used in software compensation weight determination as a function of $E_{Raw}$ . . . . .	102
5.17	The software compensation weight applied to a calorimeter hit as a function of calorimeter hit energy density for various cluster energies. . . . .	103
5.18	The energy resolution as a function of the MC energy for single $K_L^0$ events using various energy correction settings. The detector model used was the nominal ILD detector model. . . . .	105

5.19	The jet energy resolution as a function of the jet energy for a variety of different energy correction options. These results were produced for the nominal ILD detector model. . . . .	105
5.20	The contributions to the jet energy resolution as a function of the jet energy for a variety of different energy correction options. (a) is the intrinsic energy resolution of the detector and (b) is the total confusion term. The quadrature sum of both yields the standard reconstruction performance. These results were produced for the nominal ILD detector model. . . . .	106
5.21	The energy resolution as a function of calorimeter timing window for (a) 100 GeV $\gamma$ events and (b) 50 GeV $K_L^0$ events using the nominal ILD detector model. . . . .	108
5.22	The distribution of the time of the calorimeter hits, corrected for time of flight to the impact point, for 91 GeV $Z \rightarrow u\bar{d}s$ di-jet events. . . . .	109
5.23	The jet energy resolution as a function of jet energy for various calorimeter timing cuts. The results shown use the nominal ILD detector model. . . . .	109
6.1	The energy resolution as a function of ECal cell size for 100 GeV $\gamma$ s using the nominal ILD detector model with (a) the silicon and (b) the scintillator ECal option. . . . .	114
6.2	The jet energy resolution as a function of ECal cell size for various jet energies using the nominal ILD detector model with (a) the silicon and (b) the scintillator ECal option. . . . .	115
6.3	The contributions to the jet energy resolution as a function of ECal cell size using the nominal ILD detector model for (a) the silicon ECal option and 45 GeV jets, (b) the scintillator ECal option and 45 GeV jets, (c) the silicon ECal option and 250 GeV jets and (d) the scintillator ECal option and 250 GeV jets. The black curves correspond to the standard reconstruction, the blue curves to the intrinsic energy resolution contribution to the jet energy resolution, the red curves to the confusion contribution to the jet energy resolution and the magenta curves to the confusion contribution to the jet energy resolution related solely to $\gamma$ reconstruction. . . . .	116

---

6.4	The energy resolution as a function of number of layers in the ECal for 100 GeV $\gamma$ s using the nominal ILD detector model with (a) the silicon and (b) the scintillator ECal option. . . . .	117
6.5	The jet energy resolution as a function of number of layers in the ECal for various jet energies using the nominal ILD detector model with (a) the silicon and (b) the scintillator ECal option. . . . .	118
6.6	The contributions to the jet energy resolution as a function of number of layers in the ECal using the nominal ILD detector model for (a) the silicon ECal option and 45 GeV jets, (b) the scintillator ECal option and 45 GeV jets, (c) the silicon ECal option and 250 GeV jets and (d) the scintillator ECal option and 250 GeV jets. The black curves correspond to the standard reconstruction, the blue curves to the intrinsic energy resolution contribution to the jet energy resolution, the red curves to the confusion contribution to the jet energy resolution and the magenta curves to the confusion contribution to the jet energy resolution related solely to $\gamma$ reconstruction. . . . .	119
6.7	The energy resolution as a function of HCal cell size for 50 GeV $K_L^0$ events using the nominal ILD detector model. . . . .	123
6.8	The jet energy resolution as a function of HCal cell size for various jet energies using the nominal ILD detector model. . . . .	124
6.9	The contributions to the jet energy resolution as a function of HCal cell size using the nominal ILD detector model for (a) 45 GeV jets and (b) 250 GeV jets. The black curves correspond to the standard reconstruction, the blue curves to the intrinsic energy resolution contribution to the jet energy resolution, the red curves to the confusion contribution to the jet energy resolution and the magenta curves to the confusion contribution to the jet energy resolution related solely to $\gamma$ reconstruction.	124
6.10	The energy resolution as a function of number of layers in the HCal for 50 GeV $K_L^0$ events using the nominal ILD detector model. . . . .	126
6.11	The jet energy resolution as a function of number of layers in the HCal for various jet energies using the nominal ILD detector model. . . . .	127

6.12 The contributions to the jet energy resolution as a function of number of layers in the HCal using the nominal ILD detector model for (a) 45 GeV jets and (b) 250 GeV jets. The black curves correspond to the standard reconstruction, the blue curves to the intrinsic energy resolution contribution to the jet energy resolution, the red curves to the confusion contribution to the jet energy resolution and the magenta curves to the confusion contribution to the jet energy resolution related solely to $\gamma$ reconstruction. . . . .	127
6.13 The energy resolution as a function of sampling frequency in the HCal for 50 GeV $K_L^0$ events using the nominal ILD detector model. . . . .	129
6.14 The jet energy resolution as a function of sampling frequency in the HCal for various jet energies using the nominal ILD detector model. . . . .	129
6.15 The contributions to the jet energy resolution as a function of sampling frequency in the HCal using the nominal ILD detector model for (a) 45 GeV jets and (b) 250 GeV jets. The black curves correspond to the standard reconstruction, the blue curves to the intrinsic energy resolution contribution to the jet energy resolution, the red curves to the confusion contribution to the jet energy resolution and the magenta curves to the confusion contribution to the jet energy resolution related solely to $\gamma$ reconstruction. . . . .	130
6.16 The fraction of the total calorimetric energy deposited in the HCal as a function of time for 25 GeV $K_L^0$ events using the steel and tungsten HCal options. Results are shown for both the QGSP_BERT and QGSP_BERT_HP physics lists. The calorimeter hit times have been corrected for straight line time of flight to the impact point. . . . .	133
6.17 The jet energy resolution using the nominal ILD detector as a function of the magnetic field strength for various jet energies. . . . .	136

---

6.18 The contributions to the jet energy resolution as a function of the magnetic field strength using the nominal ILD detector model for (a) 45 GeV jets and (b) 250 GeV jets. The black curves correspond to the standard reconstruction, the blue curves to the intrinsic energy resolution contribution to the jet energy resolution, the red curves to the confusion contribution to the jet energy resolution and the magenta curves to the confusion contribution to the jet energy resolution related solely to $\gamma$ reconstruction. . . . .	138
6.19 The mean number of reconstructed charged particles as a function of the magnetic field strength for 91 GeV $Z \rightarrow u\bar{d}s\bar{s}$ di-jet events. The nominal ILD detector model was used and the pattern recognition has been fully cheated using the MC information. . . . .	138
6.20 The jet energy resolution using the nominal ILD detector as a function of the ECal inner radius for various jet energies. . . . .	139
6.21 The contributions to the jet energy resolution as a function of the ECal inner radius using the nominal ILD detector model for (a) 45 GeV jets and (b) 250 GeV jets. The black curves correspond to the standard reconstruction, the blue curves to the intrinsic energy resolution contribution to the jet energy resolution, the red curves to the confusion contribution to the jet energy resolution and the magenta curves to the confusion contribution to the jet energy resolution related solely to $\gamma$ reconstruction.	140
7.1 Gauge boson self-coupling vertices in the standard model. . . . .	142
7.2 Four-point vertex proposed for explanation of beta decay by Fermi. . . . .	143
7.3 Example of vector boson scattering Feynman diagrams showing sensitivity to quartic gauge boson self-interaction vertices. The diagrams selected here are relevant for the CLIC experiment. In these diagrams $q$ represents $u, \bar{u}, d, \bar{d}, s, \bar{s}, c, \bar{c}, b$ or $\bar{b}$ ; $l$ represents $e^\pm, \mu^\pm$ or $\tau^\pm$ ; and $\nu$ represents $\nu_e, \bar{\nu}_e, \nu_\mu, \bar{\nu}_\mu, \nu_\tau$ and $\bar{\nu}_\tau$ . . . . .	144
7.4 The event weight as a function of the anomalous couplings $\alpha_4$ and $\alpha_5$ for a selection of $\nu\nu qqqq$ final state events at 1.4 TeV. . . . .	148

7.5 The reconstructed masses for different choices of jet algorithm for 1.4 TeV $\nu\nu\text{qqqq}$ final state events. The masses are determined by forcing the events into 4 jets and then pairing the jet pairs to form candidate bosons. The jet pairing configuration is determined by pairing jets such that the mass differences between the two candidate bosons is a minimum. These samples should be dominated by vector boson scattering involving pairs of outgoing W bosons and so it is expected that a peak at the W boson mass, $m_W = 80.385 \pm 0.015$ GeV [11], should be observed. As this does not occur for the Cambridge-Aachen algorithm or the EE_kt algorithm they were deemed unsuitable for this analysis. In the case of the kt algorithm and the EE_kt algorithm an R parameter of 0.7 was used. . . . .	152
7.6 $\chi^2$ sensitivity distributions from a fit to $M_{VV}$ for the signal $\text{qqqq}\nu\nu$ final state only at 1.4 TeV. These results use the optimal jet algorithm configuration of selected PFOs and an R parameter of 0.9 in the $k_t$ algorithm. (a) $\chi^2$ sensitivity contours in $\alpha_4$ and $\alpha_5$ space. (b) $\chi^2$ as a function of $\alpha_4$ assuming $\alpha_5 = 0$ . (c) $\chi^2$ as a function of $\alpha_5$ assuming $\alpha_4 = 0.154$	
7.7 The jet energy resolution as a function of the jet energy for the $\nu\nu\text{qqqq}$ final state at 1.4 TeV. . . . .	157
7.8 Distribution of variables cut on in the preselection at 1.4 TeV. (a) The transverse momentum of the visible system. (b) The number of isolated leptons in the system. (c) The legend for the preceding plots. . . . .	159
7.9 Background rejection as a function of signal efficiency for a variety of MVA options at 1.4 TeV. . . . .	160
7.10 Impact of preselection and MVA on the reconstructed invariant mass of the bosons arising from jet pairing at 1.4 TeV. (b) No cuts applied. (b) Preselection cuts applied. (c) MVA with preselection applied. (d) The legend for the event selection plots. . . . .	161
7.11 The sensitivity of $M_{VV}$ to the anomalous gauge couplings $\alpha_4$ and $\alpha_5$ at 1.4 TeV. The jet algorithm used was the longitudinally invariant kt algorithm with an R parameter of 0.9 and Selected PFOs were used. This distribution is for the $\nu\nu\text{qqqq}$ signal final state only. . . . .	164

---

7.12 The sensitivity of various variables to the anomalous gauge couplings $\alpha_4$ and $\alpha_5$ at 1.4 TeV. The jet algorithm used was the longitudinally invariant kt algorithm with an R parameter of 0.9 and Selected PFOs were used. This distribution is for the $\nu\nu\text{qqqq}$ signal final state only. (a) shows the distribution of $\cos\theta_{\text{jets}}^*$ and (b) shows the distribution of $\cos\theta_{\text{Bosons}}^*$ . . . . .	164
7.13 A selection of plots showing how the event weight changes when varying the anomalous couplings $\alpha_4$ and $\alpha_5$ for 1.4 TeV $\nu\nu\text{qqqq}$ final state events. The hollow circles show the event weight produced from the generator, while the surface shown is found using bicubic interpolation between those points. . . . .	166
7.14 $\chi^2$ sensitivity distributions from a fit to $M_{VV}$ at 1.4 TeV. Results include the effect of backgrounds after the application of a series of preselection cuts and MVA. (a) $\chi^2$ sensitivity contours in $\alpha_4$ and $\alpha_5$ space. (b) $\chi^2$ as a function of $\alpha_4$ assuming $\alpha_5 = 0$ . (c) $\chi^2$ as a function of $\alpha_5$ assuming $\alpha_4 = 0$ . . . . .	168
7.15 68% sensitivity contour including systematic errors, of varying magnitudes, in dominant background cross sections. . . . .	169
7.16 Distributions of $M_{VV}$ for the $\nu\nu\text{qqqq}$ , with and without the effect from anomalous couplings, and the combined dominant background processes $\gamma_{\text{BS}}\text{e}^\pm \rightarrow \text{qqqq}\nu$ . . . . .	170
7.17 $\chi^2$ sensitivity distributions from a fit to $M_{VV}$ at 3 TeV. Results include the effect of backgrounds after the application of a series of preselection cuts and MVA. (a) $\chi^2$ sensitivity contours in $\alpha_4$ and $\alpha_5$ space. (b) $\chi^2$ as a function of $\alpha_4$ assuming $\alpha_5 = 0$ . (c) $\chi^2$ as a function of $\alpha_5$ assuming $\alpha_4 = 0$ . . . . .	173



# List of tables

2.1	The mass, spin and electric charge (Q) of the leptons found in the Standard Model [11]. Neutrino masses have not been included in the above table as precise measurements are yet to be made. However, oscillations between different neutrino flavour states have been observed, which indicates that the flavour and mass eigenstates differ and that the neutrinos have a non-zero mass. The current upper bound on neutrino mass measurements is 2 eV. . . . .	12
2.2	The mass, spin and electric charge (Q) of the quarks found in the Standard Model [11]. Each of the particles in the above table corresponds to three fermion fields, one for each of the three colours of the SU(3) symmetry. . . . .	12
2.3	The mass, spin and electric charge (Q) of the gauge bosons found in the Standard Model [11]. The $\gamma$ and $g_s$ theoretically have zero mass, which is consistent with measurements. The upper bound on the $\gamma$ mass has been measured at $10^{-18}$ eV, while gluon masses of up to a few MeV have not been precluded. The upper bound on the magnitude of the charge of the $\gamma$ is measured at $10^{-35}$ . . . . .	13
3.1	The approximate jet fractions and energy resolutions for charged particles ( $X^\pm$ ) of energy $E_{X^\pm}$ , photons ( $\gamma$ ) of energy $E_\gamma$ and neutral hadrons ( $X^0$ ) of energy $E_{X^0}$ . Taken from [24]. . . . .	24
3.2	Coverage of the supplementary silicon tracking systems in the ILD detector. In this table $\theta$ is the polar angle with respect to the beam direction. Taken from [26]. . . . .	30

3.3	Comparison of the nuclear interaction length $\lambda_I$ , radiation length $X_0$ and Moli��re radius for iron, copper, tungsten and lead. Table taken from [24]. . . . .	33
3.4	Comparison of the ECal energy resolutions for various experiments. . . . .	33
3.5	Comparison of the HCal energy resolutions for various experiments. . . . .	35
3.6	Coverage of the forward calorimeters in the ILD detector. . . . .	37
3.7	Example calculation of the confusion contributions to the jet energy resolution. These jet energy resolutions are for 250 GeV jets using the nominal ILD detector model. . . . .	49
4.1	A list detailing the alignment of the CCPDv3 and CLICpix coupling pads for the devices considered in this study. . . . .	61
4.2	The average fit parameters for even columns of CLICpix sensor. The reported error was calculated using the standard error in the mean when averaging the fit parameters across the matrix. . . . .	73
4.3	The average fit parameters for odd columns of CLICpix sensor. The reported error was calculated using the standard error in the mean when averaging the fit parameters across the matrix. . . . .	74
5.1	The train structure for 500 GeV ILC and 3 TeV CLIC [4, 26]. . . . .	108
6.1	The configuration of the ECal in the nominal ILD detector model. The parameters are given for the nominal silicon model as well as the alternative scintillator option. . . . .	112
6.2	The longitudinal structure of the ECal models considered in the optimisation study. The radiation length of tungsten absorber is 3.504mm [58]. Note that a presampler layer contributes one extra layer to the cumulative number of layers. . . . .	117
6.3	The configuration of the HCal in the nominal ILD detector model. . . . .	121
6.4	Cell size layout of various HCal models considered. . . . .	128
6.5	The configuration of the steel and tungsten HCal options. . . . .	132

6.6	The energy resolution using the nominal ILD detector with various HCal options determined using 50 GeV $K_L^0$ events. . . . .	133
6.7	The jet energy resolution using the nominal ILD detector with various HCal options for various jet energies. . . . .	135
6.8	The contributions to the jet energy resolution using the nominal ILD detector with various HCal options for 45 and 250 GeV jet energies. . .	135
7.1	Cross sections of signal and background processes at 1.4 TeV . . . . .	147
7.2	Cross sections for selected processes showing the effect of the anomalous gauge couplings $\alpha_4$ and $\alpha_5$ at 1.4 TeV. . . . .	149
7.3	The efficiency of isolated lepton finding at 1.4 TeV for the $\nu\nu\text{qqqq}$ and $\bar{\nu}\text{qqqq}$ final states. . . . .	155
7.4	Selection summary at 1.4 TeV. The EPA and BS subscript on the incoming photon indicates whether the photon is generated from the equivalent photon approximation or beamstrahlung. Cells omitting the efficiency indicate an efficiency of less than 0.1%. . . . .	162
7.5	Cross sections of signal and background processes at 3 TeV . . . . .	171
7.6	Selection summary at 3 TeV. The EPA and BS subscript on the incoming photon indicates whether the photon is generated from the equivalent photon approximation or beamstrahlung. Cells omitting the efficiency indicate an efficiency of less than 0.1%. . . . .	172